Springer ThesesRecognizing Outstanding Ph.D. Research

Clara Guglieri Rodríguez

Relationship Between Structure and Magnetic Behaviour in ZnO-Based Systems



Springer Theses

Recognizing Outstanding Ph.D. Research

Aims and Scope

The series "Springer Theses" brings together a selection of the very best Ph.D. theses from around the world and across the physical sciences. Nominated and endorsed by two recognized specialists, each published volume has been selected for its scientific excellence and the high impact of its contents for the pertinent field of research. For greater accessibility to non-specialists, the published versions include an extended introduction, as well as a foreword by the student's supervisor explaining the special relevance of the work for the field. As a whole, the series will provide a valuable resource both for newcomers to the research fields described, and for other scientists seeking detailed background information on special questions. Finally, it provides an accredited documentation of the valuable contributions made by today's younger generation of scientists.

Theses are accepted into the series by invited nomination only and must fulfill all of the following criteria

- They must be written in good English.
- The topic should fall within the confines of Chemistry, Physics, Earth Sciences, Engineering and related interdisciplinary fields such as Materials, Nanoscience, Chemical Engineering, Complex Systems and Biophysics.
- The work reported in the thesis must represent a significant scientific advance.
- If the thesis includes previously published material, permission to reproduce this must be gained from the respective copyright holder.
- They must have been examined and passed during the 12 months prior to nomination.
- Each thesis should include a foreword by the supervisor outlining the significance of its content.
- The theses should have a clearly defined structure including an introduction accessible to scientists not expert in that particular field.

More information about this series at http://www.springer.com/series/8790

Clara Guglieri Rodríguez

Relationship Between Structure and Magnetic Behaviour in ZnO-Based Systems

Doctoral Thesis accepted by the University of Zaragoza, Spain



Author
Dr. Clara Guglieri Rodríguez
Consejo Superior de Investigaciones
Cientificas
University of Zaragoza
Zaragoza
Spain

Supervisor
Prof. Jesús Chaboy
Consejo Superior de Investigaciones
Cientificas, Instituto de Ciencia de
Materiales de Aragon Zaragoza
University of Zaragoza
Zaragoza
Spain

ISSN 2190-5053 Springer Theses ISBN 978-3-319-18886-7 DOI 10.1007/978-3-319-18887-4

ISSN 2190-5061 (electronic)

ISBN 978-3-319-18887-4 (eBook)

Library of Congress Control Number: 2015940001

Springer Cham Heidelberg New York Dordrecht London © Springer International Publishing Switzerland 2015

This work is subject to copyright. All rights are reserved by the Publisher, whether the whole or part of the material is concerned, specifically the rights of translation, reprinting, reuse of illustrations, recitation, broadcasting, reproduction on microfilms or in any other physical way, and transmission or information storage and retrieval, electronic adaptation, computer software, or by similar or dissimilar methodology now known or hereafter developed.

The use of general descriptive names, registered names, trademarks, service marks, etc. in this publication does not imply, even in the absence of a specific statement, that such names are exempt from the relevant protective laws and regulations and therefore free for general use.

The publisher, the authors and the editors are safe to assume that the advice and information in this book are believed to be true and accurate at the date of publication. Neither the publisher nor the authors or the editors give a warranty, express or implied, with respect to the material contained herein or for any errors or omissions that may have been made.

Printed on acid-free paper

Springer International Publishing AG Switzerland is part of Springer Science+Business Media (www.springer.com)

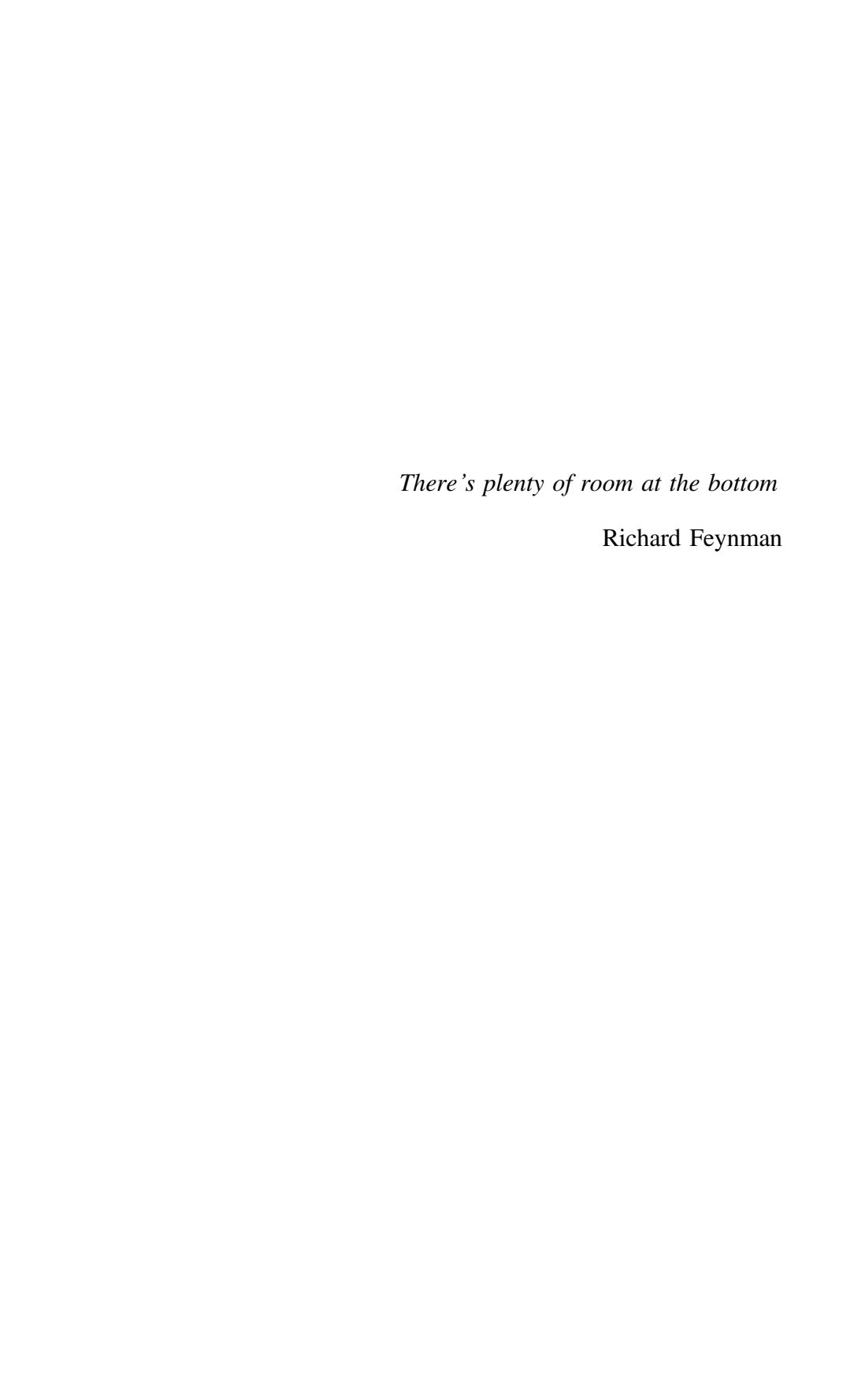
Parts of this thesis have been published in the following journal articles:

As a result of the work described in this dissertation, the following papers have been published:

- 1. Development of a well defined ZnO-ZnS interface in THIOL-capped ZnO nanoparticles exhibiting anomalous magnetic properties. C. Guglieri and J. Chaboy. J. Phys. Chem. C, 114, 19629 (2010).
- 2. XAS characterization of the interface in capped ZnO nanoparticles. C. Guglieri and J. Chaboy. Diamond Light Source Proceedings, Vol 1, e143, SRMS-7 (2011).
- 3. X-ray absorption study of the local order around Mn in Mn:ZnO thin films: the role of vacancies and structural distortions. C. Guglieri, E. Céspedes, C. Prieto and J. Chaboy. J. Phys.: Condens. Matter 23, 206006 (2011).
- XMCD proof of ferromagnetic behaviour in ZnO nanoparticles. C. Guglieri,
 M. A. Laguna-Marco, M. A. García, N. Carmona, E. Céspedes, M. García-Hernández, A. Espinosa, and J. Chabov. J. Phys. Chem. C, 116, 6608 (2012).
- Relationship between the magnetic properties and the formation of a ZnS/ZnO interface in S-capped ZnO nanoparticles and ZnS-ZnO thin films. C. Guglieri, A. Espinosa, N. Carmona, M. A. Laguna-Marco, E. Céspedes, M. L. Ruiz-González, J. M. González-Calbet, M. García-Hernández, M. A. García, and J. Chaboy. J. Phys. Chem. C, 117 (23), 12199 (2013).
- Evidence of oxygen ferromagnetism in ZnO based materials.
 C. Guglieri, E. Céspedes, A. Espinosa, M. A. Laguna-Marco, N. Carmona, Y. Takeda, T. Okane, T. Nakamura, M. García-Hernández, M. A. García, J. Chaboy. Adv. Funct. Mater. 24, 2094–2100 (2014).

Additional publications in different related fields are:

- Raman and X-ray absorption spectroscopy study of the phase evolution induced by mechanical milling in R₂O₃:TiO₂ mixtures. J. Chaboy, M. L. Sanjuán, C. Guglieri, S. Díaz-Moreno, G. Aquilanti, L. Olivi, A. F. Fuentes. Phys. Rev. B 84, 104207 (2011).
- On the origin of the magnetism of Mn-Zn-O systems: structural, electronic, and magnetic study of exotic MnO_{2-S}/ZnO thin films. E. Céspedes, M. A. Laguna-Marco, F. Jiménez-Villacorta, J. Chaboy, R. Boada, C. Guglieri, A. de Andrés and C. Prieto. J. Phys. Chem. C, 115 (49), 24092 (2011).





Supervisor's Foreword

One of the main goals of material science nowadays is the development of multifunctional materials combining properties that are not found together in traditional materials. For instance, the coexistence of semiconductor properties (the basis for microprocessors) and room temperature ferromagnetism (as non-volatile memories) in a single material will push the development of new optoelectronic devices with higher reliability and lower power consumption.

Discoveries of room-temperature ferromagnetism (RTFM) in semiconductors hold great promise for future spintronics technologies. Unfortunately, this ferromagnetism remains poorly understood and the debate concerning the nature, carrier-mediated defect-mediated, of ferromagnetism in semiconducting oxides is still open. In addition, elucidating whether or not this ferromagnetism is intrinsic, as is required for spintronic applications, has been cited as among the most important problems to emerge in magnetism in recent years.

ZnO constitutes a paradigmatic case among the so-called Diluted Magnetic Semiconductor (DMS) materials consisting of a semiconductor matrix with a small amount of dispersed magnetic impurities. Although initially 3D magnetic elements were employed as impurities, the appearance of ferromagnetism in ZnO has also been reported in the absence of magnetic elements, e.g. for non-magnetic transition metals or even non-metals like N or C. Yet, even after more than ten years of intense research, it is not clear whether these materials are intrinsically ferromagnetic and experimental confirmations are required for the clarification of this exotic magnetic behaviour.

Clara Guglieri's thesis work aimed to provide a full characterization of this new magnetic behaviour emerging in traditionally "non-magnetic" materials. To this end ZnO nanoparticles capped with different organic molecules were synthetized as well as different ZnO/ZnS heterostructures. All these materials show magnetic properties ranging from pure diamagnetism to the appearance of room temperature ferromagnetism. Clara started a systematic and deep study of the structural, electronic and magnetic properties of these materials (including 10 different characterization techniques) confirming the reproducibility of the results.

Even when the reliability of the macroscopic results revealing RTFM behaviour was obtained by accurate full sets of control experiments, further confirmation was obtained using X-ray magnetic circular dichroism (XMCD). Indeed, applying X-ray Absorption Spectroscopy (XAS) and related methods to the study of these ZnO-based materials proved to be critical for understanding the observed magnetic phenomena due to the element-specific character of these techniques.

Apart from confirming the intrinsic nature of the observed RTFM, the combination of XAS, XMCD and ab-initio calculations carried out by Clara led to the identification of a direct relationship between the magnetic behaviour and size reduction through the formation of an interface in these materials, where the ferromagnetism resides. The fact that the structural details of the interface (thickness, interpenetration, etc.) determine the particular magnetic properties of each system allows one to understand irreconcilable results previously reported for seemingly identical materials.

The final step in Clara's thesis was the discovery of the ferromagnetic polarization of the O(2p) states. The occurrence of ferromagnetic behaviour at the oxygen atoms in these and similar systems has so far been sought in vain. Guglieri's findings provide, for the first time, direct support of claims regarding the appearance of oxygen magnetism in oxide semiconductors at the nanoscale.

In my opinion, Clara's thesis provides important insights into an issue that has remained unsolved for more than 10 years of research. The results end the long-standing controversy about the existence of intrinsic RTFM in ZnO-based systems, providing new insights to finally establish the mechanism that induces the ferromagnetic order in these systems. Clara's thesis brings support to this new route towards room-temperature semiconductor spintronics and, consequently, to pushing the development of new functional materials.

Zaragoza, Spain February 2015 Prof. Jesús Chaboy

Contents

1	Intr	oduction	1			
	1.1	1 State of the Art				
	1.2	.2 Outlook of This Dissertation				
	1.3	Dissertation Structure	6			
	Refe	erences	6			
2	Syn	thesis and In-house Characterization of Materials	11			
	2.1	Synthesis	11			
		2.1.1 Nanoparticles	11			
		2.1.2 Thin Films and Multilayers	14			
	2.2	Structural Characterization	16			
		2.2.1 X-ray Diffraction (XRD)	16			
		2.2.2 X-ray Reflectivity (XRR)	20			
		2.2.3 Transmission Electron Microscopy (TEM),				
		High Resolution Transmission Electron				
		Microscopy (HRTEM) and Energy Dispersive				
		X-ray Spectroscopy (EDX)	21			
	2.3	Optical Absorption	24			
	2.4	Magnetic Characterization: AC Susceptibility				
		and Magnetization	26			
	Refe	erences	34			
3	XAS	S and XMCD Spectroscopies	37			
	3.1	X-ray Absorption Spectroscopy	38			
	3.2	X-Magnetic Circular Dichroism	45			
	3.3	Experimental Methods and Procedures	50			
		3.3.1 Synchrotron Radiation Facilities	50			
		3.3.2 BL39XII Reamline at SPring-8 Facility	51			

xiv Contents

		3.3.3 BL25SU Beamline at SPring-8 Facility	56				
		3.3.4 BL23SU Beamline at SPring-8 Facility	58				
		3.3.5 XAFS Beamline at Elettra Facility	60				
	3.4	Ab-Initio Calculations of XANES Spectra	63				
	Refe	erences	65				
4		c K-edge X-ray Absorption Study of ZnO-Based					
	Mag	gnetic Semiconductors	67				
	4.1	Zn K-edge XAS Study of ZnO NPs Capped with Organic					
		Molecules: Structural Versus Electronic Effects	68				
	4.2	Zn K-edge XAS Study of ZnO NPs Capped with Thiol					
		Derivatives and ZnS/ZnO Thin Films	80				
	4.3	XAS Study of the Local Order Around the Transition					
		Metal on Mn:ZnO Thin Films: The Role of Vacancies					
		and Structural Distortions	84				
	4.4	Conclusions	94				
	Refe	erences	95				
5	Zine	c K-edge XMCD Study of ZnO-Based Magnetic					
		iiconductors	97				
	5.1	Zn K-edge and L _{2,3} -edge XMCD Study of ZnO					
		NPs Capped with Different Organic Molecules	97				
	5.2	Zn K-edge XMCD Study of ZnO NPs Capped with Thiol					
		Derivatives and ZnS/ZnO Thin Films	105				
	5.3	Conclusions	109				
	Refe	erences	110				
6	Soft	X-ray XAS and XMCD Study of ZnO-Based					
•		gnetic Semiconductors	111				
	6.1	O K-edge Study of ZnO-Based Materials	112				
	6.2	S K-edge XAS Study of the Local Structure of Sulphur					
	0.2	in Thiol-Capped ZnO Nanoparticles	119				
	6.3	Conclusions	131				
		erences	132				
7	C.,	nmary and Conclusions	135				
7	Sun	illiary and Conclusions	133				
Αį	Appendices						

Chapter 1 Introduction

1.1 State of the Art

In the last few years, the prediction and observation of ferromagnetic behaviour in semiconductor materials has emerged as one of the most interesting topics in material science [1]. Assuming that ferromagnetism (FM) can be obtained up to ambient temperatures (usually denoted as high-temperature HTFM, or room temperature ferromagnetism RTFM), these materials would present many practical applications, especially for the development of new spintronic devices (such as spin-valves, polarized light emitters, chips that integrate memory and microprocessor functions, magnetic devices exhibiting power gain, etc.) [2–7].

The most common approach to induce ferromagnetism in semiconductors is to dope them with a few percent of magnetic atoms, typically transition metal (TM) atoms [6]. In these materials, denoted as Diluted Magnetic Semiconductors (DMSs), the magnetic cations, randomly distributed inside the semiconductor lattice, provide unfilled 3d states that could achieve ferromagnetic coupling [8] through the sp-d exchange interaction.

In the 80s, II–VI semiconductors were studied, mainly Mn:ZnTe and Mn:CdTe [9]. Despite their interesting optical properties, they did not result useful as DMSs due to several shortcomings: the n- and p-doping could not be optimized, and, even if that problem was solved, the expected Curie temperature (T_C) would be rather low due to the influence of the short-range antiferromagnetic superexchange between the Mn cations [10].

Later on, attention was paid to III-V semiconductors, like GaAs [11–15] and InAs [16, 17], doped with several TMs—Mn, in particular. The outstanding low-temperature functionalities demonstrated by Chiba et al. [18, 19] led to a growing interest in these compounds. The initial problems caused by the low solubility limits of the TM ions were overcome by Munekata et al. [16] succeeding in increasing the solubility limit of Mn into InAs thin films prepared by low-temperature molecular beam epitaxy (MBE). Finally, in 1992 Ohno et al. reported ferromagnetism up to

2 1 Introduction

35 K in Mn:InAs films [20] and later, in Mn:GaAs with T_C up to 110 K [11]. Despite the antiferromagnetic coupling being less relevant in III-V DMSs [21] the highest reported T_C , about 170 K for Mn:GaAs [22], was however still low for technological applications.

More recently, the interest has shifted to the so called Diluted Magnetic Oxides (DMOs), i.e. oxide semiconductors such as TiO₂, ZnO and SnO₂ doped with transition metal impurities. These materials offer some advantages such as wide band gap (about 3-4 eV, which are suitable for short wavelength light applications within the visible spectrum), ecological safety and durability, low cost, high n-type carrier concentrations and the capability of being grown at low temperatures [23]. The work on DMOs was driven by the theoretical prediction of high T_C for wide band gap semiconductors: based on the mean field Zener model, Dietl et al. predicted T_C above room temperature for Mn:GaN and Mn:ZnO [21]; in addition, Sato and Katayama-Yoshida covered the first principles design for both semiconductor and oxide spintronics [24], and theoretically predicted HTFM for a ZnO matrix doped with V, Cr, Fe, Co and Ni (while Ti and Cu doping would result in a paramagnetic ordering). Since then, there have been numerous reviews about GaN and other wide bandgap semiconductors [7, 25, 26], and T_C higher that 300 K have been found for several DMOs. Indeed, the first evidence of HTFM was reported for Co:TiO₂ [27–30], and similar results were found in Co:SnO₂ [31–37] (obtaining high values of the T_C and magnetic moment, 650 K and $\sim 7.5 \,\mu_B/\text{Co}$) and ZnO compounds doped with TMs such as Sc [38, 39], Ti [38, 40], V [41], Cr [38, 42, 43], Mn [44–50], Fe [32, 51], Co [38, 52–54], Ni [55] and Cu [42, 56, 57].

Despite the large body of research performed to date, two main issues remain still open. The first question is regarding the mechanism responsible for the origin of HTFM in wide gap DMSs and DMOSs, which is not yet understood and different theoretical models have been proposed to account for the occurrence of HTFM in both DMSs and DMOs [14, 21, 46, 52, 58–64]; the second question is regarding the very nature of the observed FM behaviour.

Dietl et al. [21] proposed the mean-field Zener's model based on indirect super-exchange interaction mediated by free holes from shallow acceptors. In this theory, the delocalized holes mediate a RKKY-like interaction between the localized TM ions resulting in the ferromagnetism [65–68]. The magnetic behaviour would be dependent on the magnetic dopant concentration as well as on the carrier type and density [69–72]. According to this model HTFM was expected only for p-type materials [21, 73]. Moreover, it was implicit that carrier-mediated FM interactions may be also possible in marginally semiconducting materials, such as in heavily doped semiconducting oxides. On the other hand, Coey et al. proposed a bound magnetic polaron (BMP) model [52] that should be applicable to both p- and n-type host materials. This model is based on the double exchange interaction, explained by hopping between two neighbour TM ions [24, 74–76]. The coupling is usually assigned to carriers residing on defects, such as vacancies [60, 77] or on residual impurities, such as hydrogen [61]. A detailed revision of most of the proposed models can be found in Ref. [64] and references therein.

1.1 State of the Art 3

Comparison with experimental reports does not shed light on the mechanism responsible for the observed HTFM. In fact, this behaviour was observed in systems for which ab-initio calculations predicted the opposite outcome [24], and different models, like the mean field Zener's model and spin-spin double exchange interaction, were proposed to explain the occurrence of FM in the same DMSs compounds [78].

The role of the dopant is also controversial. On the one hand, experimental findings from optical and transport studies differ from the expected hole concentration needed for the carrier-mediated FM [79]. On the other hand, while most models claim that the FM depends on the dopant concentration, the same behaviour was found in nanostructured systems doped with non-magnetic elements (B, P, N, C) and even without any kind of doping [80]. To explain this d^0 magnetism, different exchange interaction of the p-states as well as the presence of vacancies have been proposed [81–83]. In line with those results, Sánchez et al. [62] recently explored the effects of the higher surface to volume ratio in nanoscale systems to induce magnetic order in DMOSs. They predicted that broken symmetries on the surface enhance the spin polarization induced by the TM dopant and, additionally, it promotes the formation of a p-magnetic state even in the absence of magnetic ions.

The other main issue that remains an open question in this field is whether the observed FM is actually intrinsic. To date, there are many inconclusive and even contradictory experimental results [84, 85] and along with HTFM spin-glass or superparamagnetic behaviour have been reported for nominally identical systems [86, 87]. Moreover, a number of authors have claimed the observation of HTFM in several DMSs and DMOs that have not been confirmed by other groups. As a consequence, for most of the experimental results, doubts arose about the real origin of the observed HTFM [44, 88]. In some cases it was demonstrated that the observed magnetic behaviour was not due to the TM doping itself but rather extrinsic and related to contamination or to the segregation of metallic clusters and secondary phases [86, 87, 89–95].

These controversial results show that the magnetism is very sensitive to the preparation conditions [96]. For example, the HTFM found in Co:TiO₂ varies widely with the growth method, indicating that either elemental Co or an unknown Co-Ti-O phase has been produced within the TiO₂ matrix [28]. Consequently, recent works pointed out that the magnetic properties are not exclusively related to the presence of the magnetic ions but strongly determined by the structural defects [52, 77, 97–104] and the presence of surface, grain boundaries or interfaces [105, 106]. In this respect, several authors [98, 99] showed that Mn:ZnO nanoparticles (NPs) and thin films only show HTFM when capped with molecules that introduce p-type defects, while capping introducing n-type defects leads to no HTFM. On the contrary, for Co:ZnO films the presence of n-type defects favours the appearance of HTFM. In the same line, it was found that the magnetic properties of Co and Mn doped ZnO powder samples are modified by thermal annealing in different atmospheres that favour the presence of p- or n-type defects [107]. Finally, Coey et al. [52] claimed that doping ZnO thin films with non magnetic 3d ions (as Ti or V) also leads to HTFM behaviour. Moreover, in some systems the effect appears even without doping [104, 108–110]. Taking into account the fact that superexchange or double exchange interactions

4 1 Introduction

cannot account for the observed HTFM with a concentration of magnetic ions of a few percent, those results point out the importance of the electronic structure of the semiconductor (modified by both the presence of the magnetic impurity and the defects) in the appearance of the observed magnetism.

All in all these controversial results make one wonder "if the dilute doping of the oxides with magnetic cations may be something of a smokescreen as far as the magnetism is concerned" [81].

Indeed, it was reported that ZnO NPs capped with organic molecules and without any 3d doping display an intrinsic FM contribution [111], in line with previous results in Au NPs [112-114]. The initial findings on ZnO NPs capped with tryoctylphoshopine (TOPO), dodecylamine (AMINE) and dodecanethiol (THIOL) were addressed to the alteration of the electronic configuration of the ZnO system caused by the capping molecule [111]. This starting approach shows certain parallelism with the charge-transfer model used to account for the peculiar magnetic behaviour of thiol-capped Au NPs [112, 115, 116]. This model states that the thiol molecules strongly bond to the NP surface and causes charge-transfer effects from the gold to the sulphur ligand [112, 117]. As a consequence, the number of holes in the Au 5d band increases (otherwise completely full and giving rise to the diamagnetic behaviour of bulk gold), which might lead to the occurrence of magnetic moment at the gold sites. Experimental support for the charge transfer mechanism was supposedly obtained from X-ray Absorption Near Edge Spectroscopy (XANES) experiments performed at the Au L_{2 3}-edges [118, 119], in particular from the modification of the near-edge region of the spectra recorded in the NPs with respect to that of bulk Au. Making a parallel to the gold case, García et al. have interpreted the modifications observed in the Zn K-edge of capped ZnO NPs with respect to that of bulk ZnO in terms of the aforesaid charge-transfer effects [113, 118–120].

A common characteristic in the works proposing the existence of charge-transfer effects in those thiol-capped systems from XANES measurements is the fact that they do not at all consider the influence of possible structural modifications, due to the capping, in the absorption spectra. However the XANES region of the spectra is highly sensitive to the bonding geometry of the absorption atoms, which casts serious doubts on the reliability of the conclusions derived based exclusively on fingerprint XANES analyses. This is of particular relevance in those systems in which the magnetic properties strongly depend on local structural details [1, 121]. Indeed, the standard methods available for solving the atomic structure of bulk crystals fail for these materials due to nanoscale effects arising from the inherently very small crystalline sizes, the large surface-volume ratio, near-surface relaxation, local lattice distortions, etc. These uncertainties make it clear that more powerful experimental tools are needed to obtain an accurate structural and magnetic characterization of capped NPs. In particular, this renders critical in the case of ZnO NPs capped with organic molecules, where the capping might lead to structural modifications at the surfaces or interfaces.

1.2 Outlook of This Dissertation

At present, the influence of the doping in driving the HTFM in DMSs and DMOs is seriously questioned, and the finding of similar magnetic behaviour in non doped ZnO NPs reinforces those doubts. For these systems the observed HTFM behaviour has been accounted for in terms of charge-transfer effects between the organic capping and the surface Zn atoms, neglecting the structural ones.

In this work we face the study of the magnetic behaviour of undoped ZnO materials and its relationship with the local crystalline structure. In this way, the aim of this Thesis was firstly to determine the intrinsic character of the reported HTFM and, once that matter is clarified, the theoretical and experimental study of the modifications on the local structure induced by the capping, as well as its relation with the magnetic behaviour. To this end element-specific tools, i.e. X-ray Absorption Spectroscopy (XAS) and X-ray Magnetic Circular Dichroism (XMCD) have been applied in addition to standard characterization tools.

XAS and XMCD experiments have been performed at the Zn K-edge in the beamline BL39XU of the SPring-8 synchrotron radiation facility. In view of the results obtained, complementary XAS and XMCD experiments were also performed at the O K-edge and S L-edge at the SPring-8 BL23SU and BL25SU beamlines, and at the S K-edge at the XAFS beamline of the Elettra synchrotron radiation facility. The recording, analysis and discussion of all these XAS and XMCD measurements constitute the main body of this Ph.D. Thesis.

The fulfilment of the proposed objectives in the project implied, however, the characterization of samples by using different experimental techniques, also including different synthesis and preparation methods. This part of the study was done in collaboration with different groups: Miguel Ángel García (*Institute for Ceramic and Glass* ICV-CSIC); Mar García-Hernández, Ana Espinosa, Eva Céspedes and María Ángeles Laguna-Marco (*Material Science Institute of Madrid* ICMM); Noemi Carmona (Department of Materials Physics, *University Complutense at Madrid*, UCM); María Luisa Ruíz-González and José María González-Calbet (Inorganic Chemistry Department, *University Complutense at Madrid*, UCM), that also participated in some of the synchrotron radiation experiments.

Notwithstanding our active participation in the synthesis and characterization of the samples prior to the synchrotron radiation experiments, we sustain that the main authorship of that work should be assigned to these groups. For this reason we do not consider it appropriate to include in the Ph.D. thesis an exhaustive description of this characterization since this description can also be found elsewhere [122]. Only a brief outline of the synthesis and characterization methods is presented here. In turn, a detailed description of the XAS and XMCD experimental method is presented.

6 1 Introduction

1.3 Dissertation Structure

After this brief introduction, aimed at showing the state of the art in the field of Diluted Magnetic Semiconductors, this Thesis is organized as follow:

Chapter 2 is meant to explain the standard techniques used for both, the structural and magnetic characterization of the samples, as well as to the obtained results. These macroscopic tools are insufficient for a proper description of nanostructured systems and, consequently X-ray Absorption (XAS) and X-ray Magnetic Circular Dichroism (XMCD) experiments were performed. A detailed explanation of these techniques and the analysis processes performed, are displayed in Chap. 3. The main body of this work is based on the results brought by these advanced techniques, which provide atomic and shell-specific description of both local structure and magnetic properties.

In Chap. 4 the study of Zn K-edge XAS is presented. The structural effects will be carefully analysed. With this aim in mind, the same study is carried out in different batches of NPs, and it is extended to the case of ZnO/ZnS heterostructures, as it will be explained. The XMCD spectra recorded at the Zn K-edge are studied in Chap. 5. The final objective will be to determine the intrinsic character of the HTFM behaviour and its origin, taking into account the findings of Chap. 4 regarding the structural effects.

Finally in Chap. 6, the XAS and XMCD analysis are carried out at the oxygen K-edge and the sulphur L and K-edges, in order to get deeper insight of the nature of this exotic magnetism. Our results indicate the occurrence of a FM oxygen state.

All the results of this work are summarized in the final conclusions.

References

- 1. S.A. Chambers, Surf. Sci. Rep. 61, 345 (2006)
- 2. C. Timm, J. Phys.: Condens. Matter 15, R1865 (2003)
- 3. S. Wolf, Science 294, 1488 (2001)
- 4. I. Malajovich, J. Berry, N. Samarth, D. Awschalom, Nature 411, 770 (2001)
- 5. J. Furdyna, J. Appl. Phys. 64, R29 (1988)
- 6. H. Ohno, Science 281, 951 (1998)
- 7. S. Pearton, C. Abernathy, D. Norton, Mat. Sci. Eng. R 40, 137 (2003)
- 8. S. Pearton, W. Heo, M. Ivill, D. Norton, T. Steiner, Semicond. Sci. Tech. 19, R59 (2004)
- 9. D. Awschalom, M. Flatté, Nat. Phys. 3, 153 (2007)
- 10. G. Medvedkin, T. Ishibashi, T. Nishi, K. Hayata, Jpn. J. Appl. Phys. 39, 949 (2000)
- H. Ohno, A. Shen, F. Matsukura, A. Oiwa, A. Endo, S. Katsumoto, Y. Iye, Appl. Phys. Lett. 69, 363 (1996)
- A. Esch, J. Boeck, G. Verbanck, A. Steenbergen, P. Wellmann, B. Grietens, R. Bogaerts, F. Herlach, G. Borghs, Phys. Rev. B 56, 13103 (1997)
- J. Okabayashi, A. Kimura, O. Rader, T. Mizokawa, A. Fujimori, T. Hayashi, M. Tanaka, Phys. Rev. B 58, R4211 (1998)
- 14. F. Matsukura, H. Ohno, A. Shen, Y. Sugawara, Phys. Rev. B 57, R2037 (1998)
- Y. Ohno, D. Young, B. Beschoten, F. Matsukura, H. Ohno, D. Awschalom, Nature 402, 790 (1999)

References 7

 H. Munekata, H. Ohno, S. Molnar, A. Segmüller, L. Chang, L. Esaki, Phys. Rev. Lett. 63, 1849 (1989)

- 17. A. Oiwa, T. Słupinski, H. Munekata, Appl. Phys. Lett. **78**, 518 (2001)
- D. Chiba, M. Sawicki, Y. Nishitani, Y. Nakatani, F. Matsukura, H. Ohno, Nature 455, 515 (2008)
- 19. A. Chernyshov, M. Overby, X. Liu, J. Furdyna, Nat. Phys. **5**, 656 (2009)
- 20. H. Ohno, H. Munekata, T. Penney, S. Molnár, L. Chang, Phys. Rev. Lett. 68, 2664 (1992)
- 21. T. Dietl, F. Matsukura, J. Cibert, D. Ferrand, Science 287, 1019 (2000)
- M. Wang, R. Campion, A. Rushforth, K. Edmonds, C. Foxon, B. Gallagher, Appl. Phys. Lett. 93, 132103 (2008)
- T. Fukumura, Y. Yamada, H. Toyosakia, T. Hasegawab, H. Koinumac, M. Kawasakia, Appl. Surf. Sci. 223, 62 (2004)
- 24. K. Sato, H. Katayama-Yoshida, Jpn. J. Appl. Phys. 39, 555 (2000)
- S. Pearton, C. Abernathy, M. Overberg, G. Thaler, D. Norton, N. Theodoropoulou, A. Hebard, Y. Park, F. Ren, J. Kim, L. Boatner, J. Appl. Phys. 93, 1 (2003)
- 26. T. Graf, S. Goennenwein, M. Brandt, Phys. Status Solidi b 239, 277 (2003)
- 27. Y. Matsumoto, M. Murakami, T. Shono, T. Hasegawa, Science 291, 854 (2001)
- S. Chambers, S. Thevuthasan, R. Farrow, R. Marks, J. Thiele, L. Folks, M. Samant, A. Kellock, N. Ruzycki, D. Ederer, U. Diebold, Appl. Phys. Lett. 79, 3467 (2001)
- S. Shinde, S. Ogale, S. Sarma, J. Simpson, H. Drew, S. Lofland, C. Lanci, J. Buban, N. Browning, V. Kulkarni, J. Higgins, R. Sharma, R. Greene, T. Venkatesan, Phys. Rev. B 67, 115211 (2003)
- 30. S. Duhalde, M. Vignolo, F. Golmar, C. Chiliotte, Phys. Rev. B 72, 161313 (2005)
- S. Ogale, R. Choudhary, J. Buban, S. Lofland, S. Shinde, S. Kale, N. Kulkarni, J. Higgins, C. Lanci, J. Simpson, N. Browning, S. Sarma, H. Drew, R. Greene, T. Venkatesan, Phys. Rev. Lett. 91, 077205 (2003)
- 32. J.M.D. Coey, A. Douvalis, C. Fitzgerald, M. Venkatesan, Appl. Phys. Lett. 84, 1332 (2004)
- 33. C. Fitzgerald, J. Appl. Phys. **95**, 7390 (2004)
- 34. A. Punnoose, J. Hays, V. Gopal, V. Shutthanandan, Appl. Phys. Lett. 85, 1559 (2004)
- C. Fitzgerald, M. Venkatesan, L. Dorneles, R. Gunning, P. Stamenov, J.M.D. Coey, P. Stampe,
 R. Kennedy, E. Moreira, U. Sias, Phys. Rev. B 74, 115307 (2006)
- Y. Xiao, S. Ge, L. Xi, Y. Zuo, X. Zhou, B. Zhang, L. Zhang, C. Li, X. Han, Z. Wen, Appl. Surf. Sci. 254, 7459 (2008)
- 37. K. Gopinadhan, S. Kashyap, D. Pandya, S. Chaudhary, J. Appl. Phys. 102, 113513 (2007)
- 38. M. Venkatesan, C. Fitzgerald, J. Lunney, J.M.D. Coey, Phys. Rev. Lett. 93, 177206 (2004)
- J.M.D. Coey, M. Venkatesan, C. Fitzgerald, L. Dorneles, P. Stamenov, J. Lunney, J. Magn. Magn. Mater. 290, 1405 (2005)
- L. Dorneles, D. O'Mahony, C. Fitzgerald, F. McGee, M. Venkatesan, I. Stanca, J. Lunney, J.M.D. Coey, Appl. Surf. Sci. 248, 406 (2005)
- 41. N. Hong, J. Sakai, A. Hassini, J. Appl. Phys. 97, 10D312 (2005)
- 42. K. Ueda, H. Tabata, T. Kawai, Appl. Phys. Lett. **79**, 988 (2001)
- H. Liu, X. Zhang, L. Li, Y. Wang, K. Gao, Z. Li, R. Zheng, S. Ringer, B. Zhang, X. Zhang, Appl. Phys. Lett. 91, 072511 (2007)
- 44. D. Kundaliya, S. Ogale, S. Lofland, S. Dhar, C. Metting, S. Shinde, Z. Ma, B. Varughese, K. Ramanujachary, L. Salamanca-Riba, T. Venkatesan, Nat. Mater. 3, 709 (2004)
- 45. K. Sharma, G. Varma, J. Appl. Phys. **102**, 056105 (2007)
- M. García, M. Ruiz-González, A. Quesada, J. Costa-Kramer, J. Fernández, S. Khatib, A. Wennberg, A. Caballero, M. Martin-González, M. Villegas, F. Briones, J. González-Calbet, A. Hernando, Phys. Rev. Lett. 94, 217206 (2005)
- R. Sanz, J. Jensen, G. González-Díaz, O. Martínez, M. Vázquez, M. Hernández-Vélez, A. Linköping Nanoscale, Res. Lett. 4, 878 (2009)
- 48. J.H. Guo, A. Gupta, P. Sharma, K. Rao, M. Marcus, C. Dong, J. Guillen, S.Butorin, M. Mattesini, P. Glans, K. Smith, C. Chang, R. Ahuja, J. Phys.: Condens. Matter 19, 172202 (2007)

8 1 Introduction

- 49. J. Kim, H. Kim, D. Kim, Y. Ihm, W. Choo, J. Appl. Phys. 92, 6066 (2002)
- P. Sharma, A. Gupta, K.V. Rao, F.J. Owens, R. Sharma, R. Ahuja, J.M. Guillen, B. Johansson, G.A. Gehring, Nat. Mater. 2, 673 (2003)
- 51. X. Wei, C. Song, K. Geng, F. Zeng, B. He, F. Pan, J. Phys.: Condens. Matter 18, 7471 (2006)
- 52. J.M.D. Coey, M. Venkatesan, C. Fitzgerald, Nat. Mater. 4, 173 (2005)
- 53. A. Pakhomov, B. Roberts, K. Krishnan, Appl. Phys. Lett. **83**, 4357 (2003)
- Z. Jin, T. Fukumura, M. Kawasaki, K. Ando, H. Saito, T. Sekiguchi, Y. Yoo, M. Murakami,
 Y. Matsumoto, T. Hasegawa, H. Koinuma, Appl. Phys. Lett. 78, 3824 (2001)
- 55. X. Liu, F. Lin, L. Sun, W. Cheng, X. Ma, W. Shi, Appl. Phys. Lett. 88, 062508 (2006)
- 56. D. Buchholz, R. Chang, J. Song, J. Ketterson, Appl. Phys. Lett. **87**, 082504 (2005)
- 57. C. Sudakar, J. Thakur, G. Lawes, R. Naik, V. Naik, Phys. Rev. B 75, 054423 (2007)
- 58. A. Hernando, P. Crespo, M. García, J. Phys.: Conf. Ser. 292, 012005 (2011)
- 59. T. Dietl, A. Haury, Y. d' Aubigné. Phys. Rev. B 55, R3347 (1997)
- 60. Q. Wang, Q. Sun, P. Jena, Y. Kawazoe, Phys. Rev. B 79, 115439 (2009)
- 61. C. Park, D. Chadi, Phys. Rev. Lett. 94, 127204 (2005)
- 62. N. Sánchez, S. Gallego, M. Muñoz, Phys. Rev. Lett. 101, 067206 (2008)
- 63. M. Muñoz, S. Gallego, N. Sanchez, J. Phys.: Conf. Ser. 303, 012001 (2011)
- 64. A. Zunger, S. Lany, H. Raebiger, Physics **53**, 1 (2010)
- 65. T. Dietl, F. Matsukura, H. Ohno, Phys. Rev. B 66, 033203 (2002)
- 66. F. Pan, C. Song, X. Liu, Y. Yang, F. Zeng, Mat. Sci. Eng.: R 62, 1 (2008)
- 67. C. Liu, F. Yun, H. Morkoç, J. Mat. Sci.: Mat. Electron. 16, 555 (2005)
- 68. R. Janisch, P. Gopal, N. Spaldin, J. Phys.: Condens. Matter 17, R657 (2005)
- Y. Nishitani, D. Chiba, M. Endo, M. Sawicki, F. Matsukura, T. Dietl, H. Ohno, Phys. Rev. B 81, 045208 (2010)
- 70. A. MacDonald, P. Schiffer, N. Samarth, Nat. Mater. 4, 195 (2005)
- K. Edmonds, K. Wang, R. Campion, A. Neumann, N. Farley, B. Gallagher, C. Foxon, Appl. Phys. Lett. 81, 4991 (2002)
- M. Mayer, P. Stone, N. Miller, H. Smith, O. Dubon, E. Haller, K. Yu, W. Walukiewicz, X. Liu, J. Furdyna, Phys. Rev. B 81, 045205 (2010)
- 73. T. Dietl, Semicond. Sci. Tech. 17, 377 (2002)
- 74. M. Berciu, R. Bhatt, Phys. Rev. Lett. 87, 10723 (2001)
- 75. S. Sarma, E. Hwang, A. Kaminski, Phys. Rev. B 67, 155201 (2003)
- 76. K. Sato, H. Katayama-Yoshida, Jpn. J. Appl. Phys. 40, 485 (2001)
- 77. D. Chakraborti, G. Trichy, J. Prater, J. Narayan, J. Phys. D: Appl. Phys. **40**, 7606 (2007)
- 78. K. Sato, H. Katayama-Yoshida, P. Dederichs, J. Supercond. Nov. Magn. 16, 31 (2003)
- 79. K. Burch, D. Awschalom, D. Basov, J. Magn. Magn. Mater. 320, 3207 (2008)
- 80. A. Sundaresan, R. Bhargavi, N. Rangarajan, U. Siddesh, Phys. Rev. B 74, 161306 (2006)
- 81. J.M.D. Coey, Curr. Opin. Solid State Mater. Sci. 10, 83 (2006)
- 82. M. Geshi, A.I.P. Conf, Proc. 772, 327 (2005)
- 83. O. Volnianska, P. Boguslawski, J. Phys.: Condens. Matter 22, 073202 (2010)
- T. Fukumura, Z. Jin, A. Ohtomo, H. Koinuma, M. Kawasaki, Appl. Phys. Lett. 75, 3366 (1999)
- 85. S. Jung, S. An, G.-C. Yi, C. Jung, S.-I. Lee, S. Cho, Appl. Phys. Lett. 80, 4561 (2002)
- S. Ye, V. Ney, T. Kammermeier, K. Ollefs, S. Zhou, H. Schmidt, F. Wilhelm, A. Rogalev, A. Ney, Phys. Rev. B 80, 245321 (2009)
- 87. M. Opel, K. Nielsen, S. Bauer, S. Goennenwein, J. Cezar, D. Schmeisser, J. Simon, W. Mader, R. Gross, Eur. Phys. J. B 63, 437 (2008)
- 88. G. Lawes, A. Risbud, A. Ramirez, R. Seshadri, Phys. Rev. B 71, 045201 (2005)
- 89. J. Park, M. Kim, H. Jang, S. Ryu, Y. Kim, Appl. Phys. Lett. 84, 1338 (2004)
- 90. P. Sati, C. Deparis, C. Morhain, S. Schäfer, A. Stepanov, Phys. Rev. Lett. 98, 137204 (2007)
- 91. T. Kaspar, T. Droubay, S. Heald, M. Engelhard, P. Nachimuthu, S. Chambers, Phys. Rev. B 77, 201303 (2008)
- A. Ney, M. Opel, T. Kaspar, V. Ney, S. Ye, K. Ollefs, T. Kammermeier, S. Bauer, K.-W. Nielsen, S. Goennenwein, M. Engelhard, S. Zhou, K. Potzger, J. Simon, W. Mader, S. Heald, J. Cezar, F. Wilhelm, A. Rogalev, R. Gross, S. Chambers, New J. Phys. 12, 013020 (2010)

References 9

K. Rode, R. Mattana, A. Anane, V. Cros, E. Jacquet, J. Contour, F. Petroff, A. Fert, M. Arrio,
 P. Sainctavit, P. Bencok, F. Wilhelm, N. Brookes, A. Rogalev, Appl. Phys. Lett. 92, 012509 (2008)

- 94. M. Kobayashi, Y. Ishida, J. Hwang, T. Mizokawa, A. Fujimori, K. Mamiya, J. Okamoto, Y. Takeda, T. Okane, Y. Saitoh, Y. Muramatsu, A. Tanaka, H. Saeki, H. Tabata, T. Kawai, Phys. Rev. B **72**, 201201 (2005)
- 95. H. Xu, H. Zhu, X. Shan, Y. Liu, J. Gao, X. Zhang, J. Zhang, P. Wang, Y. Hou, D. Yu, J. Phys.: Condens. Matter 22, 016002 (2010)
- 96. A. Bonanni, T. Dietl, Chem. Soc. Rev. 39, 528 (2010)
- 97. A. Punnoose, H. Magnone, M. Seehra, J. Bonevich, Phys. Rev. B 64, 174420 (2001)
- 98. K.R. Kittilstved, D.R. Gamelin, J. Am. Chem. Soc. 127, 5292 (2005)
- 99. K. Kittilstved, N. Norberg, D. Gamelin, Phys. Rev. Lett. 94, 147209 (2005)
- T. Kaspar, S. Heald, C. Wang, J. Bryan, T. Droubay, V. Shutthanandan, S. Thevuthasan,
 D. McCready, A. Kellock, D. Gamelin, S. Chambers, Phys. Rev. Lett. 95, 217203 (2005)
- 101. W.A. Schwartz, D. Seattle, D. Schwartz, Adv. Mat. 16, 2115 (2004)
- M. Gacic, G. Jakob, C. Herbort, H. Adrian, T. Tietze, S. Brück, E. Goering, Phys. Rev. B 75, 205206 (2007)
- J.W. Chiou, H.M. Tsai, C.W. Pao, K.P. Kumar, S.C. Ray, F.Z. Chien, W.F. Pong, M.H. Tsai,
 C.H. Chen, H.J. Lin, J.J. Wu, M.H. Yang, S.C. Liu, H.H. Chiang, C.W. Chen, Appl. Phys.
 Lett. 89, 043121 (2006)
- 104. N. Hong, J. Sakai, V. Brizé, J. Phys.: Condens. Matter 19, 036219 (2007)
- E. Céspedes, J. García-Lopez, M. García-Hernández, A. de Andrés, C. Prieto, J. Appl. Phys. 102, 033907 (2007)
- B. Straumal, A. Mazilkin, S. Protasova, A. Myatiev, P. Straumal, G. Schütz, P. van Aken, E. Goering, B. Baretzky, Phys. Rev. B 79, 205206 (2009)
- D. Rubi, J. Fontcuberta, A. Calleja, L. Aragonés, X. Capdevila, M. Segarra, Phys. Rev. B 75, 155322 (2007)
- 108. J.M.D. Coey, M. Venkatesan, C. Fitzgerald, Nat. Mater. 430 (2004)
- J.M.D. Coey, M. Venkatesan, P. Stamenov, C. Fitzgerald, L. Dorneles, Phys. Rev. B 72, 024450 (2005)
- 110. N. Hong, N. Poirot, J. Sakai, Phys. Rev. B 77, 033205 (2008)
- M.A. García, J.M. Merino, E. Fernández-Pinel, A. Quesada, J. de La Venta, M.L. González, G.R. Castro, P. Crespo, J. Llopis, J.M. González-Calbet, A. Hernando, Nano Lett. 7, 1489 (2007)
- 112. P. Crespo, R. Litrán, T. Rojas, M. Multigner, J.M. de la Fuente, J.C. Sánchez-López, M.A. García, A. Hernando, S. Penadés, A. Fernández, Phys. Rev. Lett. 93, 087204 (2004)
- 113. I. Carmeli, G. Leitus, R. Naaman, S. Reich, Z. Vager, J. Chem. Phys. 118, 10372 (2003)
- 114. P. Zhang, T. Sham, Phys. Rev. Lett. 90, 245502 (2003)
- J.S. Garitaonandia, M. Insausti, E. Goikolea, M. Suzuki, J.D. Cashion, N. Kawamura,
 H. Ohsawa, I.G. de Muro, K. Suzuki, F. Plazaola, T. Rojo, Nano Lett. 8, 661 (2008)
- 116. E. Guerrero, T. Rojas, M. Multigner, P. Crespo, M. Muñoz-Marquez, M. García, A. Hernando, A. Fernández, Acta Mater. **55**, 1723 (2007)
- 117. P. Zhang, T.K. Sham, Appl. Phys. Lett. **81**, 736 (2002)
- R.E. Benfield, D. Grandjean, M. Kröll, R. Pugin, T. Sawitowski, G. Schmid, J. Phys. Chem. B 105, 1961 (2001)
- 119. P. Crespo, M. García, E. Fernández-Pinel, Acta Phys. Pol. A 113, 515 (2008)
- 120. Y. Yamamoto, T. Miura, T. Teranishi, M. Miyake, Phys. Rev. Lett. 93, 116801(4) (2004)
- 121. M. Murakami, T. Shono, T.H. Matsumoto, Science **291**, 854 (2001)
- 122. C. Guglieri, M.A. Laguna-Marco, M.A. García, N. Carmona, E. Céspedes, M. García-Hernández, A. Espinosa, J. Chaboy, J. Phys. Chem. C 116, 6608 (2012)

Chapter 2 Synthesis and In-house Characterization of Materials

2.1 Synthesis

2.1.1 Nanoparticles

ZnO nanoparticles (NPs) were synthesized through a sol-gel method in collaboration with Dr. Noemi Carmona, at the Complutense University of Madrid.

The sol-gel method has gained notoriety in the glass and ceramic fields. Indeed, it has grown to be so important that in the 1990s more than 35,000 papers were published worldwide on the process [1–4]. This method is a cheap and low-temperature technique that allows for the fine control of the product's chemical composition. Inorganic oxide materials with desirable properties of hardness, optical transparency, chemical durability, tailored porosity, and thermal resistance, can be produced at room temperatures, as opposed to the much higher melting temperatures required in the production of conventional inorganic glasses [2]. Even small quantities of dopants, such as organic dyes and rare earth elements, can be introduced in the sol and end up uniformly dispersed in the final product.

The applications for sol gel-derived products are numerous, and derived from the various material shapes generated in the gel state (aerogels, monolith ceramics, glasses, films, fibers, and monosized powders such as nanospheres). Among the aforesaid applications are included protective and porous films, optical coatings, window insulators, dielectric and electronic coatings, high temperature superconductors, reinforcement fibres, fillers, and catalysts, (bio)sensors, medicine applications (e.g., controlled drug release), reactive material and separation (chromatography) technology.

Three reactions are generally used to describe the sol-gel process: hydrolysis, alcohol condensation and water condensation. The 'sol' (solution) evolves towards the formation of a gel-like diphasic system containing both a liquid and a solid phase whose morphologies range from discrete particles to continuous polymer networks.

Typical precursors are metal alkoxides and metal chlorides, which undergo hydrolysis and polycondensation reactions to form a colloid. The basic structure or morphology of the solid phase can range anywhere from discrete colloidal particles to continuous chain-like polymer networks [5]. In the case of colloid, the volume fraction of particles (or particle density) may be so low that a significant amount of fluid may need to be removed initially for the gel-like properties to be recognized. The simplest method to accomplish that is to allow time for sedimentation to occur, and then pour off the remaining liquid. Removal of the remaining liquid (solvent) phase requires a drying process, which is typically accompanied by a significant amount of shrinkage. In principle, the ultimate structure of the final component would be strongly influenced by changes imposed upon the structural template during this phase of processing. However, the characteristics and properties of a particular sol-gel inorganic network are related to a number of factors that affect the rate of hydrolysis and condensation reactions [6], such as pH, temperature and time of reaction, reagent concentrations, catalyst nature and concentration, molar ratios, ageing temperature and time. Thus, by controlling these factors, it is possible to vary the structure and properties of the sol-gel-derived inorganic network over wide ranges [7]. In addition, the degree of order appears to be limited by the time and space allowed for longer-range correlations to be established, and so, defective polycrystalline structures would appear to be the basic elements of nanoscale materials science [8].

For the synthesis of our NPs, dimethyl sulfoxide (DMSO, $(CH_3)_2SO$, 99.9%, Sigma Aldrich) and absolute ethanol $(CH_3CH_2OH, 99.95\%, Panreac)$ were used as solvents; zinc acetate dihydrate $(Zn(CH_3CO_2)_2 \cdot 2H_2O, 98\%, Sigma Aldrich)$ as precursor; tetramethylamonium hydroxide pentahydrate (TMAH, N(CH₃)₄OH, 97%, Sigma Aldrich) to perform the hydrolysis and trioctylphosphine (hereafter TOPO), dodecylamine (hereafter AMINE), and dodecanethiol $(CH_3(CH_2)_{11}SH, 98\%, Sigma Aldrich)$ as capping agents.

5 mmol of zinc acetate was dissolved with continuous stirring in DMSO and the solution was kept at $60\,^{\circ}$ C. Then, a 7.5 mmol solution of TMAH in ethanol at $60\,^{\circ}$ C was dropped to the previous one. After t_{add} min stirring, where t_{add} is the time waited once the synthesis was initiated, a 7.5 mmol solution of the capping agent was added all at once. Since the capping molecule should stop the growth of the NPs, the idea of varyng t_{add} is to get NPs of different sizes, being supposedly bigger as t_{add} is increased. The obtained ZnO NPs that precipitated were filtrated and washed using absolute ethanol at $60\,^{\circ}$ C to remove unreacted precursors, and the washing process was repeated three times. The purified NPs were then left to dry in air for 2 days.

The samples, listed in Table 2.1, were prepared in several series (labelled from 1 to 5), each series using identical starting solution. The first synthesis was made by adding the capping agent 20 min after the addition of the TMAH. Part of the samples were placed inside a petri-dish and submitted to a thermal treatment at $350\,^{\circ}$ C in a muffle furnace for 1 h (heating time from 20 to $350\,^{\circ}$ C was 1 h and cooling process took another hour). This process removes the organic part of the samples. We refer to these samples as calcinated. In the second batch of samples only dodecanethiol was used as capping agent and t_{add} was varied between 0 and 30 min in order to prepare ZnO NPs of different sizes, being $t_{add} = 5$ min (hereafter

2.1 Synthesis

Table 2.1 List of the ZnO NPs synthesized through sol-gel method in this work

Sample	Capping agent	t _{add} (min)	
ТОРО	Trioctylphosphine	20	
AMINE	Dodecylamine	20	
20-12C-1 (THIOL)	Dodecanethiol	20	
20-12C-1-Calc	Dodecanethiol	20	
5-12C-2	Dodecanethiol	5	
15-12C-2	Dodecanethiol	15	
30-12C-2	Dodecanethiol	30	
7-12C-3	Dodecanethiol	7	
9-12C-3	Dodecanethiol	9	
12-12C-3	Dodecanethiol	12	
20-4C-4	Butanethiol	20	
20-8C-4	Octanethiol	20	
20-12C-4	Dodecanethiol	20	
30-4C-4	Butanethiol	30	
30-8C-4	Octanethiol	30	
30-12C-4	Dodecanethiol	30	
40-4C-4	Butanethiol	40	
40-8C-4	Octanethiol	40	
40-12C-4	Dodecanethiol	40	
50-4C-4	Butanethiol	50	
50-8C-4	Octanethiol	50	
50-12C-4	Dodecanethiol	50	
TOPO-5	Trioctylphosphine	20	
AMINE-5	Dodecylamine	20	
20-12C-5 (THIOL-5)	Dodecanethiol	20	

5-12C-2 sample), 15 min (15-12C-2), and 30 min (30-12C-2). Similarly, in a third series the samples 7-12C-3, 9-12C-3, 12-12C-3 were synthesized. To study the influence of the length of the carbon chains into the magnetic properties of the NPs, a new series of samples were prepared by using different capping organic molecules: butanethiol (CH₃CH₂CH(SH)CH₃, 98%, Sigma Aldrich) (4 carbon atoms in the organic chain, referred as t_{add} -4C-4), octanethiol (CH₃(CH₂)₇SH, 98.5%, Sigma Aldrich) (8 carbon atoms, t_{add} -8C-4) and dodecanethiol (12 carbon atoms, t_{add} -12C-4). Additionally, a final series was prepared by repeating the parameters (capping and t_{add}) of the first one.

It has to be mentioned at this point that among the main drawbacks of the preparation of NPs stand out the reproducibility of each synthesis and the stability of the NPs once prepared. It is well known that the reaction yield in the preparation of the NPs is low, and so the same process is typically repeated several times until enough

sample amount is obtained. Synthesis reproducibility has been tested by performing X-ray diffraction (XRD) and X-ray Absorption Spectroscopy (XAS) analysis. Major differences are observed between nominally identical samples from different batches indicating the low reproducibility of the synthesis method. As a consequence, in this study samples synthesized in the same way but from different batches are clearly labelled as different samples (e.g. 20-12C-1 and 20-12C-4). This implies that the whole characterization of the samples has been carried out for each specimen. On the other hand, the stability of the as synthesized ZnO NPs has been proved by overlapping of successive XAS spectra recorded during the 3 years period on the same samples and specimens. No modification of the absorption spectra has been found on the same specimens measured at the initial run and upto 3 years later, either in different specimens prepared from the same sample. As it will be discussed in the next chapters, this indicates that the observed properties are intrinsic and stable in time.

2.1.2 Thin Films and Multilayers

ZnO/ZnS multilayers were prepared by RF-sputtering in collaboration with Dr. Eva Céspedes at the Institute of Materials Science of Madrid (ICMM). The specific equipment used consists of a PLS 500 Pfeiffer high vacuum system equipped with a TMH 520 turbomolecular pump. Details of this equipment can be found elsewhere [9].

The sputtering deposition method [10–14] is a physical vapour deposition process in which a bulk starting material (target) is eroded by a particle bombardment and subsequently deposited onto a substrate. The process is presented in Fig. 2.1 in its simplest form: a target material is placed in a vacuum chamber filled with a gas at a reduced pressure and a negative potential, that accelerates the electrons present in the process chamber towards the grounded chamber wall, is set on. The electrons collide with gas molecules and generate electron-ion pairs. The ions from the electron-ion pairs are accelerated towards the target (cathode) and upon impact with the target surface two events take place: (i) an atomic collision cascade in which some of the target material can be ejected and condense onto the surrounding surfaces, and (ii) a number of secondary emitted electrons are accelerated and ionize the gas molecules. The described cathodic process is also called DC sputtering. A disadvantage of the diode sputtering is that the deposition rate is slow and the electron bombardment of the substrate is extensive, what can cause overheating and structural damage. However, those problems are solved by the use of magnetron sputtering, i.e. by using magnets behind the cathode to trap the free electrons in a magnetic field directly above the target surface. These electrons are not free to bombard the substrate to the same extent as in diode sputtering. At the same time the circular path carved by these same electrons when trapped in the magnetic field, enhances their probability of ionizing a neutral gas molecule by several orders of magnitude. This rise in available ions significantly increases the rate at which target material is eroded and subsequently deposited onto the substrate. In addition, a problem of DC sputtering is that the target must be a conducting material to avoid charging.

2.1 Synthesis

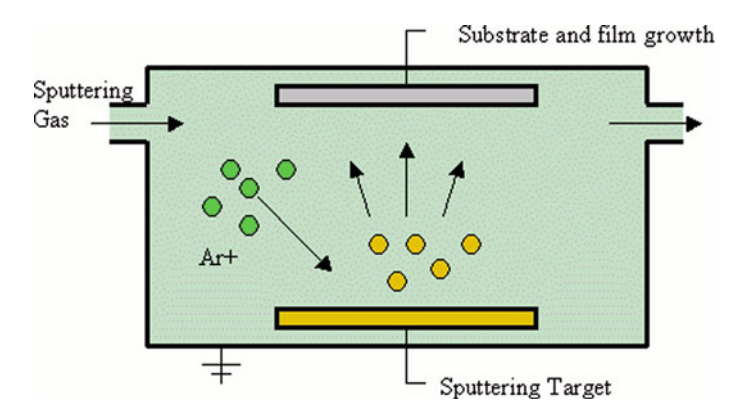


Fig. 2.1 Schematized sputtering process. Positive ions from a gas discharge are accelerated towards a target and create upon impact: (i) an atomic collision cascade in which some of the target material can be ejected and condense onto the surrounding surfaces, and (ii) a number of secondary emitted electrons which are then accelerated and ionize the gas molecules

If an isolating target material is set on a negative potential the ion collisions will charges up the surface of the target, resulting in an electrical breakdown in the form of arcing. This can be avoided with the use of radio frequency (RF) sputtering. In this mode of sputtering, the sign of the anode-cathode bias is varied at a high rate (the Federal Communications Commission has reserved a frequency of 13.56 MHz for the plasma processing techniques an so is the most widely used [15]). Since electrons are lighter, they follow better the changes in the AC electric field. Hence, a large electron current is drawn at the target followed by a small positive ion current, making the net current flow different from zero over the complete period of one cycle. Thus, the target self-biases to a negative potential to avoid a net current though the capacitor. A combination of capacitors and inductors is used to form an impedance matching network which maximizes the power delivery by forming an effective coupling of the RF power supply and the target. The impedances of materials with high resistivity that cannot be DC sputtered drop with increasing frequency and so, high frequencies pass current through dielectric targets.

In this work, ZnO/ZnS multilayers were prepared by RF-sputtering on fused silica substrates at room temperature by alternative sputtering from ZnO and ZnS two-inch ceramic targets. Residual chamber pressure was in the 10^{-7} mbar range. Both ZnO and ZnS layers were prepared using Ar at 5.1×10^{-3} mbar and 20 W. Growth rates, measured by X-ray reflectivity, were about 1.5 and 3.5 nm/min for ZnO and ZnS, respectively. Deposition started with ZnO and a last additional ZnO 4 nm layer was deposited on top. Following this procedure, two samples labelled $(\text{ZnO}_{4\text{nm}}/\text{ZnS}_{4\text{nm}})_{10}$ (+ZnO 4 nm) and $(\text{ZnO}_{2\text{nm}}/\text{ZnS}_{2\text{nm}})_{20}$ (+ZnO 4 nm) were prepared, keeping constant the ZnO and ZnS total thickness and modifying the number of interfaces.

In addition, a Zn-O-S thin film (ZnS/ZnO 50%/50%) was prepared by RF co-sputtering from ZnO and ZnS two-inch ceramic targets placed at 15°. The sample

was grown using Ar gas (9.1 sccm), on Si(100) and quartz substrates at room temperature. The base pressure provided by the vacuum system was 1×10^{-6} mbar and the working pressure was 5.2×10^{-3} mbar. The RF power supplied was about 20 W for ZnS and 30 W for ZnO. Under these conditions, the growth rate is nominally the same for both targets and the samples were grown for 24 min, corresponding to a nominal 100 nm thickness, in agreement with X-ray reflectivity data (see Sect. 2.2.2). A part of the co-sputtered samples was annealed in a quartz tube placed inside a furnace and under an O_2 controlled flow (5 sccm, 5.0×10^{-3} mbar pressure).

2.2 Structural Characterization

2.2.1 X-ray Diffraction (XRD)

X-ray diffraction (XRD) measurements were performed in a Bruker D8 fast X-ray diffractometer (Lynxeye) from the ICMM diffraction service, in collaboration with Dr. Eva Céspedes, Dr. Ana Espinosa and Dr. M. Ángeles Laguna-Marco.

The XRD patterns of the AMINE, TOPO and THIOL NPs (first series) are shown in Fig. 2.2. The patterns were indexed on the basis of a ZnO wurtzite (W-ZnO) type unit cell. The particle size (D_{XRD}) has been calculated by measuring the full width at half maximal (FWHM) intensity of three Bragg diffraction peaks, centred at $2\theta = 31.1^{\circ}$, 34.3° and 36.2°, those correspond to the (100), (002) and (101) reflection from the wurtzite structure. For obtaining the values of the FWHM, each peak was fitted by a Gaussian or Lorentzian curve (see Fig. 2.3). Then, we averaged the values obtained by using the Scherrer formula for each peak:

Fig. 2.2 X-ray diffraction patterns of **a** the bulk ZnO and ZnS references and **b** the series-1 of ZnO NPs capped with organic molecules (TOPO, AMINE and THIOL)

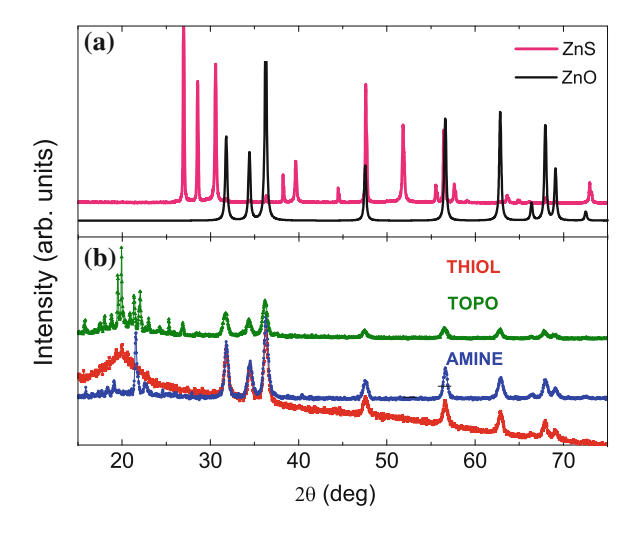
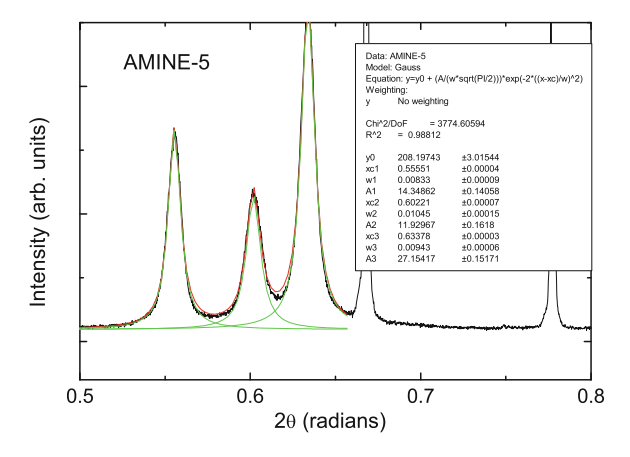


Fig. 2.3 Standard procedure to calculate the crystal grain size (D_{XRD}) of the NPs. In the case of AMINE-5 the peaks are fit by Gaussian curves. The peaks position and FWHM are obtained from the fit and introduced in the Scherrer formula (see text)



$$l = \frac{K \cdot \lambda}{R \cos \theta} \tag{2.1}$$

where l is the crystallite size, λ is the wavelength of the X-ray radiation used (in our case the Cu K_{α} , that is, 1.5418 Å), B is the peak width (radians) due to particle size effect, and θ is the Bragg angle. The numerical factor K depends on the crystal shape and the definitions of the average crystallite size (for example, if the cube root of the crystallite volume is used instead of the definition above) and the width (for example, if the integral line width is used, rather than the FWHM). In the absence of detailed shape information K=0.9 is a good approximation, hence we adopted this value. The results of our analysis are summarized in the Table 2.2.

The XRD patterns show also the presence of an amorphous phase and low angle peaks coexisting with the crystalline W-ZnO like. Similar behaviour is found in the ZnO NPs obtained in different batches, the main difference being the amount ratio of the amorphous and the crystalline phases. This is exemplified in Figs. 2.4 and 2.5, where representative XRD patterns of samples of series-2, -4 and -5 are shown.

As shown in these figures the crystallinity of the samples and the amount of the amorphous phases strongly depend on the synthesis conditions. However no relationship can be established with any of the parameters varied through the synthesis process. In addition, in some of the samples the amorphous phase is dominant, which prevents us from applying the Scherrer formula to determine the particle size.

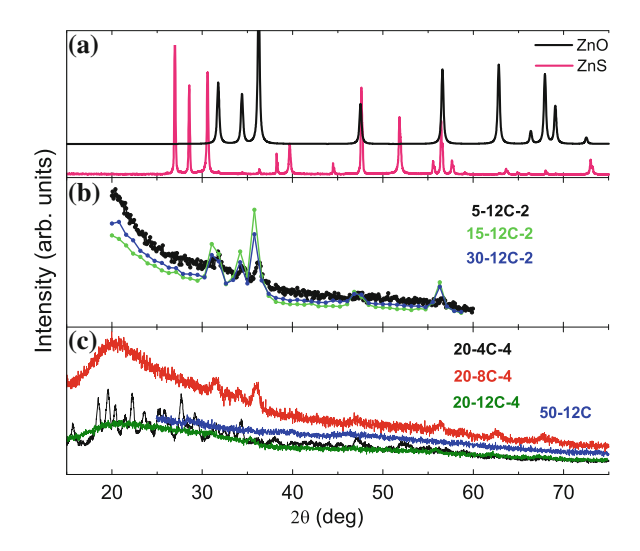
In principle, the existence of an amorphous phase and low angle peaks could be addressed to the organic part of the material. In order to verify this possibility some of the samples were subjected to a calcination process aimed to remove the organic part of the material. This is shown in Fig. 2.6 where the thermal gravimetric analysis (TGA) in the case of AMINE is reported.

However the result of the calcination is not so satisfactory. Despite the original amorphous component disappears, there is an unexpected broadening of the X-ray

Sample	D_{XRD} (nm)
AMINE	18 ± 2
TOPO	15 ± 2
20-12C-1 (THIOL)	14 ± 2
20-12C-1 calcinated	15 ± 2
5-12C-2	13 ± 2
15-12C-2	10 ± 2
30-12C-2	12±2
20-8C-4	8 ± 2
20-12C-4	8 ± 2
50-4C-4	14±2
50-8C-4	8 ± 2
AMINE-5	16 ± 2
TOPO-5	13 ± 2
20-12C-5 (THIOL-5)	10 ± 2

Table 2.2 D_{XRD} of capped ZnO NPs

Fig. 2.4 X-ray diffraction patterns of **a** the bulk ZnO and ZnS references, **b** the series-2 of ZnO NPs (5-12C-2, 15-12C-2 and 30-12C-2) and **c** representative NPs of the series-4 (20-4C-4, 20-8C-4, 20-12C-4 and 50-12C-4)



diffraction peaks. This is clearly illustrated in Fig. 2.7 where the XRD patterns of the 20-12C-1 sample prior and after calcination are shown. After calcination the XRD pattern indicates the occurrence of a ZnS phase. The peaks associated to the W-ZnO remain unaffected, but the ZnS phase appears highly disordered. This suggests that, in case of the ZnS phase being at the surface of the NPs, surrounding a ZnO core, the interface between the ZnO and ZnS phases would not be a pristine one, so that interpenetration of phases can not be ruled out.

Fig. 2.5 X-ray diffraction patterns of **a** the bulk ZnO and ZnS references, **b** the series-5 of ZnO NPs capped with organic molecules (TOPO, AMINE and THIOL)

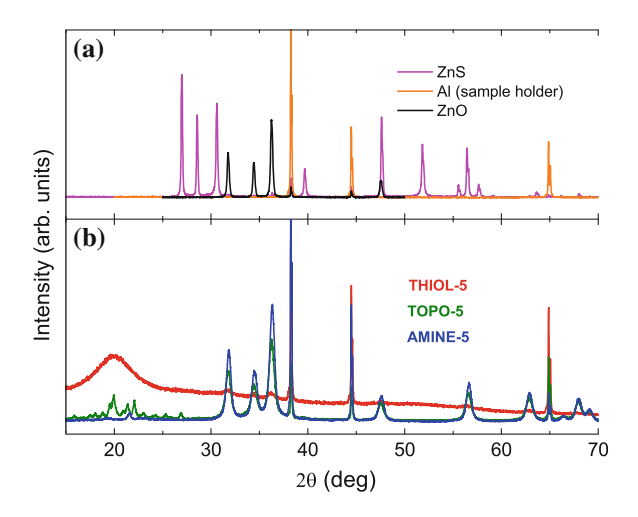


Fig. 2.6 Thermal gravimetric treatment of the AMINE sample

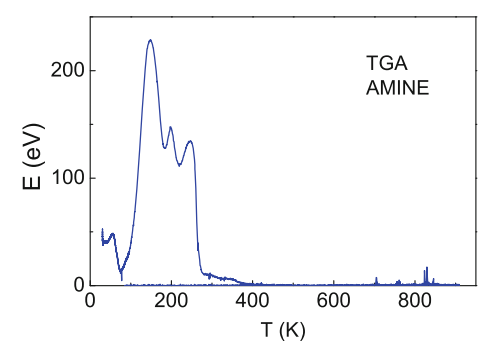
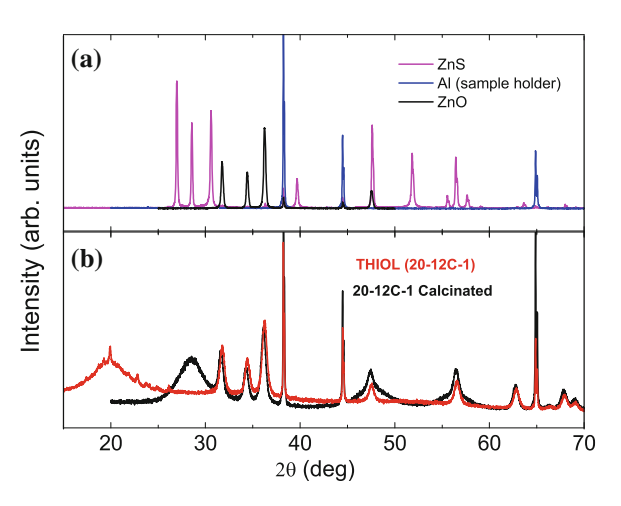


Fig. 2.7 X-ray diffraction patterns of **a** the bulk ZnO and ZnS references, **b** 20-12C-1 sample prior and after calcination



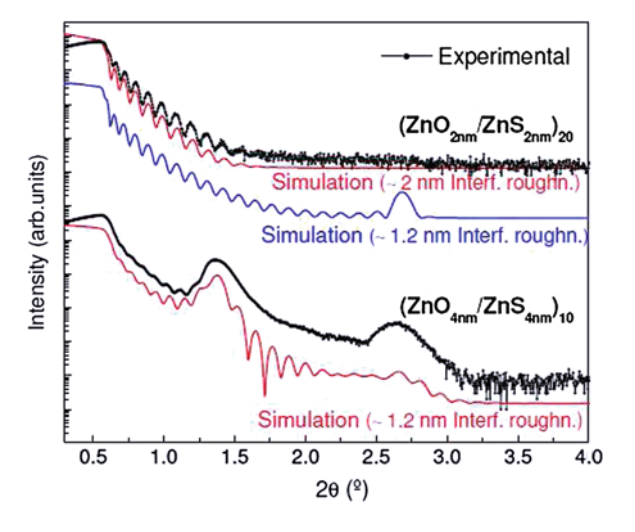
These results are also consistent with those found in the case of ZnO/ZnS multilayers (not shown) and the lack of diffraction peaks, even after annealing, in the case of the sample obtained by co-sputtering, indicating its high degree of structural disorder.

2.2.2 X-ray Reflectivity (XRR)

X-ray Reflectivity (XRR) measurements of the thin-film samples, were made in collaboration with Dr. Eva Céspedes at the ICMM by using a Bruker D8 X-ray diffractometer and Cu K_{Ω} radiation.

The X-ray reflectivity spectra of both films are shown in Fig. 2.8, where Kiessig fringes, related to the total multilayers thickness, appear for both samples. Satellite maxima, associated with the bilayer period, are observed only for $(ZnO_{4nm}/ZnS_{4nm})_{10}$ (+ZnO 4 nm) film, pointing to smoother ZnO/ZnS interfaces than for the $(ZnO_{2nm}/ZnS_{2nm})_{20}$ one. The existence of flatter ZnO/ZnS interfaces in the $(ZnO_{4nm}/ZnS_{4nm})_{10}$ (+ZnO 4 nm) sample is confirmed by XRR simulations performed by means of Xreal software (developed by Dr. Neil Telling [16]). Despite complex fits are away from the aim of this work these simulations, that mostly reproduce the shape of the experimental data, indicate a larger mean interface roughness for sample $(ZnO_{2nm}/ZnS_{2nm})_{20}$ and what is more important, an average interface roughness of the order of the layer thickness, i.e., around 2 nm. That points towards differences in the morphology of both mutilayers, laying $(ZnO_{2nm}/ZnS_{2nm})_{20}$ in the regime between continuous and non-continuous layers, leading to more disordered ZnO/ZnS interfaces. This subject will center a deeper XAS study in the next chapters.

Fig. 2.8 XRR reflectivity spectra of (ZnO_{4nm}/ZnS_{4nm})₁₀ and (ZnO_{2nm}/ZnS_{2nm})₂₀ multilayers and their simulations (see text for details)



2.2.3 Transmission Electron Microscopy (TEM), High Resolution Transmission Electron Microscopy (HRTEM) and Energy Dispersive X-ray Spectroscopy (EDX)

TEM, HRTEM and EDX measurements were undertaken by Dr. M. L. Ruíz-González and Dr. J. González-Calbet at the Complutense University of Madrid. A 200 kV JEOL2000FX transmission electron microscope and a JEOL3000FEG electron microscope fitted with an Oxford LINK EDX analyser were used.

Figure 2.9 shows the results obtained in the case of samples of series-1. Panel (a) of this figure shows a representative low magnification image of the TOPO sample evidencing an average size of 15–20 nm, in agreement with XRD data. HRTEM images and corresponding FT are shown in panels (b) and (c). They allow to distinguish interplanar distances of 2.5 nm, in agreement with the formation of wurtzite ZnO NPs.

Representative HRTEM images of the samples of the second series of synthesis are shown in Figs. 2.10, 2.11 and 2.12. The images indicate the low crystallinity of the samples although some NPs are clearly visible. This result is in agreement with the XRD data, indicating that the degree of crystallinity of the NPs strongly depends on the synthesis batch.

Finally, energy dispersive X-ray analysis (EDX) excludes the presence of magnetic impurities within the sensitivity $(0.01\,\%)$ of this technique. In addition the EDX analysis provides an estimate of the ratio of the Zn versus S content in both the crystalline and amorphous phases. The fact that Zn is also present in the amorphous phase indicates that it is not due to the organic part of the capping molecules but to low crystallinity regions of the NPs.

In the case of multilayers, cross-sectional TEM images are shown in Fig. 2.13 for both ZnO_{4nm}/ZnS_{4nm} and ZnO_{2nm}/ZnS_{2nm} samples. According to the expected

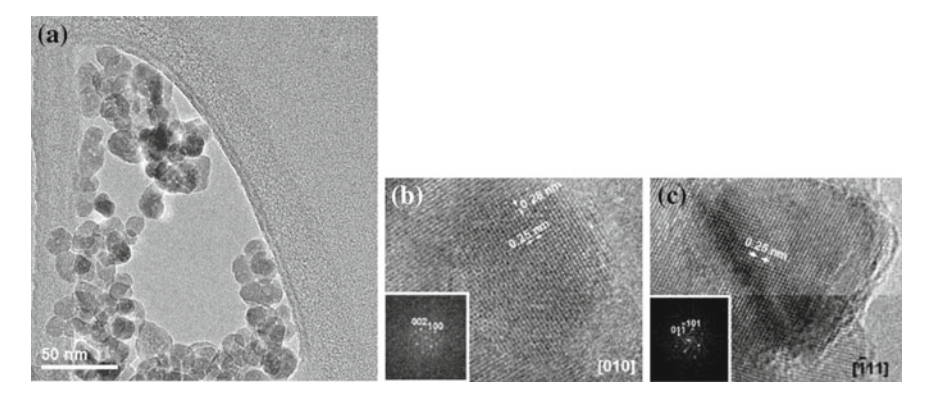


Fig. 2.9 Low magnification (a) and HRTEM (b,c) images, including their corresponding FT, of the TOPO sample

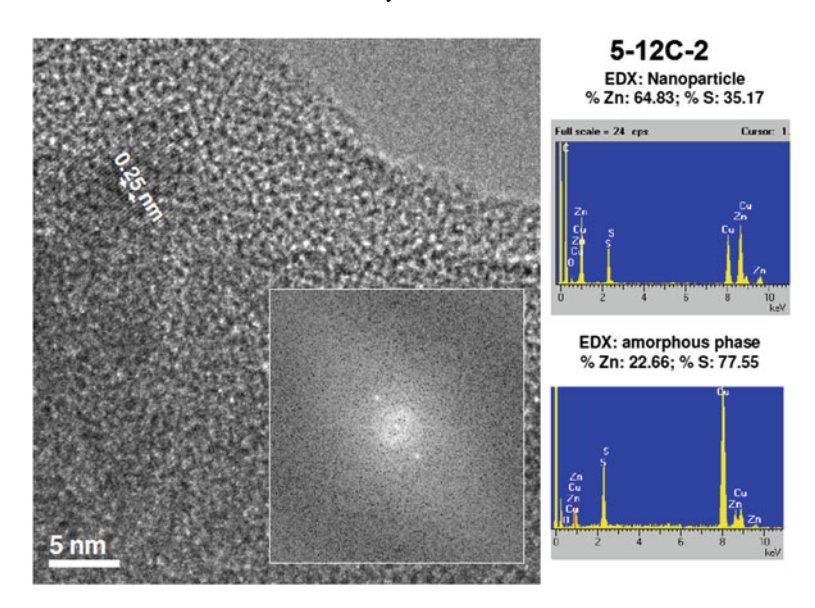


Fig. 2.10 HRTEM and EDX of the 5-12C-2 sample

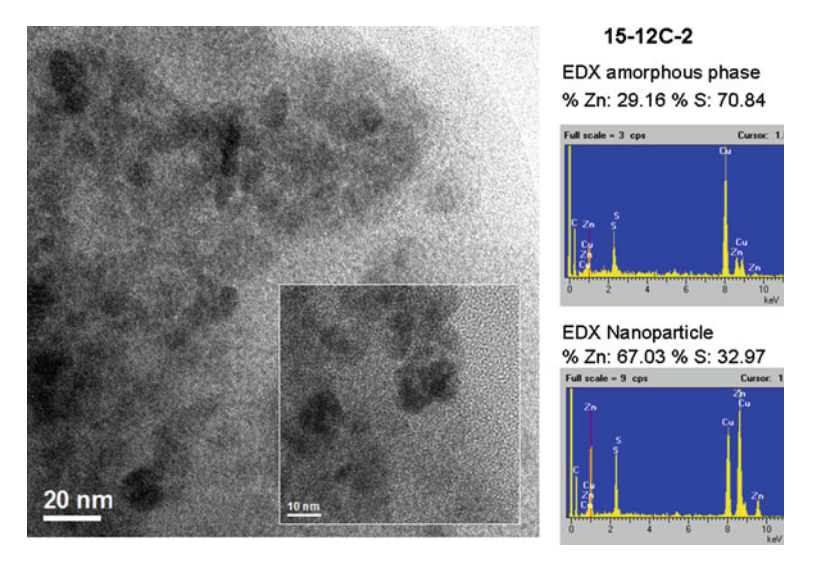


Fig. 2.11 HRTEM and EDX of the 15-12C-2 sample

values, layer thickness of 4 ± 1 and 2 ± 1 nm are obtained from TEM for each ZnO and ZnS layer forming the $(ZnO_{4nm}/ZnS_{4nm})_{10}$ and $(ZnO_{2nm}/ZnS_{2nm})_{20}$ samples, respectively. Despite heterostructure periodicity is distinguished for both samples, TEM insets of Fig. 2.13 confirm the presence of more disorder ZnO/ZnS regions coexisting in the $(ZnO_{2nm}/ZnS_{2nm})_{20}$ sample.

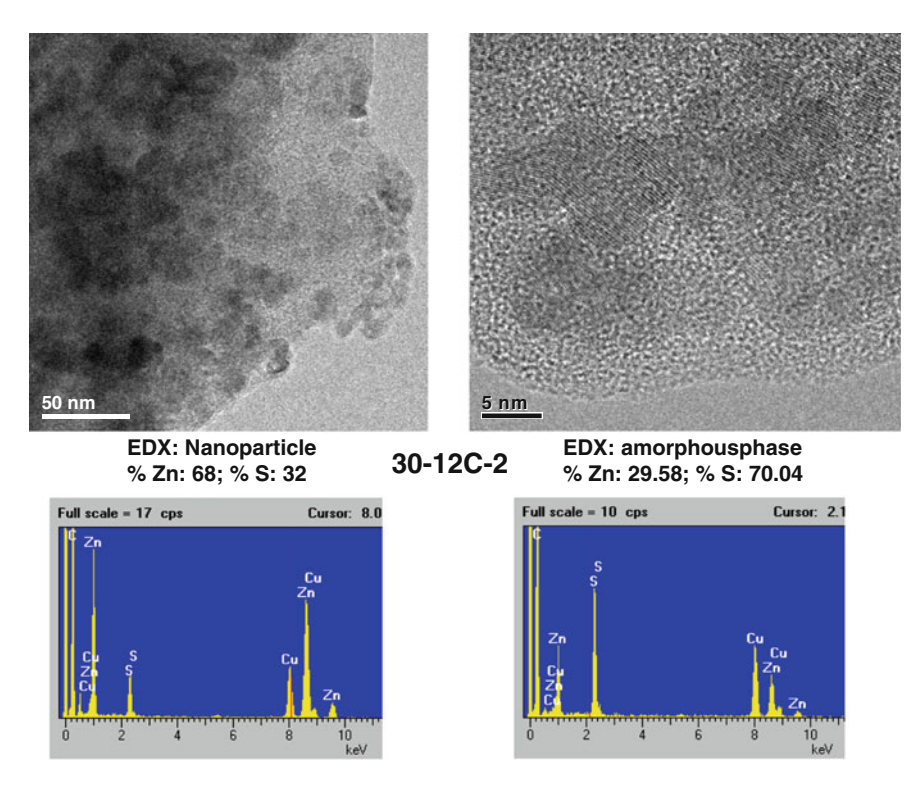


Fig. 2.12 HRTEM and EDX of the 30-12C-2 sample

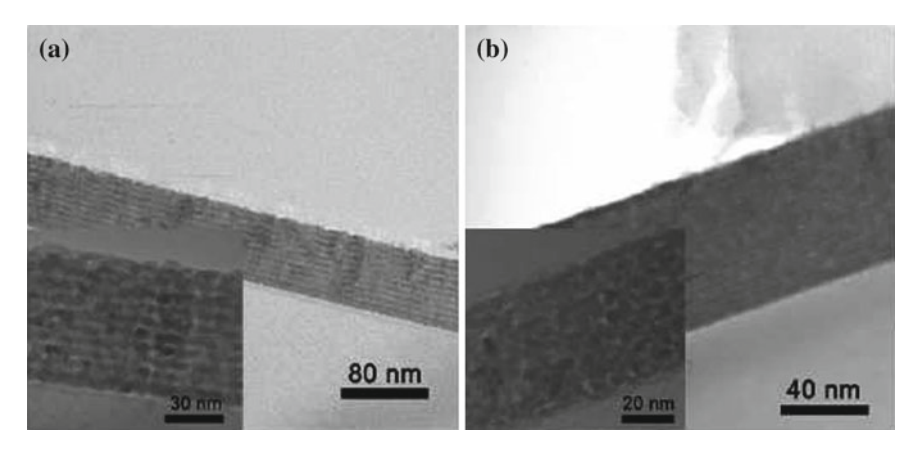


Fig. 2.13 Cross-sectional TEM images of a $(ZnO_{4nm}/ZnS_{4nm})_{10}$ and b $(ZnO_{2nm}/ZnS_{2nm})_{20}$ multilayers

2.3 Optical Absorption

Optical absorption and luminescence studies were conducted in collaboration with Dr. M.A. García and the Institute of Ceramic and Glass (ICV). Some of the measurements are previous to the development of this PhD work [17] but they have been included here for the sake of completeness.

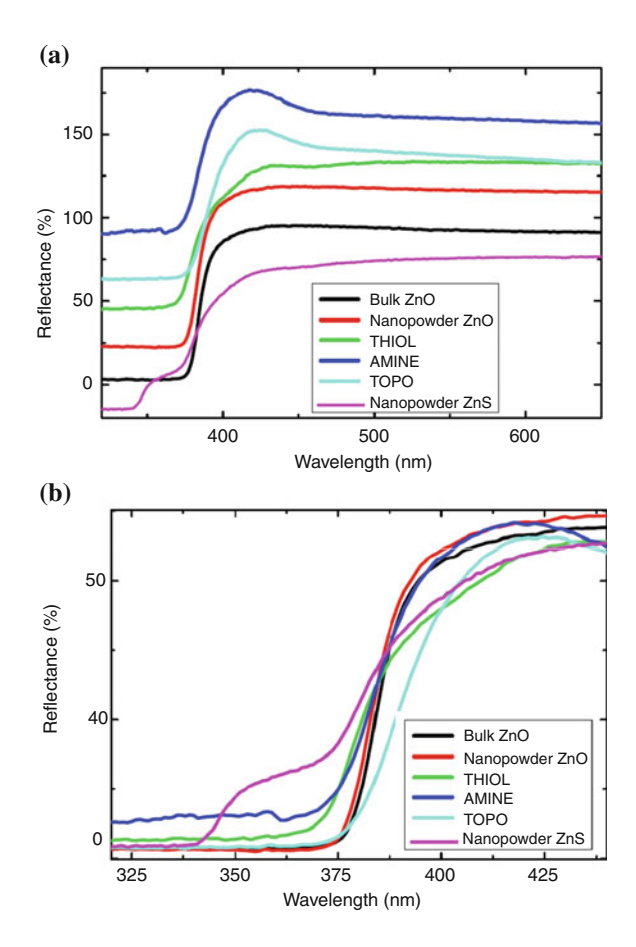
Photoluminescence (PL) excitation and emission spectra were recorded with a Perkin-Elmer LS-5 spectrofluorometer performing the appropriate correction for the lamp intensity and photomultiplier spectral response. Powder samples were placed in a circular sample holder and covered with a quartz window. No significant contribution from the sample holder or from the quartz window to the emission or excitation bands in the spectral region of interest was found. Reflectance was measured with a Shimadzu 3100 monochromator with an integrating sphere attached to collect both specular and diffuse reflectance using the same sample holder than for the PL measurements. No significant contribution of the sample holder nor from the window was found.

As ZnO is a degenerated semiconductor with an energy gap (3.35 eV) in the UV-Vis part of the spectrum, optical spectroscopy probing transitions between valence and conduction band provides useful information about its electronic structure. Figure 2.14 shows the integrated reflectance of the samples in the 350–650 nm range. Bulk ZnO exhibits a typical plain profile at the visible part of the spectrum with a sharp decay at \sim 400 nm reflecting the ZnO bandgap. A reference sample of ZnO nanopowder (particle size \sim 50 nm) presented a very similar spectrum with slight modifications at the gap energy. ZnO nanoparticles exhibit also the reflectance decay at the bandgap, confirming that they retain the semiconductor character of ZnO. However, clear differences at the edge region are found with respect to the bulk and nanopowder ZnO samples. The nanoparticles show an increase in reflectance close to the edge (\$\sigma420\text{ nm}\$) indicative of a different electronic structure at the bottom of the conduction band. In addition, the bandgap decay results sharper for the bulk and nanopowder while the nanoparticles exhibit a wider profile indicative of a more heterogeneous material and also a different density of available states. As it will be discussed later, the heterogeneity detected for the nanoparticles is in agreement with the formation of a layer at the particle surface. In addition, the bandgap profile depends on the capping molecule.

In the case of wurtzite ZnS, the energy gap is $\backsim 3.7$ [18], so different density of available states is present. Thiol samples, 5-12C-2, and NPs of the series-4 present, according to the XRD analysis (Sect. 2.2.1), a W-ZnS phase. As seen in Fig. 2.15, the edge region of those samples is displaced to lower wavelength, in agreement with the presence of a phase with a different density of states.

The photoluminescence spectra of the ZnO NPs are reported in Fig. 2.16. The emission spectra upon excitation with 320 nm light show a broad band centred at about 600 nm for the three samples. This emission is shifted with respect to the typical emission of bulk ZnO (centred at 550 nm) and its intensity depends on the capping molecule. This emission band is ascribed to an energy level induced by

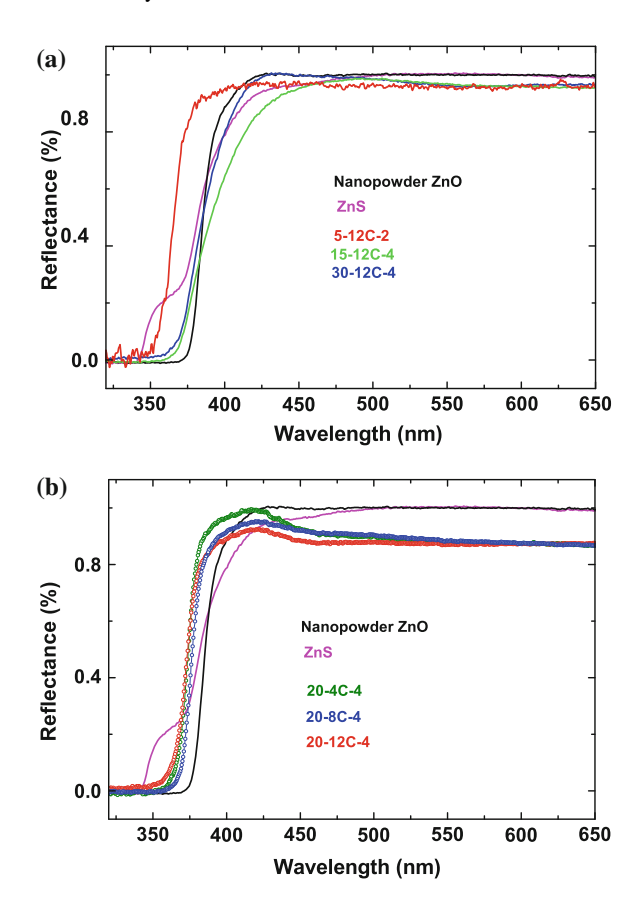
Fig. 2.14 a Diffuse reflectance spectra for the series-1 of ZnO nanoparticles. Bulk and nanopowder ZnO references are also shown for comparison purposes. Curves are vertically displaced for clarity. b Detail of the band-gap profile



the presence of defects in ZnO. Although the particular defect responsible for the emission is still under discussion, it is commonly accepted that oxygen vacancies are involved [19].

The excitation spectra for the 570 nm emission exhibit a narrow peak at about 390 nm which correspond to the ZnO bandgap. The spectra show variations in intensity and a slight shifts depending on the capping molecule, peaking at 389 nm for THIOL, 397 nm for AMINE, and 390 for TOPO. The changes in the photoluminescence features are indicative of differences in the electronic configuration of the particle depending on the capping molecule. In particular, surface states are known to provide an alternative decay path for excited electrons; thus the changes in the PL intensity are associated with the presence and concentration of these surface states that will be determined by the bonds established between the ZnO particle and the capping molecule.

Fig. 2.15 Diffuse reflectance spectra for the series-2 (a) and -4 (b) of ZnO nanoparticles. Bulk and nanopowder ZnO references are also shown for comparison purposes

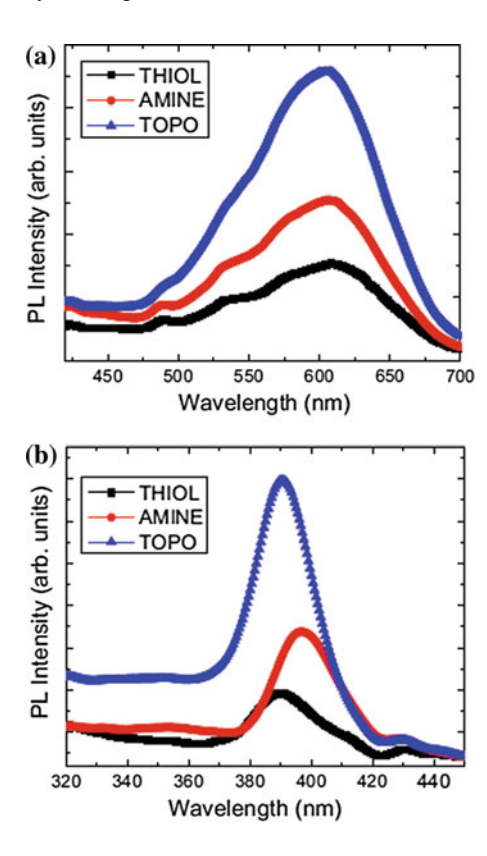


2.4 Magnetic Characterization: AC Susceptibility and Magnetization

The macroscopic magnetic measurements have been performed at the ICMM in collaboration with Dr. A. Espinosa and Dr. Mar García-Hernández. Magnetic measurements were performed using a Quantum Design superconducting quantum interference device (SQUID) magnetometer (Quantum Design MPMS-5S).

As discussed in the introductory chapter the reliability of the HTFM behaviour in DMSs and DMOs based on magnetization data centres a long-standing controversy. By this reason special care was taken during samples manipulation and handling. All possible sources of experimental errors, exhaustively reported in [20] were considered and avoided. Samples (always handled with nonmetallic tools) were placed into a gelatin capsule and mounted on straws. A gelatin capsule without any powder was also mounted on a straw and measured for control. Zn precursor (Zinc acetate hihydrate) was measured to detect contamination in the starting powder.

Fig. 2.16 a Emission spectra upon excitation with 320 nm light. b Excitation spectra for the 570 nm emission



The measurements protocol is shown through Figs. 2.17 and 2.18. The samples are mounted on a straw as shown in 2.17. For all the samples magnetization vs applied magnetic field are recorded at low ($T=5\,\mathrm{K}$) and high temperatures ($T=250\,\mathrm{K}$ or $T=300\,\mathrm{K}$). In addition, the temperature dependence of magnetization is also recorded. Samples are field cooled ($H_{FC}=5\,\mathrm{T}$) and the M(T) curve is recorded by applying a $H_{mes}=1000\,\mathrm{Oe}$ magnetic field. Similar measurements are performed for the empty sample holder, and they are compared to those of the samples prior preforming the mass normalization. For selected samples, several masses were measured in order to determine whether the magnetic signal scales with the mass.

Figure 2.19 summarizes the results of the SQUID measurements in the case of samples from the series-1. The same is shown in Fig. 2.20 for the sample holder.

Samples exhibit an overall diamagnetic behaviour at $T=5\,\mathrm{K}$ (see panel a of Fig. 2.19). In addition, the thermal dependence of the magnetization (Fig. 2.19b) points out the existence of a paramagnetic signal following a Curie-Weiss law. By assuming that the paramagnetic susceptibility is negligible at 300 K, as the M(T) is flat at this temperature, the diamagnetic susceptibility is determined from the M(T) at high temperature. Then, by considering that the diamagnetic contribution is

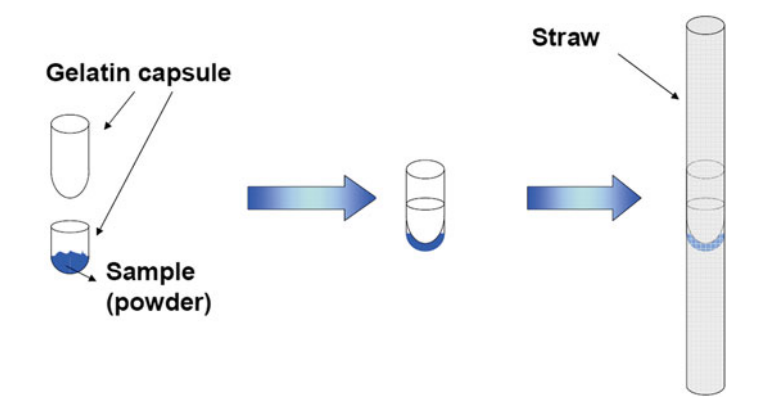


Fig. 2.17 Standard assembly of the sample: for measurements the sample is placed inside a gelatin capsule and mounted on a straw (No cotton, kapton or any other fixing materials are used)

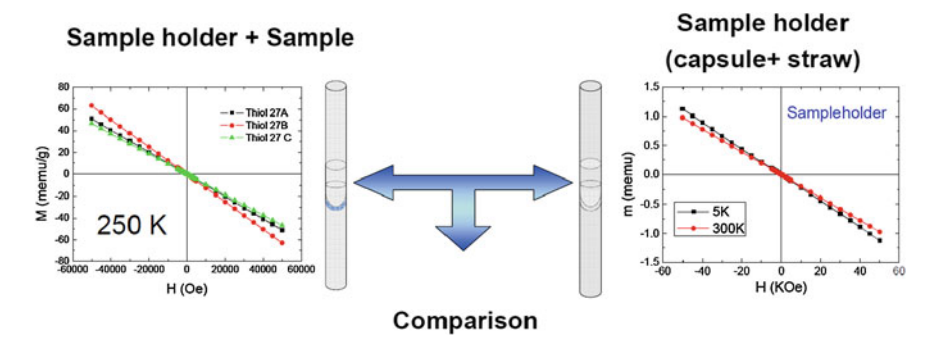


Fig. 2.18 The measurements are performed for the empty sample holder, in order to compare with the experimental results and remove any spurious signal

thermally independent the paramagnetic component at low temperature is determined from the difference in the low and high temperature susceptibility.

By subtracting a linear background to the M(H) curves (see panels c and d of Fig. 2.19) it is observed that the paramagnetic signal, recorded at 5 K, is negligible at high temperature, while a non-saturated ferromagnetic-like (FML) contribution is found. By FML behaviour we mean that the magnetization of the samples show most of the typical ferromagnetic characteristic, as remanence, coercivity and saturation.

As shown in Fig. 2.20 the magnetization curves of the sample holder used for the measurements exhibit a diamagnetic behaviour at both T=5 and 300 K. Moreover, the Curie-Weiss decay observed for the sample holder is 50 times smaller than for the THIOL sample. After subtracting a linear background the magnetization curves show also a FML component but it is at least five times smaller than that of any of the samples. In addition, this FML contribution strongly decays at high temperature being more than 20 times smaller at 300 K, while the observed decrease in the samples is

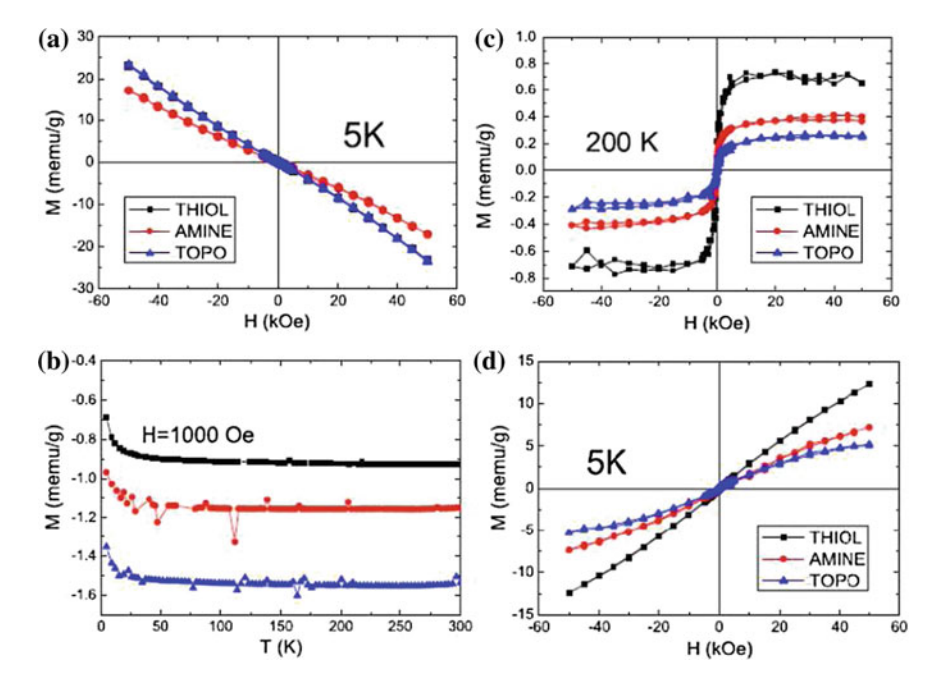


Fig. 2.19 a Magnetization curves of TOPO, THIOL and AMINE. b Thermal dependence of the magnetization under an applied field of 1000 Oe. c, d Magnetization curves after subtracting the diamagnetic contribution, showing the paramagnetic and ferromagnetic components

significantly smaller (Fig. 2.19b). Finally, it should be noted that, when normalized to the mass (Fig. 2.20d), the FML components of the samples overlap indicating that this signal is not a background but it really arises from the sample. SQUID measurements on the precursor found no magnetic signal up to a resolution of 5×10^{-5} emu/g that is two orders of magnitude smaller than the FML signal reported here. The thermal dependence of the magnetization resulted different for each capping molecule, highlighting the influence of the surface bonds in this magnetism.

In the case of samples of series-1 the FML contribution shows hysteresis ($H_C \sim 200\,\text{Oe}$) which remains also identical at high temperature. The value of the saturation magnetization, $\sim 2\,\text{memu/g}$, is in agreement with the values previously reported, although the dependence with the capping molecule is fairly different [21].

It is interesting at this point to compare the magnetic behaviour of the THIOL sample prior and after the calcination process. As shown in Fig. 2.21 despite both samples exhibit similar FML properties, the paramagnetic contribution is clearly reinforced in the calcinated sample. According to the XRD data, this seems related to the growth of ZnS-like regions upon calcination and the decrease of the amorphous phase. Therefore we can not rule out the importance of the structural conformation of the bonding region with the capping molecule into determining the magnetic properties of the samples.

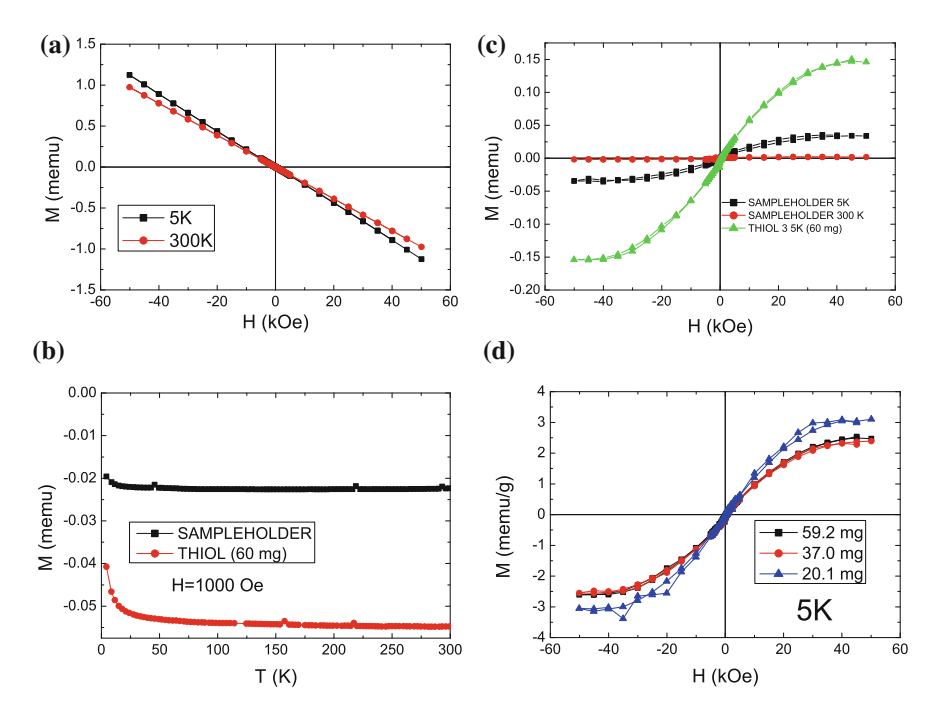
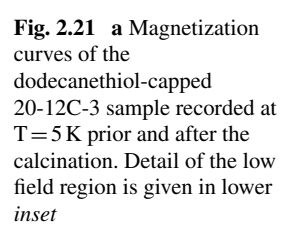
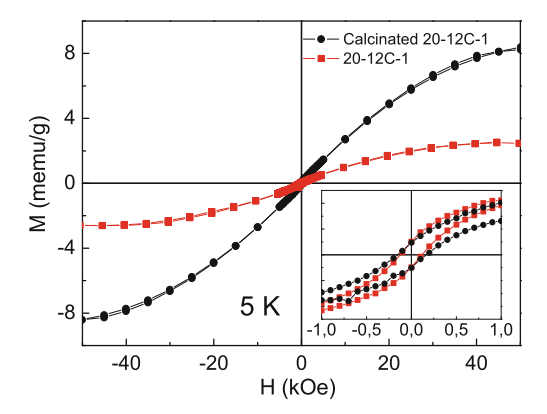


Fig. 2.20 a Magnetization curves of the sample holder used for the measurements. **b** Thermal dependence of the magnetization (curve for THIOL sample is also presented for comparison purposes). **c** Magnetization curves after subtracting a linear background. **d** Ferromagnetic component for the THIOL sample at 5 K measured on three different specimens of 20, 40, and 60 mg





This behaviour is in agreement with the results found in the case of samples of series-2. The XRD patterns of the 15-12C-2 and 30-12C-2 samples (presented in Fig. 2.4) evidence a higher crystallinity of the ZnO component. As shown in Table 2.3 and Fig. 2.22, the decrease of the relative amount of the amorphous phase coincides

Sample	χ_{PM} (emu/g·Oe) (5 K)	H_c (5 K) Oe	H_c (250 K) Oe
20-12C-1	2.00×10^{-7}	180	180
20-12C-1 Calcinated	3.20×10^{-7}	250	200
5-12C-2	1.98×10^{-7}	150	300
15-12C-2	1.12×10^{-7}	250	200
30-12C-2	8.30×10^{-8}	300	230

Table 2.3 Coercivity and paramagnetic susceptibility (χ_{PM}) of series-1 and -2 (Thiol-capped NPs)

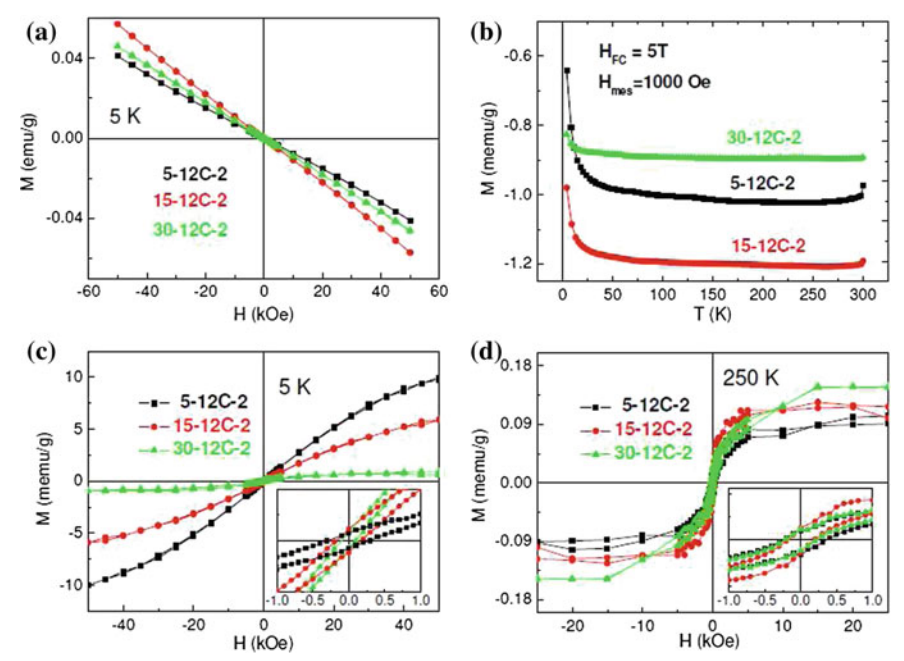


Fig. 2.22 a Magnetization curves of the dodecanethiol-capped ZnO NPs (12C-2 series) measured at $T=5\,\mathrm{K}$. b Thermal dependence of the magnetization under an applied field of 1000 Oe. c $T=5\,\mathrm{K}$ magnetization curves after subtracting the diamagnetic linear background (see text for details). In the *inset* a detail of the low field region, demonstrating the existence of remanence and hysteresis, is shown. d Same as panel c for $T=250\,\mathrm{K}$

with the decrease of the paramagnetic component. That is supported as well by the results of the series-5 samples (see Fig. 2.23).

It is important to note also that the occurrence of FML behaviour does not depend on the length of the organic molecule used for the capping. As a representative example of samples of series-4 we show in Fig. 2.24 the M(H) curves recorded for sample 20-4C-4, as well as the values of H_C in Table 2.4. Interestingly, despite coercivity is found, the FML/paramagnetic ratio found for these samples, showing the lowest cristallinity through the studied series, is the smallest within the synthesized series of NPs.

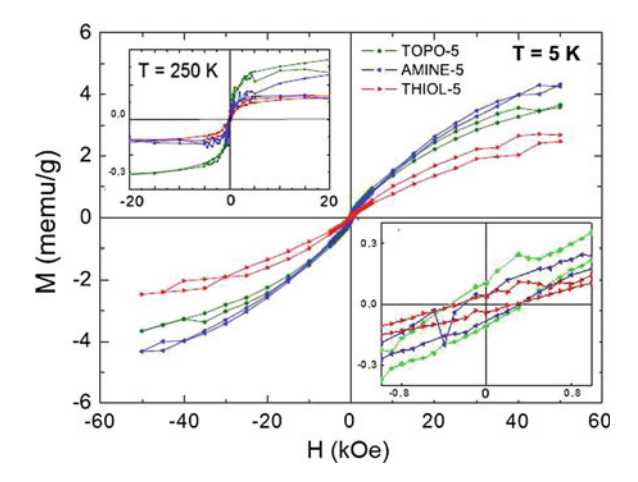


Fig. 2.23 Magnetization curves of the series-5 TOPO, THIOL and AMINE-capped ZnO NPs measured at $T=5 \, \text{K}$. In the *inset* a detail of the low field region, demonstrating the existence of remanence and hysteresis, is shown. The *upper inset* show the magnetization curves at $T=250 \, \text{K}$

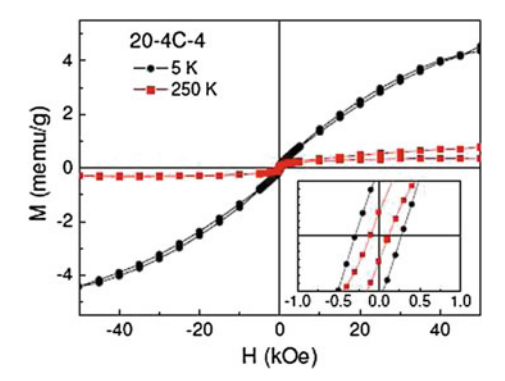


Fig. 2.24 Magnetization curves of the butanethiol-capped 20-4C-4 sample measured at both $T=5\,\mathrm{K}$ and $T=250\,\mathrm{K}$. Detail of the low field region is reported in the *inset*

These results suggest that amorphous phase enhances the paramagnetic contribution. Thus, an analogous study was carried out for thin films and ZnO/ZnS heterostructures, which present a high structural order. However, the comparison of M(H) curves (see Fig. 2.25) of the heterostructures with that of the ZnO monocrystal, indicates that the crystallinity does not explain the FML behaviour by itself. The ZnO monocrystal reference presents a pure paramagnetic behaviour at low temperature while the magnetic signal becomes nearly zero at room temperature. This could means that the FML response should be somehow related to the modification of the original W-ZnO crystal structure.

To further consider that possibility a deeper study of the heterostructures is carried out. The FML contribution is maximized in the case of the $(ZnO_{4nm}/ZnS_{4nm})_{10}$

Sample	H_c (Oe) T = 5 K	H_c (Oe) T = 250 K
20-12C-4	150	150
20-12C-4	180	180
30-12C-4	300	230
20-4C-4	410	110
20-8C-4	-	150
20-12C-4	-	180
50-4C-4	-	100
50-8C-4	360	160
50-12C-4	310	140

Table 2.4 H_C values determined for ZnO NPs of series-4

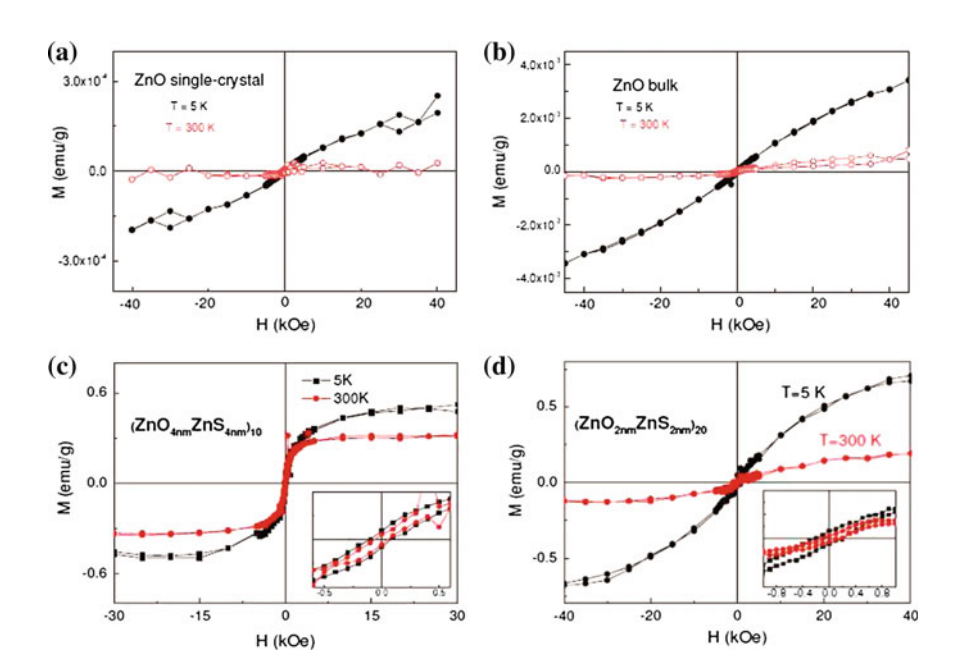
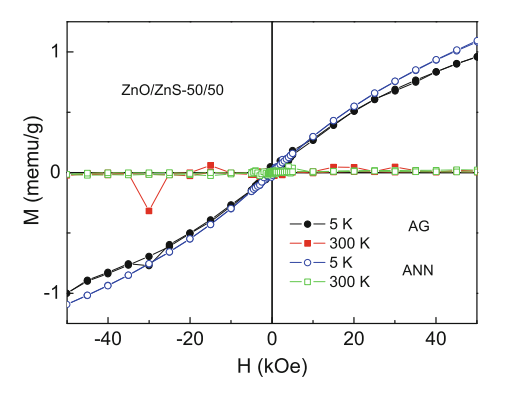


Fig. 2.25 a Magnetization curves of a ZnO single crystal and b bulk ZnO measured at $T=5\,K$ and $T=300\,K$. c Magnetization curves of the $(ZnO_{4nm}/ZnS_{4nm})_{10}$ thin film measured at $T=5\,K$ and at room temperature. d Same as above in the case of the $(ZnO_{2nm}/ZnS_{2nm})_{20}$ sample

heterostructure which shows this behaviour at both T=5 K and at room temperature (see Fig. 2.25). In contrast, the FML signal weakens for the $(ZnO_{2nm}/ZnS_{2nm})_{20}$ sample, which presents larger mean interface roughness and what is more important, an average interface roughness of the order of the layer thickness.

These results point out that the FML component should be related to the development of pristine ZnO/ZnS interfaces. In order to test that, another ZnO/ZnS film was prepared by co-sputtering aiming to maximize the disorder and interpenetration at

Fig. 2.26 Magnetization curves of the ZnS/ZnO-50/50 sample obtained by ZnS-ZnO co-sputtering: AG (as grown) and ANN (after annealing)



the ZnO/ZnS interfaces. As discussed in the previous section this sample shows an amorphous structure. As shown in Fig. 2.26 the FML is not observed in the sample obtained for co-sputtering, whose magnetization curves approach those obtained in the ZnO single crystal reference (see Fig. 2.26).

References

- L.L. Hench, J.K. West, Chem. Rev. 90, 33 (1990)
- C. Brinker, G. Scherer, Sol-Gel Science: The Physics and Chemistry of Sol-Gel Processing (Academic Pr. Inc., Boston, 1990)
- 3. L. Klein, Sol Gel Optics: Processing and Applications (Kluwer Academic Publisher, Berlin, 1994)
- 4. O. Lev, M. Tsionsky, L. Rabinovich, V. Glezer, S. Sampath, I. Pankratov, J. Gun, Anal. Chem. 67, 22A (2012)
- 5. L. Klein, G. Garvey, J. Non-Cryst. Solids 38–39, 45 (1980)
- 6. S. Sakka, K. Kamiya, J. Non-Cryst. Solids 48, 31 (1982)
- 7. C. Brinker, J. Non-Cryst. Solids 100, 31 (1988)
- 8. G. Whitesides, J. Mathias, C. Seto, Science **29**, 5036 (1991)
- E. Céspedes, Ferromagnetism in wide band gap materials Mn-ZnO and Mn-Si₃N₄ thin films, PhD Thesis, Universidad Autónoma de Madrid, 2009
- 10. W.R. Grove, Philos. Trans. Roy. Soc. London 142, 87 (1852)
- 11. E. Goldstein, Philos. Mag. **15**, 372 (1908)
- 12. R. Parsons, Thin Film Processes II. Part II-4: Sputter Deposition Processes (Gulf Professional Publishing, Boston, 1991)
- D. Smith, Thin-Film Deposition: Principles and Practice (McGraw Hill Professional, New York, 1995)
- J.M. Albella, Láminas delgadas y recubrimientos: preparación, propiedades y aplicaciones, Biblioteca de Ciencias, CSIC (2003)
- K. Zoerb, Differential Sputtering Yields of Refractory Metals by Ion Bombardment at Normal and Oblique Incidences, PhD Thesis, Colorado State University, 2006
- N. Telling, S. Guilfoyle, D. Lovett, C. Tang, M. Crapper, M. Petty, J. Phys. D: Appl. Phys. 31, 472 (1998)
- J. Chaboy, R. Boada, C. Piquer, M.A. Laguna-Marco, M. García-Hernández, N. Carmona, J. Llopis, M.L. Ruíz-González, J. González-Calbet, J.F. Fernández, M.A. García, Phys. Rev. B 82, 064411 (2010)

References 35

- 18. N. Üzar, M. Arikan, Bull. Mater. Sci **34**, 287 (2011)
- A. van Dijken, E.A. Meulenkamp, D. Vanmaekelbergh, A. Meijerink, J. Phys. Chem. B 104, 4355 (2000)
- 20. E. Fernández-Pinel, J. de La Venta, A. Quesada, M. García, J. Appl. Phys. 105, 1 (2009)
- M.A. García, J.M. Merino, E. Fernández-Pinel, A. Quesada, J. de La Venta, M.L. González, G.R. Castro, P. Crespo, J. Llopis, J.M. González-Calbet, A. Hernando, Nano Lett. 7, 1489 (2007)

Chapter 3 XAS and XMCD Spectroscopies

The fact that the nanoparticles and the multilayers present, along with a main paramagnetic response, signs of a ferromagnetic-like (FML) contribution, whereas bulk ZnO references and the cosputtered thin film show only paramagnetism suggests that the FML response is related to the formation of a core-shell structure or interface on the ZnO. Moreover, the fact that the FML component is reinforced in the $(\text{ZnO}_{4\text{nm}}/\text{ZnS}_{4\text{nm}})_{10}$ heterostructure, especially when compared to the $(\text{ZnO}_{2\text{nm}}/\text{ZnS}_{2\text{nm}})_{20}$ one, suggests that this effect is not only related to the formation of the ZnS-ZnO interface but also to its degree of structural disorder. Clearly, if the observed ferromagnetism is constrained to the interface of the core-shell nanoparticle (and the ZnO/ZnS interface of the multilayers), it is necessary to obtain a precise structural characterization of the systems prior to establish the precise origin of this magnetic behaviour.

The characterization of the samples reported in the precedent chapter points out the occurrence of high temperature ferromagnetism (HTFM). However, as it was indicated in Chap. 1, claims of HTFM in this type of systems (both doped and undoped) are still subject of controversy over its intrinsic character [1–9]. Therefore it renders necessary to use characterization tools able to provide atom-specific magnetic properties.

Both objectives can be coped by using X-ray Absorption Spectroscopy techniques. In particular, using X-ray Magnetic Circular Dichroism (XMCD) willF provide an unambiguous proof on the extrinsic or extrinsic origin of the HTFM behaviour determined in our samples from macroscopic magnetometry measurements. The combined use of both XAS and XMCD will allow us to establish on firmer grounds the relationship between the magnetic properties and the local structure of the systems under study.

XAS and XMCD are, nowadays, two well known experimental techniques. The principles, capabilities and applications of these techniques can be found elsewhere [10–14]. Hence, we limit ourselves here to present a brief outline of the techniques and a detailed description of the different experimental set-up and methods of analysis used in the course of this work.

3.1 X-ray Absorption Spectroscopy

X-ray absorption spectroscopy (XAS) has proven to be an outstanding structural tool by allowing the determination of the local environment around a selected atomic species in a great variety of systems. An important advantage of this technique is its utility for heterogeneous samples in such a way that a wide variety of solid and liquids, can be examined directly and non-destructively. Additionally, since the local structure does not depend on long-range crystalline order, the structure of amorphous phases (and that of dissolved species) is easily achieved.

The basic process of X-ray absorption is the excitation of electrons from deep core levels of a selected atom by the absorption of a photon. When X-rays pass through any sort of material, ¹ a proportion of them will be absorbed. The phenomenon is schematized in Fig. 3.1. The absorption of X-rays by atoms is smoothly varying with photon energy except at some discrete energies where abrupt increases occur, called absorption edges. These edges correspond to the X-ray photon attaining enough energy to free or excite a bound electron in the atom. The absorption of X-rays on the high energy of the absorption edges does not vary monotonically in condensed matter but has a complicated behaviour which extends past the edge by an amount typically of the order of 1 keV (Fig. 3.2).

According to Fermi's Golden Rule the transition probability per unit of time from a core state to a final state can be written as:

$$\chi(k) = \frac{2\pi}{\hbar} |\langle f | H_{int} | i \rangle|^2 |\rho_f(\hbar\omega - E_c), \tag{3.1}$$

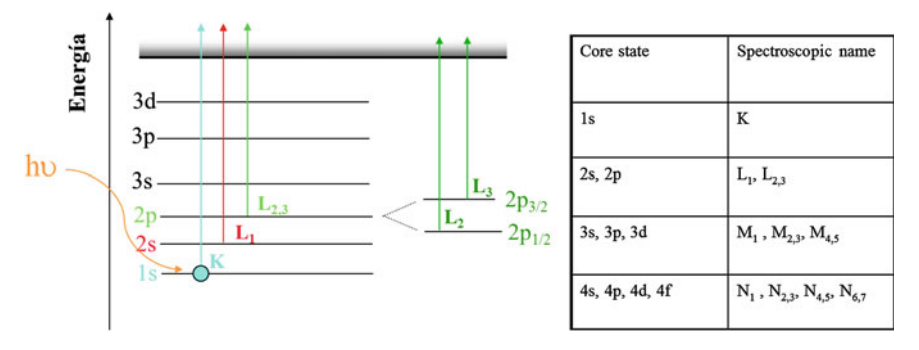
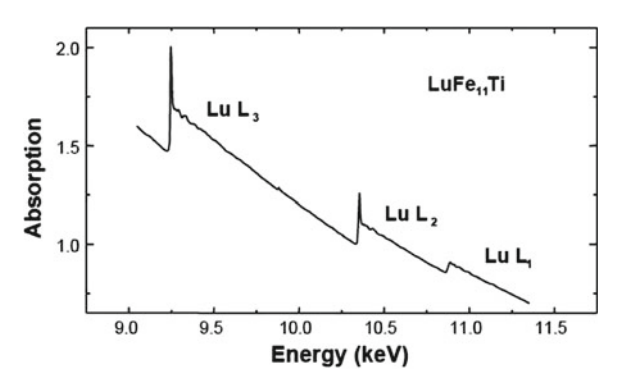


Fig. 3.1 Scheme of the excitation of an electron by the absorption of a X-ray photon. Each transition is characterized by the initial and final states of the excited electron and is usually labelled by the spectroscopic name

¹The expression relating the intensity of the incident beam, I_0 , and the intensity of the beam after crossing a sample of thickness x, I, is the so-called Lambert equation: $I = I_0 e^{-\mu x}$, where μ is the absorption coefficient.

Fig. 3.2 X-ray absorption spectra of LuFe₁₁Ti at the Lu L-edges, involving different final state symmetry: L₃ $(2p_{3/2} \leftrightarrow \epsilon d_{3/2}, d_{5/2})$, L₂ $(2p_{1/2} \leftrightarrow \epsilon d_{3/2})$, L₁ $(2s_{1/2} \leftrightarrow p_{1/2}, p_{3/2})$



where $|\langle f|H_{int}|i\rangle|$ is the matrix element of the electromagnetic field operator, H_{int} , between the initial core-electron state $|i\rangle$ and the final valence state $|f\rangle$, $\rho_f(E)$ is the density of empty states at the energy E above the Fermi level and E_C is the core-electron binding energy. The evaluation of this transition probability requires several approximations concerning both the description of the initial and final states and the interaction operator.

In relation to the description of initial and final states, the simplest approach to the description of X-ray absorption spectra employs the single-electron model as a starting point. In this picture, all the electrons of the system remain passive during the absorption process except the photo-excited core-electron, which is excited to the unoccupied states of the system. This picture allows an easy description of both the core initial states and the delocalized final states (band, continuum states), as only the excited electron is taken into account.

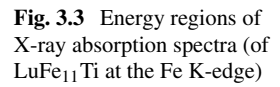
Regarding the interaction operator, when the energy of the incident photon is within the X-ray region it is customary, and usually valid, to make the electric dipolar approximation,²

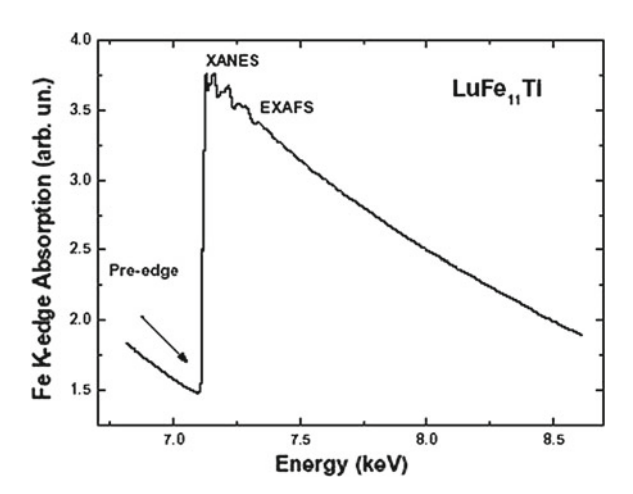
$$|\langle f|H_{int}|i\rangle|\alpha|\langle f|\epsilon \mathbf{r}|i\rangle|$$
 (3.2)

where ϵ is the polarization vector. Since the dipole operator, $\epsilon \mathbf{r}$, is odd and acts only on the radial part of the electronic wave-function (the X-ray photon carries angular momentum one and no spin), transitions can be made only between states which have opposite parity and differ in angular momentum by one: $\Delta l = \pm 1$ and $\Delta s = 0$, the dipole selection rules.

Usually the X-ray absorption spectrum is divided in several regions (see Fig. 3.3) depending on the energy of incoming photons:

²This approximation is correct if the wavelength is larger than the atomic size. If $\lambda \sim 1$ Å, this approximation becomes invalid, except for $r \ll 1$ which is generally the case for core electrons. In the soft X-ray range ($\lambda \geq 5$) all the electrons can be treated in this approximation. In the hard X-ray range ($0.5 \leq \lambda \leq 5$), this approximation remains only valid if we consider interactions with very localized core electrons.





- 1. The pre-edge and edge region, which extends from about 20 eVs below the edge to a few eV above it.
- 2. The XANES (X-ray Absorption Near Edge Spectroscopy) region which extends up to 50–100 eV above the edge.
- 3. The EXAFS (Extended X-ray Absorption Fine Spectroscopy) region which extends from up to 1000 eV beyond the edge.

The physical origin of the absorption features in the pre-edge and edge regions depends on the material, i.e. Rydberg states in free atoms, bound valence states or bound multiple scattering resonances in molecules, unoccupied local electronic states in metals and insulators [15]. Thus, analysis of these near-edge features in the spectrum of a particular sample can provide information about vacant orbitals, electronic configuration and the site symmetry of the absorbing atom.

The underlying physics of the process that occur to produce the XANES and EXAFS structures in the X-ray absorption spectra is easy to understand. The photon is completely absorbed and kicks out a core photoelectron from the absorbing atom leaving behind a core hole. This photoelectron will be ejected with an energy equal to energy of the incoming photon less its binding energy when in the core. This photoelectron will interact with the surrounding atoms. Considering the wave nature of the ejected photoelectron, and regarding the atoms as point scatterers, a simple picture can be drawn in which the backscattered waves interfere with the forward wave to produce either peaks or wells. This is an interference effect on the final state (see Fig. 3.4).

Since the absorption coefficient depends on the dipole matrix element between the initial core state state and the photoelectron's final state, which in turn is a superposition of the outgoing and backscattered spherical waves, the phase relationship between outgoing and backscattered waves depends on the photoelectron wavelength and the interatomic distance. The variation of this phase relationship as a function of the photon energy influences the final state amplitude at the core site, giving rise to an

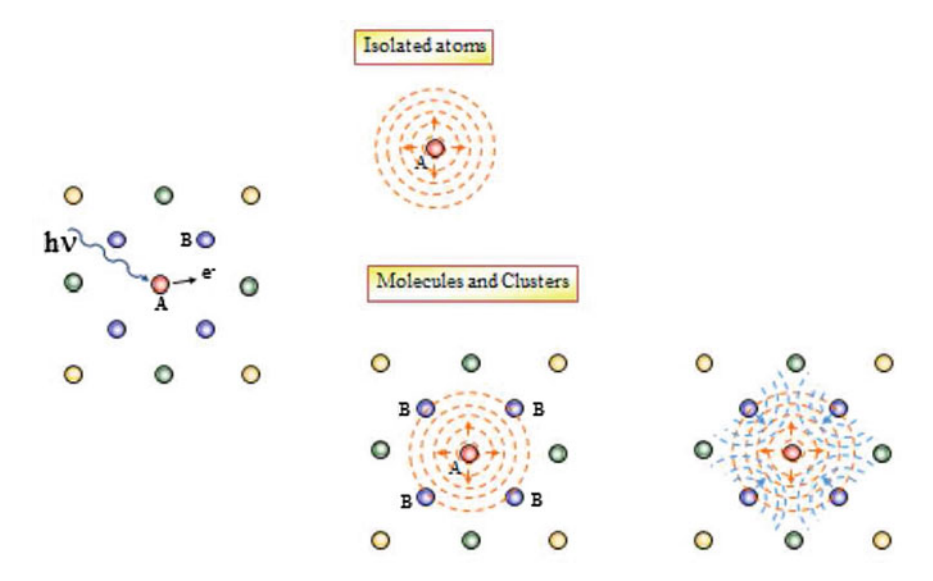


Fig. 3.4 Schematic illustration of the interference phenomena giving rise to the modulations (EXAFS) in the X-ray absorption cross-section

interference phenomenon which modulates the absorption coefficient. This leads to the oscillatory nature of the interference effect. Since backscattering amplitude and phase are dependent on the type of atom doing the backscattering and its distance from the central atom, information regarding the coordination environment of the absorbing atom can be obtained by analysing the XANES and EXAFS.

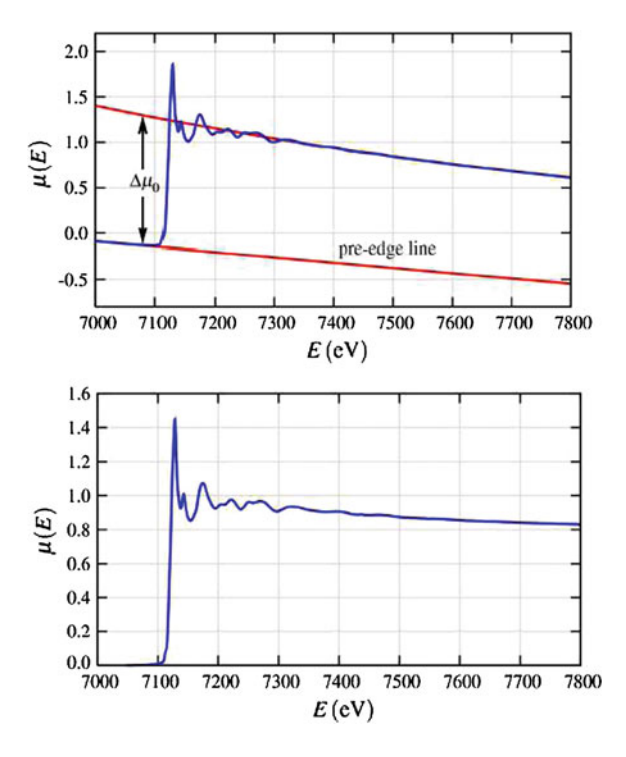
The analysis of the absorption in the XANES region is usually made on normalized spectra. The XAS spectrum is superimposed over a curve (called Victoreen curve) whose origin are all the possible absorption processes occurring in the compound corresponding to less energetic edges. Victoreen curve is determined in a empirical way assuming a dependence on energy:

$$\mu_V = A - C/E^3 + D/E^2 \tag{3.3}$$

Usually, considering Victoreen curve as a straight line at each edge is a good approximation. This line is obtained by fitting the values of an energy range at the pre-edge region to a linear function and the extra contribution is removed by simple subtraction of this line. The intensity of the post-edge region varies from one sample to other due to the difference of thickness between the samples. To remove this dependence, the spectra are normalized to the average absorption coefficient at high energy so that in this energy region the averaged intensity is always one no matter the thickness of the sample (Fig. 3.5).

In the case of the high-energy region of the spectrum the analysis is made on the so-called $\chi(k)$ EXAFS signal. This signal is obtained as $\chi(E)$ =

Fig. 3.5 XAS pre-edge subtraction and normalization (*top*). First, a pre-edge line (or simple polynomial) is fitted to the spectrum for energies below the edge. The jump in the edge is approximated, and the spectrum is normalized by this value. The resulting normalized spectrum is shown in the *bottom panel* (from [16])



 $(\mu(E) - \mu_0(E))/\mu_0(E)$, where $\mu_0(E)$ is the atomic absorption coefficient of the isolated atom. Then, the expression is transformed to the k-space as: $k = \sqrt{2m_e(E-E_0)/\hbar^2}$ (an example is shown in Fig. 3.6).

The EXAFS signal is theoretically accounted for in terms of the Fermi's Golden Rule, to calculate the cross section of absorption in the electronic dipole approximation. That description leads to the following expression for the EXAFS region when only single-scattering processes are taking into account:

$$\chi(k) = \frac{\mu(k) - \mu_0(k)}{\mu_0(k)} = -\sum_i \frac{N_i S_0^2}{k r_i^2} |f_i(k, \pi)| \sin(2kr_i + \phi_i) e^{(-2k^2 \sigma_i^2)} e^{\frac{-2r_i}{\lambda(k)}}$$
(3.4)

where N_i is the number of neighbouring atoms surrounding the absorber at radial distance r_i and with and scattering amplitude of $f_i(k,\pi)$, λ is the mean free path of the photoelectron and S_0^2 is the amplitude reduction factor (due to inelastic scattering); k is the photoelectron wavenumber, ϕ_i is the photoelectron phase shift due to the scattering from the atom i and the absorber, $exp(-2k^2\sigma_i^2)$ is the so-called Debye-Waller factor, associated to the thermal oscillations and/or structural disorder.

According to this expression EXAFS can be described as a series of periodic sine waves that decay in intensity as the incident energy increases from the absorption

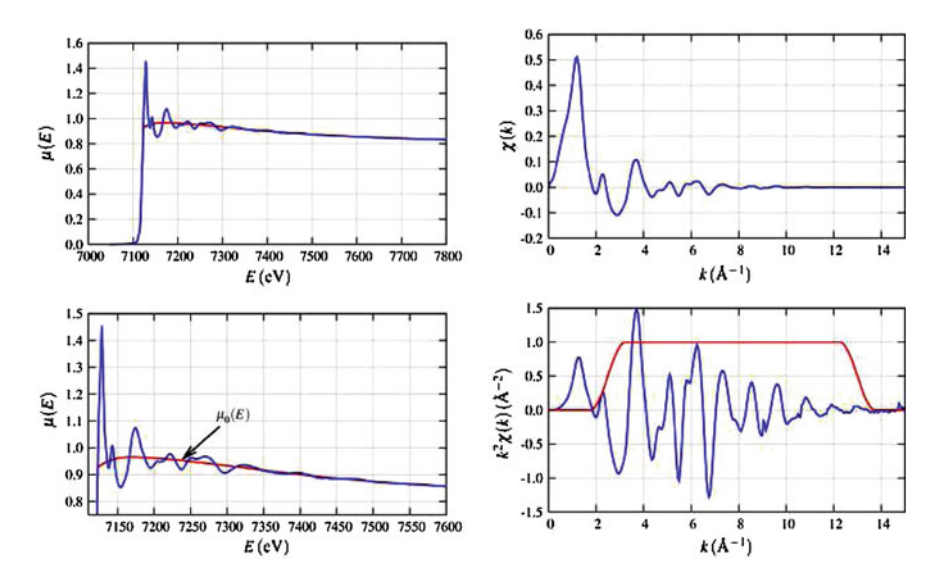


Fig. 3.6 Background correction and extraction of the $\chi(E)$ signal, and the resulting $\chi(k)$ and $k^2 \cdot \chi(k)$ EXAFS signals after transformation to k-space (photoelectron wavenumber)

edge. These sine waves result from the interaction of the elected photoelectron with the surrounding atomic environment. As such, their amplitude and phase depend on the local structure of excited atom and, consequently, the EXAFS provides direct, local structural information about the atomic neighbourhood of the element being probed (identity of neighbouring atoms, their distance from the excited atom, the number of atoms in the shell, and the degree of disorder in the particular atomic shell).

Although the EXAFS formula provides a complete description of the EXAFS oscillations, it is not a particularly convenient form for visualizing the information content of an EXAFS spectrum. Fourier transformation can be used to decompose a frequency-space signal into its different constituent frequencies. This is shown if Fig. 3.7. The Fourier transform (FT) of an EXAFS spectrum gives a pseudo-radial distribution function [17]. It is pseudo in that the FT amplitude cannot be related directly to electron density around the absorber due to the backscattering amplitude and the damping factors, and because the apparent distances in the FT are shifted by about 0.5 Å, due to the phase shifts. However, the FT is a useful way of judging qualitatively which coordination shells may be present in a system and for comparing a fit to the data.

As a final remark we like to note that the only distinction between XANES and EXAFS regions is the relative weight of the multiple scattering processes of the excited photoelectron. Usually it is considered that in the EXAFS region only single-scattering processes are important contrary to the XANES region in which due to the low kinetic energy of the ejected photoelectron multiple scattering processes are

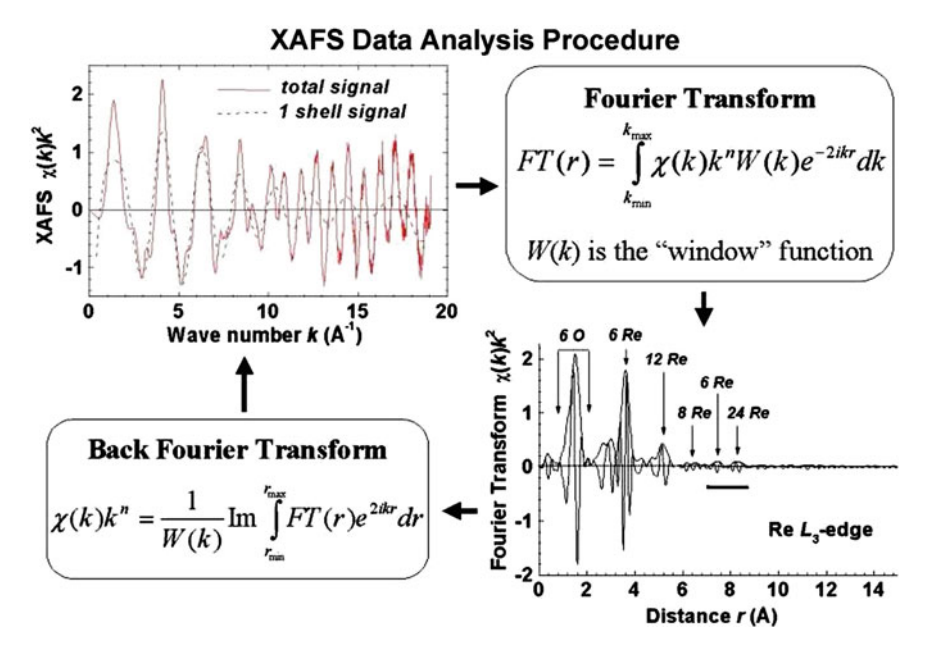


Fig. 3.7 This figure (from http://www.dragon.lv/exafs/aboutexafs.htm) shows an example of the Fourier filtering procedure for the first coordination shell XAFS in ReO₃ (Re L₃-edge). The total XAFS signal (*red solid line*) is first Fourier transformed (FT) from k to R-space, and then, the first shell contribution from 1 to 2.2 Å is back-FT into k-space (*black dashed line*)

dominant (as schematized in Fig. 3.8). This confers to XANES a higher sensitivity to the bonding geometry of the absorber (overall symmetry, distances and bond angles) than for EXAFS. However ab-initio computation of XANES spectra is not so straightforward as for EXAFS, as XANES computation requires sophisticated simulation tools.

The main characteristic of both XANES and EXAFS spectroscopy are summarized below:

- 1. EXAFS spectroscopy allows determining the chemical environment of a single element in terms of the number and type of its neighbours, inter-atomic distances and structural disorder. This determination is confined to a distance given by the mean free path of the photoelectron in the condensed matter, which is between 5 and 10 Å radius. These characteristics make EXAFS a powerful structural local probe, which does not require a long-range order. Since EXAFS is a technique selective for a particular element and sensible only for a short-range order, it is one of the most appropriate spectroscopies to be applied in the following cases:
 - Amorphous solids,
 - Liquids and solutions,
 - Biomolecules,
 - Homogeneous and heterogeneous catalysts.

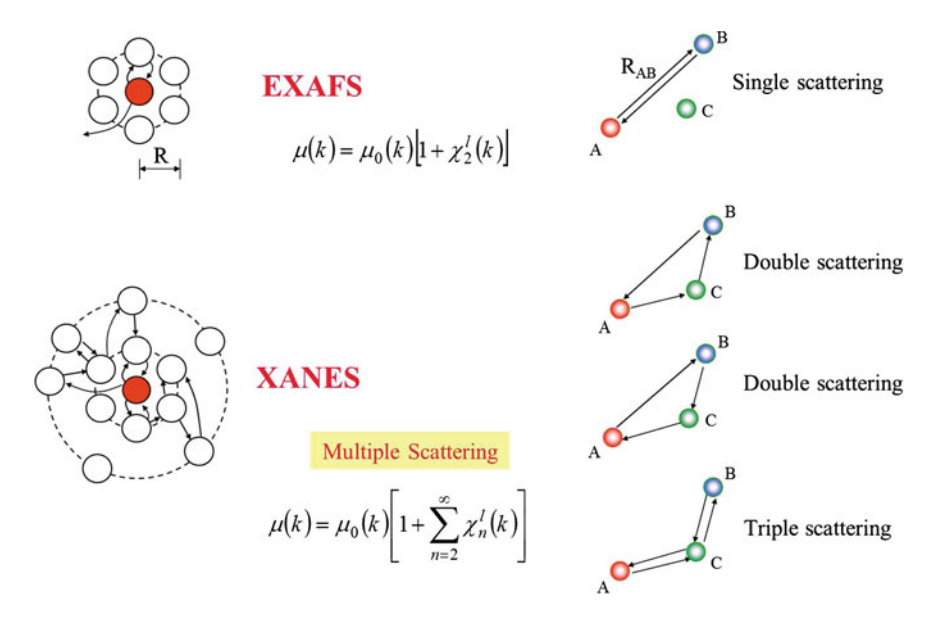


Fig. 3.8 Single and multiple-scattering processes in X-ray absorption

2. XANES spectroscopy provides both electronic and geometric structural description. The XANES region holds important chemical information, especially formal valences (very difficult to experimentally determine in a nondestructive way) and coordination environment, which can be determined by direct fingerprint comparison. Besides, it presents some advantages over the study of the EXAFS region: (i) it is highly sensitivity to the bonding geometry so it provides, contrary to the EXAFS analysis, an unambiguous determination of the coordination polyhedron, (ii) it is a much larger signal than EXAFS, so XANES information can be obtained at lower concentrations, and at worse sample conditions. On the other hand the interpretation of XANES is complicated by the fact that there is not a simple analytic description of XANES, which renders necessary the use of sophisticated computational codes.

3.2 X-Magnetic Circular Dichroism

XMCD can be defined as the difference of the X-ray absorption coefficient $\mu_c = (\mu^- - \mu^+)$ for antiparallel, μ^- , and parallel, μ^+ , orientation of the incident photon helicity and sample magnetization.³

³Some authors define XMCD as the difference for antiparallel and parallel orientation of the incident photon helicity and the direction of the majority spins. This definition needs the knowledge of the

Thus, XMCD consists basically on recording XAS spectra under two particular conditions: (i) the incident light is circular polarized and (ii) the sample under study has a net magnetization. Therefore, XMCD exhibits the same **element and shell selectivity** properties as the standard XAS, i.e. by tuning the appropriate energy one can choose the electron (transition) to excite, i.e., the precise final state to explore.

In addition, when XAS is performed with polarized X-rays, some extra selection rules have to be taken into account, thus extending the range of information available from this technique. Right circularly polarized light (RCP)⁴ carries helicity, i.e. angular momentum along the direction of propagation, $\nu + 1$ (-1 for LCP). Therefore, within the electric dipolar approximation approach, $|\langle I|H_{int}|f\rangle|\alpha|\langle i|\epsilon \mathbf{r}|f\rangle|$, and taking into account conservation of angular momentum,⁵ absorption of RCP light gives rise to transitions with $\Delta m_j = +1$ ($\Delta m_j = -1$ for LCP). That is, the dipole selection rules for RCP (LCP) light are:

$$\Delta j = 0, \pm 1$$
 $\Delta l = \pm 1$ $\Delta s = 0$ and $\Delta m_j = +1$ $(\Delta m_j = -1)$ (3.5)

The extra selection rule $\Delta m_j = \pm 1$ is at the origin of XMCD. As we will see below this extra selection rule allows us to scan the difference in the density of empty states with different spin moment supplying magnetic information on the material under study.

One can qualitatively understand the basic principle of XMCD by using the oneelectron model along with the two-step approach formulated by G. Schütz and coworkers [18]. According to this model, in a first step, partially spin-polarized core electrons are excited from an unpolarized initial core state [19] by a circularlypolarized photon. Due to the conservation of angular momentum in the absorption process, the angular momentum of the photon is entirely transferred to the photoelectron. As there is no explicit spin dependence, electronic spins remain unaltered unless they are coupled to the orbital momenta by strong spin-orbit interaction. Thus, in the absence of a connection between the spin and orbital part of the electron angular momentum, both LCP and RCP light will excite 50% electrons with spin-up and 50% with spin-down. However, when spin-orbit is present, the angular moment of the photon can be partially transferred to the spin through the spin-orbit coupling. The photoelectrons are therefore ejected with a spin polarization⁶ (i.e. there

⁽Footnote 3 continued)

relationship between M and S of the selected shell of the selected atom, which is not evident in some cases

⁴**Sign convention**: In this thesis we are using the physics definition for right and left polarization of the light: right corresponds to $+\hbar$ (positive helicity) and left corresponds to $-\hbar$ (negative helicity) (In the optical definition the signs are just the opposite).

⁵We are considering the quantification axis is parallel to the photon propagation direction.

⁶If the photoelectron originates from a spin-orbit split level, e.g. the $p_{3/2}$ level (L_3 -edge), its angular momentum can be transferred in part to the spin through the spin-orbit coupling. Right-circularly-polarized photons transfer to the electron a momentum opposite to that from left-circularly-polarized photons; hence, photoelectrons with opposite spins are created in the two cases. Since the $p_{3/2}$ (L_3)

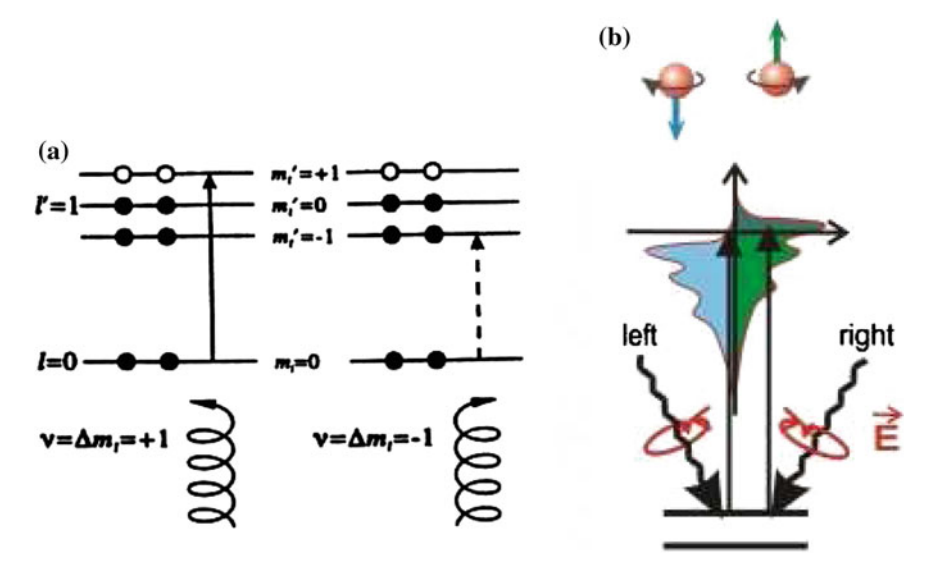


Fig. 3.9 a The atom exhibits dichroism if the absorption is different for $\nu=\pm 1$. b Magnetic materials with net magnetization present different occupancy of spin-up and spin-down final states

is an imbalance between spin-up and spin-down excited electrons) (Fig. 3.9). In the second step the spin-polarized photoelectrons will probe, taking into account the Pauli exclusion principle, the spin polarization of the final empty states. Consequently, the XMCD spectrum reflects the difference in the density of empty states with different spin moment. (The magnetic properties of the sample are probed in the second step because the spin-split valence shell acts as a detector for the spin of the excited photoelectron).

The transition probability is proportional to both the electron polarization, P_e also called Fano parameter⁷ [19], and the spin-density differences $\Delta \rho = \rho \uparrow -\rho \downarrow$, $\rho \uparrow and \rho \downarrow$ being the majority- and minority-like final state densities, in the form:

$$\frac{\mu^{-}(E) - \mu^{+}(E)}{\mu^{-}(E) + \mu^{+}(E)} = P_e \frac{\Delta \rho}{\rho}$$
(3.6)

In order to understand more clearly this picture, we present below the application of this model to the particular case of the L_{2,3}-edge XMCD spectra ($2p \rightarrow 3d$ transitions) of a 3d transition metal.

In the first step the core electrons are excited by a circularly-polarized photon from the initial $2p_{3/2}$ (L₃-edge) and $2p_{1/2}$ (L₂-edge) that can be characterized by

⁽Footnote 6 continued)

and $p_{1/2}$ (L₂) levels have opposite spin-orbit coupling (1+s and 1-s, respectively) the spin polarization will be opposite at the two edges.

⁷The Fano parameter can be calculated under certain assumptions: $P_e = 0.01 \, \text{K}$ and L_1 -edge; $P_e = -0.5 \, L_2$ -edge; $P_e = 0.25 \, L_3$ -edge.

the quantum numbers j and m_j with j = l + s and j = l - s, respectively. For the final 3d states we shall assume a Stoner model: there is no spin-orbit splitting and the exchange interaction splits the band into spin-up and spin-down components. Therefore we will have five degenerate spin-up states with density of states, DOS, $\rho \uparrow$ and five degenerate spin-down states with DOS $\rho \downarrow$.

For evaluation of the matrix elements it is useful to express the dipole operator in terms of spherical harmonics:

$$\epsilon \cdot \mathbf{r} = \sqrt{\frac{4\pi}{3}Y_1^1 \cdot r} \quad \text{for RCP light}$$
 (3.7)

$$\epsilon \cdot \mathbf{r} = \sqrt{\frac{4\pi}{3} Y_1^{-1} \cdot r} \quad \text{for LCP light}$$
 (3.8)

Since the dipole operator does not act on the spin-state, the matrix elements can be written with regard to a ll, m_l , s, m_s basis (the product of spherical harmonics and a spin dependent function). According to the dipole selection rules the transitions occur from 2p states |ll|, m_l into the 3d states with |l| + 1, $m_l \pm 1$ and the possible matrix elements are obtained from:

$$\sqrt{\frac{4\pi}{3}}\langle l+1, m_l \pm 1 | Y_1^{\pm 1} | l, m_l \rangle R = -\sqrt{\frac{(l \pm m_l + 2)(l \pm m_l + 1)}{2(2l+3)(2l+1)}} R$$
 (3.9)

where the radial part is given by:

$$R = \langle n', l+1|r|n, l\rangle \tag{3.10}$$

and can be assumed as constant for the considered transitions.

The angular part of the matrix elements

$$I_{jm}^{\pm} = \left| \frac{4\pi}{3} \langle j', m \pm 1 | Y_1^{\pm 1} | j, m \rangle \right|^2$$
 (3.11)

is listed in Table 3.1 for the $|jm_m\rangle$ sub-levels with respect to the spin and circular polarization of the X-rays. It shows that at the L₃-edge right circular polarized light prefers excitation of spin-up electrons, while the situation is the opposite at the L₂-edge.

In the second step, taking into account the Pauli exclusion principle and the different DOS for spin-up, $\rho \uparrow$, and spin-down $\rho \downarrow$, (in a material with net magnetization) we obtain a different transition probability, i.e., a different absorption for left and right circular polarized light as shown in Table 3.2.

Thus, from this picture it is easy to see both, why the absorption is different for left and right circular polarized light and why the XMCD is related to the magnetism of the band we are probing.

of light					
j, m _j	$ m_l, m_s $	I+	I-		
$\frac{3}{2}$, $+\frac{3}{2}$	$ +1 \uparrow \rangle$	$(\frac{2}{5})\uparrow$	$(\frac{1}{15})\uparrow$		
$\frac{3}{2}$, $+\frac{1}{2}$	$\begin{vmatrix} \sqrt{\frac{1}{3}} + 1 \downarrow \rangle + \sqrt{\frac{2}{3}} 0 \rangle$	$(\frac{2}{15})\downarrow + (\frac{2}{15})\uparrow$	$(\frac{1}{45})\downarrow + (\frac{2}{15})\uparrow$		
$\frac{3}{2}, -\frac{1}{2}$		$(\frac{2}{15}) \downarrow + (\frac{1}{45}) \uparrow$	$(\frac{2}{15}) \downarrow + (\frac{2}{15}) \uparrow$		
$\frac{3}{2}, -\frac{3}{2}$	$ -1\downarrow\rangle$	$(\frac{1}{15})\uparrow$	$(\frac{2}{5})\downarrow$		
$\frac{1}{2}$, $+\frac{1}{2}$	$\begin{vmatrix} \sqrt{\frac{2}{3}} I + 1 \downarrow \rangle - \sqrt{\frac{1}{3}} I 0 \\ \uparrow \rangle \end{vmatrix}$	$\left (\frac{4}{15}) \downarrow + (\frac{1}{15}) \uparrow \right $	$(\frac{2}{45})\downarrow + (\frac{1}{15})\uparrow$		
$\frac{1}{2}, -\frac{1}{2}$	$ \sqrt{\frac{1}{3}} 0 \downarrow \rangle - \sqrt{\frac{2}{3}} -1 \rangle $	$(\frac{1}{15})\downarrow + (\frac{2}{45})\uparrow$	$(\frac{1}{15})\downarrow + (\frac{4}{15})\uparrow$		

Table 3.1 The angular part of the matrix elements for excitations from 2p core levels $|i m_j\rangle$ decomposed into $|l=1, m_l, s=1/2, m_s\rangle$ and catalogued with respect to spin and circular polarization of light

Table 3.2 The X-ray absorption for RCP (LCP) light involves preferentially spin up (spin down) electron on the $2p_{3/2}$ core level (L₃-edge)

	I+	I-	ΔΙ (α ΧΜCD)
L ₂	$\frac{1}{3} \rho \downarrow + \frac{1}{9} \rho \uparrow$	$\frac{1}{9} \rho \downarrow + \frac{1}{3} \rho \uparrow$	$\frac{2}{9} \left(\rho \downarrow - \rho \uparrow \right)$
L_2	$\frac{1}{3} \rho \downarrow + \frac{5}{9} \rho \uparrow$	$\left \frac{5}{9}\rho\downarrow+\frac{1}{3}\rho\uparrow\right $	$\frac{2}{9}(-\rho\downarrow+\rho\uparrow)$

The opposite situation is observed for the $2p_{1/2}$ core level (L₂-edge)

In the explanation given above we have used a band (Stoner) model to describe the final 3d states. Alternatively, one can consider an atomic picture with spin-orbit splitting in both initial and final states. In this case, dichroic intensity can be obtained following the procedure described above if the degeneracy of final states is assumed lifted and the different m_j final states have different occupation.

The one-electron picture can be also used to explain the XMCD signal at the K-edge of the transition metals. In these cases, due to the spherical symmetry of the initial state (no spin-orbit coupling in the initial state), a small spin-orbit coupling of the final p states is invoked to account for the spin-dependent of X-ray absorption [19]. In addition, the XMCD signal at the K-edge of the 3d transition metal element is much weaker than at the $L_{2,3}$ -edges, since we are not probing the 3d, responsible for magnetism in 3d metals, but the extended 4p band. The XMCD effect at the K-edge of 3d transition metals is only about 10^{-3} (or less) of the absorption jump, whereas at the $L_{2,3}$ -edges is of the same order of the absorption jump.

3.3 Experimental Methods and Procedures

3.3.1 Synchrotron Radiation Facilities

Synchrotron radiation has a number of unique properties that have established it as a powerful research tool for material sciences, crystallography, surface physics, or chemistry, among other areas of research [10, 20, 21]. The main properties of the emitted radiation depend on the characteristics of the storage ring are summarized below:

- 1. High intensity.
- 2. Very broad and continuous spectral range from infrared up to the hard X-ray region. A monochromatic source can be achieved with the aid of monochromators, which are adjusted to the required wavelength.
- 3. Natural narrow angular collimation.
- 4. High degree of polarization.
- 5. Pulsed time structure.
- 6. High brilliance of the source due to small cross section of the electron beam and high degree of collimation of the radiation.
- 7. Ultra-high vacuum environment and high beam stability.
- 8. All properties quantitatively evaluable.

The synchrotron radiation is generated when electrons travelling at high speed are forced to change the direction of their motion under the effect of magnetic fields. The synchrotron facilities, where this radiation is produced and used, are high energy, electron or positron circular accelerators. They consist of circular rings where the electrons are forced to follow circular paths under the action of magnets placed along the circumference (bending magnets, wigglers or undulators). The electrons enter the storage ring only after they have been accelerated in a linear accelerator or (LINAC) until their energy reaches several millions of electron (MeV). Here the electrons may be further accelerated to higher energies by the radio frequency (RF) electric fields. Moreover, the energy lost during each turn is regained in passing through the RF. When the electrons reach the expected energy they are forced to follow circular paths by the magnets: they are deflected from their straight path by several degrees, which causes them to emit the synchrotron radiation that will be used in the beamlines for experiments. In that way, the most powerful applications of X-rays into address electronic and magnetic aspects of condensed matter utilize this fully polarized, tunable synchrotron radiation, where the X-ray energy is tuned to the absorption edge of a magnetic atom [88].

The needed measurements for the presented work were carried out in three different beamlines from two synchrotron facilities: SPring-8 and Elettra, *third generation synchrotron radiation sources* which operate with electron energies of 8 and 2–2.4 GeV respectively. The description of the beamlines is displayed in the following.

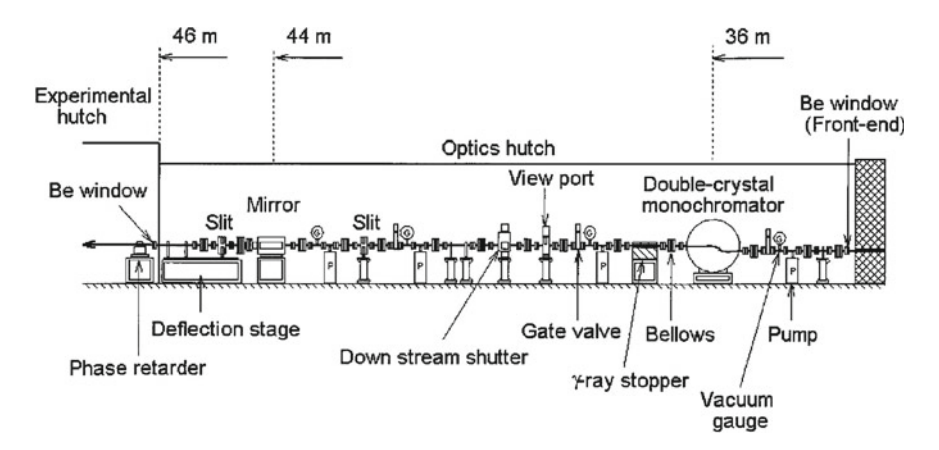


Fig. 3.10 BL39XU beamline layout

3.3.2 BL39XU Beamline at SPring-8 Facility

The whole Zn K-edge XAS and XMCD spectra were performed at the BL39XU beamline of the SPring-8 facility [22]. BL39XU is an undulator beamline that is dedicated to hard X-ray spectroscopy and diffractometry requiring control of the X-ray polarization state. One of the major applications of this beamline is XMCD spectroscopy and resonant X-ray magnetic scattering in 3d transition metals and compounds, rare-earth elements and 5d metals. The beamline layout is shown in Fig. 3.10.8

3.3.2.1 Optics Hutch

Typically, the optical set-up required to obtain a focused, monochromatic and circularly polarized beam in a synchrotron station is very complex and in this thesis only the main components will be described (see Fig. 3.11).

The light source is an in-vacuum type undulator of the SPring-8 standard type. It provides extremely high brilliance X-ray linearly polarized in the horizontal plane. The fundamental, third and fifth harmonics cover the photon energy range between 5 and 70 keV. The undulator gap is changed at each energy point so that one can obtain a very smooth I_0 spectrum as if using a "white source". BL39XU is also equipped with a rotated-inclined double-crystal monochromator. The monochromator angle tuning is combined with undulator gap tuning to maximize the photon flux onto a sample and to keep it almost constant. The combination of fundamental/third harmonic of undulator radiation with the Si (111) or Si (220) reflection of the monochromator enables an energy range from 5 to 37 keV.

⁸Figures from http://www.spring8.or.jp/wkg/BL39XU/instrument/lang-en.

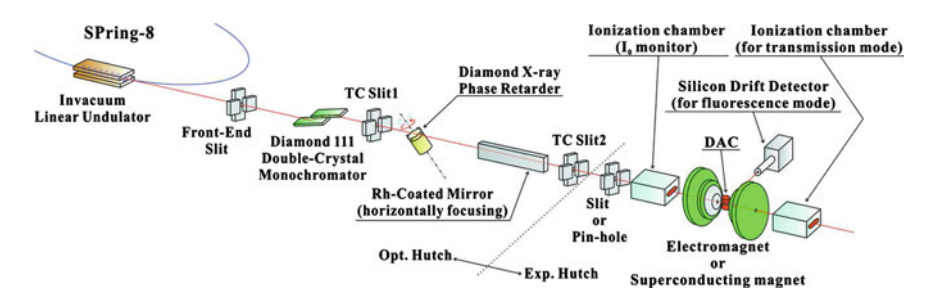


Fig. 3.11 BL39XU beamline layout

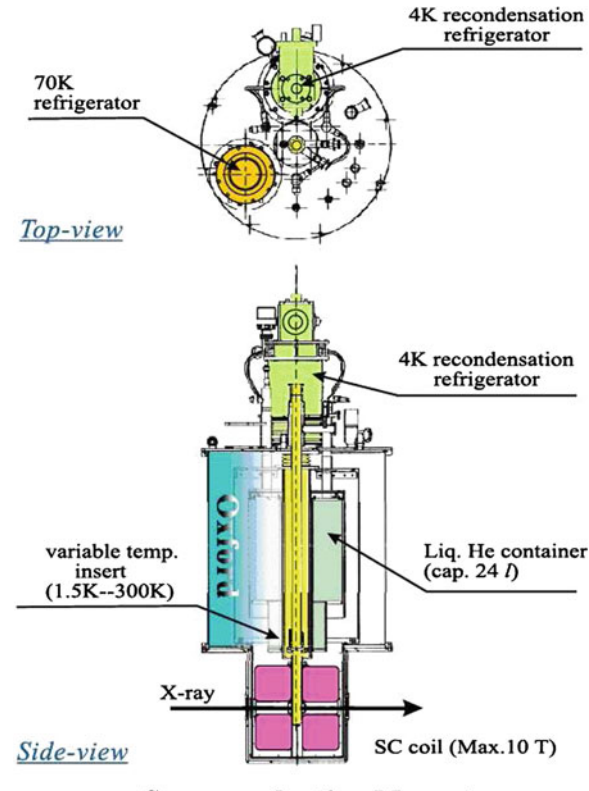
Once monochromatic linear polarized radiation is obtained, the right/left circular polarization states of X-ray are selected by using a diamond X-ray phase retarder (XPR) that acts as a quarter wave plate with high efficiency [23]. The XRP, which is used in the off-Bragg transmission geometry, exploits the birefringence of crystals for σ and π electric field components (σ and π represent the perpendicular and parallel to the scattering plane, respectively) for geometries on or close to diffraction conditions. This birefringence leads to a phase shit between σ and π components of the transmitted X-rays. For a polarization transformation from linear to circular, the phase plate is arranged to satisfy the following two conditions: both σ and π electric field components must have an equal amplitude and a phase shift of $(n + 1/2)\pi$ radians must be produced. The former condition is satisfied by tilting the diffraction lattice plane by 45° with respect to the polarization plane of the incident beam, and the latter by tuning the offset angle from the diffraction condition. Crystals of various thickness (0.10, 0.34, 0.45, 0.73, 1.4, 2.7 and 4.7 mm) are available to optimize both polarization purity and X-ray intensity after the phase plate at X-ray energy of interest. They are used at both the (220) Laue or (111) Bragg transmission geometry. Finally a horizontal-focusing-mirror is placed after of focusing the beam, that also removes the amount of harmonics to less than 10^{-4} .

3.3.2.2 Experimental Hutch

The experimental station is equipped with two ionization chambers to measure the intensity of the beam before and after the sample. Three different lengths, 4, 14 and 30 cm, of separation between the electrodes are available, and suitable absorbing gas $(N_2 \text{ or } Ar)$ is selectable depending on X-ray energy range.

A 10T superconducting magnet (SCM) with a variable temperature insert (VTI) allows measurements between 2 and 300 K. Figure 3.12 shows a schematic drawing of the SCM system. The SCM is designed to perform XMCD experiments up to 10T. A maximum of 6 samples can be placed in the sample holder which, in turn is placed inside a 25 mm-diameter cylinder in the VTI. The split-type superconducting coils design includes also an horizontal magnet clear bore so that the sample can be placed in the middle of the magnet and the X-ray beam, moving parallel to the field

Fig. 3.12 Superconducting magnet at the BL39XU beamline



Superconducting Magnet

in the horizontal direction, is incident on a cold, magnetized sample. The SCM has X-ray transparent Be windows at both front and back (on the field axis) and on both sides (perpendicular to the field). The opening size of the front and back windows is 10 mm diameter, while the sides are 20 mm diameter. This design of the coils and the windows allows XMCD measurements in either transmission or fluorescence mode as well as non-resonant magnetic diffraction experiments with a 90° scattering angle. The SCM is equipped with a liquid helium recondensing cooler which enables continuous operation of the SCM for more than 7 days with no additional coolant needed.

3.3.2.3 Experimental Procedures

For the measurements, homogeneous layers of the powdered samples were made by spreading of fine powders of the material on an adhesive tape. Thickness and homogeneity of the samples were optimized to obtain the best signal-to-noise ratio, giving a total edge jump ~ 1 . Once the samples are inside the SCM, the temperature

and applied magnetic field conditions are set. To this respect, it is important to indicate that samples must be inserted or removed at $T=300\,\mathrm{K}$ and $H=0\,\mathrm{T}$. We have verified in all the cases that the recorded spectra are not affected by the long beam-exposure time needed.

The spectra of the nanoparticles and reference samples (bulk ZnS, bulk ZnO and a $2.5\,\mu m$ thick Zn foil) were recorded in the transmission mode. In this geometry the sample is magnetized by an external magnetic field applied in the direction of the incident beam and the intensity of the X-ray beam before and after the sample is measured using radiation ionization chambers.

In the case of the thin film samples the spectra were recorded in the fluorescence mode by using a PIN photodiode detector. Nearly normal incidence (\sim 2°), the detector mounted at 90° and a small detection angle were the experimental geometry used to minimize distortions due to self-absorption effects.

As explained before, the XMCD spectrum was obtained as the difference of the absorption coefficient $\mu_c = (\mu^- - \mu^+)$ for antiparallel, μ^- , and parallel, μ^+ , orientation of the photon helicity and the magnetic field applied to the sample. Therefore, XMCD experiments can be performed in two different ways: either by changing the helicity and keeping a constant orientation of the magnetic field, or by changing the direction of the magnetic field at a constant helicity. The XMCD spectra are obtained following the "static procedure", i.e., after acquisition, normalization and subtraction of μ^- and μ^+ spectra. However, at the BL39XU beamline, the helicity-modulation technique (HMT) has been implemented [24]. This method makes possible to record high quality XMCD spectra in shorter acquisition time than if the static method is used. A dichroic signal in the order of 10^{-4} is obtained with a good signal-to-noise ratio for 10 s-integration time at each energy point.

HMT technique has been developed by combining fast polarization switching in XPR with a phase-sensitive (lock-in) detection system (see Fig. 3.13). The magnetic field remains fixed through the measurement. The XPR is mounted on a piezo-driven stage, which oscillates at 40 Hz around the Bragg angle θ_B with an amplitude $\pm\theta$. Thus, the helicity of the photons alternates from LCP to RCP and the absorption coefficient oscillates as well with a 40 Hz frequency. For our measurements, a 1.4 mm thick XPR in 220 Laue geometry was used. The intensity of the incident and transmitted beam are measured by ionization chambers and converted into voltage signals, $V(I_0)$ and V(I), by current amplifiers. The ac component is proportional to XMCD and is directly measured using an amplifier locked to the helicity modulation frequency. The dc component corresponds to the average absorption coefficient and is measured with a digital voltmeter.

In that way, XMCD values are directly recorded at each energy point, thus minimizing possible errors coming from data treatment of the XAS spectra. In order to remove any possible spurious contribution to the signal, the XMCD recording procedure has been carried out for both directions of the applied magnetic field, which yields the same signal but with opposite sign: XMCD⁺ = $\mu^+ - \mu^-$ + spurious signal, and XMCD⁻ = $\mu^- - \mu^+$ + spurious signal. The final XMCD signal is than obtained as (XMCD⁺ – XMCD⁻)/2. This modus operandi allows to improve the statistics and remove any spurious contribution.

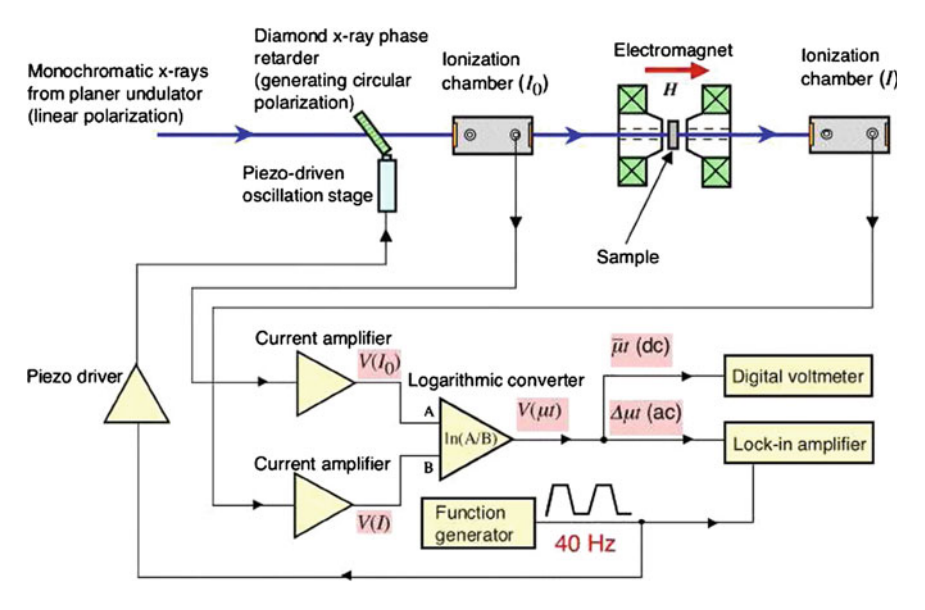


Fig. 3.13 The set-up scheme of XMCD measurements in HMT

A a final remark, though the initial experiments were performed by using the Si (111) monochromator, it was later changed by a (220) monochromator. We checked by measuring the ZnO and ZnS references that the spectra recorded with the new configuration are identical, though a fixed shift in the energy scale had to be corrected.

3.3.2.4 XAS and XMCD Data Analysis

The absorption spectra were analysed according to standard procedures, as described in earlier sections. A straight line was used to subtract the absorption background, and the spectra were normalized to the averaged absorption coefficient at high energy ($\backsim 9.7\,\text{keV}$) to eliminate the dependence of the absorption on the sample thickness. In order to perform a systematic analysis, the same normalization criteria were used for all spectra. That included the choice of the same normalization energy range for all the spectra measured at the same edge.

During each experimental run the Zn K-edge spectrum of the same ZnO reference sample was recorded, and the origin of the energy scale E_0 was chosen at the inflection point of the absorption edge. This E_0 was applied to all the spectra recorded in the same run. In that way, a unique energy scale has been used for all the spectra presented in this work. That allow us to clearly distinguish any edge-shift associated with structural modifications, i.e. to the modification of the interatomic distances [25, 26].

The XMCD spectra are obtained as the difference of the absorption coefficient $\mu_c = (\mu^- - \mu^+)$ for antiparallel, μ^- , and parallel, μ^+ , orientation of the photon helicity and sample magnetization. When using the HMT method this difference is performed automatically at each energy point, and the normalized XMCD is obtained via simple division by the XAS edge-jump.

3.3.3 BL25SU Beamline at SPring-8 Facility

The experiments at the sulphur L-edges were carried out at the BL25SU beamline in SPring-8 in total electron yield (TEY) mode [27]. BL25SU is designed for research on electronic structures, magnetic states and surface structures of solids with high energy-resolution circularly-polarized soft X-rays. Four kinds of spectroscopic techniques are available for public use: high energy-resolution photoemission spectroscopy, magnetic circular dichroism of core absorption, two-dimensional angular distributions of photoelectrons, photoelectron emission microscope. Measurements are performed in ultra high vacuum conditions down to 10^{-8} Pa.

3.3.3.1 Optics Hutch

The circular polarized radiation is obtained at BL25SU along the same optical axis by twin helical undulators (THU) [27]. THU consists of two helical undulators and five kicker magnets which generate a bump electron orbit at each undulator (see Fig. 3.14). Moreover, the kicker magnets alternately separate the photon beams horizontally by 0.3 mrad in order to minimize the overlap between the cones of fundamental radiation with opposite helicities from the two devices. When the bump orbit is excited at the first undulator (ID1), the radiation of ID1 is deflected to an off-axis direction and that of the second undulator (ID2) exclusively comes to the beamline. The helicity can be

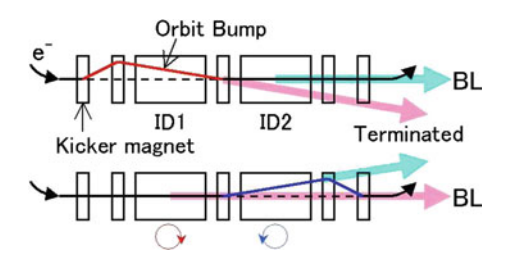


Fig. 3.14 Basic scheme of the THU When the bump orbit is excited at the first undulator (ID1), the radiation of ID1 is deflected to an off-axis direction and that of the second undulator (ID2) exclusively comes to the beamline. The helicity can be switched by switching the position of the bump orbit between ID1 and ID2. Two periodical switching modes at 1 and 10 Hz are currently available

changed by switching the position of the bump orbit between ID1 and ID2. The most unique performance of the undulator is the switching of right-circular-polarization (RCP) and left-circular-polarization (LCP) radiation by periodic phase shift of the magnet rows. Periodical switching of the helicity (by using kicker magnets) modes at 0.1, 1 and 10 Hz are available, and excitation patterns of the bump orbits are trapezoidal for the 0.1 and 1 Hz modes, and are sine curves for the 10 Hz modes, respectively. The helicity switching is utilized for circular dichroism measurements of core absorption, PED and PEEM.

The optical system presents a constant-deviation monochromato that includes a spherical mirror and a varied-line-spacing plane grating (VLSPG) between entrance and exit slits. Energy scan is performed by a single rotation of the VLSPG, which allows simple mechanical control and high energy tunability. The deviation angle of the VLSPG can be chosen from two discrete angles of 174° and 176° corresponding to the lower and higher energy sides. VLSPGs with two different central groove densities of 600 and 1,000 lines/mm are also selectable. An energy range from 0.22 to 2 keV is covered by changing combinations of the deviation angles and VLSPGs.

3.3.3.2 Experimental Hutch

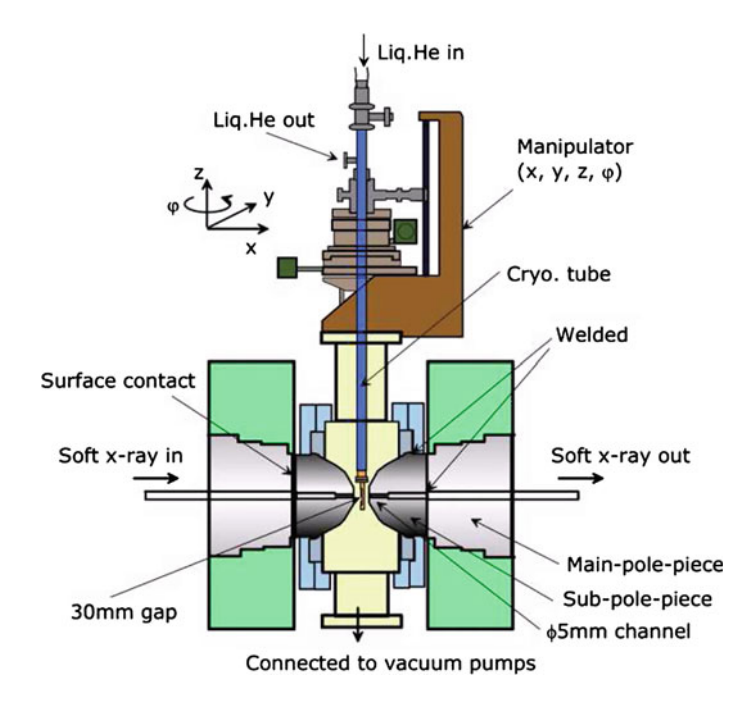
The experimental station of BL25SU consists of an UHV (ultra high vacuum) measurement chamber which is equipped with a water-cooled type electromagnet (shown in Fig. 3.15). The electromagnet generates a variable magnetic field up to $1.9\,\mathrm{T}$ at the sample position. Sample temperature can be controlled from 10 to $300\,\mathrm{K}$.

3.3.3.3 Experimental Procedures

The measurements of our ZnO based compounds were performed in total electron yield mode (TEY), applying a bias voltage⁹ with the electric field E perpendicular to the axis c direction.

That measurement system involves the sample drain current (I) normalized by incident photon flux (I_0) monitored with a Au-coated SiO₂ refocusing toroidal mirror. Each of the signals I_0 and I is converted by a current amplifier into a voltage, and then to a frequency. These signals are fed into separate counters for individual polarization. Despite of the large band gap presented by semiconductors like ZnO, TEY mode is still suitable; the suppression of the electron excitation process by the band gap

⁹The absorbed X-ray intensity is not measured directly in TEY measurements, but rather the photoelectrons that are created by the absorbed X-ray. The created holes in the photoabsorption process are filled by Auger decay (dominant in the soft X-ray region). As they leave the sample, the primary Auger electrons create scattered secondary electrons which dominate the total electron yield intensity. The TEY cascade involves several scattering events and originates from an average depth, the electron sampling depth L. Electrons created deeper in the sample lose too much energy to overcome the work function of the sample and therefore do not contribute to the TEY. The sampling depth L in TEY measurements is typically a few nanometers [11].



 $\textbf{Fig. 3.15} \quad \text{Schematic view of the UHV measurement chamber at BL25SU which is equipped with an electromagnet} \\$

can be made up for the reduced electron scattering in these materials, so excited electrons have larger escape depth. Besides, semiconductors show a lower surface barrier potential compared to metals, all of that in favour of higher kinetic electron yield [28].

For the measurements, the films were cut on smaller pieces of about $3\times3\,\mathrm{mm}^2$ and placed on the Cu-holder by using carbon tape. In the case of powder samples the compound was directly spread over the carbon tape. To increase the measured signal, conductor wires were welded on the edge of each sample. In addition, Ar-ion sputtering (Ar pressure $10^{-2}\,\mathrm{Pa}$) was performed for 90 min, to remove any surface oxidization. Since the helicity switching produced interference on I_0 the measurement were performed by fixing the helicity and reversing it at the following scan.

3.3.4 BL23SU Beamline at SPring-8 Facility

The experiments at the O K-edge (edge energy \sim 545 eV) were carried out at the BL23SU beamline in SPring-8 [29]. BL23SU is a soft X-ray undulator beamline of Japan Atomic Energy Agency (JAEA). The magnetic circular dichroism (MCD) Station at the BL23SU focuses on the study of the electronic structures which are related

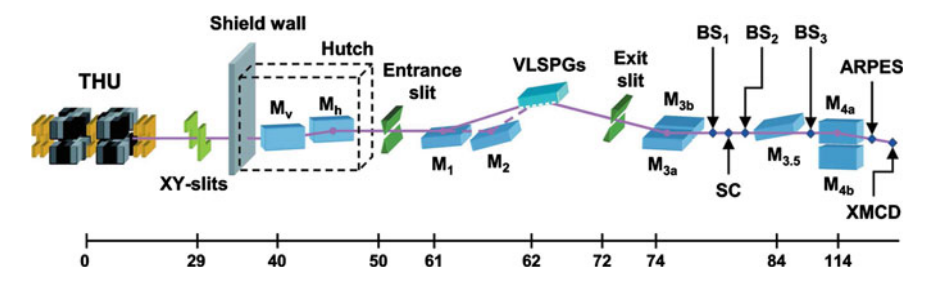
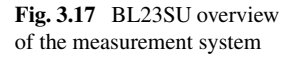
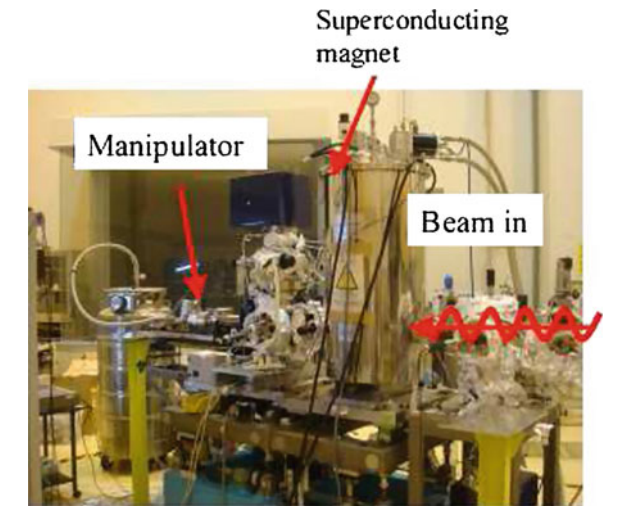


Fig. 3.16 Schematic of the BL23SU beamline. M_1 and M_2 : vertical focusing mirrors. M_{3a} vertical collimating mirror. M_{3b} , $M_{3.5}$, M_{4a} and M_{4b} refocusing toroidal mirrors. BS₁–BS₃ biophysical spectroscopy stations. *SC* surface chemistry station





with the magnetic properties of strongly correlated electron systems. Main character of the XMCD measuring system is a superconducting magnet (SCM), which produces fields of up to 10 T. In addition, temperature of the sample is controlled from room temperature to 10 K. Photon flux is better than 1×10^{11} with the energy resolution $E/\Delta E = 10.000$. A schematic overview of the main beamline components of BL23SU is shown in Fig. 3.16 [29].

The optical system consists of a varied-line-spacing plane gratin type (VLSPG) monochromator, that presents an entrance slit, spherical mirrors, varied-line-spacing plane gratings, an exit slit, a post-focusing mirror, and refocusing toroidal mirrors.

The XMCD end-station terminates BL23SU at approximately 120 m from the light source. The experimental ultra hight vacuum (UHV) chamber is equipped with the SCM and a sample holder attached to a liquid-He cryostat reaching a sample temperature of 10 K (Fig. 3.17).

As for BL25SU circular polarized light is produced by using a THU system. In this case the highest mechanical switching rate is at the frequency up to 0.5 Hz.

3.3.4.1 Experimental Procedures

Both XANES and XMCD were recorded at the O K-edge by using the TEY mode. Measurements were performed at room temperature and at $T=10\,\mathrm{K}$, and the applied magnetic field was varied between H=0 and $10\,\mathrm{T}$.

In addition, element specific magnetic hysteresis measurements (ESMH) were performed. In this case the XMCD is recorded for a fixed energy while the applied magnetic field is varied, similar to the magnetization hysteresis measurements with conventional magnetometers. O K-edge ESMH measurements were performed at $T = 10 \, \text{K}$ by fixing the energy of the incoming photons to those energies at which the main features of the XMCD spectra occur (see Chap. 6).

For the measurements the samples used were 20-12C-1 (THIOL) and AMINE-5 powder samples and the $(ZnO_{4nm}/ZnS_{4nm})_{10}$ heterostructure. The measurements were performed in total electron yield mode (TEY), with the electric field E perpendicular to the axis c direction. The samples were placed in a sample holder inside the ultra high vacuum chamber. The powdered samples were spread over $5\times 5\,\text{mm}^2$ pieces of carbon tape fixed on the Cu-holder. The films were fixed on the sample holder by carbon tape as well.

3.3.5 XAFS Beamline at Elettra Facility

Spectra at the sulphur K-edge were recorded at the XAFS beamline of Elettra synchrotron light source [30].

3.3.5.1 Optics Hutch

At the XAFS beamline the synchrotron radiation light comes from a bending magnet. The optic hutch is shown in Fig. 3.18. A mask is placed at 13.3 m downstream the bending magnet source. It consists of a copper support with two 20 mm wide rectangular slots defined by tungsten alloy blades of 0.2 and 2 mm height. The two slots are used respectively to align and define the correct shape of the X-ray beam before the next optical element. The second optical element is a mirror placed 16.5 m from the source. The mirror provides vertical collimation and consists of a silicon ingot with platinum coating. It has an optically active length of 1000 mm and width of 60 mm, respectively, and it is positioned at 3 mrad respect to the direct beam. The mirror is water cooled and is operated under ultra high vacuum conditions. Two pairs of entrance W alloy slits define the shape of the beam impinging on the monochromator, which is placed at 21.7 m from the source. It is a double flat crystal double

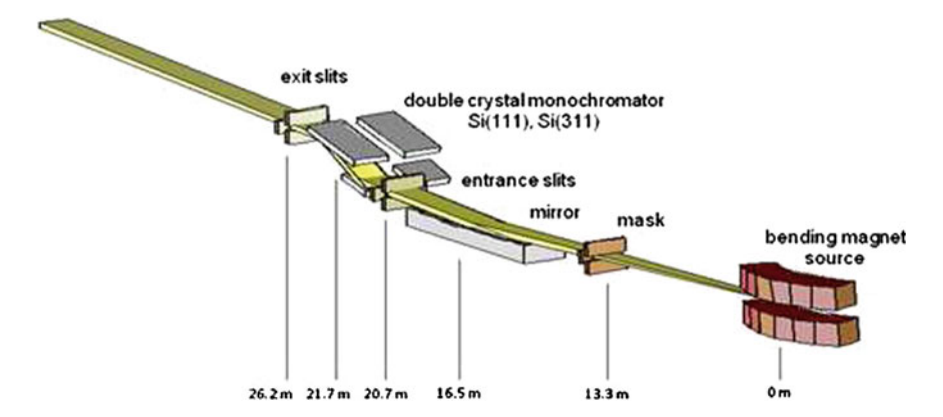


Fig. 3.18 Scheme of the optical hutch of the XAFS beamline at ELETTRA. The beam reaching the mirror is defined by the mask, besides the the beam is collimated vertically before the double crystal monochromator in order to obtain the intrinsic energy resolution

cam Kohzu apparatus, and it covers an energy range of range 2.4–27 keV, using interchangeable under vacuum pairs of Si(111) and Si(311) crystals. Two successive Bragg reflections, with an inherent energy resolution given by the Darwin angular width [15], directs photons of the desired energy parallel to the incoming beam direction, but offset upward by 25 mm. The detuning of the second crystal provides harmonic rejection at working energies below 9 keV.

3.3.5.2 Experimental Hutch and Procedures

The standard sample environment set up is dedicated only to transmission mode. It includes three ionization chambers (Oxford Instruments) for beam intensity measurements, which are filled with optimal He, Ne, Ar, Kr gas mixtures and operates at a field of $2\,\mathrm{kV}$ per $30\,\mathrm{cm}$ of length. The sample temperature is controlled by using a liquid-N₂ cryostat, though this device allows measurement just at fixed temperature of $77\,\mathrm{K}$. The obtained signals are amplified by Keithley picoamperomers and digitalized by a voltage to frequency converters. In this way the typical photon flux at the sample for standard beam size and ring current is in the 10^{10} photon/s range, hence the noise level contribution due to the photon statistics in the normal transmission geometry can be limited below the 10^{-4} level [30].

Our experiments were performed at room temperature. The energy of the incoming X-ray beam was tuned with a Si(111) double-crystal monochromator. By using this set-up the energy resolution is $\Delta E/E = 10^{-4}$. Harmonic rejection was achieved by detuning the second crystal from parallel alignment. The energy of the S K-edge XAS spectra was calibrated by measuring the XANES of FeS reference.

For the measurements, the sample were initially prepared on adhesive kapton tape. However, the recorded signal was too small, and sulphur contamination came

from the tape. Hence, to avoid contamination, obtain homogeneous samples and improve the signal-to-noise ratio, the powder samples were spread over membranes (microporous plastic films with specific pore size ratings), by dissolving and then filtering it. The amount of powder on the membrane was optimized to obtain the best signal-to-noise ratio in each case.

3.3.5.3 XAS Data Analysis

The absorption spectra were analysed according to standard procedures [12]. XANES spectra were normalized, after background subtraction, to the averaged absorption coefficient at high energy. EXAFS signals were extracted from the spectra by using the Athena program package [31]. The EXAFS signal, $\chi(k)$, have been obtained after removing the background by a cubic spline polynomial fitting and by normalising the magnitude of the oscillations to the edge jump. The corresponding pseudoradial distribution function around the photoabsorbing atom has been obtained by performing the Fourier transform (using a sine window) in the range $2.0 \le k \le 10.7 \text{ Å}^{-1}$.

The fitting of the S K-edge EXAFS signal were made by using the VIPER program [32]. In all cases de backscattering amplitude, phase and photoelectron mean free path were obtained from the experimental EXAFS spectrum of the W-ZnS reference. The EXAFS fitting has been performed for the contribution of the first coordination shell. For that purpose the EXAFS contribution of this shell was isolated by Fourier filtering: the $\chi(k) \cdot k$ EXAFS signals ere Fourier transformed in the range $2.15 \le k \le 10.25 \ \text{Å}^{-1}$. First shell contribution was isolated by back-transforming into k-space in the $1.25 \le R \le 2.95$. Then the differences in the local environment of S were assessed by analysing the filtered EXAFS signals. We have evaluated the quality of the fits in base based on the statistic R and χ^2 parameters [33]. χ^2 is defined as:

$$\chi^2 = \frac{N_{\text{ind}}}{N} \sum_{i=1}^{N} \left[\frac{y_i - f_i}{\epsilon_i} \right]^2$$
 (3.12)

where y are the experimental data, f the fitted data and N the number of points for both $\chi(k)$ and $\chi(R)$. The best number to use for the sum over the number of data points is then N_{ind} defined as $N_{ind} \approx (2\Delta k \Delta R)\pi + 1$ [34], where Δ k and Δ R are the k and R range of the usable data under consideration. At the R-space the "data" y actually represents the real and imaginary components of $\chi(R)$, and the "model" f will also be the Fourier transform of the parametrized model for $\chi(k)$. On the other hand, ϵ , is the uncertainty in the "data". Of course, it depends on the details of the data transformation (for example, whether fitting in R or q space). Estimating the noise level in any given spectrum should generally involve a proper statistical treatment of the data. For an individual spectrum, what can be done easily and automatically is to estimate the noise level assuming that the data is dominated by noise that is independent of R, i.e., white noise. ϵ is usually taken to be a scalar value.

Reduced- χ^2 is defined as $\chi^2/(p-N_{\rm ind})$ where p is the number of fitted parameters. If the difference between fit and measurement is entirely attributable to measurement uncertainty, then the Reduced- χ^2 should be around 1. Unfortunately, because ϵ is difficult to estimate, the actual value of the reduced- χ^2 is far greater than 1 and it is not very useful for judging the quality of the fit. However it is very helpful for comparing two fits on the same set.

The alternative statistic \mathcal{R} is often used as a supplement to χ^2 . The \mathcal{R} factor is defined as:

$$\mathcal{R} = \frac{\sum_{i=1}^{N} [y_i - f_i]^2}{\sum_{i=1}^{N} y_i^2}$$
 (3.13)

For very good data, the fitting procedure can pick up very subtle variations between the constrained model and the sample. That can make the fit statistically poor. And yet the constrained model is good. The R-factor reflects this notion of closeness of fit

As it will be detailed in Chap. 6, the fitting of the EXAFS signals were carried out for for the first coordination shell. The initial step was the fit of the W-ZnS reference spectrum. The obtained values of coordination number (N), interatomic distances, Debye-Waller factor σ^2 and energy shift Δ E₀ from the W-ZnS reference will be used as a reference for the fits of the studied NPs.

In addition, a similar study was made by using the theoretical phases and amplitudes calculated by using the FEFF-6 code [16, 31, 35, 36]. The fitting to the experimental data was carried out in both R-space and k-space, by using the programme ATHENA within the IFEFFIT package. The fit was made by imposing the theoretical coordination number values of W-ZnS. As discussed in Chap. 6 no significant was found in the results obtained by both methods.

3.4 Ab-Initio Calculations of XANES Spectra

The computation of the Zn, O and S K-edge XANES spectra has been performed by using the multiple-scattering program CONTINUUM [37], based on the one-electron full-multiple-scattering theory [38, 39], and included in the MXAN program package [40, 41]. A complete discussion of the procedure can be found elsewhere [26, 42, 43].

The potential for the different atomic clusters was approximated by a set of spherically averaged muffin-tin (MT) potentials built by following the standard Mattheis' prescription [44]. The muffin-tin radii were determined following the Norman's criterion and by imposing initially a 10% overlapping factor [45]. The Coulomb part of each atomic potential was generated using charge densities for neutral atoms obtained from the tabulated atomic wave functions by Clementi and Roetti [46]. We

also checked that using charge densities from a non-local selfconsistent Dirac-Fock code [47] does not modify the result.

During the computations special attention has been paid to determine the best choice for the overlapping factor between the muffin-tin spheres and for the exchange and correlation part of the final state potential [48, 49].

It should be stressed that no free parameter has been used during the calculations. The theoretically calculated spectra have been directly compared to the experimental XANES spectrum, that is, no fitting procedure has been used. The assessment of the quality of the theoretical computations is based on the correct reproduction of the shape and energy position of the different spectral features and of their relative energy separation and the intensity ratio. Finally, excepting the case of calculation at the O K-edge, the theoretical spectra have been convoluted with a Lorentzian shape function to account for the core-hole lifetime ($\Gamma = 1.5$ and $\Gamma = 0.59\,\mathrm{eV}$ for the Zn and S K-edge, respectively $\Gamma = 1.5\,\mathrm{mas}$ and the experimental resolution ($\Gamma = 1\,\mathrm{eV}$).

Throughout this study we have followed the same computational procedure. Firstly, we have determined the minimum size of the cluster needed to reproduce all the spectral features. This is made by adding progressively coordination shells surrounding the absorbing atom up to convergence is obtained, that is, the addition of further shells does not lead to the modification of the calculated spectra. In a second step we have checked the influence of the overlapping factor among the muffin-tin spheres used to built up the scattering potential into the reproduction of the experimental XANES spectra. Initially, the computation of XANES has been made for a fixed size cluster by imposing a 10% overlapping factor (hereafter ov) and then, computations have been repeated by using a lower 1 % factor (the default value in several codes). In addition we have also studied the effect of modifying the value of the maximum angular momentum quantum number, l_{max} , needed to account for the experimental absorption spectrum in the first $\backsim 50 \, \text{eVs}$. Last but not least we have studied the best choice of the exchange and correlation part of the final state potential(ECP) [48, 49, 51] to reproduce not only the spectral shape but also the intensity of the computed spectral features and their relative energy separation. To this end we have performed the computations by using the energy dependent Hedin-Lundqvist (HL) [52] and the Dirac-Hara (DH) [53, 54] ECP potentials. Moreover, we have also performed the computations by using only the real part of the HL ECP (hereafter real Hedin-Lundqvist), and by adding to the DH ECP the imaginary part of the HL one (hereafter complex Dirac-Hara).

In all the cases the initial computations have been deserved for the appropriate references (bulk ZnO and ZnS) for which the crystal structures are well known. This allowed us to determine the best choice of these computational parameters (ov, $l_{\rm max}$ and ECP) which have been fixed for the following of calculations.

¹⁰No convolution has been applied for the O K-edge spectra.

It should be also noted that the energy scale of each computation is referred to its own muffin-tin potential. Therefore, it is necessary to correct the energy scale of the computed spectra in order to compare the calculations in a unique energy scale and monitor the edge-shift associated to the different structural arrangement around Zn, that is, to the modification of the interatomic distances [25, 55–57].

References

- 1. S.A. Chambers, Surf. Sci. Rep. **61**, 345 (2006)
- 2. Y. Matsumoto, M. Murakami, T. Shono, T. Hasegawa, Science 291, 854 (2001)
- 3. G. Lawes, A. Risbud, A. Ramirez, R. Seshadri, Phys. Rev. B 71, 045201 (2005)
- 4. E. Fernández-Pinel, J. de La Venta, A. Quesada, B.M. García, J. Appl. Phys. 105, 1 (2009)
- 5. C. Abernethy, G. Codd, M. Spicer, J. Am. Chem. Soc. 125, 1128 (2003)
- 6. T. Dietl, Nat. Mater. 9, 965 (2010)
- 7. H.K.-Y. Sato, Phys. E 10, 251 (2001)
- J. Chaboy, R. Boada, C. Piquer, M.A. Laguna-Marco, M. García-Hernández, N. Carmona, J. Llopis, M.L. Ruíz-González, J. González-Calbet, J.F. Fernández, M.A. García, Phys. Rev. B 82, 064411 (2010)
- 9. J.M.D. Coey, S. Chambers, MRS Bull. 13, 1053 (2008)
- 10. E. Beaurepaire, Magnetism and Synchrotron Radiation (Springer, Berlin, 2010)
- J. Stöhr, H. Siegmann, Magnetism: From Fundamentals to Nanoscale Dynamics (Springer, Berlin, 2007)
- 12. G. Bunker, Introduction to XAFS (Cambridge University Press, Cambridge, 2010)
- 13. P.A. Lee, P.H. Citrin, P. Eisenberger, B.M. Kincaid, Rev. Mod. Phys. 53, 769 (1981)
- 14. D.E. Sayers, E.A. Stern, F.W. Lytle, Phys. Rev. Lett. 27, 1204 (1971)
- 15. D. Koningsberger, R. Prins, *X-ray Absorption: Principles, Applications, Techniques of EXAFS, SEXAFS, and XANES* (Wiley, New York, 1988)
- M. Newville, Fundamentals of XAFS, Consortium for Advanced Radiation Sources, University of Chicago, 2004
- 17. D. Koningsberger, B. Mojet, G. van Dorssen, D. Ramaker, Top. Cat. 10, 143–155 (2000)
- 18. G. Schütz, W. Wagner, W. Wilhelm, P. Kienle, R. Zeller, Phys. Rev. 58, 131–136 (1987)
- 19. U. Fano, Phys. Rev. 178, 131 (1969)
- 20. P. Duke, Synchrotron Radiation (Oxford University Press, Oxford, 2008)
- 21. P. Willmott, An Introduction to Synchrotron Radiation (Wiley, Chichester, 2011)
- 22. H. Maruyama, M. Suzuki, N. Kawamura, M. Ito, J. Synchr. Radiat. 6, 1133 (1999)
- 23. K.N.K. Hirano, K. Izumi, M. Ito, Jpn. J. Appl. Phys. **30**, L407 (1991)
- M. Suzuki, N. Kawamura, M. Mizumaki, A. Urata, H. Maruyama, S. Goto, T. Ishikawa, Jpn. J. Appl. Phys. 37, L1488 (1998)
- 25. F. Farges, Phys. Chem. Miner. 36, 463 (2009)
- 26. J. Chaboy, J. Synchr. Radiat. 16, 533 (2009)
- 27. T. Muro, T. Nakamura, T. Matsushita, K. Fukumoto, AIP Conf. Proc. 879, 571 (2007)
- 28. B.H. Frazer, B. Gilbert, B.R. Sonderegger, G. de Stasio, Surf. Sci. 537, 161 (2003)
- Y. Saitoh, Y. Fukuda, Y. Takeda, H. Yamagami, S. Takahashi, Y. Asano, T. Hara, K. Shirasawa, M. Takeuchi, T. Tanaka, H. Kitamura, J. Synchr. Radiat. 19, 388 (2012)
- 30. A. di Cicco, G. Aquilanti, M. Minicucci, J. Phys.: Conf. Ser. 190, 012043 (2009)
- 31. B. Ravel, M. Newville, J. Synchr. Radiat. 12, 537 (2005)
- 32. K.V. Klementiev, J. Phys. D: Appl. Phys. 34, 209 (2001)
- 33. L.O.G. Vlaic, Croatica Chemica Acta **77**, 427 (2004)
- 34. E.A. Stern, Phys. Rev. B 48, 9825 (1993)
- 35. M. Newville, J. Synchr. Radiat. **8**, 96 (2001)

- 36. M. Newville, J. Synchr. Radiat. 8, 322 (2001)
- 37. C.R. Natoli, M. Benfatto (Unpublised)
- 38. C.R. Natoli, M. Benfatto, Journal de Physique (Paris) Colloques 47, C8 (1986)
- 39. C. Natoli, D. Misemer, S. Doniach, F. Kutzler, Phys. Rev. A 22, 1104 (1980)
- 40. M. Benfatto, S. Longa, J. Synchr. Radiat. 8, 1087 (2001)
- 41. M. Benfatto, A. Congiu-Castellano, A. Daniele, S. DellaLonga, J. Synchr. Radiat. 1, 267 (2001)
- 42. J. Chaboy, S. Quartieri, Phys. Rev. B **52**, 6349(9) (1995)
- 43. J. Chaboy, A. Muñoz-Páez, F. Carrera, P. Merkling, Phys. Rev. B 71, 134208 (2005)
- 44. L. Mattheiss, Phys. Rev. A 133, 1399 (1964)
- 45. J. Norman, Mol. Phys. 81, 1191 (1976)
- 46. E. Clementi, C. Roetti, Atomic Data Nucl. Data Tables 14 (1974)
- 47. Ankudinov, B. Ravel, J. Rehr, S. Conradson, Phys. Rev. B 58, 7565 (1998)
- 48. J. Chaboy, N. Nakajima, Y. Tezuka, J. Phys.: Condens. Matter 19, 66206 (2007)
- 49. J. Chaboy, H. Maruyama, N. Kawamura, J. Phys.: Condens. Matter 19, 16214 (2007)
- 50. M. Krause, T. Ridge, J. Oliver, J. Phys. Chem. Ref. Data **8**, 329 (1979)
- 51. C. Guglieri, J. Chaboy, J. Phys. Chem. C 114, 19629 (2010)
- 52. B.L.L. Hedin, J. Phys. C: Solid State Phys. 4, 2064 (1971)
- 53. S. Hara, J. Phys. Soc. Jpn. 22, 710 (1967)
- 54. R. Gunnella, M. Benfatto, A. Marcelli, C.R. Natoli, Solid State Commun. 76, 109 (1990)
- 55. M. Tromp, J. Moulin, G. Reid, J. Evans, AIP Conf. Proc. 882, 669 (2007)
- 56. P. Glatzer, G. Smolentsev, G. Bunker, J. Phys.: Conf. Ser. 190, 012046 (2009)
- 57. A.H. de Vries, L. Hozoi, R. Broer, Int. J. Quantum Chem. 91, 57 (2003)

Chapter 4 Zinc K-edge X-ray Absorption Study of ZnO-Based Magnetic Semiconductors

In the precedent chapter we have reported the results of the structural and magnetic study of our systems obtained by using in-house (XRD, XRR, HRTEM, M(H,T), etc.) experimental techniques. The combined analysis of these results suggests that the magnetic behaviour observed through the whole series of NPs and thin films could be related to structural effects. More in particular to the local structural ordering in the region where the capping molecules bond to the ZnO NPs and in the interfaces between the ZnO and ZnS layers in the thin films.

These structural details are hidden to the standard characterization tools and, therefore, more powerful experimental tools are needed to obtain an accurate structural and magnetic characterization of the ZnO-based NPs and thin films. Then, we have proceeded to apply the X-ray absorption spectroscopy technique to study these problems.

In this way, aimed to get an accurate determination of the structural effects associated to the capping of ZnO NPs with organic molecules we have performed a detailed study of the Zn K-edge XAS spectra in these materials. At present, structural parameters are commonly derived from the analysis of the extended X-ray absorption spectra. However, the accuracy of the structural determination obtained by EXAFS can in several cases be inconclusive due to the well-known limitations of the EXAFS fitting methodology to determine coordination number and polyhedral environments. This matter becomes further complicated if more that one structural environment, as here presumed, is present in the material. In this case the study of the near-edge region of the absorption spectrum might be preferred because XANES exhibits higher sensitivity than EXAFS to the details of the bonding geometry of the absorption site (overall symmetry, distances and bonding angles) [1–4]. For these reasons we have focussed our study to the XANES region of the XAS spectra.

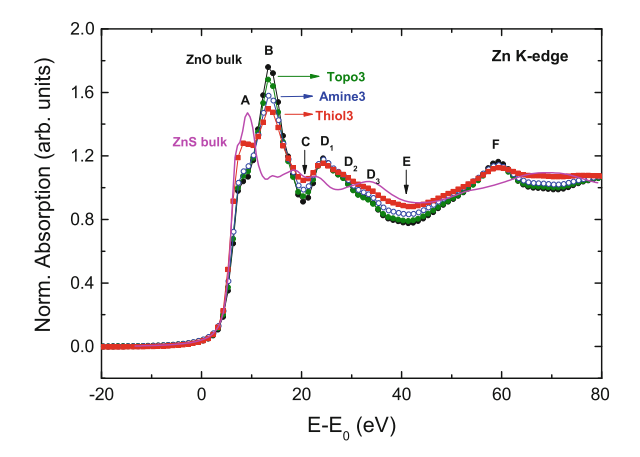
4.1 Zn K-edge XAS Study of ZnO NPs Capped with Organic Molecules: Structural Versus Electronic Effects

The initial study was deserved to the same samples used by García et al. in [5], that is, the series-1, TOPO, AMINE and THIOL (20-12C-1) samples in which differences reside in the organic molecule used as capping agent.

As shown in Fig. 4.1, in the case of the uncapped ZnO samples the Zn K-edge spectrum is characterized by a main absorption peak (B) located at \backsim 7.5 eV above the absorption edge. In addition, the spectrum shows a positive spectral feature (D₁) at \backsim 18 eV with a double shoulder-like structure at higher energies (D₂ \backsim 21 eV, D₃ \backsim 26 eV), that lies between the two well-resolved negative dips, C (\backsim 14 eV) and E (\backsim 35 eV). For higher energies, a second positive resonance (F) is found at \backsim 53 eV above the edge. This spectral profile is retained in the case the AMINE and TOPO samples, for which only a small decrease in the intensity of the main absorption line (peak B) is observed. In contrast, the intensity of the main absorption line of the ZnO sample capped with THIOL shows a strong reduction. As discussed in the introductory chapter, this variation of the white line intensity has been previously addressed as an evidence of the occurrence of charge transfer. However special caution has to be given to directly relate the modification of the white-line intensity to charge-transfer effects because both the spectral shape and the intensity of the main absorption features are intimately linked to the local structure of the absorbing atom [6, 7].

In the case of THIOL not only the white-line intensity but the overall spectral shape in the first 10 eVs above the edge are strongly modified with respect to bulk ZnO. In particular, the intensity of the low-energy shoulder (A) of the main absorption line grows and, at the same time, despite the Zn K-edge XANES spectrum of this sample is similar to those of TOPO and AMINE, an overall reduction of its amplitude is observed. In contrast to a Zn-S charge transfer effect, it cannot be a priori disregarded the possibility that the capping leads to the formation of Zn-S bonds at the surface of

Fig. 4.1 Comparison of the experimental Zn K-edge XANES of ZnO nanoparticles capped with TOPO (green), AMINE (blue), and THIOL (red). For the sake of comparison, the XANES spectra of both bulk ZnO (black) and ZnS (magenta) are also shown



the nanoparticle. If the interatomic Zn-S distance is different from that of Zn-O in the NPs, the intensity of the main XANES features might change even in the absence of charge transfer effects. Then, it is interesting to consider how the possible formation of Zn-S bonds at the surface of the NP affects the XANES. Indeed, it is worth to mention that the position of the enhanced peak A coincides with that of the white line of the Zn K-edge XANES spectrum of ZnS, which may indicate the presence of ZnS in the materials.

To asses the aforesaid possibility, we have performed a detailed ab-initio computation of the Zn K-edge XANES spectra of these ZnO NPs by considering a different local structure of the Zn atoms in the inner part of the NP and those at the surface, where the bonding with the capping molecule takes place. The computation of the Zn K-edge XANES spectra was carried out by using the multiple-scattering code CONTINUUM [8] following the computational procedure detailed Chap. 2.

The initial computations have been deserved for both bulk ZnO and ZnS references, for which the crystal structures are well known. This has allowed us to determine the best choice of these computational parameters (ov, $l_{\rm max}$ and ECP), that have been maintained fixed for the rest of the study.

Zinc oxide crystallizes in three forms (see Fig. 4.2): hexagonal wurtzite (space group P6₃mc; lattice parameters a=3.25 Å and c=5.21 Å), cubic zinc-blende (space group F43m; lattice parameters a=4.47 Å), and the rarely observed cubic rocksalt (Fm3m; a=4.28 Å) [9–11]. The wurtzite structure is the most stable at ambient conditions whereas the zinc-blende form can be stabilized by growing ZnO on substrates with cubic lattice structure. In both cases, the zinc and oxide centres are tetrahedral. Finally, the rocksalt (NaCl-type) structure is only observed at relatively high pressures about 10 GPa. On the other hand, Zn sulphide crystallizes in wurtzite (a=3.82 Å and c=6.26 Å) and cubic zinc-blende (a=5.41 Å) [12, 13]. Accordingly

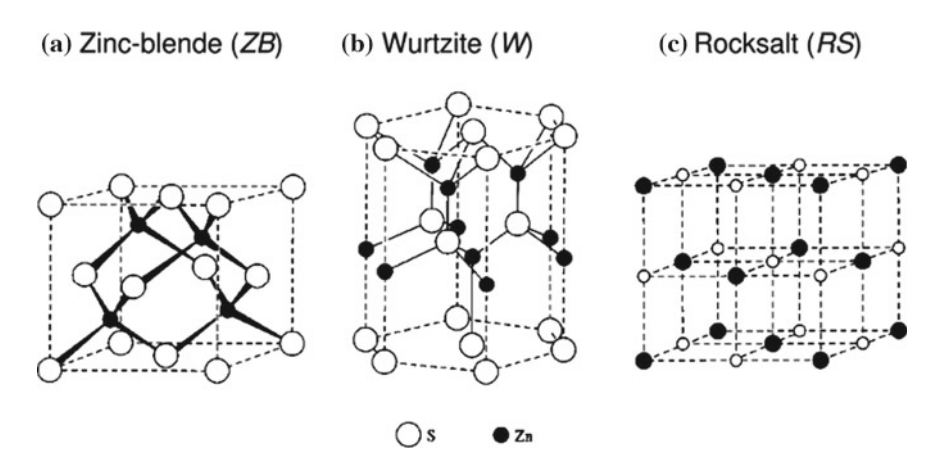


Fig. 4.2 Representation of the ZnO crystal structures: \mathbf{a} hexagonal wurtzite (W), \mathbf{b} cubic zincblende (ZB), and \mathbf{c} cubic rocksalt (RS). The *black* and *white spheres* indicate the Zn cations and anions (O, S), respectively

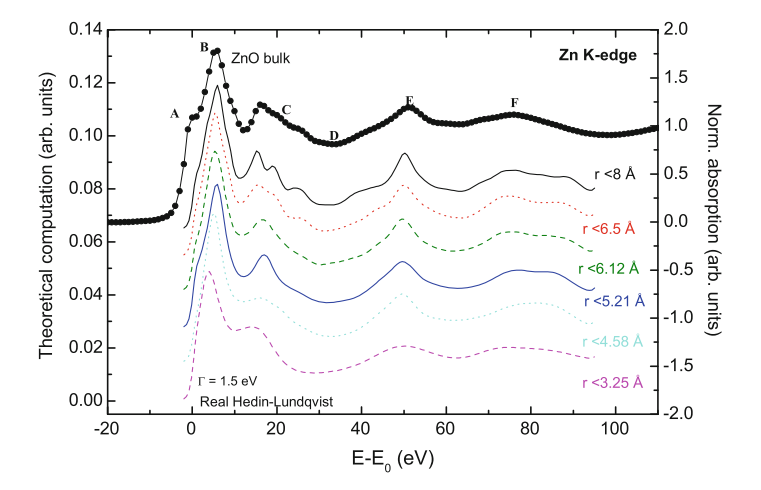


Fig. 4.3 Comparison between the experimental Zn K-edge of hexagonal ZnO and the theoretical spectra calculated for different cluster sizes

to our XRD characterization, computations have been initially performed for both ZnO and ZnS with wurtzite structure (W-ZnO and W-ZnS). However, being interested into determining the structural arrangement of Zn near the surface of the NPs, where the bonding to the organic molecule takes place, we have made also the calculations for the other structures.

The first step was to determine the cluster size needed to the correct reproduction of all spectral features presented in the experimental XANES spectra. As shown in Fig. 4.3, the computations performed for clusters smaller than 5 Å do not reproduce properly the experimental spectra in the energy region beyond the main peak (B). As the cluster includes contributions from further coordination shells around the absorbing Zn, the computations start to account for the feature located at $\sim 20\,\mathrm{eV}$ above the absorption edge. This structure, showing three peaks (see Fig. 4.1), is perfectly reproduced in the computation in which the contributions from neighbouring atoms located within the first 8 Å around photoabsorbing Zn are included. Similar results are found in the case of ZnS (Fig. 4.4). Accordingly, we have fixed to 8 Å the cluster size to perform further calculations.

Despite of the good agreement between the experimental data and the precedent calculations, the energy of the calculated absorption maxima (see Figs. 4.3 and 4.4) falls short of the experimental one. Trying to improve the agreement between the experimental and the theoretical spectra we have investigated the influence of both the overlapping factor between the muffin-tin spheres and the ECP. The calculations above were performed by imposing an overlapping factor of 1% and by using the real part of the Hedin-Lundqvist ECP. We have verified that the choice of the overlap factor slightly affects both the shape and the intensity of the computed spectral features. However, this does not hold regarding their relative energy separation. This is shown in Fig. 4.5, where computations were performed for both 1 and 10% overlapping

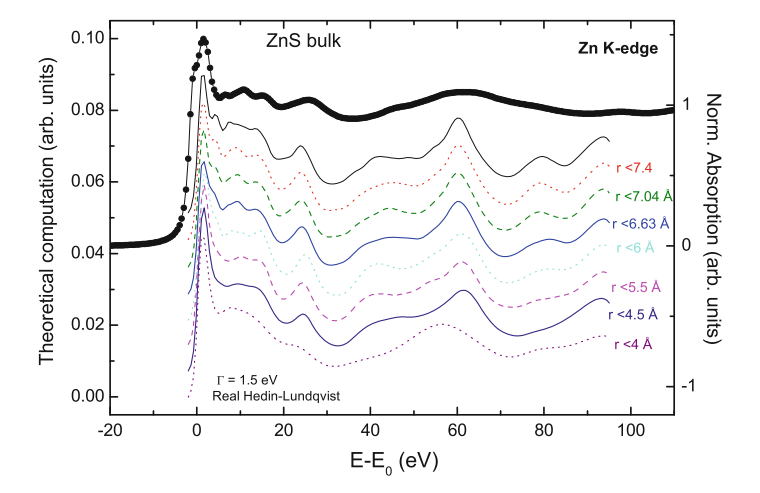


Fig. 4.4 Comparison between the experimental Zn K-edge of hexagonal ZnS and the theoretical spectra calculated for different cluster sizes

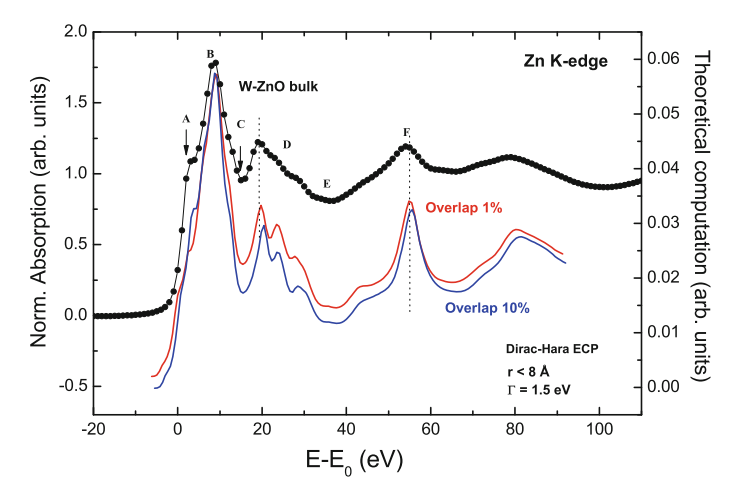
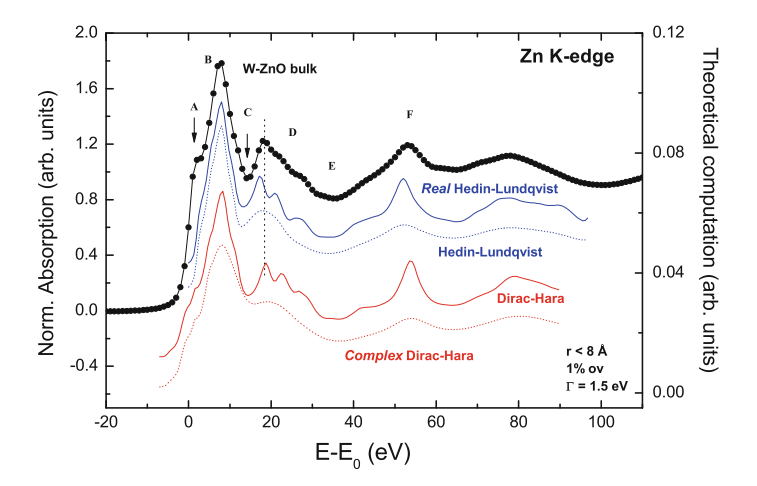


Fig. 4.5 Comparison between the Zn K-edge of W-ZnO and ab-initio calculations by using the *real* DH ECP and by imposing a 1 or a 10% overlapping factor

factor. Although both calculations lead to a good agreement with the experimental spectrum, that performed by using ov=1% shows a better reproduction of the relative energy of the different spectral features.

In contrast, the choice of the ECP renders critical for the correct reproduction of the experimental spectra. We have tested the performance of different ECP potentials. The results of the computations are shown in Fig. 4.6. Despite the agreement between the computations and the experimental signal is noticeable in all cases, computations performed by using the real Dirac-Hara ECP yields the best reproduction of the



 $\textbf{Fig. 4.6} \quad \text{Comparison between the Zn K-edge of W-ZnO and ab-initio calculations by using different ECP potentials}$

relative energy position among the experimental absorption features. The fact that the HL potential leads to a contraction of the energy scale of the computation has been previously addressed in a variety of systems [3, 14, 15]. These works showed that, as in the present case, the absorption maxima calculated by using the HL ECP fall short of the experimental ones, especially regarding the energy region between 30 and 70 eV above the edge. In the particular case of ZnO, this anomalous contraction, evident from inspection of the energy separation of the three well-resolved negative dips (C \sim \text{...} $14 \,\mathrm{eV}$, E $\sim 35 \,\mathrm{eV}$ and H $\sim 62 \,\mathrm{eV}$), has also been reported by independent calculations [16], although no comment was deserved. It should be noted that this drawback is not associated with the use of overlapping atom potentials versus self-consistent field (SCF) potentials. The SCF potentials can lead to an improvement of the Fermi level determination in such a way that typical errors in the Fermi level are 1 and \sim 3 eV with self-consistent and overlapped atom potential calculations, respectively. However, it has been previously demonstrated that the DH ECP improves the HL performance no matter whether the SCF or non-SCF method is used [4]. Summarizing, the best agreement between the computations and the experimental spectra of both ZnO and ZnS references has been obtained by using a 8 Å cluster radius, 1% overlapping factor, $l_{\text{max}} = 4$, and the Dirac-Hara ECP potential. Therefore, all the computations henceforth have been made by fixing these computational parameters.

Now we are able to tackle the main aim of this work, that is, to investigate the influence of the capping process into the local structure of the Zn atoms. Then we have focussed our study into evaluate how the contribution of additional Zn-S, Zn-N or Zn-O scattering paths influences the XANES spectra of the capped NPs in comparison to those of the bulk references. The case of TOPO has not been considered because Zn-O bonds with the organic molecules are indistinguishable from those of the ZnO NPs. As a first test, two small ZnO clusters were built, including only

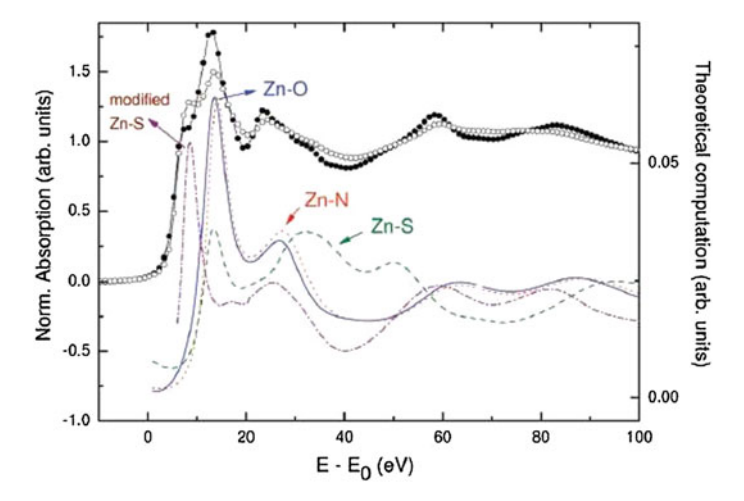


Fig. 4.7 Comparison of the experimental Zn K-edge XANES spectra of bulk ZnO and THIOL sample and the theoretical signal computed for a ZnO cluster (*blue*, *solid line*) and the same cluster in which the O neighbours have been substituted by N (*red*, *dots*) and S (*green*, *dashes*) at the same atomic position. The *dotted-dashed line* corresponds to a ZnO cluster in which S atoms substituting O have been placed at a greater interatomic distance (see text for details)

the first two coordination shells around Zn (i.e., 4 O + 12 Zn). In each cluster the four oxygen atoms were substituted by nitrogen and sulphur, respectively, at the same crystallographic positions. This initial step was envisaged to determine how the different backscattering properties of both N and S with respect to those of O affect the XANES profile. In other words, if XANES is sensitive to the occurrence of such Zn-N and Zn-S contributions against the Zn-O ones.

As shown in Fig. 4.7, the substitution affects quite differently the XANES profile as N (AMINE-like) or S (THIOL-like) are involved. In the case of N-O substitution, the computation yields similar results as for the original bulk-like ZnO cluster. However, when sulphur atoms are placed at the oxygen positions the computed spectrum is dramatically affected and it does not resemble the experimental one at all. These results illustrate the well-known fact that not only the interatomic distances but also the backscattering properties of the neighbour atoms determine the XANES-EXAFS oscillations. More interestingly, these calculations also suggest that in the case of the THIOL sample the sulphur atoms do not simply substitute the oxygen ones in the W-ZnO structure. Therefore, we have performed a similar computation in which the interatomic Zn-S distance is set equal to that found in W-ZnS. After this modification, the computation yields a similar profile as found in the case of the ZnO and ZnN clusters but the main absorption line is shifted to lower energy, which is in agreement with the characteristic low-energy shoulder (A) that appears more marked in the case of the THIOL samples. It should be stressed that the computed spectra are displayed in a unique energy scale, i.e. the observed shift is inherent to the modification of the interatomic distance.

These results point out that the interaction of the ZnO NP with the THIOL does not correspond to a simple bonding effect in which one oxygen atom is substituted

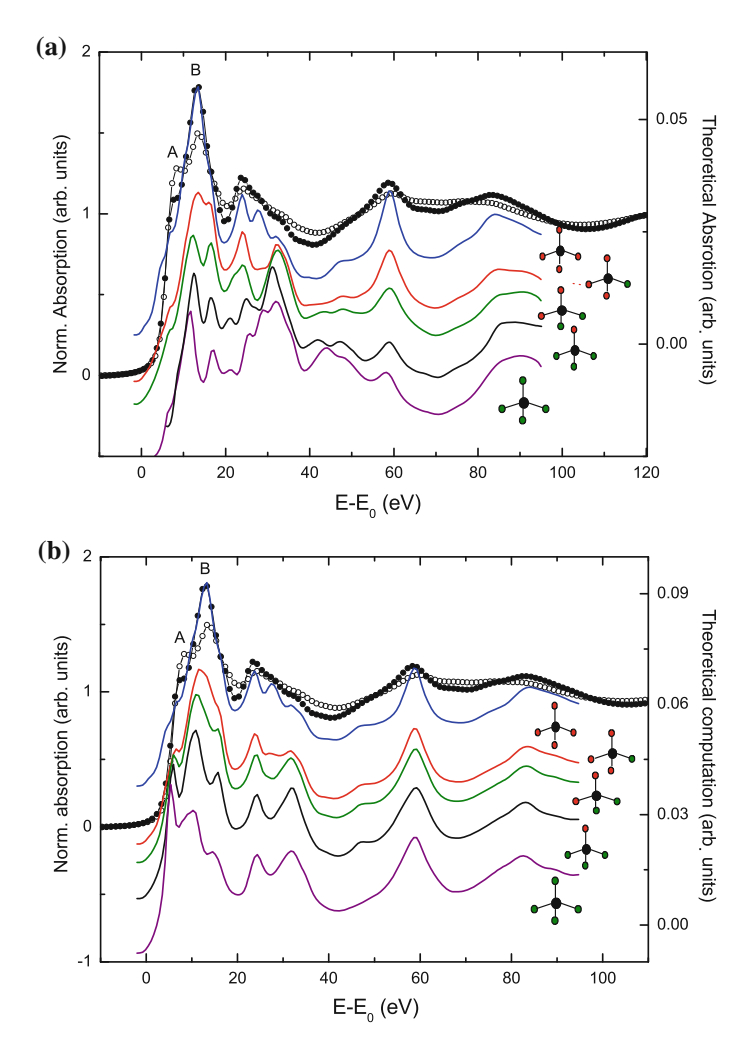


Fig. 4.8 Comparison of the experimental Zn K-edge XANES spectra of bulk ZnO and THIOL and the theoretical signals computed for a 8 Å W-ZnO cluster and for the same cluster in which the O nearest-neighbours have been progressively substituted by S at **a** the same atomic positions and **b** at the Zn-S interatomic distance corresponding to W-ZnS (this cluster is referred as W-ZnOS)

by a sulphur one, but the local environment of the Zn atoms is strongly modified. To verify these results on bigger clusters, we have performed computations for a ZnO cluster including coordination shells within the first 8 Å around Zn (177 atoms), and we have simply substituted the four nearest-neighbours O atoms by sulphur ones, while the rest of the cluster remains unvaried. This substitution has been made progressively, that is, by increasing the number of S atoms in the first coordination sphere. The S atoms have been placed at the same crystallographic positions of the

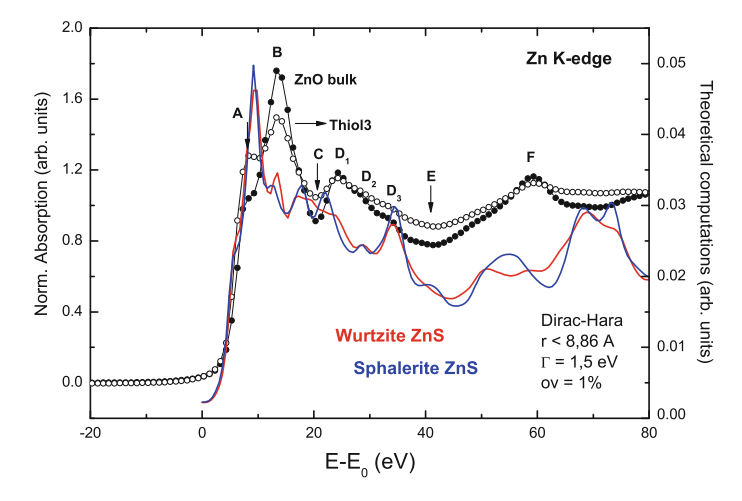


Fig. 4.9 Comparison of ZnS in wurtzite and sphalerite structures

substituted O atoms in the ZnO frame (Fig. 4.8a) and also by considering the increase of the Zn-S interatomic distance as for W-ZnS (Fig. 4.8b).

It should be noted that only the Zn-S interatomic distance of the S atoms in the first neighbouring shell has been modified, while the rest of the cluster (Zn-Zn and Zn-O distances) remains unchanged. As shown in these figures, despite only four neighbour atoms have been changed in the cluster, the effect on the XANES spectra is dramatic. Confirming the results of the computations performed for small clusters, the simply substitution of S at the O position does not reproduce the experimental spectra. In contrast, when the interatomic distance of the substituted Zn-S bonds are set equal to those of W-ZnS (hereafter W-ZnOS) the theoretical spectra resemble the experimental ones. In particular, the intensity ratio of peaks A and B is inverted in both ZnO and W-ZnOS calculations, which mimics the experimental differences of the Zn K-edge XANES spectra of both bulk ZnO and THIOL-capped ZnO NPs samples: the intensity of the main absorption line (B peak) decreases and that of the low energy A peak increases as the ZnO NPs are capped with THIOL.

For the sake of completeness we have also computed the Zn K-edge absorption for two hexagonal wurtzite (W-ZnS) and cubic zinc-blende (ZB-ZnS) ZnS clusters. Both computations, reported in Fig. 4.9, point out that the Zn K-edge XANES of these ZnS polymorphs show an absorption profile whose maxima and minima are in opposition to those of the ZnO spectrum and, consequently, they will be easily detected if present. On the contrary, these results indicate that a well defined ZnS shell with wurtzite structure is formed during the capping of the ZnO NPs.

A final study has been deserved to determine if the observed ZnS structure corresponds to a germ inserted within a ZnO matrix or, on the contrary, it corresponds to the formation of a ZnS interface between the ZnO NP and the organic molecules. It should be noted to this respect that, according to the results in Fig. 4.3, a small

cluster of about 4.5 Å around an absorbing Zn atom will account for the main spectral features of the XANES spectra of W-ZnS. Consequently, a thin ZnS interface formed at the surface of the ZnO NPs will account also for the observed modifications in the XANES of the THIOL sample with respect to that of bulk ZnO. Trying to get a deeper insight in the presence of such ZnS interface, we have have built up the expected Zn K-edge XANES signal by considering that the experimental XANES spectrum corresponds to the weighted addition of contributions coming from Zn atoms within the ZnO frame at the inner part of the particle and from those bonded to S near the surface. To this aim, we have separately added to the theoretical signal computed for a 8 Å ZnO cluster (i) the theoretical XANES spectrum obtained on the same cluster by substituting the four next-neighbours oxygen atoms by sulphur ones and by imposing the Zn-S interatomic distance of W-ZnS, and (ii) the theoretical signals computed for W-ZnS. The results, reported in Fig. 4.10, shows that as the weight of the ZnS contribution increases the computed signal agrees with the observed evolution of XANES from bulk ZnO to the THIOL sample. Although both approaches yield similar results, the computation obtained by considering a wurtzite ZnS cluster shows a better agreement with the experimental data. A closer inspection of the comparisons reported in Fig. 4.10 shows that, contrary to the experimental behaviour, in the case of computations made by inserting the ZnS germ within the ZnO frame there is a slight shift of the computed structures towards higher energy and the D₁ peak is strongly depressed. In contrast, computations performed by considering the presence of a well-defined ZnS interface show a remarkable good agreement with the experimental spectra.

The results obtained through this study disregard the possibility that the capping leads to the formation of single bonds at the surface of the NP. On the contrary they point out the formation of a well defined ZnS interface in which ZnS adopts the local structure of wurtzite (W-ZnS). As it will discussed in the next chapters, this result renders crucial into the understanding of the origin of the observed HTFM behaviour: at the same time that it demonstrates the inappropriateness of the charge-transfer model, it suggests that the *exotic* HTFM observed in theses systems is related to this interface whose details (thickness, interpenetration, etc.) should determine the particular magnetic properties of each system.

The current XANES study evidences the formation of a well defined interface (see Fig. 4.11) between the NPs and the organic molecules in the case of THIOL sample. This identification was favoured by the great different of the backscattering properties of S and O atoms. Unfortunately the same does not hold in the case of AMINE samples, in which N and O scatterers are involved and even more obviously in the TOPO case, where only Zn-O bonds occur. Therefore it is necessary to use a different approach to asses if a similar interface is formed in the case of AMINE and TOPO samples.

To this aim it is interesting to note the significant differences occurring in the intensity of the main absorption line of TOPO and AMINE samples and that of bulk ZnO. As shown in Fig. 4.1 the XANES of both the NPs and the bulk ZnO reference show the same spectral profile for energies higher than the white line (peak B). In particular, there is no difference in the shape, nor in the relative intensity of

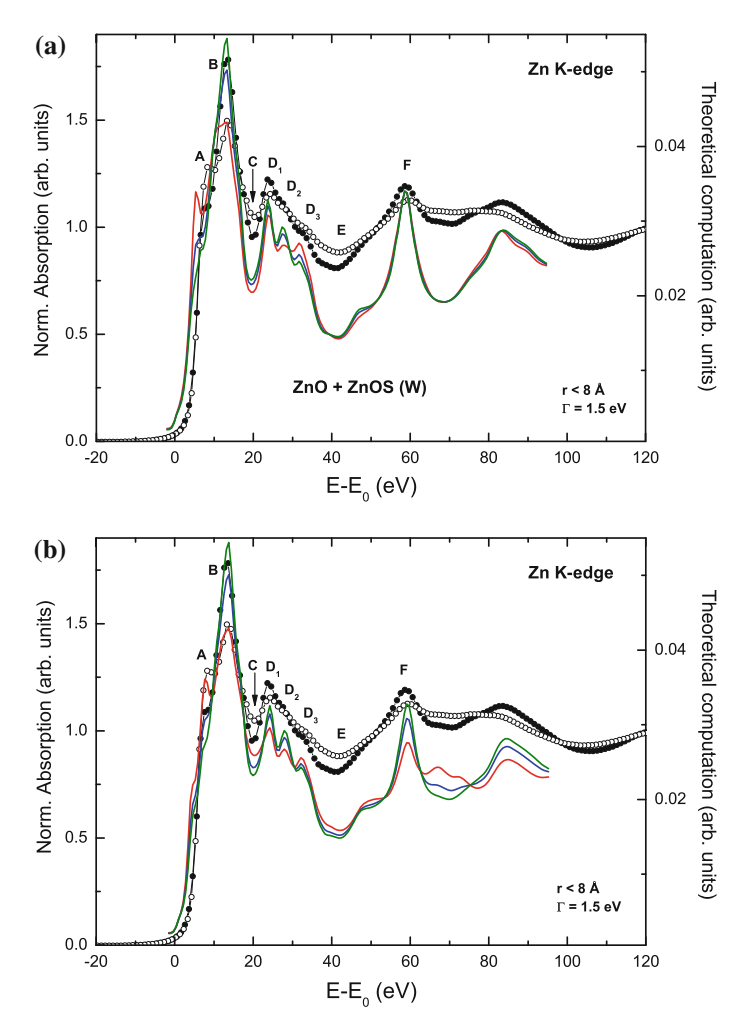


Fig. 4.10 a Comparison of the experimental Zn K-edge XANES spectra of bulk ZnO and THIOL sample and the spectra obtained by adding the theoretical signal computed for a 8 Å ZnO cluster and the same cluster in which the four O next-neighbours have been replaced by S and by imposing the Zn-S interatomic distance of ZnS-W (ZnOS) with different relative weights: pure ZnO (*black line*), 90 % ZnO + 10 % ZnOS (*green line*); 75 % ZnO + 25 % ZnOS (*blue line*); 50 % ZnO + 50 % ZnOS (*red line*). **b** Same as above but weighting the theoretical signals computed for hexagonal W-ZnO and W-ZnS

the three-peaks structure (D_1, D_2, D_3) occurring at $\sim 20\,\text{eV}$ above the edge. This spectral feature is characteristic of the W-ZnO crystal structure. Indeed, the ab-initio calculations indicated that it is necessary to include all the scattering contributions within a cluster of at least 6.5 Å around photoabsorbing Zn in order to obtain a proper reproduction of this spectral feature. Moreover, the calculations clearly show

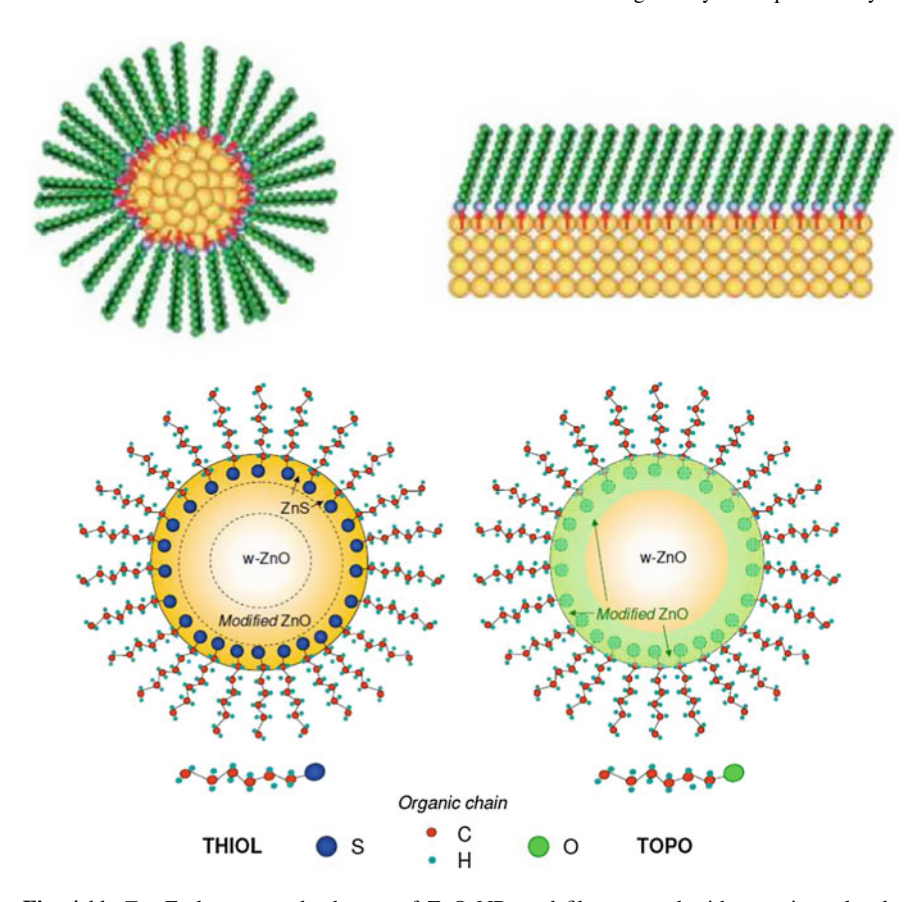
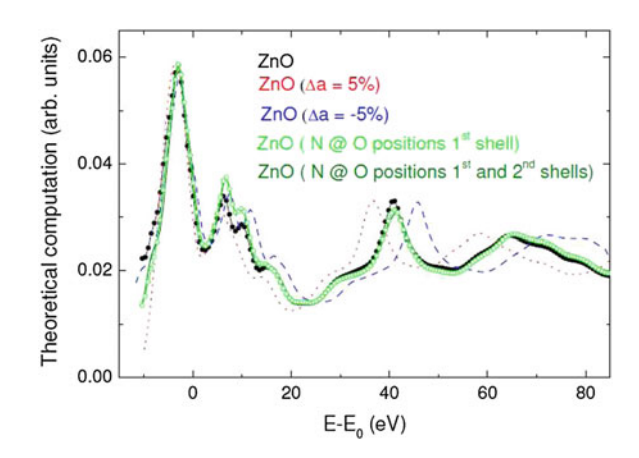


Fig. 4.11 *Top* Early proposed schemes of ZnO NPs and films capped with organic molecules [5, 17, 18]. In the *bottom panel* the bonding scheme suggested by this XAS study is sketched

Fig. 4.12 Comparison of the Zn K-edge XAS spectra of ZnO computed for a 8 Å wurtzite ZnO cluster and for the same cluster in which the cell parameter has been increased and decreased by a ±5 %. Similar calculations have been performed by replacing the oxygen atoms by nitrogen ones in the first two oxygen coordination shells around photoabsorbing Zn



the sensitivity of its spectral shape (relative energy and intensities) to small modification of the local structure. This is shown in Fig. 4.12 where computations have been performed by modifying the cell parameters of the wurtzite ZnO structure by a $\pm 5\,\%$, i.e. the original lattice parameters (a = 3.25 Å and c = 5.21 Å) were changed from a = 3.09 Å and c = 4.95 Å, to a = 3.41 Å and c = 5.50 Å, respectively. In contrast, the substitution of O by N at the next-neighbouring coordination shells, without varying the interatomic distances, do not modify this spectral shape. Consequently, the fact that the white line decreases for TOPO and AMINE while the D structure remains unchanged suggests the presence of Zn atoms in a short-range ordered phase overimposed to that of W-ZnO, where we intend by short range that the Zn coordination extends only to a few coordination shells. The expected contribution of such a phase should be single-oscillation-like and, consequently, it does not interfere the D structure of ZnO, while a different main-line intensity likely occurs. Under these circumstances the the overall profile of bulk ZnO should be retained while the white-line intensity should be affected.

As outlined above, the short-range character of this aforesaid phase means that the coordination of Zn extends only to a few neighbouring shells. The contribution of this additional phase to the white-line region should be significantly smaller than that of bulk-ZnO and nearly flat (structureless) at the energy region where the D structure appears. Therefore, detailed ab-initio computations were carried out to demonstrate that the differences of the experimental XANES spectra recorded for bulk ZnO and for the capped ZnO NPs can be accounted for in terms of a two-phase scheme: the expected bulk-like ZnO contribution and a short range ZnO phase. To this aim we have calculated the total absorption of the capped ZnO NPs by weighting the theoretical spectrum of bulk-ZnO and of a small ZnO cluster in which only the first two coordination shells around Zn are considered. Figure 4.13a shows that the Zn K-edge XANES spectrum of TOPO is well reproduced when the contribution of the new phase reaches a 20% of the total signal. The experimentally observed decrease of the white-line intensity while the rest of the spectrum remains unvaried is well reproduced by the calculation. As a final test we have also considered the possibility of the Zn-O and Zn-Zn interatomic distances increasing as to resemble the ZnS case. In the last case the theoretical spectrum (Fig. 4.13b) displays, in addition to the decrease of peak B, a slight reduction of peaks D₁ and E. Moreover, feature A is better resolved. All those results point out the modification of Zn-O bonds at the studied phase. Making a parallel to the THIOL case this new phase should be located in the near surface region, that is, at the interface between the ZnO bulk-like core of the NP and the capping molecules (see Fig. 4.11).

These results indicate that also in the case of TOPO and AMINE an interface is formed between the core of the ZnO NP and the capping molecule. Estimates of the amount of Zn atoms at this interface have been derived from the ratio of the white line intensity with respect to that of bulk ZnO. In this way we obtain that the amount of Zn atoms at the interface is about 15, 10 and 5% for AMINE, TOPO and THIOL respectively.

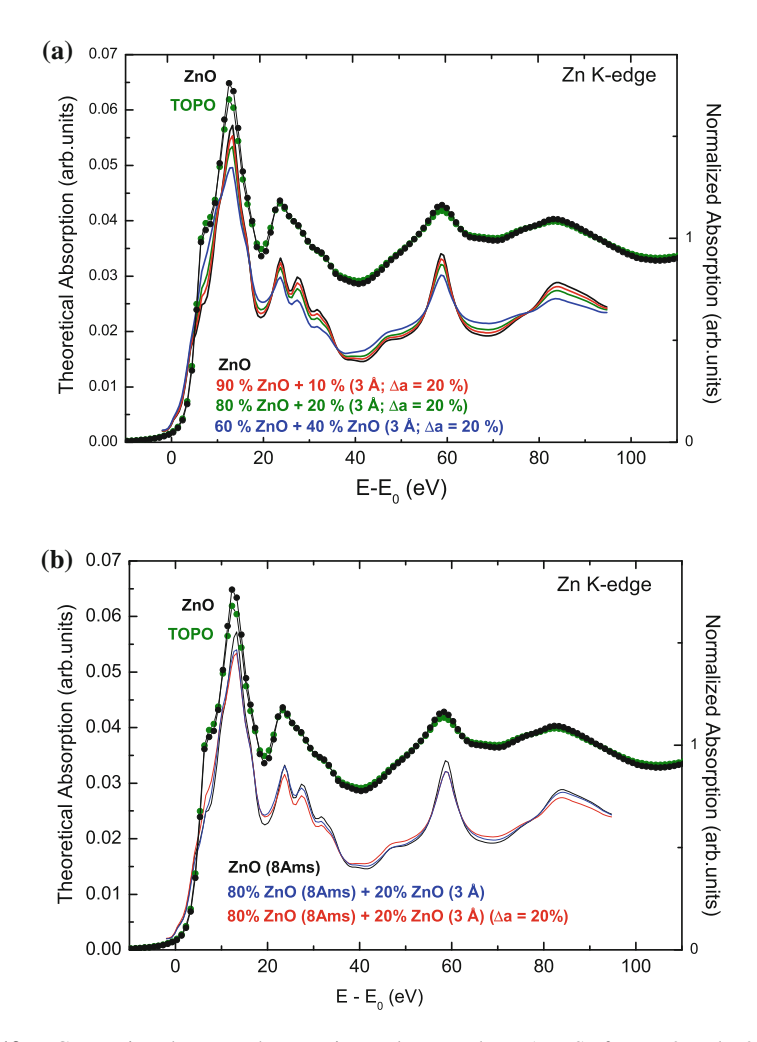


Fig. 4.13 a Comparison between the experimental Zn K-edge XANES of W-ZnO and TOPO and the weighted sum of theoretical spectra computed for long and short range ZnO clusters (see text for details). **b** Comparison between the experimental Zn K-edge XANES of wurtzite-ZnO and TOPO sample and the weighted sum of computations performed for the original 8 Å W-ZnO cluster and (i) a short-range order W-ZnO cluster (3 Å), (ii) the same cluster but considering a distortion of the interatomic distances (see text for details)

4.2 Zn K-edge XAS Study of ZnO NPs Capped with Thiol Derivatives and ZnS/ZnO Thin Films

The results presented in the previous section were obtained for the first batch of samples that were produced. As discussed in Chap. 2, additional batches of thiol-capped samples were produced by varying two of the synthesis parameters: (i) t_{add} , that is, the time waited once the synthesis was initiated, before adding the organic

Zho 141 s	
Sample	Weight ZnO-ZnS (±10%)
20-12C-1 (THIOL)	50–50
Calcinated 20-12C-1	40–60
5-12C-2	35–65
15-12C-2	65–35
30-12C-2	50–50
7-12C-3	10–90
9-12C-3	10–90
12-12C-3	12–88
20-4C-4	28–72
20-8C-4	35–65
20-12C-4	31–69
50-4C-4	32–68
50-8C-4	32–68
50-12C-4	25–75

Table 4.1 Contribution of ZnO and ZnS like regions to the total XANES spectra of THIOL-capped ZnO NPs

Those values have been obtained by fingerprint comparison with the weighted sum of the W-ZnO and W-ZnS reference spectra

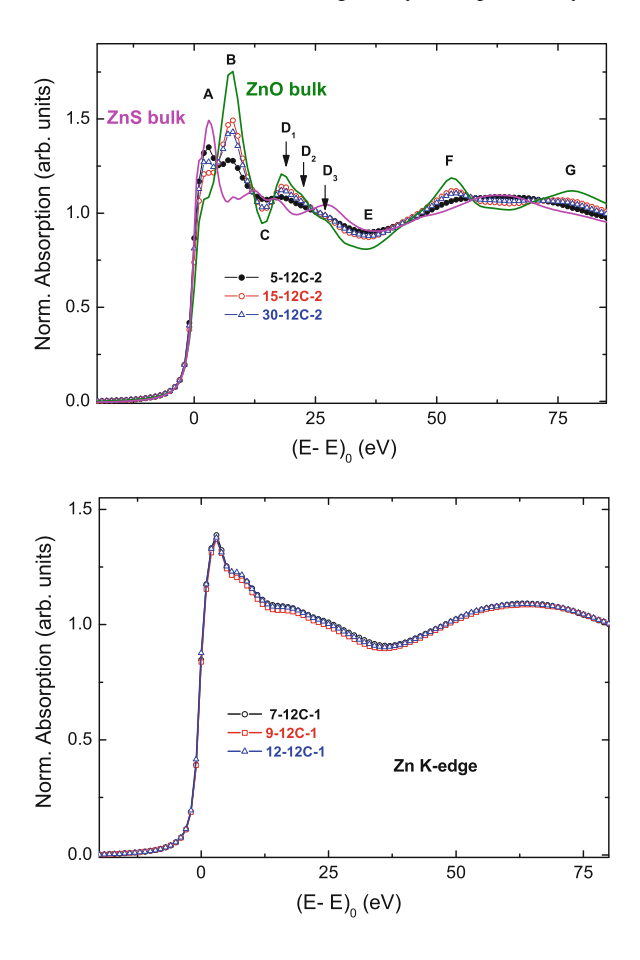
capping agent that coats the NPs and stops their growth, and (ii) the length of the carbon chains (4, 8 or 12 carbons).

The objective of the new synthesis is twofold. On the one hand we have confirmed the general character of the result previously described, i.e. that capping leads to the formation of an interface between the NP and the organic molecules. In addition we have investigated how the parameters of the synthesis influence the details of the interface and, accordingly to our hypothesis, the magnetic properties of the systems. The final series of samples are summarized in Table 4.1. Therefore we have repeated the same XANES study as above on the new samples in order to confirm the conclusions obtained in the precedent section.

The XANES spectra of the dodecanethiol capped samples of batches 1, 2 and 3 are presented in Fig. 4.14. The experimental data are in line with those of the 20-12C-1 sample (referred just as THIOL in the section before).

In all the cases the main absorption peak B is depressed with respect to that of bulk ZnO. In addition, the intensity of peak A increases as peak B decreases. Both results are in agreement with the proposed development of a W-ZnS shell surrounding the ZnO core. Moreover, the variation of the relative intensity of peak A and B through the studied series indicates that the ZnS/ZnO ratio differs for the different synthesis conditions. Estimates of the ZnS/ZnO ratio have been derived from the experimental XANES spectra by comparing them to the weighted addition of those of bulk ZnS and ZnO references. The ZnS/ZnO ratio (summarized in Table 4.1) is clearly higher for 5-12C-2 sample than for both 15-12C-2 and 30-12C-2 ones (80 %/20 % versus

Fig. 4.14 Top Comparison of the normalized Zn K-edge XAS spectra of bulk ZnO and ZnS (magenta) and those of ZnO NPs capped with dodecanethiol. Bottom Comparison of the normalized Zn K-edge XAS spectra of dodecanethiol capped W-ZnO nanoparticles obtained by varying the time at which the capping agent was added after the addition of the TMAH solution (see Chap. 2 for details)



40%/60% and 50%/50% respectively), while it is quite similar to that of 7-12C-3, 9-12C-3, 12-12C-3 samples.

Similar results are found in the case of samples from batch 4 (see Fig. 4.15), for which regardless of the chain length the ZnS phase dominates over the ZnO one. However, the contrary holds for samples of the series-2. Consequently, the variation of the ZnS/ZnO ratio does not allow us to establish a correlation with none of the parameters varied in the synthesis.

Next parameter that we have studied in connection with the XANES results is the degree of crystallinity of the samples. The XRD patterns (reported in Chap. 2) show for most of the samples the presence of an amorphous phase coexisting with wurtzite-like ZnO and ZnS ones. In agreement with the XANES results the relative amount of this amorphous phase depends on the synthesis conditions. This makes difficult to asses the crytallinity of the samples from a simple Debye-Scherrer analysis. However the combination of the XRD and the inspection of the XANES spectra can give us a clue on this issue.

Fig. 4.15 Comparison of the normalized Zn K-edge XAS spectra of the ZnO NPs obtained by using butanethiol (blue dotted line), octanethiol (red dashed line) and dodecanethiol (black solid line) and by varying the time at which the capping agent was added after the addition of the TMAH solution

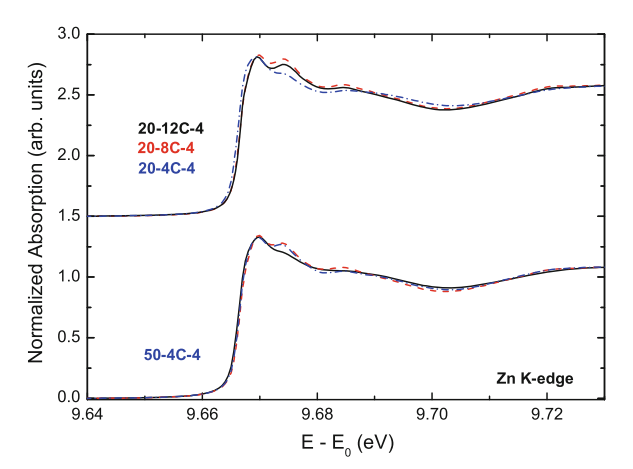
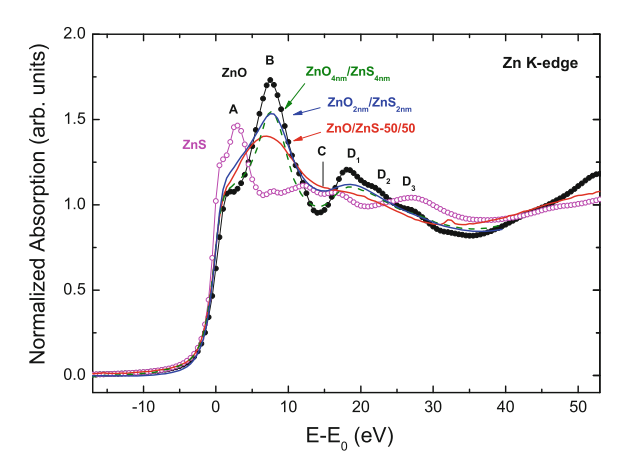


Fig. 4.16 Comparison of both the Zn K-edge XANES spectra recorded for W-ZnO, W-ZnS, (ZnO_{4nm}/ZnS_{4nm})₁₀ and (ZnO_{2nm}/ZnS_{2nm})₂₀ multilayers, and the sample obtained by ZnS-ZnO co-sputtering before any annealing process (as grown)



According to the XANES spectral shape, the crystallinity is mainly asset by the resolution of peaks A and B as well as the modifications affecting the structure D. As seen in the theoretical spectra obtained by varying the cluster size (see Fig. 4.3), just 4 coordination shells (\sim 4.5 Å) are enough to get a well resolved main absorption line B, while a longer-range order is needed for reproducing the D feature. As shown in Fig. 4.16 the spectra of the (ZnO_{2nm}/ZnS_{2nm})₂₀ and (ZnO_{4nm}/ZnS_{4nm})₁₀ heterostructures show a profile similar to that of bulk ZnO, especially that of (ZnO_{4nm}/ZnS_{4nm})₁₀, in agreement with a high crystallinity and the formation of neat interfaces derived from X-ray reflectivity (XRR) spectra (see discussion in Chap. 2). In contrast, the spectrum of the Zn-O-S film (ZnO/ZnS-50/50) prepared by RF cosputtering does not exhibit the characteristic spectral features of either W-ZnS or W-ZnO systems but a rounded maximum indicating the amorphous character of the sample. As for the NPs, despite the fact that in all cases the simultaneous presence of peaks A (more precisely its reinforcement with respect to bulk ZnO) and B indicates

the presence of ordered W-ZnS and W-ZnO regions in the materials, the fact that the three-peak structure (D_1 , D_2 and D_3) at $\backsim 20\,\text{eV}$ above the edge is ill-defined indicates that there is a certain amount of Zn atoms that is not forming part of the well defined W-ZnO and W-ZnS regions of the core and shell, but shorter-range ordered regions. One can assume that these Zn atoms are localized in the ZnO/ZnS core-shell interface in which the Zn-S and Zn-O bonds are modified with respect of the wurtzite structure.

Interestingly, as shown in the previous chapter, the FML contribution is maximized in the case of the $(ZnO_{4nm}/ZnS_{4nm})_{10}$ heterostructure, while this contribution is not observed in the sample obtained for cosputtering whose magnetization curves approach those obtained in the ZnO single crystal reference. These results suggest the need of pristine ZnS/ZnO interfaces to obtain FML behaviour in these systems. This is in agreement with the behaviour observed for samples of batch 3 and 4, for which the XANES spectra indicate that a disordered ZnS phase prevails, in agreement with the XRD.

4.3 XAS Study of the Local Order Around the Transition Metal on Mn:ZnO Thin Films: The Role of Vacancies and Structural Distortions

Throughout this chapter it has been stressed the usefulness of XAS for the determination of the local structure of the studied systems. The results obtained in the precedent sections provided a new insight into the existing relationship between the magnetic properties and the local structure of the studied ZnO-based compounds.

As discussed in the Introduction, little attention has been paid to the role of the structural effects on the magnetic properties. On the contrary, the origin of the *exotic* magnetism observed in both DMSs and DMOs has been associated, from both theoretical and experimental sides, to the occurrence of vacancies. However it does not render clear which class of defects should be the responsible of the HTFM behaviour as different types of defects, such as oxygen and/or zinc vacancies, as well as hydrogen, oxygen and zinc interstitials, have been proposed in different experimental and theoretical works [19–23].

Aiming to determine the exact type of defect that causes the HTFM in these systems several experimental tools, such as X-ray absorption spectroscopy (XAS), have been applied. However, based on similar experimental spectra, different authors report opposing conclusions regarding the nature of the defects involved in the observed HTFM. Hsu et al. [24] have concluded that oxygen vacancies enhance room temperature ferromagnetism in Co-doped ZnO films while, in contrast, Yan et al. [25], concluded that Zn vacancies induce HTFM in Mn doped ZnO. This scenario is further complicated by the results of Zhang et al. [26], who concluded from similar data that the aforesaid oxygen vacancies are located in the second shell around the magnetic ions. These contradictory results pose serious doubts about the

real capability of XAS to determine the presence of vacancies in these systems and, consequently, to shed light on the origin of the magnetism in these systems.

Here, we present an XANES study performed at both Mn and Zn K-edges in $Zn_{0.95}Mn_{0.05}O$ thin films prepared with different sputtering gases (pure Ar, Ar/N₂ and Ar/O₂), whose magnetic properties differ as a function of the different gases using during the preparation [27]. Contrary to similar studies focused on the role of vacancies, Céspedes et al. pointed out the relationship of this behaviour to the Mn short-range order in the lattice [27], as in similar Zn-Mn-O systems [28]. With this in mind, we have performed a detailed study of the local order around Mn in these thin films by means of ab-initio XANES calculations, paying an special emphasis to determine the role played by both vacancies and structural distortions.

The experimental spectra recorded at both the Mn and Zn K edge in the $Zn_{0.95}Mn_{0.05}O$ films prepared with different sputtering gases are shown in Fig. 4.17. They are compared to the experimental spectra reported by other authors [29] and to the result of the theoretical computations performed by Yan et al. [25].

The XANES spectra of our samples are similar in the high energy region to those previously reported by Pellicer-Porres et al. [29]. However, the intensity ratio between the main absorption line and the first broad resonance (about 15 eV above the main line) is markedly different in both cases. It should be noted in this respect that the computations reported by both Yan et al. and Pellicer-Porres et al. fail in reproducing this intensity ratio. Despite the poor agreement between the theoretical calculations and the experimental data in the near-edge (XANES) region, several authors conclude from their comparison the existence of both oxygen and zinc vacancies to which the HTFM observed in the materials is addressed.

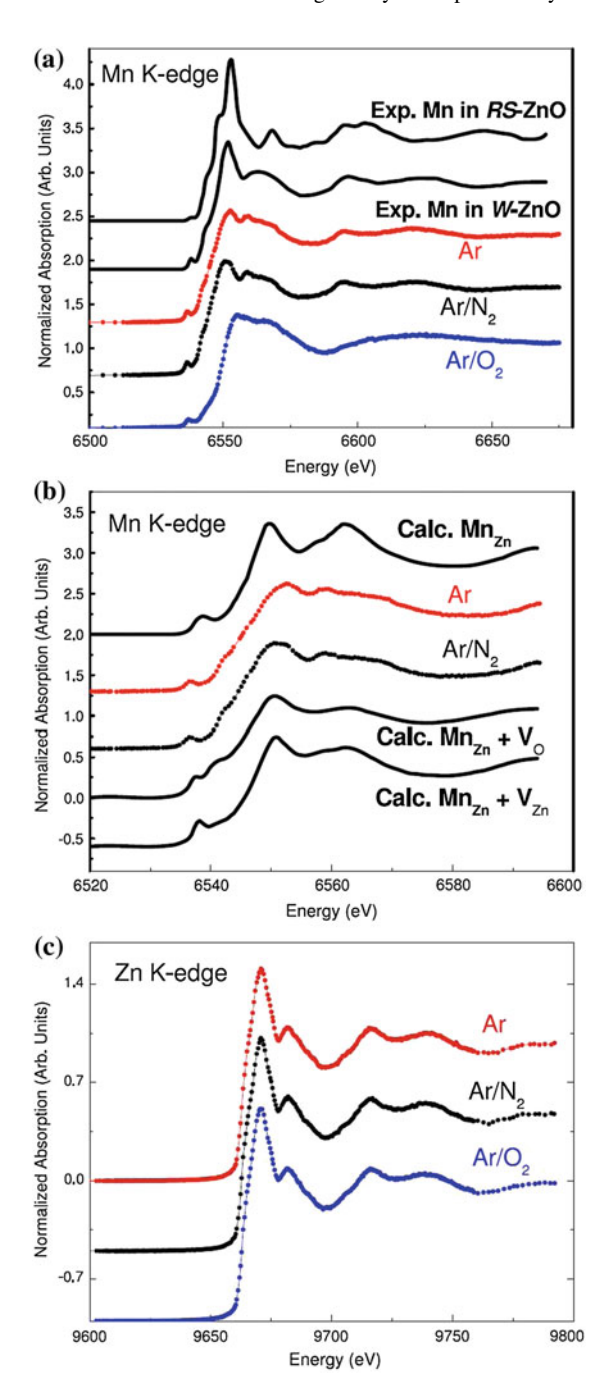
In order to obtain a deeper insight into the origin of such discrepancies we have performed an accurate and systematic ab-initio computation of both the Mn and Zn K-edge XANES spectra in $Zn_{0.95}Mn_{0.05}O$ films. For the computations, we have followed the same procedure as detailed in the previous sections. Accordingly, the Zn K-edge XANES was calculated for both wurtzite (W) and rock-salt (RS) references, while MnO was chosen as our reference for the Mn K-edge computations.

In all the cases the best reproduction of the experimental spectra (see Figs. 4.18 and 4.19) has been obtained by using a 8 Å cluster, $l_{\rm max}=3$ and ov = 1%. In the case of the Zn K-edge the best agreement with the experimental data is obtained by using the *real* DH ECP, while the *complex* one is used to account for the Mn K-edge spectra.

Following these prescriptions we have calculated the Mn K-edge XANES spectra of Mn:ZnO systems showing both the wurtzite and rock-salt structures. For these systems the XANES spectra were calculated for a simple substitutional model in which Mn substitutes Zn in the wurtzite structure. This calculation has been further extended by considering the presence of both O and Zn vacancies near the photoabsorbing atom, either Mn or Zn. Following the results of Kuzmin et al. we have not considered the off-center displacement of the photoabsorbing ions [30].

The results of these calculations are shown in Fig. 4.19. The computation performed by considering that Mn substitutes Zn in the RS-ZnO structure is well reproduced by the calculation. However, the agreement worsens in the case of the

Fig. 4.17 Comparison between the experimental Mn K-edge XANES spectra of Ar-, Ar/N2- and Ar/O2-prepared $Zn_{0.95}Mn_{0.05}O$ films: a the experimental data reported in [29] for Mn in RS-ZnO and in W-ZnO structures and b calculations reported in [25] for Mn substituting Zn in stoichiometric W structure (MnZn), W with oxygen vacancies $(Mn_{Zn} + V_O)$ and W with zinc vacancies $(Mn_{Zn} + V_{Zn})$. **c** Comparison of the Zn K-edge XANES spectra of Ar-, Ar/N2- and Ar/O2-prepared $Zn_{0.95}Mn_{0.05}O$ films



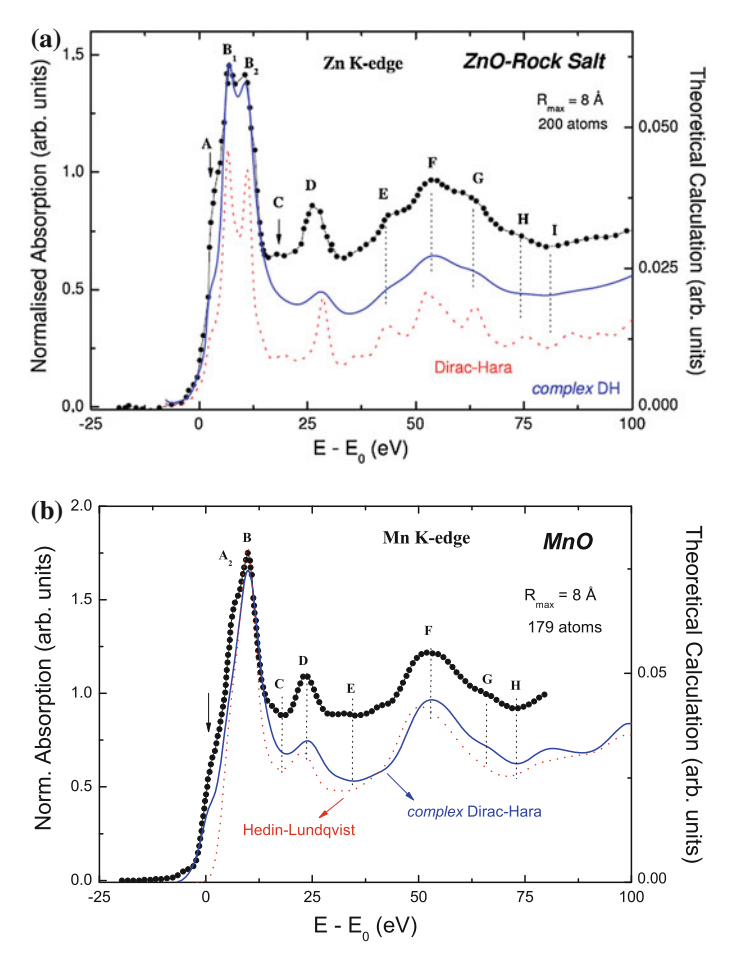


Fig. 4.18 a Comparison between the experimental Zn K-edge XANES of rock-salt ZnO and the computations performed by using both real (*red*, *dashed*) and complex (*blue*, *solid line*) DHECPs. **b** Comparison of the experimental Mn K-edge XANES spectrum of MnO and the computations performed by using complex ECPs: complex DH (*blue*, *solid line*) and HL (*red*, *dashed*). (Experimental spectra from Ref. [16])

substituted W-ZnO. The fact that the XANES spectrum of the $Zn_{0.95}Mn_{0.05}O$ thin film in the rock-salt structure is well reproduced by the computation, while the same does not hold for the same system in the wurtzite structure, suggests that the presence of vacancies is not the main responsibility of the disagreement between the theoretical and the experimental spectra of the wurtzite case, especially if one takes into account that only one atom, the photoabsorber, has been changed in clusters of 200 and 177 atoms for rock-salt and wurtzite, respectively.

To verify the role of vacancies in modifying the XANES spectral shape of the $Zn_{0.95}Mn_{0.05}O$ films we have performed several theoretical calculations by imposing

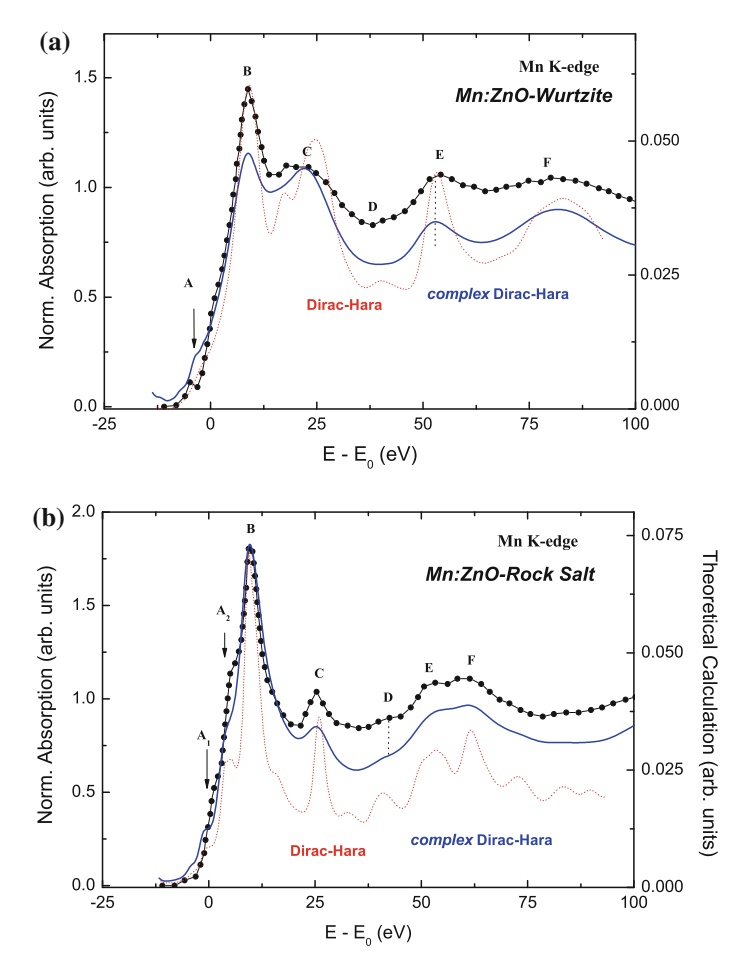


Fig. 4.19 Comparison between the experimental Mn K-edge XANES of Mn:ZnO (from Ref. [29]) and computations performed by considering that Mn substitutes Zn in the wurtzite ZnO structure. The computations were performed by using Complex Dirac-Hara (*solid line*) and Dirac-Hara (*dotted line*) ECPs

the presence of both oxygen and zinc vacancies in the first coordination shells of the photoabsorbing atom. In both the Zn and Mn K-edge computations the interatomic distances have been kept fixed as in the undoped W-ZnO.

Figure 4.20 reports the results of the calculation of the Zn K-edge XANES spectra performed on a 8 Å cluster in which the oxygen atoms have been progressively removed from the first coordination shell. The presence of a single oxygen vacancy ¹ in the tetrahedron surrounding Zn affects the whole spectral shape, that is, the

¹It is expected that the presence of vacancies induces subtle changes to the spectra. For this reason we display hereafter the result of the computations obtained by using the real DH in order to get an enhanced view of these changes.

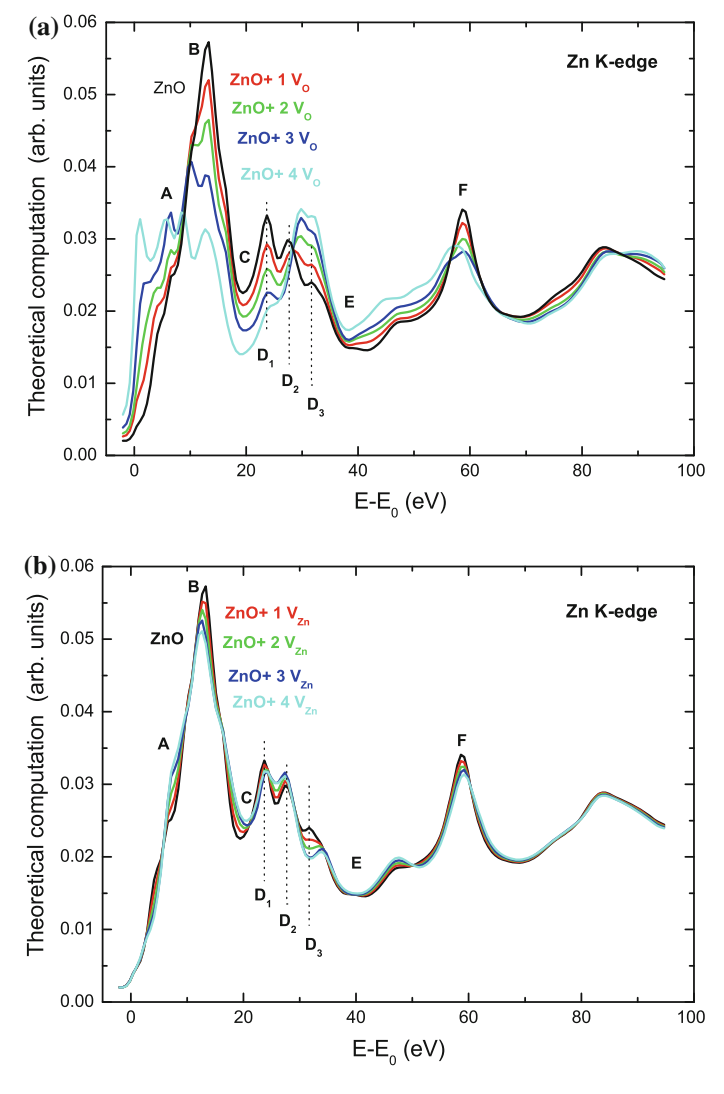


Fig. 4.20 a Comparison of the theoretical Zn K-edge XANES spectrum of W-ZnO and those calculated by considering the existence of oxygen vacancies (V_O) in the first coordination shell of photoabsorbing Zn. **b** Same as above for computations made by considering Zn vacancies (V_{Zn}) in the second coordination shell of photoabsorbing Zn

relative intensity of all the spectral features is modified. In particular, the characteristic three-peak structure centred at $\backsim 30\,\text{eV}$ above the edge is completely modified and the intensity ratio of the three (D_1 , D_2 and D_3) peaks is reversed. This is the expected result, contrary to previous reports [24], because the oxygen vacancy affects not only the single scattering process in the first coordination shell of Zn, but also

different multiple-scattering processes contributing to the spectrum. Including further oxygen vacancies in the next-neighbouring tetrahedron enhances these differences and changes this structure, characteristic of wurtzite, completely and the theoretical spectrum does not resemble the experimental one. In contrast, the inclusion of Zn vacancies in the second coordination shell does not modify significantly the spectral shape and only a slight decrease of the white-line intensity and of the main absorption features is found upon increasing the number of Zn vacancies.

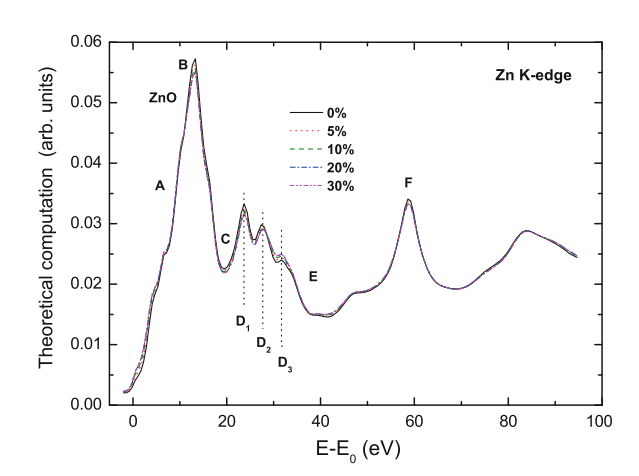
It has been previously reported that upon removing one oxygen atom from the first coordination shell a new peak appears in the pre-edge region and that its intensity becomes more pronounced if a second oxygen vacancy is created in the second oxygen coordination shell [24]. Beyond the lack of agreement with our calculations, this model is not reliable as it considers an ad-hoc arrangement of vacancies. If the oxygen vacancies are randomly distributed, the probability of photoabsorbing Zn having n vacancies in the first coordination shell can be calculated by a simple binomial distribution as:

$$P(n) = \binom{4}{n} x^n (1-x)^{4-n} \tag{4.1}$$

where x is the concentration of oxygen vacancies. Accordingly, the Zn K-edge XANES spectrum should correspond to the addition of spectra with and without oxygen vacancies weighted according to this probability. As shown in Fig. 4.21, the effects induced by the presence of oxygen vacancies are undetectable for defect concentrations of up to 30%.

Similar results are found in the case of the Mn K-edge XANES of the $Zn_{0.95}$ Mn_{0.05}O films. As shown in Fig. 4.22, the presence of either O or Zn vacancies in the next-neighbouring shells around Mn would affect the intensity of all the spectral features and not only of the pre-edge region. As in the case of the Zn K-edge, these

Fig. 4.21 Weighted sum of the theoretical W-ZnO XANES spectrum and those calculated by considering the existence of an oxygen vacancy (one V_O in the first coordination shell of photoabsorbing Zn) by assuming a binomial distribution of the oxygen vacancies with different defect concentrations: no vacancies, 5, 10, 20 and 30 %



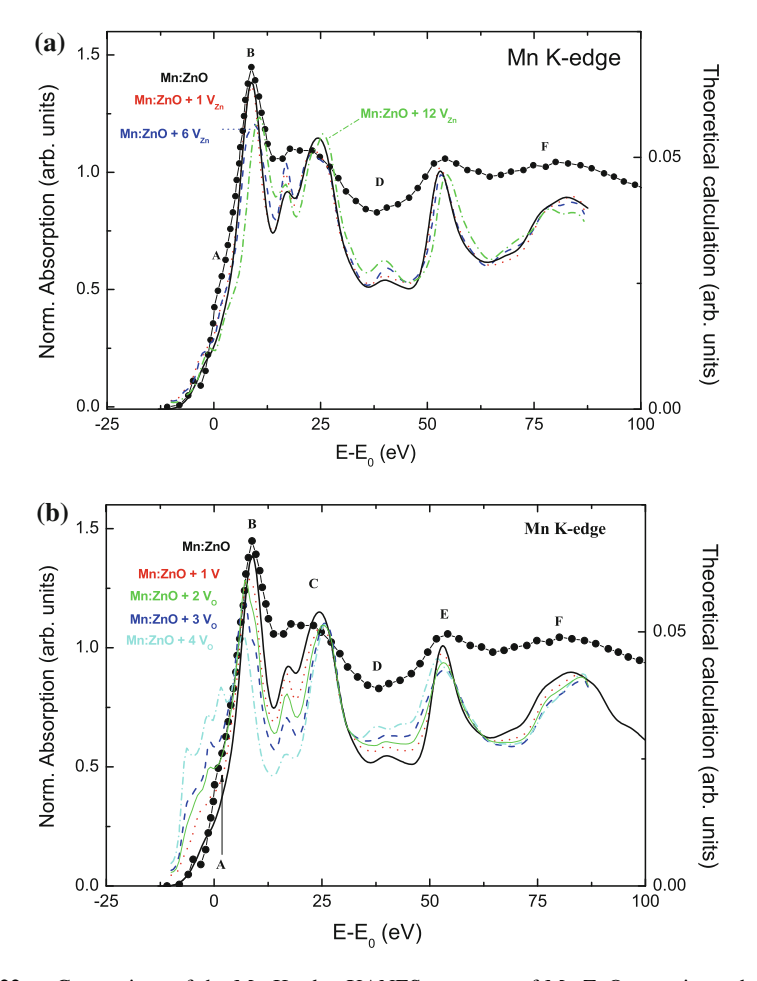


Fig. 4.22 a Comparison of the Mn K-edge XANES spectrum of Mn:ZnO-wurtzite and the theoretical calculations performed by considering the existence of Zn vacancies (V_{Zn}) in the first coordination shell of photoabsorbing Zn: no vacancies (*black*, *solid line*), $1V_{Zn}$ (red, dotted), $6V_{Zn}$ (blue, dashed) and $12V_{Zn}$ (green, dotted–dashed). **b** Comparison of the Mn K-edge XANES spectrum of Mn:ZnO-wurtzite and the theoretical calculations performed by considering the existence of oxygen vacancies (V_O) in the first coordination shell of photoabsorbing Zn: no vacancies (black, solid line), $1V_O$ (red, dotted), $3V_O$ (green, dashed) and $4V_O$ (blue, dotted–dashed)

effects become undetectable in the XANES spectra when the vacancies are randomly distributed, as illustrated in Fig. 4.23 for oxygen defects concentration of up to 50 %.

All these results indicate that the existence of both oxygen and Zn vacancies in the Mn:ZnO films have little influence on the absorption spectra recorded at both the Zn and Mn K-edge. Indeed, the theoretical computations presented here point out that if a reliable concentration of defects, randomly distributed, is taken into account, the effect of vacancies on the XANES spectra is negligible. More importantly, even

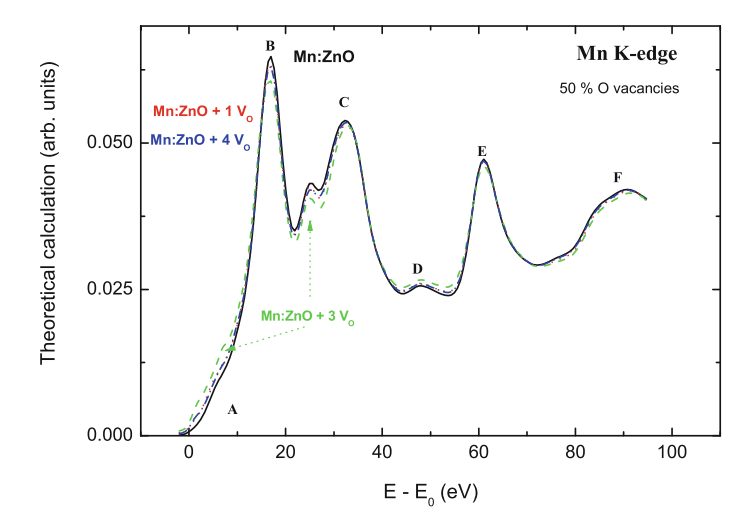


Fig. 4.23 Weighted sum of the theoretical Mn:ZnO-wurtzite XANES spectrum and those calculated by considering the existence of oxygen vacancies by assuming a binomial distribution of 50% of oxygen vacancies

maximizing their effect by choosing ad-hoc defect distributions it is not possible to recover the Mn K-edge experimental spectrum of the Mn:ZnO film in the wurtzite structure.

These results suggest that the disagreement of the theoretical computations and the Mn K-edge of the $Zn_{0.95}Mn_{0.05}O$ thin film in the wurtzite structure is not due to the presence of vacancies. In this situation, structural modifications, induced by the Mn substitution at the Zn site, appear the best explanation to account for the disagreement between the theoretical and experimental spectra.

Despite that several authors have shown that the substitution of Zn by Mn induces a structural distortion in the next-neighbouring environment of the absorbing atom [27], all the computations performed for these systems looking for the presence of vacancies have been done by considering that Mn substitutes Zn in both the W-ZnO and RS-ZnO structures without modifying the interatomic distances [24–26]. In the case of RS-ZnO, the nearest-neighbour interatomic distance is $R_{Zn-O}=2.14~\text{Å}$, while it is $R_{Zn-O}=1.97~\text{Å}$ in W-ZnO. This nearest-neighbour interatomic distance is $R_{Mn-O}=2.22~\text{Å}$ in MnO. Therefore, it seems reasonable to think that, when entering in the W-ZnO structure, Mn adapts the original ZnO tetrahedron by enlarging the R_{Mn-O} distances. Accordingly, this effect should be less marked in the case of RS-ZnO because the R_{Zn-O} distance is closer to the R_{Mn-O} of MnO than in W-ZnO. In this way, it should be possible to understand why the experimental Mn K-edge XANES spectrum of the $Z_{10.95}M_{10.05}O$ thin film in the rock-salt structure is well reproduced by the theoretical computations performed by assuming a simple Zn-Mn substitution while that in the wurtzite structure does not.

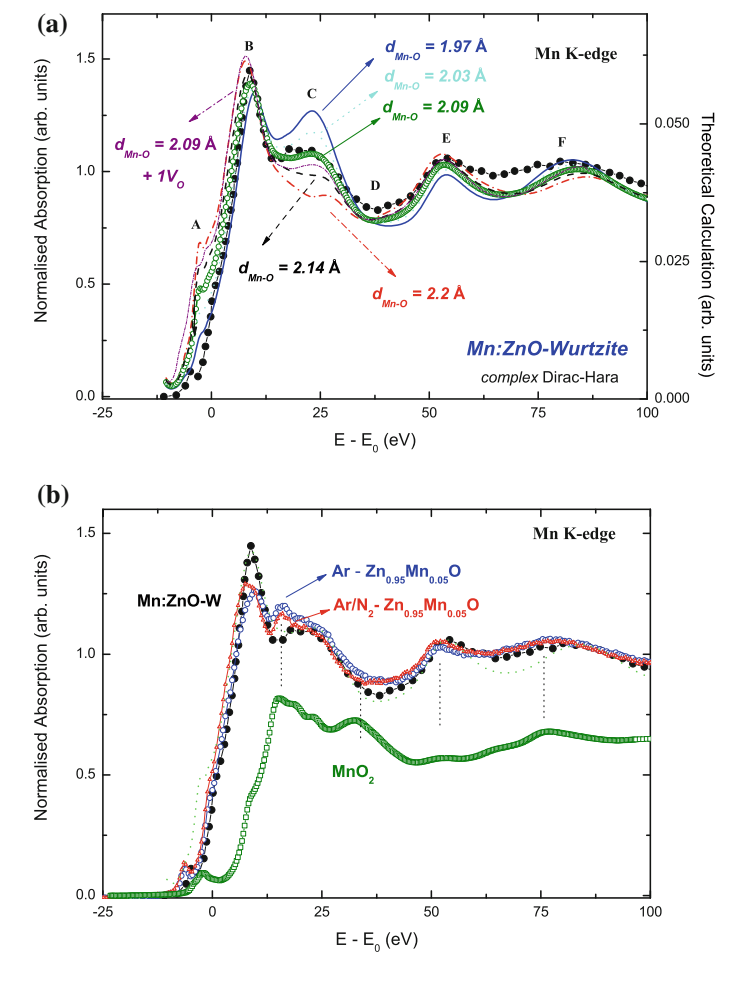


Fig. 4.24 a Comparison between the experimental Mn K-edge XANES of Mn:ZnO and computations performed by considering that Mn substitutes Zn in the wurtzite ZnO structure adapting the interatomic Mn-O distance in the first coordination shell. b Comparison between the experimental Mn K-edge XANES spectra of Mn:ZnO-wurtzite; Ar- and Ar/N₂-prepared Zn_{0.95}Mn_{0.05}O films and the theoretical computation performed by considering that Mn substitutes Zn in the wurtzite ZnO structure adapting an Mn-O interatomic distance of 2.09 Å in the first coordination shell. The experimental spectrum of MnO₂ is also shown (see text for details)

To further confirm this hypothesis we have calculated the Mn K-edge XANES spectrum of Mn:ZnO in the wurtzite phase by considering that Mn substitutes Zn in the W-ZnO frame and, in addition, by increasing progressively the interatomic R_{Mn-O} distance in the nearest-neighbour shell of Mn (MnO tetrahedron) from 1.97 Å, W-ZnO-like, to 2.22 Å, as in MnO. As shown in Fig. 4.24, the computation performed considering $R_{Mn-O}=2.03$ Å yields a good reproduction of the exper-

imental spectrum, especially regarding the broad resonance C, $\sim 20\,\mathrm{eV}$ above the edge, and the intensity ratio between this resonance and the white line (peak B). Moreover, the computation exhibits a shift towards lower energies of the edge position, as expected because the R_{Mn-O} increases, and the structure at the raising edge is slightly enhanced with respect to the computation in which Mn simply substitutes Zn without modifying the interatomic distances. The occurrence of an enlarged Mn-O interatomic distance is also in agreement with EXAFS results [29]. Finally, we have also checked in this case that adding an oxygen vacancy in the first coordination shell of Mn has no effect on the calculated spectrum.

The results of the theoretical computations point out that Mn adapts its local environment by increasing the Mn-O interatomic distance. This modification is slight depending on the different gases used in the preparation. That fact suggests that the different magnetic behaviour observed for the different samples is related to the different local structure of Mn in the films. It should be finally noted that, as shown in Fig. 4.24, there are some differences between the XANES spectra of these samples and those reported by Pellicer-Porres et al. [29]. The Mn K-edge XANES spectra of both Ar-Zn_{0.95}Mn_{0.05}O and Ar/N₂-Zn_{0.95}Mn_{0.05}O samples show a decrease of the white-line intensity and a well-defined peak at $\sim 16\,\text{eV}$ above the edge. This peak is not present in the spectrum reported in [29] nor in the theoretical calculation. The comparison of the experimental spectra with that of MnO₂ suggests that this peak is simply due to the presence of a small amount of MnO₂ in the samples, also in agreement with the white-line reduction due to the diverse Mn environments.

4.4 Conclusions

We have performed a detailed XANES Zn K-edge study of ZnO capped NPs and ZnO/ZnS multilayers. The XAS spectra recorded along a 3 year period demonstrate the high stability of the synthesized ZnO NPs. On the other hand, the XAS analysis also shows the low synthesis reproducibility since noticeable differences are observed between nominally identical samples. This indicates the need for a careful structural analysis when studying this type of samples.

We have found that the capping molecules do not bond to the ZnO through single bonds in which one atom of the molecule (S, N or O) substitutes one O from the ZnO NP as early proposed [5, 17, 18]. On the contrary, we have determined the formation of a well defined interface at the surface of the ZnO NPs.

In the case of THIOL-capped NPs, the analysis of XANES spectra, supported by detailed ab-initio calculations, demonstrates that the modification of the surface of ZnO NPs through capping with organic molecules enables the development of a well-defined W-ZnS shell at the region where the capping molecules bond the ZnO NPs. At this interface between both regions the interatomic distances should adapt to the new environment, what means that the Zn-O bond lengths enlarge up to resemble those of W-ZnS.

4.4 Conclusions 95

These results suggest that the observed HTFM response arises at this interface, whose structural details would determine the particular magnetic properties of each system. Indeed, the fact that all of the samples show similar FML magnetic properties (see SQUID magnetometry measures presented in Chap. 2) despite the different surface-to-bulk ratios suggests that ferromagnetism originates at this interface and not at the bulk-like components of the NPs. It also indicates that the occurrence of FML would not critically depend on the NP's crystalline size or on the length of the organic molecule (butanethiol, octanethiol, and dodecanethiol) but on the formation of a pristine ZnS/ZnO interface.

In addition, we have performed an XAS study of $Zn_{0.95}Mn_{0.05}O$ thin films prepared with different sputtering gases and presenting HTFM behaviour. The experimental data have been compared to ab-initio XANES computations performed at both the Zn and Mn K-edges within the multiple-scattering framework.

In the case of ZnO thin films doped with 5 at.% Mn, our results indicate that Mn substitutes Zn in the wurtzite structure. However, contrary to previous claims, the results of these computations indicate that by assuming a reliable defect concentration randomly distributed the presence of both oxygen and zinc vacancies is not detectable in the XANES spectra. On the contrary the theoretical computations presented here point out that Mn adapts its local environment by increasing the Mn-O interatomic distance with the nearest-neighbour oxygen atoms. This modification is slightly different for the $Zn_{0.95}Mn_{0.05}O$ thin films prepared with different sputtering gases, which suggests that the different magnetic behaviour observed for the different samples is related to the different local structure of Mn in the films.

References

- 1. C. Bouldin, G. Bunker, D. McKeown, R. Forman, J. Ritter, Phys. Rev. B 38, 10816 (1988)
- 2. A. Bianconi, M. Dell'Ariccia, P. Durham, J. Pendry, Phys. Rev. B 26, 6502 (1982)
- 3. S. Díaz-Moreno, A. Muñoz-Páez, J. Chaboy, J. Phys. Chem. A 104, 1278 (2000)
- 4. S. Díaz-Moreno, J. Chaboy, J. Phys. Chem. B 113, 3527 (2009)
- M.A. García, J.M. Merino, E. Fernández-Pinel, A. Quesada, J. de La Venta, M.L. González, G.R. Castro, P. Crespo, J. Llopis, J.M. González-Calbet, A. Hernando, Nano Lett. 7, 1489 (2007)
- 6. F. Farges, Phys. Chem. Miner. 36, 463 (2009)
- 7. J. Chaboy, J. Synchr. Radiat. 16, 533 (2009)
- 8. M. Benfatto, S. Longa, J. Synchr. Radiat. 8, 1087 (2001)
- 9. S. Abrahams, J. Bernstein, Acta Crystallogr. B 25, 1233 (1969)
- H. Morkoc, U. Ozgur, Zinc Oxide: Fundamentals, Materials and Device Technology (Wiley-VCH Verlag GmbH & Co. KGaA, Weinheim, 2009)
- 11. C. Bates, W. White, R. Roy, Science 137, 993 (1962)
- 12. E. Kisi, M. Elcombe, Acta Crystallogr. Sect. C Cryst. Struct. Commun. 45, 1867 (1989)
- 13. R. Wyckoff, Crystal Structures (The Chemical Catalog Company Inc., New York, 1963)
- 14. J. Chaboy, S. Quartieri, Phys. Rev. B **52**, 6349(9) (1995)
- 15. C. Guglieri, E. Céspedes, C. Prieto, J. Chaboy, J. Phys.: Condens. Matter 23, 206006 (2011)
- 16. F. Decremps, F. Datchi, A. Saitta, A. Polian, S. Pascarelli, Phys. Rev. B 68, 104101 (2003)
- 17. A. Hernando, P. Crespo, M. García, Phys. Status Solidi (B) 248, 2352–2360 (2011)

- 18. A. Ayuela, P. Crespo, M. García, New J. Phys. **14**, 013064 (2012)
- 19. N. Sánchez, S. Gallego, M. Muñoz, Phys. Rev. Lett. 101, 067206 (2008)
- 20. N. Hong, J. Sakai, V. Brizé, J. Phys.: Condens. Matter 19, 036219 (2007)
- 21. J.I. Beltrán, J. Cerdá, S. Gallego, M.C. Muñoz, J. Phys. Condens. Matter 17, 451 (2005)
- 22. X. Wang, T. Leung, B. Harmon, P. Carra, Phys. Rev. B 47, 9087 (1993)
- 23. C. Patterson, Phys. Rev. B 74, 144432 (2006) 24. H. Hsu, J. Huang, Y. Huang, Y. Liao, Appl. Phys. Lett. 88, 242507 (2006)
- 25. W. Yan, Z. Sun, Q. Liu, Z. Li, Z. Pan, J. Wang, Appl. Phys. Lett. 91, 062113 (2007)
- 26. S. Zhang, L. Zhang, H. Li, J. Li, Z. Jiang, W. Chu, J. Synchr. Radiat. 17, 600 (2010)
- 27. E. Céspedes, Ferromagnetism in Wide Band Gap Materials Mn-ZnO and Mn-Si₃N₄ Thin Films, PhD Thesis, Universidad Autónoma de Madrid (2009)
- 28. E. Céspedes, G. Castro, F. Jimenez-Villacorta, A. Andrés, C. Prieto, J. Phys.: Condens. Matter **20**, 095207 (2008)
- 29. J. Pellicer-Porres, A. Segura, J.F. Sanchez-Royo, J.A. Sans, J.P. Itie, A.M. Flank, P. Lagarde, A. Polian, Appl. Phys. Lett. 89, 231904 (2006)
- 30. A. Kuzmin, S. Larcheri, F. Rocca, J. Phys.: Conf. Ser. 93, 012045 (2007)

Chapter 5 Zinc K-edge XMCD Study of ZnO-Based Magnetic Semiconductors

The magnetic characterization of the initial TOPO, AMINE and THIOL samples, obtained by standard macroscopic methods has been presented in Chap. 2. A common result to all the investigated systems is that, in addition to an overall diamagnetic behaviour at 5 K, there is a paramagnetic signal following a Curie-Weiss law, and a ferromagnetic-like contribution (FML). As detailed in Chap. 2, the FML behaviour of the magnetization is characterized by the existence of remanence, coercivity and saturation up to room temperature [1]. Moreover, the value of the coercivity field, $H_c \sim 200$ Oe, does not change with the temperature. This behaviour is in contrast with that obtained by applying the same procedure in the case of reference bulk and single-crystal ZnO samples for which the magnetization is at least one order of magnitude smaller, it shows a clear linear trend with the applied magnetic field as well as no hysteresis. In addition, the XANES study presented in the previous chapter allows us to determine the existence of a well defined interface between the ZnO core of the NP and the capping regions. The morphology and the structural details of this interface varies from one to another sample, and this phenomenology extends also to the case of the ZnO/ZnS multilayers.

The overall results obtained by using both macroscopic and XAS characterization techniques suggest that the HTFM behaviour is related to the aforesaid interface Therefore, we have extended our study by using XMCD aiming to obtain both an unambiguous proof of the intrinsic character of the observed HTFM as well as to establish a direct relationship between the magnetic behaviour and the details of this interface.

5.1 Zn K-edge and $L_{2,3}$ -edge XMCD Study of ZnO NPs Capped with Different Organic Molecules

Figure 5.1 reports the XAS and XMCD spectra recorded at the Zn $L_{2,3}$ -edges of the AMINE sample (series-1). No XMCD signal could be observed in the measured energy region, down to the noise level, in agreement with previous works [2, 4][14].

Fig. 5.1 XAS (black) and XMCD (red) Zn L_{2,3}-edges spectra for ZnO nanoparticles capped with AMINE recorded at T=10 K and with an applied magnetic field of 5 T

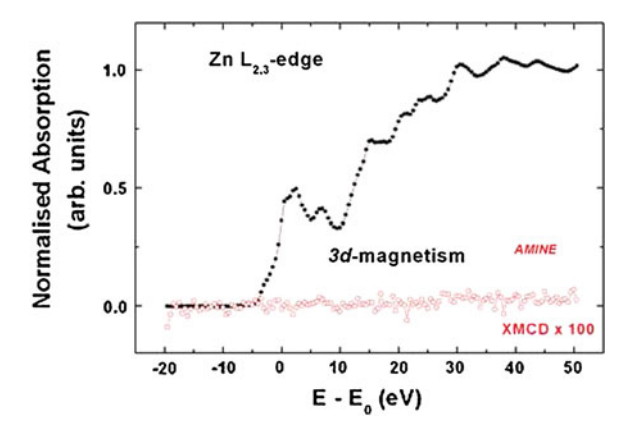
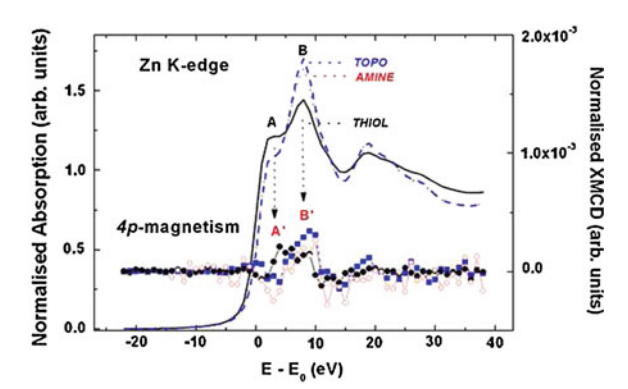


Fig. 5.2 Zn K-edge XAS (*lines*) ad XMCD spectra (*symbols*) recorded at T=4.2 K and H=10 T in the case of ZnO NPs capped with AMINE (*red*, *dots*), TOPO (*blue*, *dashes*), and THIOL (*black*, *solid line*)

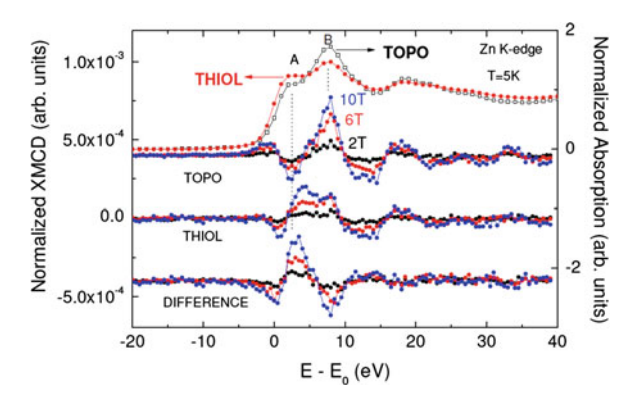


These results proved that the 3d electronic shell of Zn does not carry any measurable ferromagnetic moment ($\geq 0.005~\mu_B$) and that the presence of defects, vacancies or charge–transfer effects does not lead to a partially unfilled magnetically polarized 3d shell.

In contrast, a clear XMCD signal is found at the Zn K-edge (Fig. 5.2), which indicates that the Zn 4p states are magnetically polarized. It should be noted in this respect that if the polarization of the Zn p states is due to the existence of a 3d Zn magnetic moment, the XMCD effect at the Zn $L_{2,3}$ -edges would be well above the detection limit [5]. The intensity of the XMCD at the K-edge of transition metals is typically more than two orders of magnitude smaller than at the $L_{2,3}$ -edges [6, 7] and thus, the expected magnitude of the XMCD at the $L_{2,3}$ -edges should be greater than 10^{-2} , that is, within the present sensitivity limit at third generation sources.

This result evidences, on the one hand, the intrinsic nature of the magnetism of Zn atoms in these capped ZnO NPs. Moreover, as the X-ray absorption at the Zn K-edge probes the empty p states of Zn (actually 4sp due to hybridization) [8] this result also indicates that the magnetic polarization of the Zn atoms takes place at the sp conduction band. Therefore, the absence of XMCD signal at the

Fig. 5.3 Comparison of the XMCD recorded at different magnetic fields on TOPO and THIOL samples as well as their difference



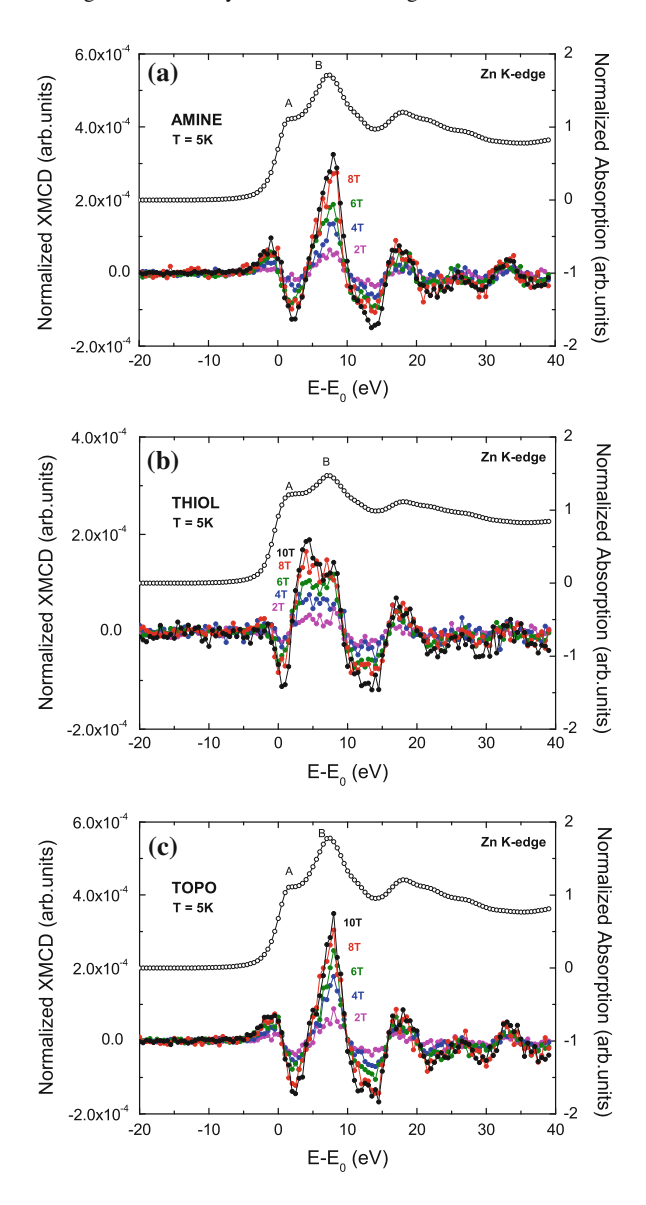
 $Zn L_{2,3}$ -edges cannot be identified with the absence of Zn magnetization, but only of 3d Zn magnetic moments. Indeed, if the observed magnetism is associated with the creation of oxygen 2p holes, the sp band of Zn should be also concerned due to the hybridization of both orbitals in ZnO. Hence, the Zn K-edge XMCD should directly reflect, in agreement with our findings, the magnetic polarization of these electronic states.

A more detailed inspection of Fig. 5.2 reveals important differences in the XMCD signals recorded for ZnO NPs capped with different organic molecules that mimic the differences in the XANES spectra. The spectral shape of the XMCD signals of TOPO and AMINE shows a narrow positive peak (B') in correspondence to the maximum of the XAS absorption (B). In contrast, this main peak broadens in the case of THIOL, appearing to be composed of two superimposed single peaks (A', B'). Each of these contributions occurs close to the energy at which the main peaks (A, B) of the XAS spectra appear. As discussed in the precedent chapter, the enhancement of peak A in THIOL with respect to TOPO or AMINE is due to the ZnS-like phase formed through the capping of ZnO with dodecanethiol [9]. These results suggest that the observed XMCD signals are due to the magnetic polarization of the conduction band of Zn in both ZnS and ZnO components.

This is verified by performing the subtraction of the dichroic signals of both THIOL and TOPO samples recorded at the same experimental conditions. As shown in Fig. 5.3, the XMCD spectrum of THIOL after subtracting the TOPO one is similar to that of both TOPO and AMINE, but shifted to lower energies, which confirms the presence of two different magnetic contributions in the THIOL samples. Since the low-energy XMCD component of THIOL is not present in TOPO and AMINE, we can conclude that this contribution stems from the Zn atoms forming the ZnS shell, whose existence has been pointed out in the previous chapter.

Next step in our study has been to determine the dependence of the Zn K-edge XMCD signals with the applied magnetic field. In particular we investigate if the XMCD versus H curve shows saturation effects as expected for a ferromagnetic behaviour. The dependence of the Zn K-edge XMCD signals as a function of the

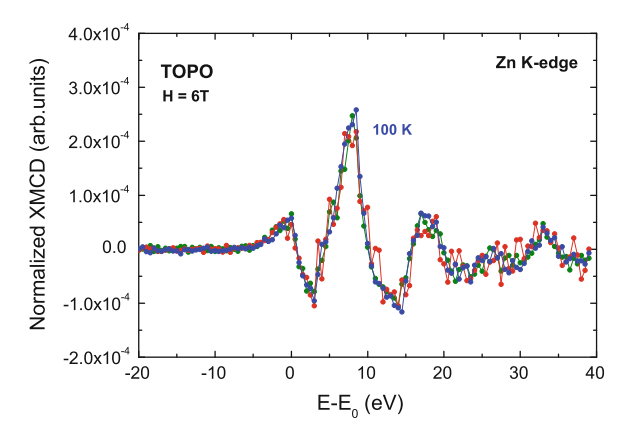
Fig. 5.4 Comparison of the normalized Zn K-edge XMCD spectra recorded as function of the applied magnetic field at T = 5 K in the case of capped ZnO NPs: AMINE, TOPO and THIOL. In all the cases the normalized Zn K-edge XANES spectra are also shown for the sake of clarity



external magnetic field, XMCD(H), for the sample of batch 1 (AMINE, TOPO and THIOL) is shown in Fig. 5.4.

In all the cases the intensity of the XMCD signal increases as the applied magnetic field does and no modification of its spectral profile is observed. Despite this common phenomenology a more detailed inspection of the XMCD(H) dependence shows important differences as a function of the organic molecule used for the capping of the ZnO NPs. For AMINE, the XMCD signals seem to increase proportionally to

Fig. 5.5 Normalized Zn K-edge XMCD spectra of TOPO recorded in a magnetic field H = 6T as a function of temperature (T = 5, 100 and 300 K)



the magnetic field, while for the TOPO sample that linearity is not so marked. In the case of THIOL, peaks A and B present different trends: apparently, the intensity of feature B saturates for values of $H \ge 4$ T, whereas peak A, associated to the ZnS-like phase, presents a linear dependence on H.

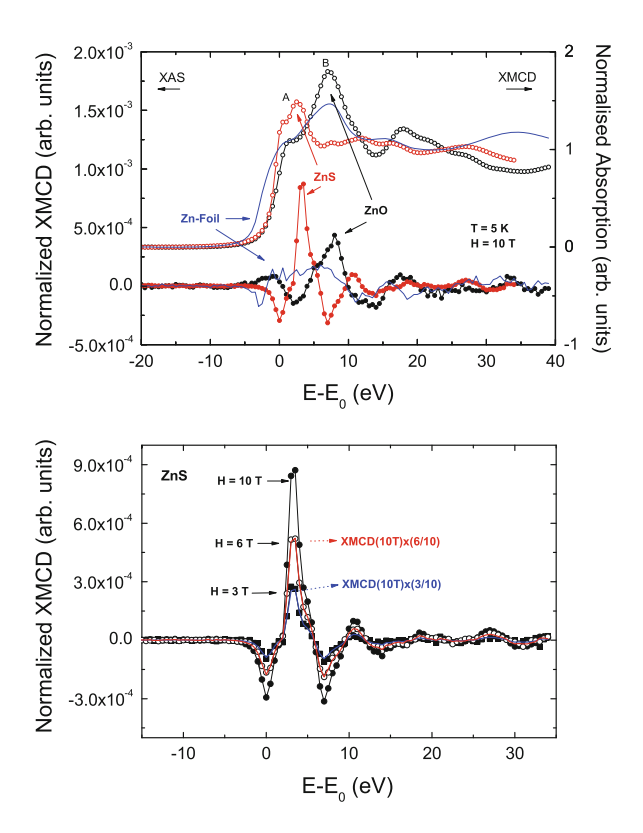
It worth to say that having no 3d localized moment in the materials, the observed XMCD signals can be due to Pauli-paramagnetism (PP), induced by the action of the external magnetic field, or to the existence of an intrinsic magnetic polarization of these Zn electronic states. The possibility of the occurrence of a Curie-Weiss-like paramagnetic contribution is excluded according to the temperature dependence of the XMCD signals [10]. A representative example of the XMCD(T) dependence is shown in Fig. 5.5. As shown in this figure no significant variation of the intensity of the main XMCD spectral feature is observed, within the signal to noise ratio, among the spectra recorded at fixed temperatures varying for $T=5\,\mathrm{K}$ and ambient.

In the case of Pauli-paramagnetism a linear dependence of the XMCD with the applied field, XMCD(H), is expected for the studied range of magnetic fields. The linear XMCD(H) dependence has been verified in the case of bulk ZnS, i.e. a reference system showing no trace of HTFM. This is shown in Fig. 5.6, where the experimental XMCD(H) signals have been compared to those obtained by the scaling of the XMCD spectra recorded at H = 10 T, i.e. $\text{XMCD}_{calc}(H) = \frac{1}{H} \times \text{XMCD}_{exp}(10 \text{ T})$. As shown in Fig. 5.6 the amplitude of the experimental signals perfectly scale with 1/H and no difference in the spectral shape is observed.

In contrast, the dependence on the applied field of the XMCD spectra recorded in the capped ZnO NPs (see Fig. 5.7) shows a different trend. While the XMCD vs H dependence is linear, within the signal to noise ratio, for AMINE, it clearly deviates from this trend in the case of TOPO for H ≥ 4 T. The behaviour of THIOL is more complex: the low energy XMCD peak, associated to the ZnS component, shows a linear trend, whereas the XMCD(H) of the high-energy peak, associated to ZnO, clearly departs from linearity.

The same behaviour is found by considering the integral of the XMCD signals instead of the peaks intensities. This is illustrated in panel d) of Fig. 5.7, where

Fig. 5.6 Top Comparison of the normalized Zn K-edge XAS and XMCD spectra of bulk reference samples ZnS, ZnO and metallic Zn recorded at H = 10T and T= 5 K. *Middle* Comparison of the normalized Zn K-edge XMCD spectra of ZnS recorded at different applied magnetic fields and those derived from the XMCD signal recorded at H = 10 Tby assuming a linear dependence with the applied field. (See text for details)



the integral of the XMCD spectra, performed in the -5.5 to 20.5 eV energy range are plotted versus the applied field. The integrated XMCD(H)/H is approximately constant for AMINE, as expected for a linear dependence, while it decreases as H increases for both TOPO and THIOL, as expected for a saturated regime.

All these results are an unambiguous proof of the existence of an intrinsic ferromagnetic-like behaviour in these capped ZnO NPs. The fact that this saturated signal is overimposed to a paramagnetic one suggests that the magnetic response is not the same for all the Zn atoms in the material. It should be noted in this respect that Zn K-edge X-ray absorption measurements, both XAS and XMCD, probe all the Zn atoms in the material, i.e. both at the core and at the surface of the NPs. The fact that the paramagnetic contribution to the XMCD signal dominates over the ferromagnetic one suggests that the later is confined near the surface and/or at the interface formed between the ZnO NPs and the capping molecule.

The existence of two different phases containing Zn has large implications in the normalization of the XMCD signals. This is clearly exemplified in the case of THIOL sample. Previously, it was seen that in the case of the ZnO NPs capped with dodecanethiol both W-ZnS and W-ZnO are present with a relative weight of about 50 %. As discussed above, each of the two main peaks of the XMCD signal of THIOL

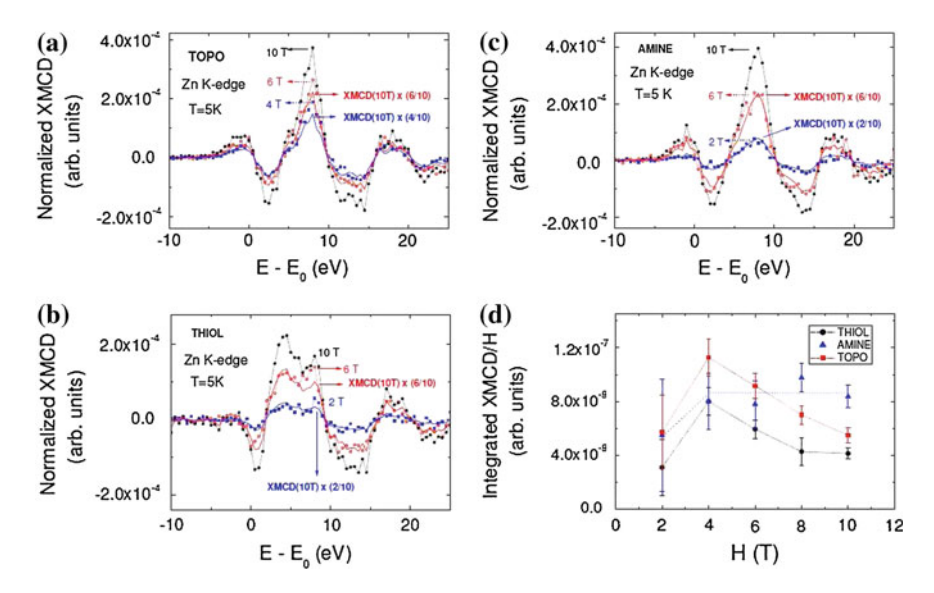


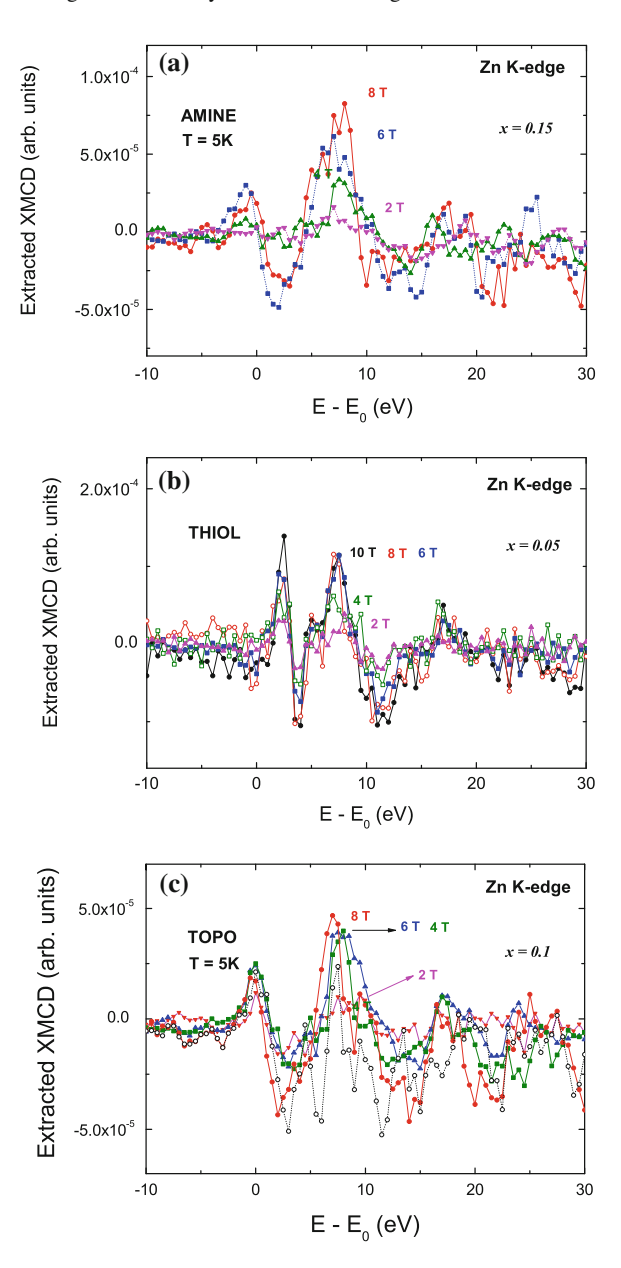
Fig. 5.7 Comparison of the normalized Zn K-edge XMCD spectra of AMINE, TOPO and THIOL recorded at different applied magnetic fields and those derived from the XMCD signal recorded at $H = 10 \, \text{T}$ by assuming a linear dependence with the applied field. The dependence on the applied field of the integrated signals is shown in panel (d)

(see Fig. 5.4) corresponds to the ZnS and ZnO phases of the capped NPs. Because both the XANES and the XMCD spectra are normalized to the absorption jump, i.e. to the total amount of Zn atoms in the sample and not only to those present in each phase, the intensity of the XMCD peaks is artificially reduced by the normalization procedure. Indeed, if one takes into account that approximately only one half of the total Zn atoms contributes to each peak, the overall XMCD signal should be enhanced by a factor two, which renders the amplitude of the ZnO contribution to the XMCD in THIOL of similar magnitude as for both TOPO and AMINE samples.

Similar reasoning should be applied to the normalization of the contribution to the XMCD coming from the Zn atoms at both the core and the interface of the nanoparticles. Accordingly, the total XMCD signal should correspond to the addition: $\text{XMCD}_{Tot} = (1-x) \times \text{XMCD}_{bulk} + x \times \text{XMCD}_{inter}$, where x is the percent of the interface with respect to the total volume of the NP (in the case of THIOL XMCD_{bulk} stands for the bulk contribution of both wurzite-like ZnS and ZnO regions). Estimates of the amount of Zn atoms at this interface have been derived in the precedent chapter from the ratio of the white line intensity with respect to that of bulk ZnO. In this way we obtain that the amount of Zn atoms at the interface is about 15, 10 and 5% for AMINE, TOPO and THIOL respectively.

Now, by assuming that the contribution of the Zn atoms in the ZnO core to the XMCD is the same as for bulk ZnO, we can extract the XMCD corresponding to the interface by subtracting from the total XMCD signal the ZnO contribution according

Fig. 5.8 Comparison of the extracted Zn K-edge XMCD(H) of AMINE (top panel), TOPO (middle) and THIOL (bottom) capped ZnO NPs after subtracting the contribution of the Zn atoms at the core



to its relative weight. The result of this procedure in shown in Fig. 5.8. In all the cases the obtained signals show similar spectral shape. This is of special significance in the case of THIOL in which two core-like signals, corresponding to the observed ZnS and ZnO contributions, have been subtracted from the total XMCD. As shown in Fig. 5.8 the extracted XMCD signal of TOPO is clearly saturated for $H\geqslant 4\,T.$ In the

case of THIOL, the extracted XMCD is saturated in the region corresponding to the Zn-O bonds while it shows a linear dependence with the applied magnetic field in the Zn-S bonds region. The case of AMINE is unclear as the lower signal to noise ratio prevents assuring that there is a real saturation effect for magnetic fields higher than H=6 T. Moreover, taking into account that the size of the NPs is ~ 20 nm, if the the FML XMCD signal stems from ~ 5 to 15% of the total amount of Zn atoms of the material, it is possible to estimate that the FML behaviour arises in a 3-8 Å region. The extent of this region is in agreement with the result of the ab-initio computations, suggesting that the FML saturated signal stems from the Zn atoms at the interface formed between the ZnO core of the NP and the organic molecule.

5.2 Zn K-edge XMCD Study of ZnO NPs Capped with Thiol Derivatives and ZnS/ZnO Thin Films

In the precedent section we have shown that XMCD measurements performed on ZnO NPs capped with different organic molecules and without any 3d doping evidence the existence of an intrinsic FML contribution. Moreover, they suggest that it stems from the interface formed between the ZnO core of the nanoparticle and the capping region created by bonding to the organic molecules.

Aimed to verify these results we have extended our XMCD study to the new series of ZnO NPs and to the ZnO/ZnS thin films. Within the different batches of NPs we have chosen for this study those of batch 2 (all of them capped with dodecanethiol). In addition, the calcinated THIOL sample, from batch 1, has been also studied. This selection is aimed to establish a relationship between the nature and order/disorder properties of the interface and the occurrence of HTFM behaviour.

The XMCD(H) signals of the calcinated THIOL sample are shown in Fig. 5.9. For the sake of comparison we have also included those of the sample prior calcination (already shown in Fig. 5.4). As discussed in the previous section the XMCD spectra of the THIOL sample show a broad peak (A', B') that we have interpreted in terms of the resulting superposition of two peaks. The lower energy peak (A') should be due to the contribution of the ZnS-like part of the sample, while peak B', at higher energies, should be due to the ZnO component. After calcination the intensity of peak A' is reinforced while that of B' decreases. The increase of the A'/B' ratio is in agreement with that of the relative ZnS/ZnO content derived from XAS data (see Table 4). It should be also noted that the comparison of the XAS and XMCD spectra with that of a Zn metal foil indicates the absence of non-bonded Zn atoms, i.e. Zn segregation upon calcination.

Regarding the XMCD(H) dependence the calcinated THIOL sample shows the expected behaviour. The field dependence of the A' intensity is linear (Fig. 5.9d), as corresponding to a Pauli-paramagnetic contribution stemming from the ZnS component in the sample. Unfortunately, its high energy tail interferes with the ZnO-like contribution which makes difficult to accurately determine the dependence of the

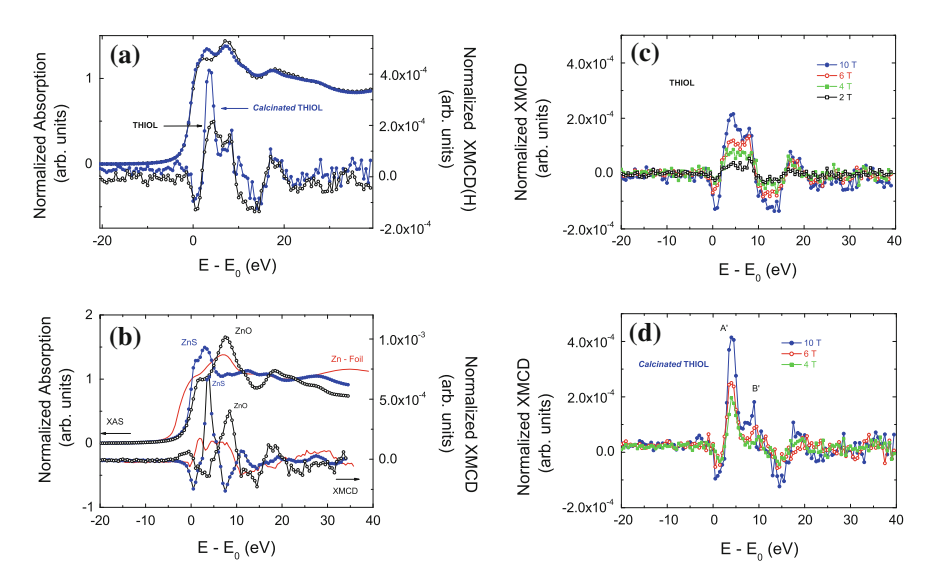
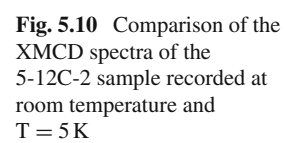
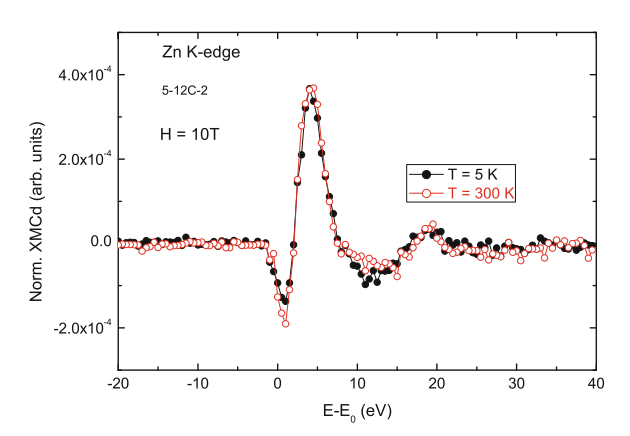


Fig. 5.9 a Comparison of the normalized Zn K-edge XAS and XMCD spectra of dodecanethiol-capped 20-12C-1 sample prior (open circles) and after the calcination process (solid circles) samples recorded at $T=5\,\mathrm{K}$ and at $H=10\,\mathrm{T}$. b Comparison of the normalized Zn K-edge XAS and XMCD spectra of bulk reference samples ZnS, ZnO and metallic Zn (red, solid line) recorded at $H=10\,\mathrm{T}$ and $T=5\,\mathrm{K}$. c Comparison of the XMCD spectra of THIOL (20-12C-1) recorded at $T=5\,\mathrm{K}$ and at different applied magnetic fields. The inset shows the variation with the applied magnetic field of the integrated XMCD corresponding to peaks A' and B' (see text for details). d Same as above in the case of the calcinated THIOL sample

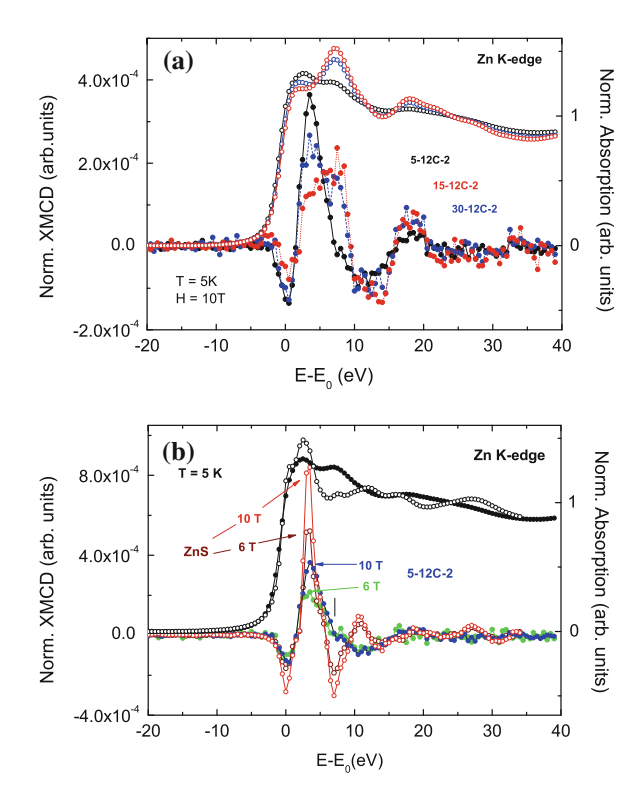




ZnO peak with the magnetic field. Nevertheless the observed evolution could be compatible with PM + FML contribution also.

The same XMCD(T) and XMCD(H) behaviour has been found for all the studied series of ZnO NPs. This is shown in Figs. 5.10 and 5.11 in the case of samples for series-2. As in the precedent cases the amplitude of the XMCD signals does not vary

Fig. 5.11 a Comparison of the normalized Zn K-edge XAS and XMCD spectra of several dodecanethiol-capped NPs in which the ZnS/ZnO ratio varied as a function of t_{add}. b Comparison of the normalized Zn K-edge XAS and XMCD spectra of bulk ZnS and 5-12C-2 sample recorded at T = 5 K and at both H = 10 T and 6 T



with temperature (see Fig. 5.10) which disregards the occurrence of Curie-Weiss paramagnetism. Moreover, the simultaneous presence of contributions associated to both W-ZnS and W-ZnO is also verified. As shown in Fig. 5.11 dodecanethiol 15-12C-2 and 30-12C-2 behave as in the THIOL case, i.e. the XMCD spectra show clearly both ZnS- and ZnO-contributions. In contrast, the 5-12C-2 sample shows a single main peak resembling that of bulk ZnS, and a only small contribution coming from the ZnO component. This smaller ZnO contribution is clearly concluded from the comparison to bulk ZnS shown in panel b of Fig. 5.11. The XMCD spectra of 5-12C-2 exhibit a positive contribution at \backsim 7 eV above the edge, where ZnS shows a negative dip whereas ZnO presents a positive peak. The modification of the XMCD intensity through the series is in full agreement with the conclusions derived from the analysis of the XAS data.

The results obtained so far bring us a new insight to the understanding of the magnetic properties of the samples and of the occurrence of HTFM behaviour. The fact that the paramagnetic contribution observed for ZnO NPs capped with dode-canethiol varies for different ZnO/ZnS ratios whereas the FML contribution remains basically the same suggests that the increase of the ZnS shell gives rise to an extra paramagnetic contribution to the total magnetization. Thus, when the ZnS component of the NPs prevails over the ZnO, the magnetization at low temperatures is dominated

by a paramagnetic contribution overimposed to the ferromagnetic one. Our results indicate that the ZnS does not contribute to the FML behaviour and, consequently, they point out the critical role played by the interface into determining the magnetic properties of the systems.

Aimed to get a deeper insight on the relationship between the magnetic and the formation of an interface on the ZnO bulk-like component of the samples we have extended the XMCD study to the case of the ZnO/ZnS thin films.

As discussed in Chap. 2 the FML contribution is maximized in the case of the $(ZnO_{4nm}/ZnS_{4nm})_{10}$ heterostructure which shows this behaviour at both $T=5\,K$ and at room temperature. The FML component is still present, although less marked, in the case of the $(ZnO_{2nm}/ZnS_{2nm})_{20}$ film, while this contribution is not observed in the sample obtained for co-sputtering whose magnetization curves approach those obtained in the ZnO single crystal reference.

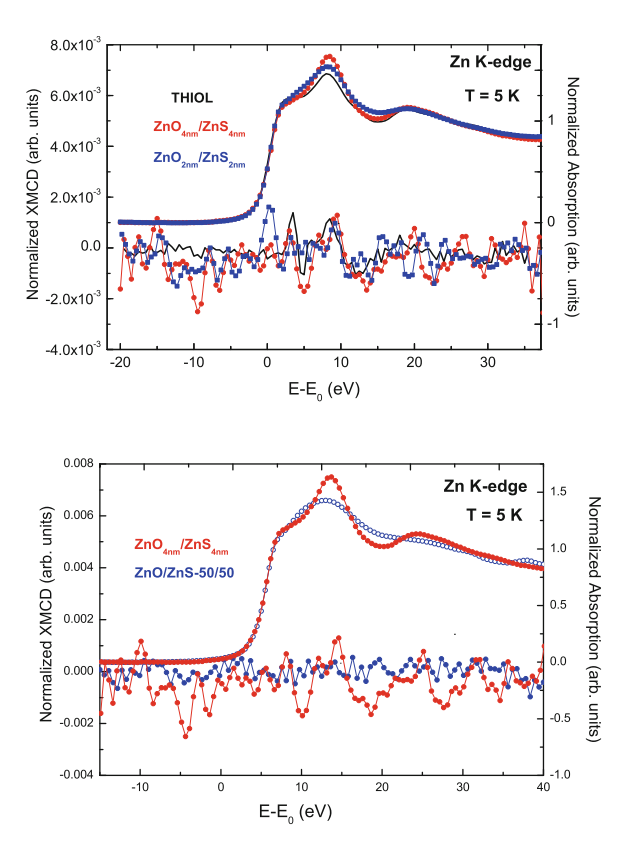
On the other hand, XRR data reveal smoother ZnO/ZnS interfaces for the $(ZnO_{4nm}/ZnS_{4nm})_{10}$ film than for the $(ZnO_{2nm}/ZnS_{2nm})_{20}$ one. For the latter sample, an average interface roughness of the order of the layer thickness, i.e., around 2 nm, was found. These results pointed towards differences in the morphology of both multilayers, with the $(ZnO_{2nm}/ZnS_{2nm})_{20}$ in the regime between continuous and non-continuous layers, leading to more disordered ZnO/ZnS interphases. In contrast with the films prepared by sequential sputtering, the XRD patterns of the Zn-O-S sample prepared by co-sputtering (ZnS/ZnO-50/50) show no peaks, both as grown and annealed samples, indicating their high degree of structural disorder. The different morphology and order/disorder properties of the interfaces in our thin films have been further verified through the XAS study reported in the precedent chapter.

The XMCD spectra recorded at the Zn K-edge in the case of both $(ZnO_{4nm}/ZnS_{4nm})_{10}$ and $(ZnO_{2nm}/ZnS_{2nm})_{20}$ heterostructures is reported in Fig. 5.12. Both signals show a well defined peak in the region associated to the ZnO contribution while just a small positive structure is observed at the position of feature A' in previous spectra. The latter may be guessed as a very weak ZnS contribution, what would agree with the increased disorder of the interface.

For the sake of comparison we have included in Fig. 5.12 the XMCD signal of THIOL after normalizing to the amount of Zn atoms contributing to the interface (see previous section for details). In contrast this normalization was not applied to the case of the thin films because XRR results indicate that the mean interface roughness is of the order of the layer thickness, i.e. 2 nm. The fact that the amplitude of the XMCD signals is similar in both cases, i.e. NPs and multilayers, yields further support to our hypothesis.

Finally, we present in Fig. 5.12 (bottom) the comparison of the XMCD spectra recorded for the thin films prepared by sequential sputtering and the highly disordered one obtained by co-sputtering. In the latter case no detectable XMCD is found, in agreement with the magnetization data, which confirms the need of pristine ZnO/ZnS interfaces to obtain the FML behaviour in these materials.

Fig. 5.12 Top Comparison of both the extracted XMCD (T = 5 K, H = 10 T) ZnK-edge of THIOL (black, solid line) after normalizing to the non-bulk phase content (see text for details) and the XMCD recorded on the $(ZnO_{2nm}/ZnS_{2nm})_{20}$ (red circles) multilayers at room temperature. For the sake of completion the XAS spectra are also shown: THIOL (black, solid line), (ZnO_{2nm}/ZnS_{2nm})₂₀ (red open circles) and (ZnO_{4nm}/ZnS_{4nm})₁₀ (blue circles). Bottom Comparison of the XMCD spectra recorded at H = 10 T on the $(ZnO_{4nm}/ZnS_{4nm})_{10}$ heterostructure (red) and the ZnS/ZnO-50/50 co-sputtered (blue) samples



5.3 Conclusions

We have performed an XMCD study of the Zn K-edge of a series of ZnO NPs capped with different organic molecules (TOPO, AMINE and THIOL) without any doping. XMCD spectra recorded at the Zn $L_{2,3}$ -edges do not show any signal down to the noise level, what confirmed that the 3d electronic shell of Zn do not carry any measurable ferromagnetic moment. On the contrary, a clear XMCD signal is found at the Zn K-edge.

These result proved the intrinsic nature of the magnetism of Zn atoms in these capped ZnO NPs, even at high temperature, and that magnetic polarization of the Zn atoms takes place at the *sp* conduction band.

The analysis of the XMCD spectra show the coexistence of both Pauli paramagnetism and intrinsic ferromagnetism in the samples. The contribution of the PP to the XMCD stems form the wurtzite-like ZnS and ZnO ordered regions of the sample while ferromagnetism originates at the interface formed between the ZnS shell and the ZnO core, that is estimated to extent over 3–8 Å depending the capping molecule. Moreover, our results demonstrate that within this interface ferromagnetism is

favoured in those regions of the interface where the local order is closer to W-ZnO than to W-ZnS.

These results were verified in the same THIOL sample after calcination and in different series of THIOL-capped NPs, produced by varying two of the synthesis parameters.

The structural modification at the surface of the ZnO NPs leads to the development of an interface in between NPs ZnO core and the shell stemming from the capping. The fact that all the samples show similar FML magnetic properties despite the different surface to bulk ratio points out that the ferromagnetic behaviour originates at this interface and not at the bulk-like components of the NPs.

The study of several ZnO/ZnS heterostructures demonstrates that increasing the disorder of this interface weakens the onset of ferromagnetic behaviour which, on the contrary, is favoured in the case of pristine ZnS-ZnO interfaces.

We can conclude that the occurrence of ferromagnetism does not critically depend on the nanoparticle crystalline size or on the length of the organic molecule but it is associated to the formation of neat, pristine ZnS-ZnO interfaces, and so the structural details of the aforesaid interface have been proved to define the magnetic properties of these systems.

References

- J. Chaboy, R. Boada, C. Piquer, M.A. Laguna-Marco, M. García-Hernández, N. Carmona, J. Llopis, M.L. Ruíz-González, J. González-Calbet, J.F. Fernández, M.A. García, Phys. Rev. B 82, 064411 (2010)
- M. Gacic, G. Jakob, C. Herbort, H. Adrian, T. Tietze, S. Brück, E. Goering, Phys. Rev. B 75, 205206 (2007)
- 3. D.J. Keavney, D.B. Buchholz, Q. Ma, R.P. Chang, Appl. Phys. Lett. 91, 012501 (2007)
- A. Barla, G. Schmerber, E. Beaurepaire, A. Dinia, H. Bieber, S. Colis, F. Scheurer, J.P. Kappler, P. Imperia, F. Nolting, F. Wilhelm, A. Rogalev, D. Müller, J. Grob, Phys. Rev. B 76, 125201 (2007)
- J. Chakhalian, J.W. Freeland, G. Srajer, J. Strempfer, G. Khaliullin, J.C. Cezar, T. Charlton, R. Dalgliesh, C. Bernhard, G. Cristiani, H.U. Habermeier, B. Keimer, Nat. Phys. 2, 244 (2006)
- J. Chaboy, L.M. García, F. Bartolomé, A. Marcelli, G. Cibin, H. Maruyama, S. Pizzini, A. Rogalev, J. Goedkoop, J. Goulon, Phys. Rev. B 57, 8424 (1998)
- 7. L. García, J. Chaboy, F. Bartolomé, J. Goedkoop, Phys. Rev. Lett. 85, 429 (2000)
- 8. G. Guo, J. Phys.: Condens. Matter **8**, 747 (1996)
- 9. C. Guglieri, J. Chaboy, J. Phys. Chem. C 114, 19629 (2010)

Chapter 6 Soft X-ray XAS and XMCD Study of ZnO-Based Magnetic Semiconductors

The results presented in the previous chapters demonstrate the intrinsic occurrence of HTFM in our ZnO-based systems, as well as the need of a well conformed interface as a prerequisite to observe the FML behaviour.

Moreover the fact that the Zn-4sp states are magnetically polarized while no net magnetic moment is found at the Zn 3d states points out that the conduction band (CB) is playing a major role in the FML development. The 4sp are hybridized with the O(2p) states at the CB [1] which suggests that the magnetism does not result from Zn(3d) orbitals but from the O(2p) orbitals. Indeed, a robust oxygen ferromagnetic state has been predicted even in the absence of magnetic atoms [2].

Consequently, the question remaining is to obtain a clear experimental evidence of this HTFM behaviour at the oxygen sites. The study of ZnO-based systems at O K-edge by means of XAS and XMCD has not been quite widespread. To our knowledge, no XMCD signal has been found at the oxygen K-edge in these systems [3, 4]. Indeed, most of the works performed to date analyse their XAS data in terms of the presence/absence of oxygen vacancies instead of the change in bond lengths here proposed as one of the main players in the occurrence of this magnetic behaviour and its relationship with the HTFM [3–6].

Here, we present the results of XAS and XMCD measurements performed at the O K-edge in some of the samples previously studied at the Zn K-edge: AMINE, THIOL and in a $(\text{ZnO}_{4\text{nm}}/\text{ZnS}_{4\text{nm}})_{10}$ (+ZnO 4nm) heterostructure. Moreover, in order to complete this study, XAS and XMCD spectra were also recorded at the S L-edge for the last samples, and at the K-edge for the thiol-capped 20-8C-4, 50-4C-4, 50-12C-4, 50-12C-2 and 30-12C-2 NPs. The study at the S L-edge results inconclusive due to the low quality of the acquired spectra and so it is presented in Fig. 6.6.

6.1 O K-edge Study of ZnO-Based Materials

The O K-edge XAS spectra recorded on the three measured samples are shown in Fig. 6.1. In the case of the AMINE sample, the absorption spectrum (recorded at $T=10\,\mathrm{K}$) is characterized by a broad, asymmetric spectral feature whose maximum lies at $\sim 536.8\,\mathrm{eV}$. This spectral shape is similar to that of bulk W-ZnO reported in literature [6–8] although, interestingly, the main absorption peak (peak D in Fig. 6.1) is sharper than in the ZnO case.

The broad spectral features between 530 and 537 eV are assigned to the transition of O(1s) electrons to the hybridized orbitals of O(2p) and Zn(4s, 4p) states, while the sharp peak at around 537 eV is due to the transition of O(1s) electrons to more localized O(2p) and O(2p) and O(2p) states [7].

The O K-edge XAS does not show any features related to the O(2p) and Zn(3d) hybridized orbitals as expected for the Zn d¹⁰ configuration in ZnO. These structures appears in 3d-oxides as sharp peaks in the low energy region (labelled A in the figure) at \sim 530 eV, as illustrated in the case of Co-doped ZnO materials [8]. At the high energy region, upto 560 eV, The spectrum shows a positive resonance with a shoulder structure (E), a marked dip (F), and a positive resonance (G).

In the case of the THIOL sample the signal to noise ratio is too low. For comparison purposes the spectrum has been smoothed (black line, recorded at $T=190\,\mathrm{K}$) so most features from W-ZnO spectra can be hinted. However no further discussion about this sample can be done.

The room temperature XAS spectrum of $(ZnO_{4nm}/ZnS_{4nm})_{10}$ (+ZnO 4nm) is similar to that of AMINE, although several differences are found. First, there is an overall reduction of the intensity in the region extending from 530 to 540 eV. In addition, a new peak is observed at \sim 532.2 eV. This peak is only detected in the first scans being disappeared after 2h of exposition to the incoming beam (inset of Fig. 6.1b). The origin of this peak remains controversial. Similar feature has been reported in Cu-doped ZnO thin films, being assigned to the hybridization of O(2p) orbitals with Cu(3d) states [6], while no peak was observed by Keavney et al. in similar systems [3]. It has been also found in several Co-doped ZnO films and accounted for in terms of oxygen defect states [5] or Zn (3d)-O(2p) hybridization [8, 9]. However the fact that in some cases this peak is also present in bulk ZnO and its dependence with the detection method or beam exposure time casts doubts over these assignments suggesting, on the contrary, that is due to surface effects (see Appendix B).

The most intriguing modification of the XAS spectra occurs, however, when the $(\text{ZnO}_{4\text{nm}}/\text{ZnS}_{4\text{nm}})_{10}$ heterostructure is measured at low temperature (T = 10 K). As shown in Fig. 6.1b the spectral profile has completely changed with respect to that recorded at room temperature. The characteristic sharp peak of ZnO (D) has been nearly suppressed and, in addition, a new prominent peak (C) arises at \sim 533.3 eV.

Contrary to peak B, observed at room temperature, no modification of this spectral profile takes place upon long beam exposure time. As followed from the discussion in Appendix B, the energy position of this additional C peak cannot be addressed to contamination by sulfates [10, 11] either to the formation of ice [12, 13]. Similarly,

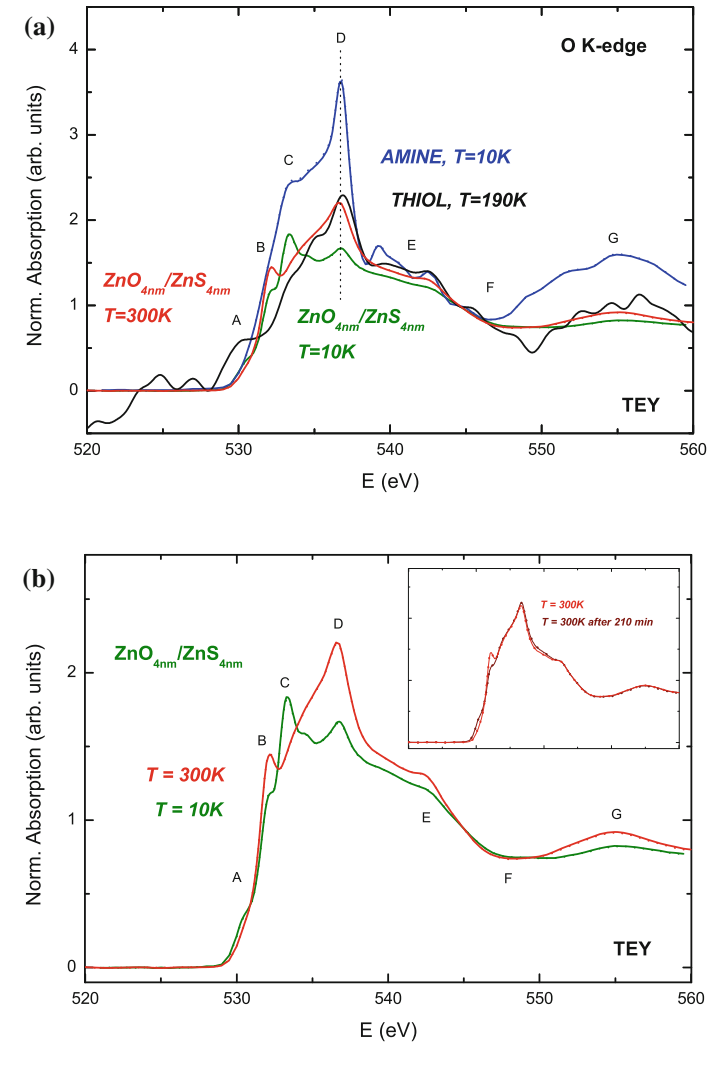


Fig. 6.1 a O K-edge XANES of ZnO_{4nm}/ZnS_{4nm} at both $T=300\,K$ and $T=10\,K$, the inside panel present the effect of measuring for 3.5 h. b Comparison of spectra at the O K-edge of ZnO_{4nm}/ZnS_{4nm} and AMINE measured at $T=10\,K$, and THIOL at $T=190\,K$

we ruled out the possibility of the new peaks being caused by preferential orientation effects [14–17]. On the contrary it renders intrinsic to the sample and most likely due to the variation of the electron escape depth in the TEY detection mode [18]. Indeed, the region of the sample probed with this detection method is limited to a depth of a few nm from the surface (\sim 4 nm) due to inelastic scattering of the secondary electrons [19]. This escape depth is similar to the nominal thickness of the outermost ZnO layer in the heterostructure and, consequently, a small variation

can imply that also the ZnO/ZnS interface is being probed. The existence of such a ZnO/ZnS has been previously evidenced by studying the Zn K-edge XANES spectra. At this interface the Zn-O and Zn-S bonding lengths depart from those of the ZnO and ZnS bulk materials. Consequently, if the TEY probes oxygen atoms from both the 4 nm (bulk-like) ZnO layer and from the ZnO/ZnS interface two different O-Zn distances should involved leading to the modification of the O K-edge spectral shape.

Aiming to verify this assignment we have performed detailed ab-initio calculations of the O K-edge XANES spectra (analogous to that at the Zn K-edge) by using the program CONTINUUM [20]. Below, the main results are presented, while the intermediate steps are displayed in Appendix C.

We built up a ZnO cluster in wurtzite structure, including the contributions from neighbouring atoms located within the first 8 Å around the photoabsorbing oxygen atom. As shown in Fig. 6.2 this calculation reproduces the characteristic ZnO spectral profile of the AMINE sample. Then, we have proceeded in a second step to evaluate the effect of the proposed Zn-O bond lengthening occurring at the ZnS/ZnO interface to account for the O K-edge XANES measured for the $(ZnO_{4nm}/ZnS_{4nm})_{10}$ at low temperature.

The O-Zn bond length in W-ZnO is 1.98 Å, while the S-Zn one in W-ZnS is 2.34 Å. Then we have considered that upon formation of the aforesaid ZnS/ZnO interface both O and S atoms adapt their interatomic distance to Zn. As a consequence the O-Zn bond should be enlarged at this interface. Therefore, computations have been firstly performed for a ZnO cluster in which the Zn-O bond length has been increased to resemble the S-Zn one in ZnS (denoted hereafter as ZnO-S d_{ZnS}). Secondly, we have also considered the substitution of oxygen atoms in the second coordination shell by sulphur ones in two different arrangements: (i) by maintaining fixed the interatomic distances as for Bulk W-ZnO and (ii) by increasing the O-Zn-S interatomic distances as in the case of W-ZnS. The results, reported in Fig. 6.2 show that in the later case the peak C, observed for $(\text{ZnO}_{4nm}/\text{ZnS}_{4nm})_{10}$ at low temperatures, is well reproduced by the calculation. This validates our interpretation of the origin of this peak in terms of the contribution from the ZnO/ZnS interface.

Recalling that XANES spectrum arises from the contribution of all oxygen atoms of the sample (at the W-ZnO like region and at the interface), the weighted addition of the computations performed for the starting W-ZnO cluster plus the modified one, in the form $(1-x) \times \text{ZnO} + x \times (\text{ZnO-S d}_{\text{ZnS}})$, shows a remarkably good agreement with the experimental spectrum, the best being obtained for $x \sim 50\%$ (see Fig. 6.2b). This validates our interpretation of the origin of this peak in terms of the contribution from the interface between the W-ZnO core NPs and ZnS shell.

The formation of such interface in the case of AMINE, involving N and O atoms, may be also inferred from the differences in the XAS profile of both AMINE and bulk ZnO. However, the expected differences in the Zn-O and Zn-N bond lengths are significantly smaller than in the case of the Zn-S one, which leads to subtle variations in the spectra (the Zn-N bond length in zinc-nitride compounds has been reported to be \backsim 1.8 Å to \backsim 1.9 Å [21]). In particular, the main difference among the spectra of bulk-ZnO and AMINE resides in the intensity of the white line (peak D), which is appreciably sharper in the former compound. Thus we have performed

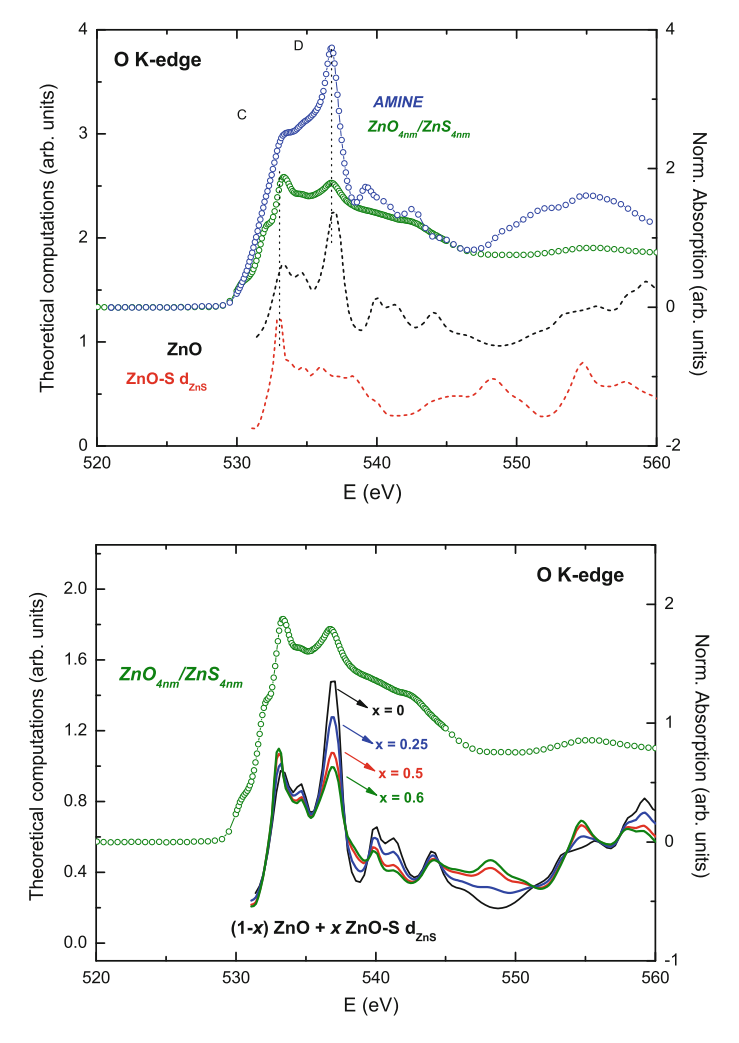


Fig. 6.2 Top Comparison of the experimental spectra of AMINE and $(ZnO_{4nm}/ZnS_{4nm})_{10}$ samples and the computation performed by using a 1% overlapping factor among the muffin-tin spheres and the Dirac-Hara exchange and correlation potential (black, dashes). The dotted line corresponds to the computation performed by substituting the oxygen atoms of the second coordination shell by sulphur ones and increasing the interatomic O-Zn-S distance as for the ZnS case (see text for details). Bottom Same comparison as above but weighting both theoretical signals

similar ab-initio calculation of the O K-edge XANES spectra as detailed above for the heterostructure. The results, summarized in Fig. 6.3, indicate that the presence of N atoms in the second coordination of the absorbing O atom, i.e. the existence of O-Zn-N bonds in the interface between the ZnO core and the capping molecule, enhances the intensity of the main absorption peak (D), in agreement with the experimental observation.

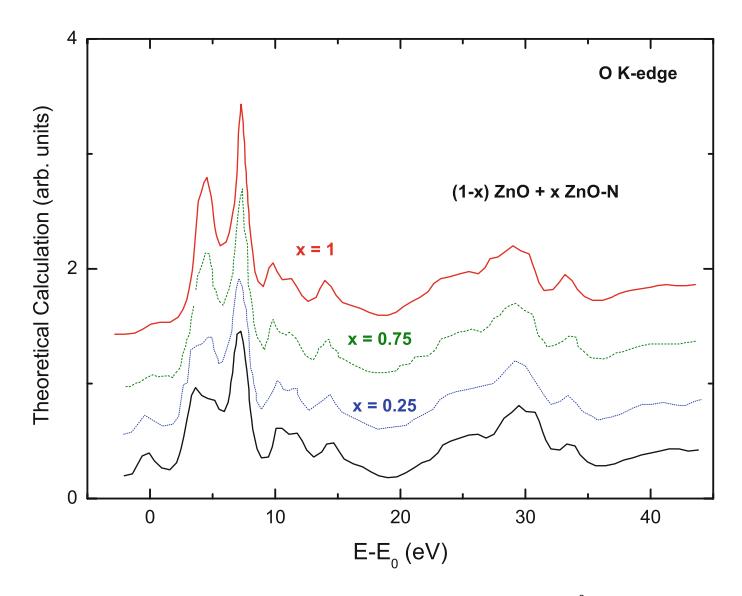


Fig. 6.3 Comparison of the theoretical spectra calculated for a ZnO 8 Å cluster (*black, solid line*) and a second ZnO one in which N substitutes O in the second coordination shell (*red*). The *dotted-dashed* correspond to different weighting of both theoretical spectra in the form (1-x)ZnO + x ZnO-N

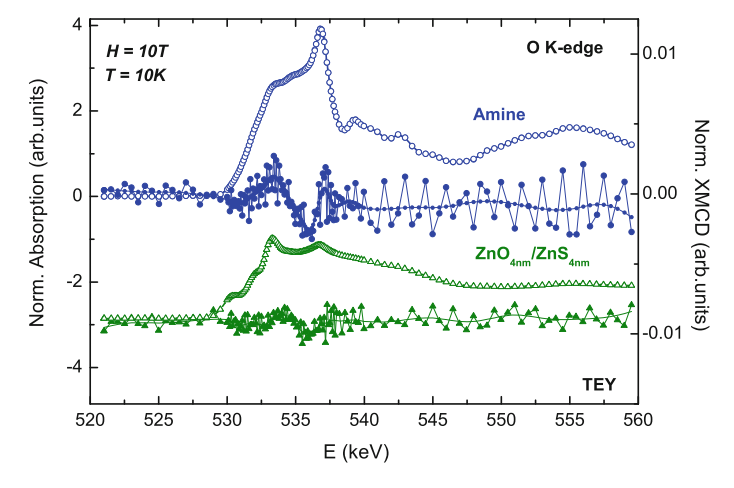


Fig. 6.4 O K-edge XANES and XMCD of AMINE and ZnO_{4nm}/ZnS_{4nm} bilayer compared

Regarding the magnetic properties, clear XMCD signals are found at the O K-edge in the case both AMINE and the ZnO_{4nm}/ZnS_{4nm} heterostructure (as shown in Fig. 6.4). The spectral shape showing two positive peaks at \sim 533.4 and \sim 537 eV and negative one at \sim 535.8 eV is similar in both cases. The existence of

XMCD at the O K-edge demonstrates the magnetic polarization of the O(2p) orbitals in these ZnO-based systems in the absence of any magnetic (3d) atom.

Indeed, the observed O K-edge XMCD clearly differs from that reported by Thakur et al. in MoO_2 thin films [22]. In this case the main XMCD features appears at lower energies, between 530 and 533 eV, as corresponding to the hybridization of the O(2p) and the partially filled 4d orbitals of Mo. The existence of this p-d hybridization in MoO_2 is clearly reflected in the XAS spectral shape contrary to our case where, as discussed above, no signature of O(2p)-Zn(3d) hybridization is found in the O K-edge XAS spectra. Hence these results give full support to the theoretical predictions of Sanchez et al. on the occurrence of oxygen ferromagnetism state in the absence of magnetic atoms [2].

Similar XMCD study was conducted at the S K and L-edges in the case of THIOL and the ZnO/ZnS heterostructures (see Figs. 6.5 and 6.6). No XMCD signal could be observed in the measured energy region, down to the noise level.

The existence of XMCD at the O K-edge indicates the magnetic polarization of the O(2p) states. However further proof studies are necessary to prove the ferromagnetic character of this magnetic polarization. To this end we have performed element specific magnetic hysteresis (ESMH) measurements. In this experiment, the energy of the photon incoming beam is fixed and the applied magnetic field is varied, which allows monitoring the dependence of the XMCD intensity with the field, $I_{XMCD(H)}$. In contrast to a standard M(H) hysteresis measurement in which the magnetic response is averaged to all the components in the material, the element-specificity of XMCD makes possible to disentangle the magnetic contribution coming from the O(2p) states exclusively [23–25].

We have recorded ESMH curves in the case of the AMINE sample fixing the energy at the point in which the XMCD intensity is maximum: 535.8 eV. In addition, we have also recorded the ESMH curves at different points of the spectrum showing no XMCD: 525, 530 and 550 eV, to be used as a reference. The subtraction of the

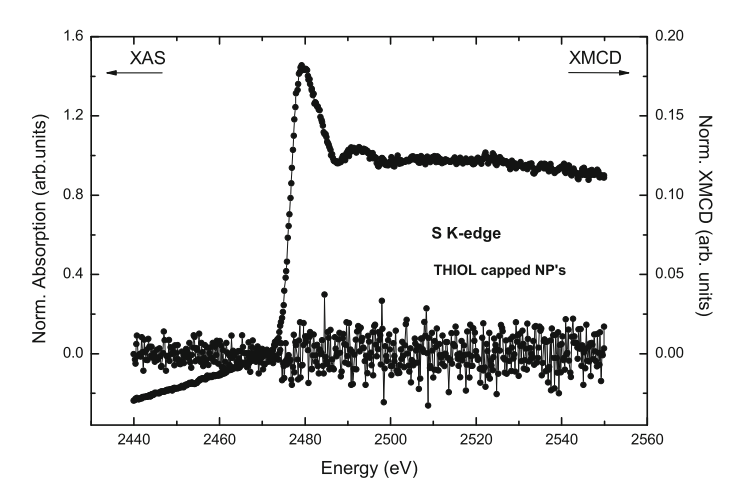


Fig. 6.5 S K-edge XANES and XMCD of ZnO NPs capped with dodecanethiol

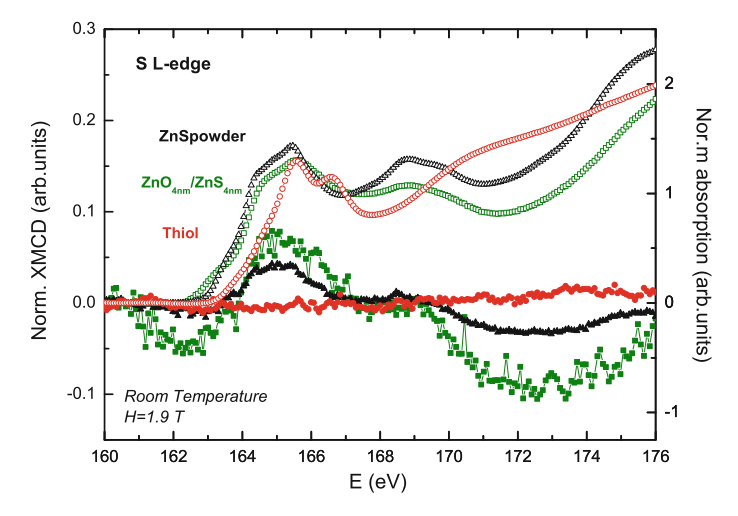


Fig. 6.6 S L-edge XANES (*empty symbols*) and XMCD (*full symbols*) of wurtzite ZnS (*black rhombus*), ZnO_{4nm}/ZnS_{4nm} bilayer (*green triangles*) and THIOL (*red circles*)

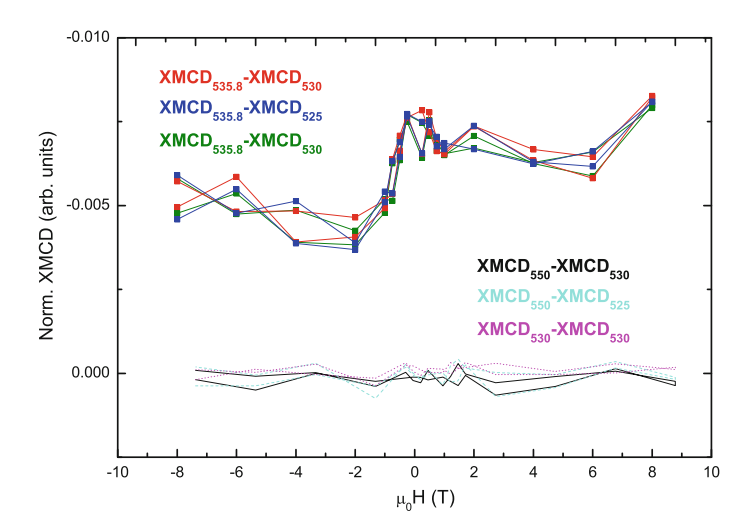


Fig. 6.7 Comparison of the signals obtained from the subtraction of the O K-edge ESMH curves recorded at $E=535.8\,\mathrm{eV}$ (highest XMCD intensity) and different reference (zero XMCD) points. The result of applying the same procedure to the curves measured at different energy reference points is also shown

ESMH signals recorded at $E = 535.8 \,\text{eV}$ and at any of these reference points cancels if present any spurious signal. The results of these measurements are reported in Fig. 6.7.

For the sake of completion we have also applied the same procedure to the ESMH curves measured at different energy reference points. The observed S-shape ESMH curves are in agreement with the occurrence of ferromagnetism arising from the

O(2p) states in these systems. Finally, it should be also noted that the ESMH curves suggest the existence of coercivity, $\sim 250 \, \text{Oe}$, that is in agreement with the results of macroscopic magnetic characterization seen in Chap. 2. Notwithstanding this, the signal to noise ratio prevent us to conclude the accuracy of this value.

In summary, the magnetic properties of ZnO NPs nanoparticles capped with dode-cylamine and a $(ZnO_{4nm}/ZnS_{4nm})_{10}$ heterostructure have been investigated by performing XAS and XMCD measurements at the O K-edges. The combined study performed by macroscopic techniques and XAS reveal the formation of neat interfaces in both systems, which show room temperature ferromagnetism in macroscopic magnetization measurements. While no appreciable XMCD were observed at the S K and L-edges, the O K-edge XMCD shows strong structures corresponding to a ferromagnetic-like magnetic polarization of the O(2p) states. All in all these results demonstrate the intrinsic occurrence of HTFM in these systems and point out that it is not related to the metallic cation (Zn) but it relays on the conduction band of the semiconductor, supporting theoretical predictions on the occurrence of oxygen ferromagnetism state in the absence of magnetic atoms.

6.2 S K-edge XAS Study of the Local Structure of Sulphur in Thiol-Capped ZnO Nanoparticles

In the previous section we have shown how the existence of a ZnS/ZnO interface is reflected in the O K-edge XAS spectra. This result is complementary to what was previously found at the Zn K-edge. The final piece of research still missing in order to complete this study should be to get a similar result by looking at the sulphur sites. Unfortunately this objective could not be fulfilled by the study of the S L-edges due to the low quality of the acquired spectra. Therefore, we have tailored an independent experiment at the S K-edge aimed to corroborate the aforesaid results.

The comparison of the XANES spectra recorded at the S K-edge on the studied samples is shown in Fig. 6.8. Spectra are characterized by a main absorption peak, consisting itself in two distinguishable peaks, A_1 and A_2 shifted by $\sim 2\,\mathrm{eV}$. A second peak, labelled as B, appears at $\sim 4\,\mathrm{eV}$ above the absorption edge, and two positive spectral resonances, D and E, lie at ~ 19 and $\sim 33\,\mathrm{eV}$ above the edge. Despite these spectral features are found in the spectra of all the investigated compounds, their relative intensities are markedly different. In the case of the W-ZnS reference, peak A_1 is clearly higher than A_2 . However this trend differs for the other samples. For example, 50-4C-4 XANES spectrum presents a feature A_2 whose intensity is higher than A_1 and shifted towards higher energy, while peak B is totally blurred. On the other hand, for 5-12C, 30-12C and 20-8C-4 it is not peak A_2 but peak B is reinforced.

This behaviour points out that the local structure around S atoms is different through the studied series of samples. This finding is in agreement with the result obtained at the Zn K-edge, which indicated the structural distortion at the developed interface. Then, we have performed several ab-initio XANES computations in order

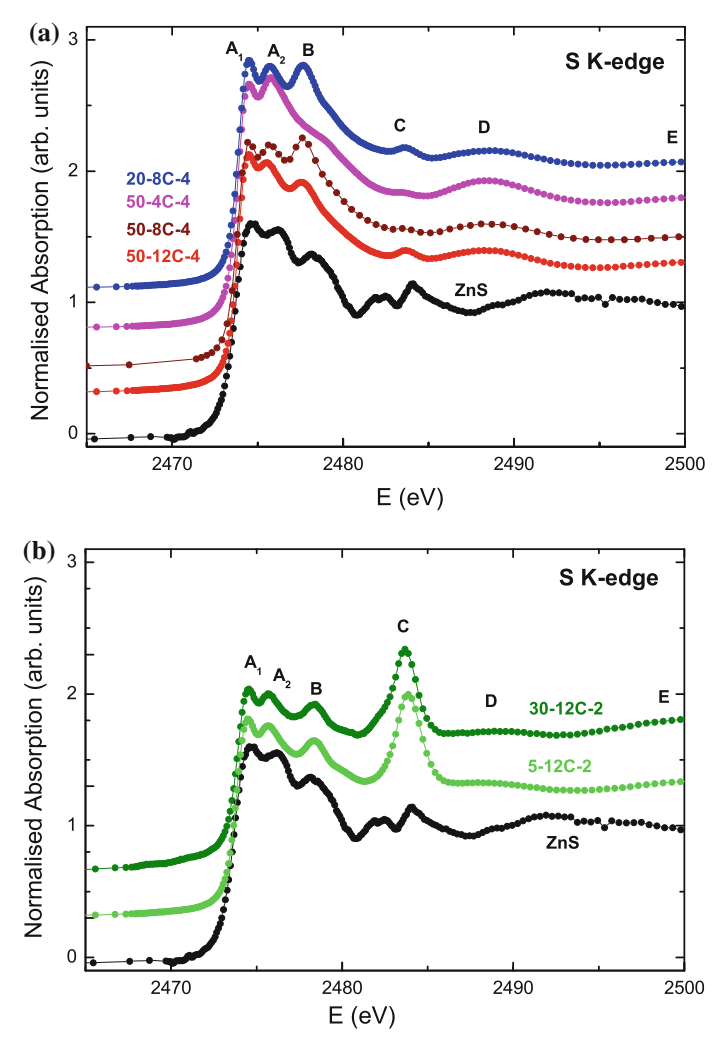


Fig. 6.8 a S K-edge spectra of the 20-8C-4, 50-4C-4, 50-12C-4 and 50-12C-4 samples compared to the W-ZnS spectrum (*black circles*). **b** S K-edge spectra of the 5-12C-2 and 30-12C-2 samples compared to the W-ZnS spectrum

to determine the origin of the different structures observed $(A_1, A_2 \text{ and } B)$ in the XANES spectra of the NPs as well as their relative variations through the series. However, prior to describe the obtained results, we would like to make a special comment on the peak labelled C, appearing in some of the samples.

This peak seems to be extrinsic to the sample. Indeed, its intensity is higher for the signals with smaller edge-jumps (0.35, 0.40, 0.36, \backsim 0.06 and \backsim 1.20 for 30-12C-2, 20-8C-4, 50-12C-4, 5-12C-2 and 50-4C-4 respectively). Moreover, it is also present in our ZnS reference, in contradiction with previous reports [26, 27].

Comparison to several sulphate S K-edge spectra [28–30] suggests that peak C is due to some sulphur contamination in the beamline, most likely SO_4 compound in formal oxidation state 6^+ [30]. Despite this inconvenience, we have taken advantage of the peak C occurrence to further verify the correct energy alignment of the recorded spectra.

The calculations were carried out again by using the multiple-scattering program CONTINUUM [20], for a wurtzite-like ZnS cluster including the contributions from neighboring atoms located within the first 8 Å around the photoabsorbing sulphur. As shown in Fig. 6.9 the use of real, both Hedin-Lundqvist and Dirac-Hara ECPs with an overlap factor of 10 % yields similar good results, although the computation performed by using the real HL leads to a better reproduction of peak A₁. Therefore all the computations reported hereafter have been obtained by using this potential.

Then, we have proceeded in a second step to evaluate the effects of the proposed Zn-S bond distortion at the ZnS/ZnO interface. We recall that the O-Zn bond length W-ZnO is 1.98 Å, while the S-Zn one in W-ZnS is 2.34 Å. We have considered that at the interface S atoms adapt their interatomic distance to Zn. Thus the computation (Fig. 6.10a) were performed for a ZnS cluster in which the Zn-S bond has been shortened to resemble the O-Zn one in ZnO (denoted hereafter as ZnS $d_{\rm ZnO}$). The result is a huge increment of peak B intensity, while those of peaks A_1 and A_2 decrease.

In addition we have also considered the effect of the different backscattering properties of both S and O atoms. To this aim we have substituted sulphur atoms in the second coordination shell by oxygen ones in two different arrangements, i.e. by (i) maintaining fixed the interatomic distances as for bulk W-ZnS (hereafter

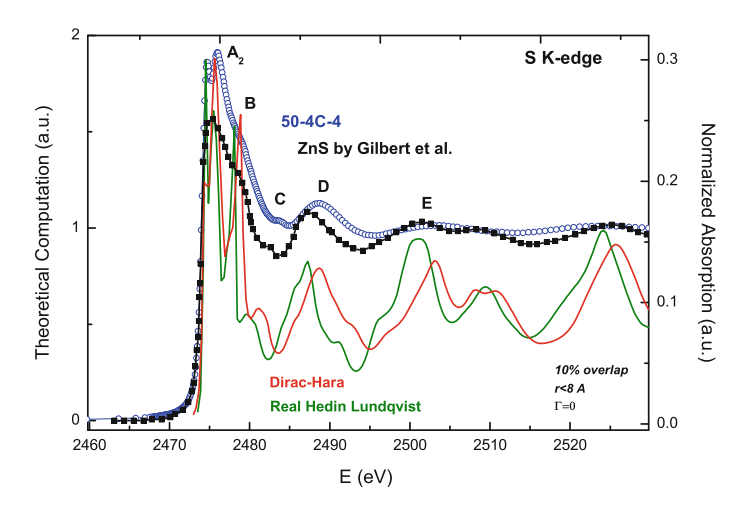


Fig. 6.9 Comparison of the experimental XANES and theoretical computations performed on a cluster of W-ZnS upto 8 Å and the spectrum of ZnS (from Ref. [26]). The calculations have been performed with different ECPs: Dirac-Hara (*red solid line*) and real Hedin-Lundqvist (*green solid line*) and a 10% overlapping factor

ZnS-O d_{ZnS}) and also by (ii) decreasing the S-Zn-O interatomic distances to those of W-ZnO (hereafter ZnS-O d_{ZnO}). In these cases, for the ZnS-O d_{ZnO} cluster, peak B rises, while for the ZnS-O d_{ZnS} cluster peak A_2 is the most reinforced (and slightly shifted to higher energies) (see Fig. 6.10b). These results allow us to conclude that peak B is related to a W-ZnO-like environment, whereas peak A_2 is enhanced when oxygen atoms are introduced in the cluster maintaining the original W-ZnS interatomic distances.

These results support the development of a ZnO/ZnS interface where interatomic distances are modified to adapt to the different configuration. In principle, such adaptation could take place in two different ways: (i) the increase of Zn-O bond length to resemble that of W-ZnS and the opposite, i.e. (ii) the decrease of Zn-S bond decrease to resemble those of W-ZnO. It renders clear that both phenomena can be simultaneous, and the final configuration strongly depends on the synthesis details of each sample. This result is in agreement with the observed variation through the series: spectra of the samples with a greater proportion of ZnS (50-4C-4, 50-8C-4 and 50-12C-4) present largest A₂/B intensity ratio, since the smaller ZnO core adapt to the predominant ZnS environment. It should be stressed that it is not strictly needed the bond length to be reduced up to that of bulk ZnO to reproduce the experimental trend. As shown in Fig. 6.10 good reproduction of the experimental data is obtained for intermediate distances.

Moreover, these results are in agreement with our earlier proposal that the structural details at the ZnS/ZnO interface vary for each sample, independently of the synthesis details. Indeed, the weighted addition of the theoretical spectra corresponding to the starting ZnS cluster and those of differently different modified clusters (recalling that XANES spectrum arises from the averaged contribution of all sulphur atoms of the sample, i.e. at the W-ZnS like region and at the interface) leads to a good reproduction of the experimental spectra. As shown in Fig. 6.11, and taking into account the lack of any convolution, the spectrum of 50-4C-4 sample is remarkably well reproduced by the average of a 40 % of the original W-ZnS cluster and 60 % of the ZnS-O dzns one. In the other cases it seems that W-ZnO interatomic distances are required, what means that some scattering paths from close ZnO-rich regions, where more likely ZnS is adapting itself to ZnO configuration, are present.

Attempting to get further confirmation of the XANES analysis conclusions, and to supplement these, we have conducted a study of the EXAFS region of the spectra (see Chap. 3 for details). The obtained EXAFS signals are presented in Fig. 6.12. The main frequency of all the spectra is similar to that of the ZnS reference, though the amplitudes are clearly reduced. This indicates that, as expected, the local arrangement of sulphur in our samples corresponds to that of W-ZnS. The comparison of the Fourier Transform (FT), reported in Fig. 6.13, also indicates a shorter local-ordering extension that in bulk ZnS. The ZnS reference displays two well differentiated peaks at 2.15 and 3.4 Å (no phase correction has been applied [31]). On the contrary, the second peak is absent or strongly smeared out in the ZnO capped NPs. It is important to stress that, contrary the XANES region, the EXAFS region of the ZnS spectrum is not concerned by the S contaminations (as seen by comparison with previous reports [32]).

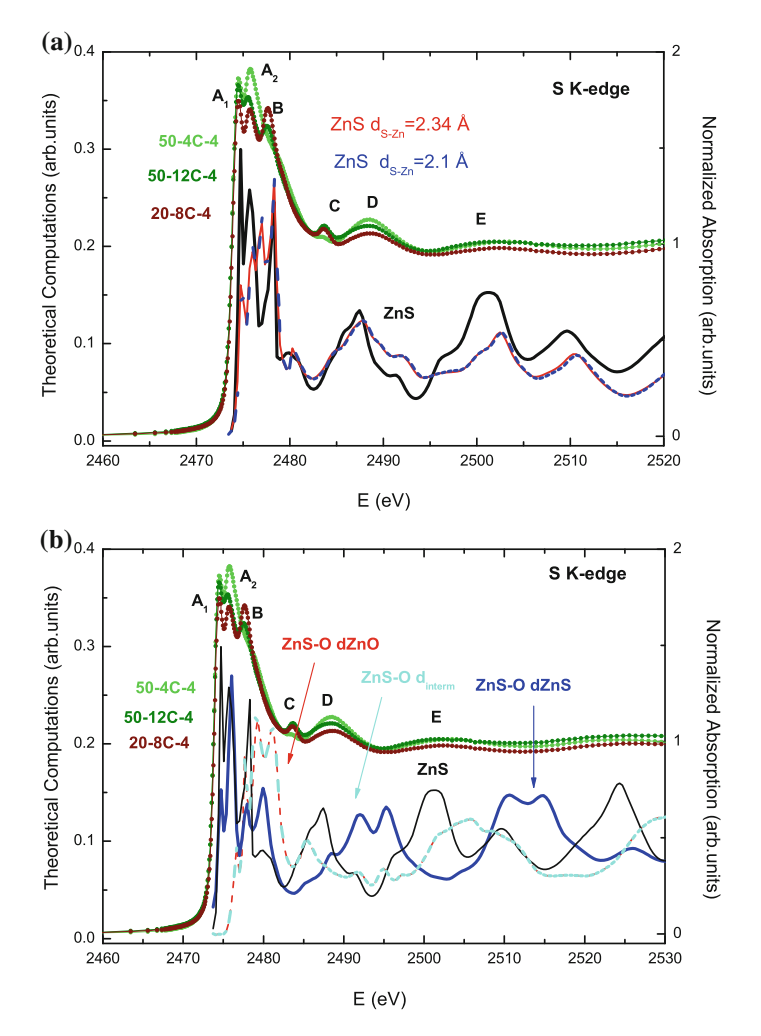
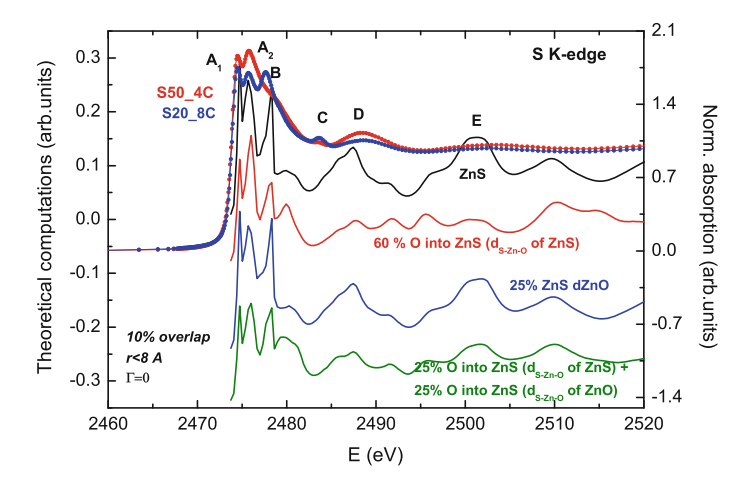


Fig. 6.10 Comparison of 50-4C-4, 50-12C-4 and 20-8C-4 spectra and the theoretical XANES computed for **a** W-ZnS and for a cluster in which the first Zn-S bond length is shortened to resemble that of W-ZnO (*red solid line*); in addition, a theoretical signal for the cluster corresponding to the intermediate configuration (*blue dashed line*); **b** W-ZnS and three different cluster in which sulphur atoms from the second coordination shell are replaced by oxygen ones. The substitution was performed in three different ways: by retaining the ZnS interatomic distances for the O-Zn-S bond (*blue solid line*), by taking those of ZnO (*red solid line*), or by assuming an intermediate bond length (see text for details) (*green dashed line*)

The quantitative analysis of the EXAFS signals has been carried out by comparing the experimental data to ab-initio calculations performed by using the FEFF code (see Chap. 3). The computations performed for W-ZnS clusters of different size are presented in Fig. 6.14. As shown, a minimum cluster size of 5.5~Å around the



 $\textbf{Fig. 6.11} \quad \text{Comparison of } 50\text{-}4\text{C-4} \text{ and } 20\text{-}8\text{C-4} \text{ spectra with theoretical calculations averaged with the original ZnS cluster}$

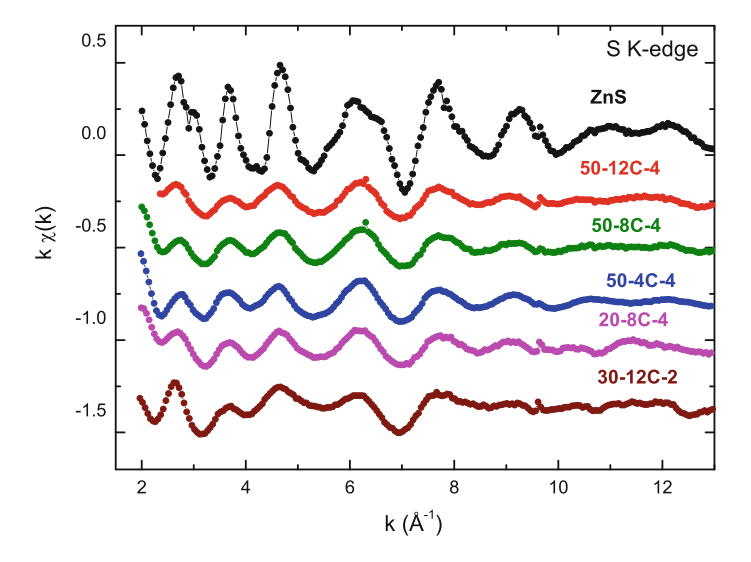
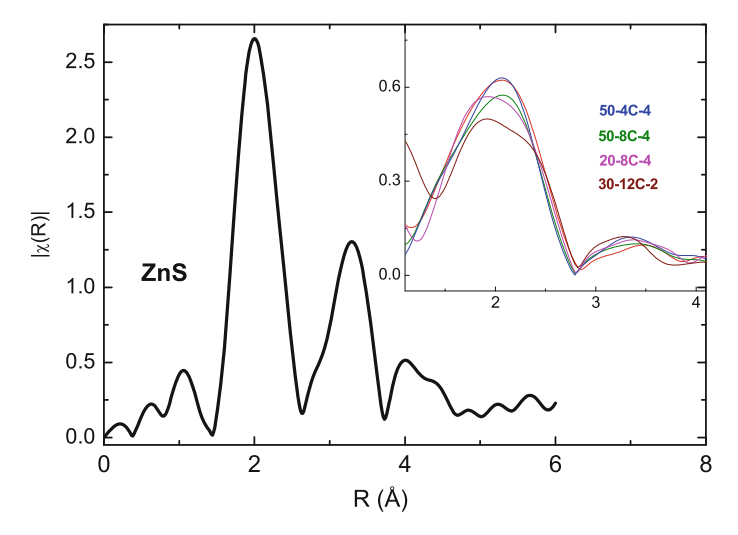


Fig. 6.12 S K-edge EXAFS spectra recorded on bulk ZnS and in different thiol-capped ZnO NPs

photoabsorbing sulphur atom (two coordination shells) is needed to reproduce the experimental spectrum. No fitting was done, so we base this assessment in the position and relative intensities of the spectral features, as well as the reproduction of the double feature of peak B.

In a second step we have proceeded to evaluate the effect of the structural modification occurring at the ZnS/ZnO interface. Owing the short-range order occurring



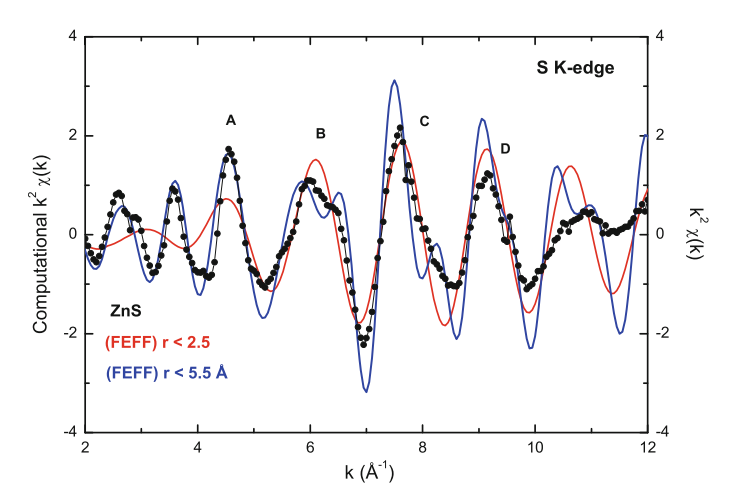


Fig. 6.14 S K-edge ZnS EXAFS (*black circles*) and theoretical FEFF calculation by using a 2.5 Å (*red solid line*) and a 5.5 Å (*blue solid line*) W-ZnS clusters

in the NPs, only the first coordination shell has been considered in the analysis. The computations included paths upto $4\,\text{Å}$ in the following way:

- 1. Computations were made for a ZnS cluster in which the Zn-S bond has been shortened to resemble the O-Zn one in bulk ZnO (hereafter as ZnS d_{ZnO}).
- 2. We considered the substitution of sulphur atoms in the second coordination shell by oxygen ones. This has been done in two different ways: (i) by keeping the

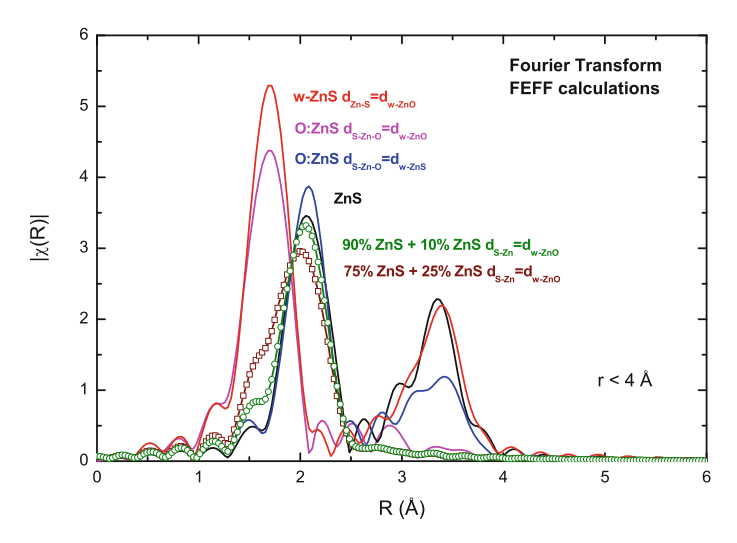


Fig. 6.15 S K-edge EXAFS theoretical signals calculated for (i) W-ZnS, (ii) W-ZnS with S-Zn bond length equal to that of W-ZnO (*red solid line*), a cluster of ZnS in which we replace S atoms by O's at the same position (*blue solid line*) and (iii) another one in which the O atoms keep a W-ZnO configuration (*pink solid line*). The weighted sum of W-ZnS cluster with the original interatomic distances and the one with shorter S-Zn bonds, being 90–10% (*green circles*) and 75–25% (*brown squares*) the tested proportions, are also shown

interatomic distances as for W-ZnS (hereafter ZnS-O d_{ZnS}) and (ii) by reducing the S-Zn-O bond lengths (hereafter ZnS-O d_{ZnO}).

When oxygen atoms are placed at the original W-ZnS arrangement the main modifications of the EXAFS signal (not shown) are the decrease of the second shoulder of peak B, and the shift of peak A. At the FT (see Fig. 6.15) those differences are just reflected in the depletion of the second peak (blue line). On the other hand, if the interatomic distances are shortened, the main FT peak is placed about 1.7 Å. In addition, the weight addition of computations for the original ZnS cluster and for the modified ZnS d_{ZnO} , in the form $(1-x) \times ZnO + x \times ZnS d_{ZnO}$, shows that, for x values ranged from a 25 to a 10 % the FT displays the same shape that for the experimental ones.

As the final step in our study, we have performed the fitting of the EXAFS signals of three different samples: 50-12C-4, 50-4C-4 and 20-8C-4. As explained in Chap. 3 the fitting of the EXAFS signals has been performed by using the experimental phases and amplitudes obtained from bulk ZnS. Two fitting strategies were adopted.

In the first case the nanoparticles were assumed to be ZnS-like, i.e. a unique S-Zn interatomic distance was considered. Initially the coordination number was fixed $(4 \times \text{Zn})$ and only the interatomic distance, r_{S-Zn} , and the Debye-Waller factor were varied (Table 6.1).

Table 6.1 Best fit parameters obtained from the analysis of the first shell contribution of the S K-edge EXAFS spectra: N coordination number; r_{S-Zn} distances S-Zn; $\Delta \sigma^2$ Debye-Waller factor relative to that of the corresponding reference sample; R reliability factor

Sample	r_{S-Zn} (Å)	N _{sphere1}	$\Delta E_0 (eV)$	$\Delta \sigma^2$	R
W-ZnS	2.34	4	_	_	_
20-8C-4	2.33 ± 0.01	4	0	0.008 ± 0.002	0.06
50-4C-4	2.34 ± 0.02	4	0	0.008 ± 0.003	0.07
50-12C-4	2.34 ± 0.01	4	0	0.009 ± 0.002	0.06

Filtering range: $2.15 \le k \le 10.25 \,\text{Å}^{-1}$; $1.25 \le R \le 2.95$. Fitting range: $1.25 \le R \le 2.95$

Table 6.2 Best fit parameters obtained from the analysis of the first shell contribution of the S K-edge EXAFS spectra: N coordination number; r_{S-Zn} distances S-Zn; $\Delta \sigma^2$ Debye-Waller factor relative to that of the corresponding reference sample: R reliability factor

Sample	r_{S-Zn} (Å)	N _{sphere1}	$\Delta E_0 (eV)$	$\Delta \sigma^2$	R
20-8C-4	2.33 ± 0.01	3.72 ± 1.79	0	0.008 ± 0.003	0.06
50-4C-4	2.34 ± 0.02	3.06 ± 1.64	0	0.005 ± 0.006	0.06
50-12C-4	2.34 ± 0.01	3.64 ± 1.45	0	0.007 ± 0.005	0.05

Filtering range: $2.15 \le k \le 10.25 \,\text{Å}^{-1}$; $1.25 \le R \le 2.95$. Fitting range: $1.25 \le R \le 2.95$

Table 6.3 Best fit parameters obtained from the analysis of the first shell contribution of the S K-edge EXAFS spectra: N coordination number; r_{S-Zn} distances S-Zn; $\Delta \sigma^2$ Debye-Waller factor relative to that of the corresponding reference sample: R reliability factor

Sample	r_{S-Zn} (Å)	N _{sphere1}	$\Delta E_0 (eV)$	$\Delta \sigma^2$	R
20-8C-4	2.33 ± 0.06	3.56 ± 2.65	-2.29 ± 7.80	0.008 ± 0.008	0.05
50-4C-4	2.34 ± 0.06	2.92 ± 2.14	-1.29 ± 8.39	0.005 ± 0.007	0.07
50-12C-4	2.34	3.62 ± 1.39	-1.26 ± 7.01	0.008 ± 0.005	0.05

Filtering range: $2.15 < k < 10.25 \text{ Å}^{-1}$; 1.25 < R < 2.95. Fitting range: 1.25 < R < 2.95

Later, also coordination number was included in the fit (Table 6.2). No reasonable agreement with the experimental spectra was obtained by using this model (even including also the ΔE_0 parameter in the fit, see Table 6.3).

Therefore we have considered the possibility of the EXAFS spectra being due to two different ZnS arrangement. The first one should correspond to that of W-ZnS, while the second one should be associated to the aforesaid ZnS/ZnO interface where the S-Zn and O-Zn bond length are though to vary with respect to those of the bulk compounds. Consequently, two different coordination spheres, i.e. interatomic distances, have been include in the fit but imposing the constraint $N_{sphere1} + N_{sphere2} = 4$. In this way the coordination numbers would indicate the relative weight of each sphere. (It should be noted that the same Debye-Waller and ΔE_0 parameters were used for both coordination spheres).

The result of the fitting are shown in Figs. 6.16 and 6.17, and the parameters are summarized in Tables 6.4 and 6.5. The second model clearly improves the agreement with the experimental data in the case of 20-8C-4 and 50-12C-4 samples. It should be noted at this point that such an improvement is expected on the basis of the increased

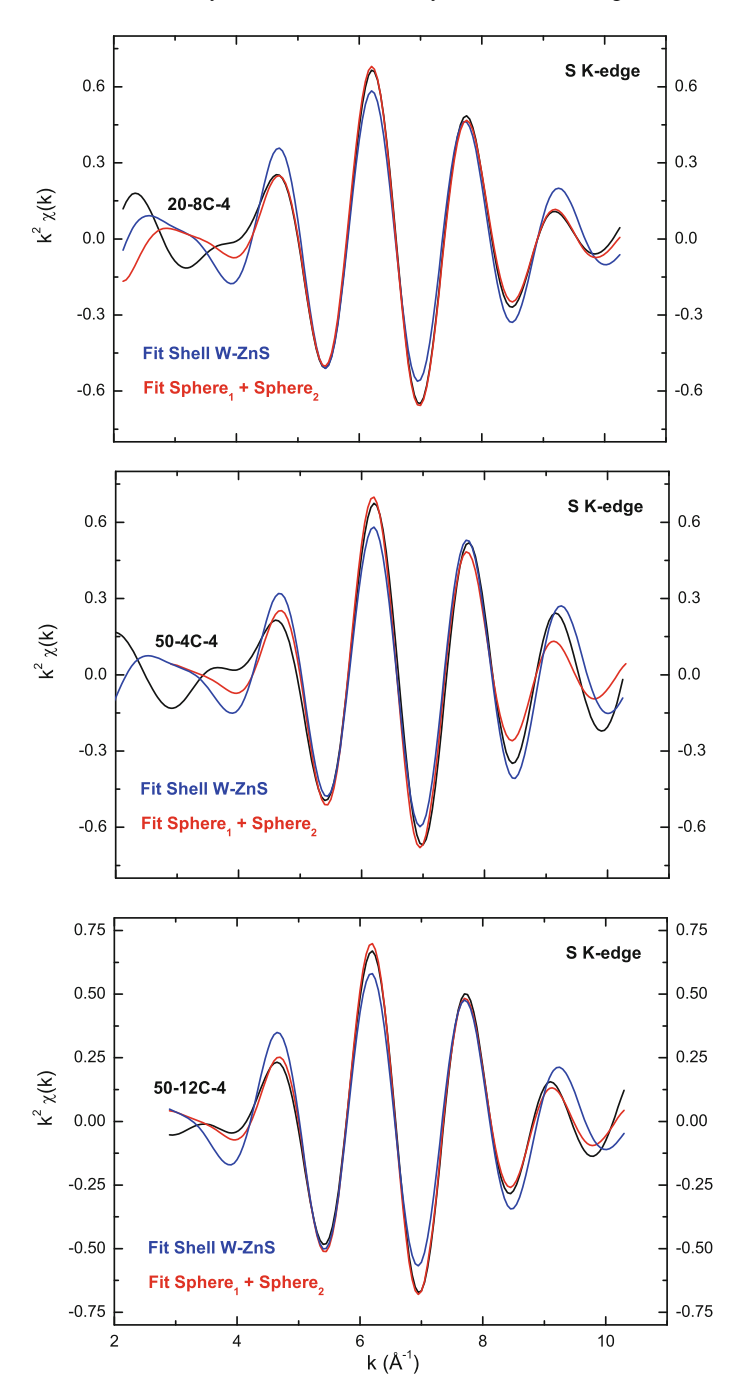


Fig. $6.16~\rm k^2$ -weighted filtered EXAFS data (20-8C-4, 50-4C-4 and 50-12C-4 samples) and best fit obtained with parameters included in Table 6.5 (see text for details)

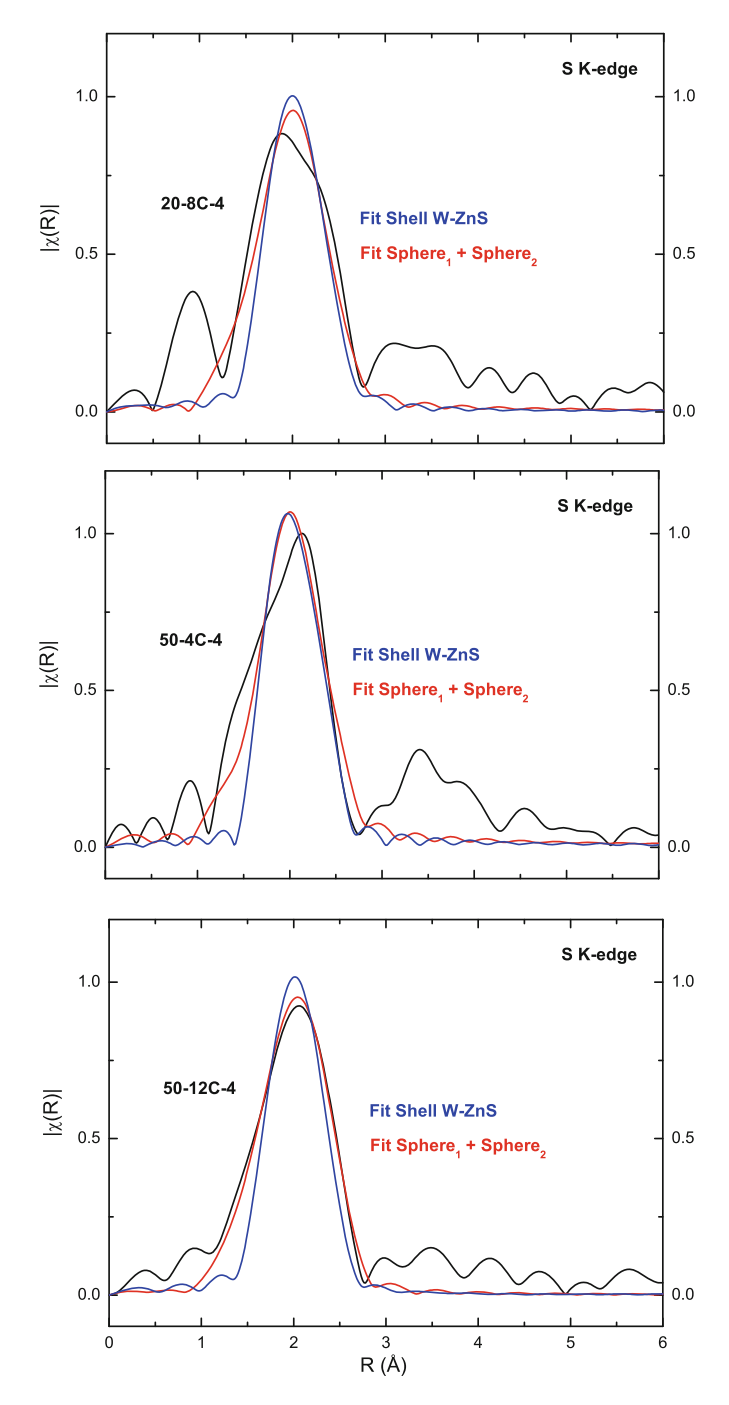


Fig. 6.17 Fourier Transforms of the EXAFS data (20-8C-4, 50-4C-4 and 50-12C-4 samples) and best fit (see text for details)

Table 6.4 Best fit parameters obtained from the analysis of the first shell contribution of the S K-edge EXAFS spectra: N coordination number; r_{S-Zn} distances S-Zn: $\Delta\sigma^2$ Debve-Waller factor relative to that of the corresponding reference sample: R reliability factor

21, 11,	2000	and taster retain	of the color of th	Sporting research	sample, is remaching) increa		
Sample	rs	$\mathbf{r}_{S-Zn}1\left(\mathbf{\mathring{A}}\right)$	N _{sphere1}	$r_{S-Zn}2(\text{\AA})$	Nsphere2	ΔE ₀ (eV)	$\Delta \sigma^2$	R
20-8C-4	2.	2.38±0.05	3.12	1.881 ± 0.032	0.88 ± 0.39	6.4±5.9	0.008 ± 0.002	9000
50-4C-4	2.	2.38±0.04	3.30	1.870 ± 0.047	0.70 ± 0.38	5.04 ± 5.68	0.007 ± 0.002	0.03
50-12C-4	2.	2.40 ± 0.02	3.093	1.892 \pm 0.015 0.91 \pm 0.19	0.91 ± 0.19	7.23 ± 2.70	0.007 ± 0.0008 0.003	0.003
Filtering ran	ge: 2.15 -	$\leq k \leq 10.25 \text{Å}^{-1}$;	Filtering range: $2.15 \le k \le 10.25 \text{Å}^{-1}$; $1.25 \le R \le 2.95$. Fitting range: $1.25 \le R \le 2.95$	itting range: 1.25 <	$R \le 2.95$			

reiai	ive to th	iat of the corre	esponding r	ererence samp	ie; K remadim	y ractor		
San	nple	$r_{S-Zn}1$ (Å)	N _{sphere1}	$r_{S-Zn}2$ (Å)	N _{sphere2}	ΔE_0	$\Delta \sigma^2$	R
						(eV)		
20-1	12C-4	2.34 ± 0.01	3.48	1.86 ± 0.05	0.52 ± 0.26	0	0.008 ± 0.001	0.01
50-4	4C-4	2.35 ± 0.02	3.47	1.85 ± 0.64	0.53 ± 0.39	0	0.007 ± 0.001	0.04
50-1	12C-4	2.35 ± 0.01	3.45	1.86 ± 0.03	0.55 ± 0.23	0	0.008 ± 0.001	0.02

Table 6.5 Best fit parameters obtained from the analysis of the first shell contribution of the S K-edge EXAFS spectra: N coordination number; r_{S-Zn} distances S-Zn; $\Delta \sigma^2$ Debye-Waller factor relative to that of the corresponding reference sample; R reliability factor

Filtering range: $2.15 \le k \le 10.25 \,\text{Å}^{-1}$; $1.25 \le R \le 2.95$. Fitting range: $1.25 \le R \le 2.95$

number of fitting parameters. However, which renders reliable the results is that the obtained interatomic distances quantitatively agree the proposed model: r_{S-Zn} of sphere₁ remains similar to that of W-ZnS, while for sphere₂ it decreases to a value close to that of r_{O-Zn} in W-ZnO.

These results are in agreement with those found in the XANES analysis, where the enhancement of peak B was addressed to the presence of shorter S-Zn bonds. That results support the aforesaid adaptation of the Zn distances to a W-ZnO-like environment at the interface. Moreover, taking the coordination number as a weight of the contribution of each sphere, the percentage of the signal arising at the interface (d_{W-ZnO}) are \sim 22% in both cases. This approximation is in line with the ab-initio calculations carried out for the study at the XANES region (see Fig. 6.11). For the latest, it was confirmed that a contribution of a 25% of the modified cluster.

In contrast, the implementation of a second sphere with W-ZnO-like interatomic distances has small impact in the fit of the 50-4C-4. Recalling its XANES spectrum does not present the feature B this result also agrees with the previous analysis.

6.3 Conclusions

The magnetic properties of THIOL and AMINE NPs and a $(ZnO_{4nm}/ZnS_{4nm})_{10}$ heterostructure have been investigated by performing XAS and XMCD measurements at the O K- and the S K-edges.

XAS spectra at the oxygen sites, supported by the corresponding ab-initio calculations, revealed the formation of neat interfaces between the W-ZnO NP core (or layer) and the organic capping (or W-ZnS layer), in agreement with the results obtained at the Zn K-edge. This enhances the initial idea of the aforesaid interface being the source of the FM. In addition, the presence of the interface could be determined at the S K-edge XANES and hinted by EXAFS spectra as well. In all cases it was seen that the structural details of the interface differ through the whole series of samples studied.

No appreciable XMCD were observed at the sulphur absorption edges, but the O K-edge XMCD shows strong structures, with identical shape and intensity for different samples. In addition, the ESMH of AMINE sample presents the step shape

characteristic of FM behaviour. Those results demonstrate the intrinsic occurrence of FM in these systems and point out that it is not related to the metallic cation (Zn) but it relays on the O(2p) states at the conduction band.

These results are in the line of theoretical studies that pointed out that, in absence of magnetic atoms, the FM behaviour of semiconducting oxides is associated to oxygen ferromagnetic states (at O-terminated surfaces [2, 33] or similarly at O atoms surrounded by Zn vacancies [34]) and hence, it is defect-mediated.

References

- 1. K. Matsunaga, F. Oba, I. Tanaka, H. Adachi, J. Electroceram. 4, 69 (1999)
- 2. N. Sánchez, S. Gallego, M. Muñoz, Phys. Rev. Lett. 101, 067206 (2008)
- 3. D.J. Keavney, D.B. Buchholz, Q. Ma, R.P. Chang, Appl. Phys. Lett. 91, 012501 (2007)
- 4. T. Tietze, M. Gacic, G. Schütz, G. Jakob, New J. Phys. 10, 055009 (2008)
- S. Krishnamurthy, C. McGuinness, L.S. Dorneles, M. Venkatesan, J.M.D. Coey, J. Appl. Phys. 99, 08M111 (2006)
- 6. P. Thakur, V. Bisogni, J. Cezar, J. Appl. Phys. 107, 103915 (2010)
- 7. J. Chen, Surf. Sci. Rep. **30**, 1 (1997)
- A.P. Singh, R. Kumar, P. Thakur, N.B. Brookes, K.H. Chae, W.K. Choi, J. Phys.: Condens. Matter 21, 85005 (2009)
- Z. Sun, W. Yan, G. Zhang, H. Oyanagi, Z. Wu, Q. Liu, W. Wu, T. Shi, Z. Pan, P. Xu, S. Wei, Phys. Rev. B 77, 245208 (2008)
- 10. N. Pangher, L. Wilde, M. Polcik, J. Haase, Surf. Sci. 372, 211 (1997)
- 11. E. Todd, D. Sherman, J. Purton, Geochim, Cosmochim, Acta 67, 2137 (2003)
- A. Nilsson, D. Nordlund, I. Waluyo, N. Huang, H. Ogasawara, S. Kaya, U. Bergmann, L.A. Naslund, H. Astram, P. Wernet, K.J. Andersson, T. Schiros, L.G.M. Pettersson, L.A. Naslund, H. Ostrom, L.G. Pettersson, J. Electron Spectrosc. Relat. Phenom. 177, 99 (2010)
- 13. S. Myneni, Y. Luo, L. Näslund, M. Cavalleri, J. Phys.: Condens. Matter 14, L213 (2002)
- J.W. Chiou, H.M. Tsai, C.W. Pao, K.P. Kumar, S.C. Ray, F.Z. Chien, W.F. Pong, M.H. Tsai, C.H. Chen, H.J. Lin, J.J. Wu, M.H. Yang, S.C. Liu, H.H. Chiang, C.W. Chen, Appl. Phys. Lett. 89, 043121 (2006)
- J.W. Chiou, J.C. Jan, H.M. Tsai, C.W. Bao, W.F. Pong, M.H. Tsai, I.H. Hong, R. Klauser, J.F. Lee, J.J. Wu, S.C. Liu, Appl. Phys. Lett. 84, 3462 (2004)
- J.W. Chiou, K.P. Kumar, J.C. Jan, H.M. Tsai, C.W. Bao, W.F. Pong, F.Z. Chien, M.H. Tsai,
 I.H. Hong, R. Klauser, J.F. Lee, J.J. Wu, S.C. Liu, Appl. Phys. Lett. 85, 3220 (2004)
- 17. J. Guo, L. Vayssieres, C. Persson, J. Phys.: Condens. Matter **14**, 6969 (2002)
- 18. E.J. Sternglass, Phys. Rev. 108, 1 (1957)
- 19. F. de Groot, A. Kotani, Core Level Spectroscopy of Solids (CRC Press, London, 2008)
- 20. C. R. Natoli, M. Benfatto, Unpublised
- 21. N. Misra, A. Dwivedi, J. Comput. Aided Metab. Mol. Des. 2, 136 (2012)
- 22. P. Thakur, J.C. Cezar, N.B. Brookes, R.J. Choudhary, R. Prakash, D.M. Phase, K.H. Chae, R. Kumar, Appl. Phys. Lett. **94**, 062501 (2009)
- 23. C. Chen, Y. Idzerda, H. Lin, G. Meigs, A. Chaiken, Phys. Rev. B 48, 642 (1993)
- 24. Y. Idzerda, H. Lin, G. Ho, G. Meigs, A. Chaiken, J. Appl. Phys. **75**, 5808 (1994)
- 25. F. Kronast, N. Friedenberger, K. Ollefs, S. Gliga, Nano Lett. 11, 1710 (2011)
- B. Gilbert, B. Frazer, H. Zhang, F. Huang, J. Banfield, D. Haskel, J. Lang, G. Srajer, G. Stasio, Phys. Rev. B 66, 245205 (2002)
- 27. D. Li, G. Bancroft, M. Kasrai, M. Fleet, X. Feng, J. Phys. Chem. Solids 55, 535 (1994)
- 28. M.O. Figueiredo, T.P.D. Silva, Eur. J. Mineral. 21, 79 (2009)

References 133

 M.J. Hackett, S.E. Smith, P.G. Paterson, H. Nichol, I.J. Pickering, G.N. George ACS Chem. Neurosci. 3, 178 (2012)

- 30. R.A. Mori, E. Paris, G. Giuli, S.G. Eeckhout, M. Kavcic, M. Zitnik, K. Bucar, L.G. Pettersson, P. Glatzel, Anal. Chem. 81, 6516 (2009)
- 31. M. Newville, Fundamentals of XAFS. Consortium for Advanced Radiation Sources (University of Chicago, Chicago, 2004)
- 32. D.R. Warburton, D. Purdie, C. Muryn, N. Prakash, Phys. Rev. B 45, 12043 (1992)
- 33. J.I. Beltrán, J. Cerdá, S. Gallego, M.C. Muñoz, J. Phys. Condens. Matter 17, 451 (2005)
- 34. Q. Wang, Q. Sun, G. Chen, Y. Kawazoe, P. Jena, Phys. Rev. B 77, 205411 (2008)

Chapter 7 Summary and Conclusions

We want to conclude with a summary of the main result obtained, as well as their relevance, in this Ph.D. Thesis.

We think that our results provide a important insight into an issue that has been controversial for more than 10 years of research. DMOs ZnO-based compounds present a ferromagnetic-like (FML) behaviour that was addressed to the 3d orbitals of the dopant atoms. When similar behaviour was found at ZnO doped with non-magnetic cations, or non-doped systems, the Zn 3d orbitals still seemed to be the most feasible source of the magnetic moment. However the mechanism that would lead to the magnetic polarization were not clear, and several phenomena, such as bound magnetic bound magnetic polarons, Zn or O vacancies and charge-transfer effect were commonly proposed. The purpose of this work was to clarify these issues.

We have performed a detailed study of ZnO NPs capped with three different organic molecules: trioctylphosphine (TOPO), dodecylamine (AMINE), and dodecanethiol (THIOL).

The NPs were characterized by conventional macroscopic techniques, among those, XRD, TEM, HRTEM, EDX, optical absorption and ac susceptibility and magnetization. XRD measurements confirmed the formation of ZnO in wurtzite structure, and the magnetometry results confirmed the occurrence of HTFM in these ZnO-based NPs obtained without any kind of doping.

Taking advantage of the element-specific information provided by XMCD measurements, it was seen that the magnetism of the NPs renders intrinsic, and it is not related to the cation 3d orbital. On the other hand a clear XMCD signal was recorded at the Zn K-edge, what means that the magnetic polarization arises at the Zn 4sp states at the conduction band (CB). Indeed, Zn K-edge XMCD versus H measurements have revealed, from the observed saturation at moderate applied fields, an intrinsic FML contribution overimposed to the main Pauli paramagnetic (PP) contribution.

Although the initial explanation for this FML involved charge-transfer effects, this assessment was based on modifications of XANES spectra, disregarding any possible structural effect, what cast doubts about that conclusion.

Thus, we have carried out an study of the structural effect on the Zn K-edge XANES spectra. The case of samples capped with dodecanethiol (THIOL) is especially significant as the XANES spectrum is highly affected by the Zn-S scattering contributions. The comparison of the experimental spectra and ab-initio computations indicates the formation of a well-defined ZnS shell at the surface of the NP in which ZnS adopts the local structure of wurtzite.

In addition, it was proved the development of an interface, in between the ZnO NP core and the ZnS shell, where the interatomic distances are distorted, in order to adapt to the different environments.

In the case of TOPO and AMINE, the fact that the white line decreases with respect to that of bulk ZnO, while the three-peaks structure (at \sim 20 eV above the edge) remains unchanged is indicative of the presence of Zn atoms forming a short-range phase overimposed to that of bulk-like ZnO.

Detailed ab-initio computations demonstrate that the differences of the experimental XANES spectra recorded for bulk ZnO and for the capped ZnO NPs can be accounted for in terms of a two-phase scheme: in addition to the expected bulk-like ZnO contribution a short-range phase, extending only to a few coordination shells, also contributes to the XANES spectra. The new phase should be located in the near surface region, i.e. at the interface between the ZnO bulk-like core of the NP and the capping molecules.

Thus, the FML contribution seems to originate at the formed interface, that is estimated to extent over 3–8 Å depending the capping molecule.

Moreover, our results demonstrate that within this interface ferromagnetism is favoured in those regions of the interface where the local order is closer to W-ZnO than to W-ZnS. Thus, the structural details of the interface (thickness, interpenetration, etc.) should determine the particular magnetic properties of each system.

In order to confirm the influence of the interface details, we have extended our study to ZnO/ZnS heterostructures, for which the surface to volume ratio is maximized. In addition, new series of NPs were synthesized by varying both, the time waited before adding the organic capping (trying to control the NPs size), and the capping itself. The samples were characterized by the same techniques. In the case of NPs, the XAS analysis shows the low synthesis reproducibility since noticeable differences are observed between nominally identical samples. This indicates the need for a careful structural analysis when studying this type of samples.

The fact that all the samples show similar FML magnetic properties despite the different surface to bulk ratio points out that FML originates at this interface and not at the bulk-like components of the NPs.

The results indicate that the occurrence of ferromagnetism does not critically depend on the nanoparticle crystalline size or on the length of the organic molecule (butanethiol, octanethiol and dodecanethiol) but on the formation of a pristine ZnS-ZnO interface. The results obtained in the case of thin films indicate that increasing the disorder of this interface weakens the onset of ferromagnetic behaviour which, on the contrary, is favoured in the case of pristine ZnS-ZnO interfaces.

These experimental findings are in agreement with the conclusion derived from most theoretical works performed to date addressing that magnetism does not result from Zn(3d) orbitals but from the O(2p) orbitals. Indeed, a robust oxygen ferromagnetic state has been predicted even in the absence of magnetic atoms. Consequently, we have tailored a series of experiments aimed to get an experimental evidence of that FML behaviour at the oxygen sites.

The magnetic properties of ZnO NPs (AMINE and THIOL) and a $(ZnO_{4nm}/ZnS_{4nm})_{10}$ heterostructure have been investigated by performing XAS and XMCD measurements at the O K-edge. In line with previous results, the XANES spectra point out the formation of an interfaces in between the ZnO core and the capping.

Moreover, a XMCD signal, corresponding the magnetic polarization of the O(2p) states, was found at the O K-edge for both samples, with similar profile despite the differences of XANES spectra. In addition, ESMH measurements in AMINE confirmed the ferromagnetic nature of the found signal. These results demonstrate that the intrinsic occurrence of HTFM is not related to the metallic cation (Zn), but it relays on the conduction band, supporting theoretical predictions on the occurrence of oxygen ferromagnetic state in the absence of magnetic atoms.

As the last step, a similar study was performed at the sulphur sites for the sake of completeness. No XMCD signal was found either at the S L- or K-edge, in agreement with the results at the Zn K-edge, which proved the FML behaviour being related to Zn-O bonds.

XAS spectra at the sulphur sites, supported by the corresponding ab-initio calculations, revealed again the formation of neat interfaces between the W-ZnO NP core (or layer) and the organic capping (or W-ZnS layer). The structural details at the interface differ on each sample, independently of the synthesis process.

Moreover, in agreement with XANES studies at the Zn K-edge, the present work has proved both, the enlargement of O-Zn bond length and the decrease of S-Zn interatomic distances, to a more W-ZnS like and W-ZnO configurations, respectively. The occurrence of both mechanisms is not equal for every sample, and it is probably not controllable. From there that the structural details, hence the magnetic properties, of this type of systems differs so widely, and the need of carrying out a detailed characterization for each sample under study. In addition, as no appreciable XMCD were observed at the sulphur absorption edges, the previously claimed dominant role of Zn-O bonds into the HTFM is confirmed, while the possibility of a oxygen ferromagnetic state is reinforced.

Finally, we want to recall that to date, several types of defects, such as oxygen and zinc vacancies, have been proposed by different authors to induce HTFM in ZnO-based DMSs. Although XAS experiments have been used to determine the exact type of defect that causes the HTFM, we have proved that this technique is not capable of such task. For that purpose we performed an XAS study of Zn_{0.95}Mn_{0.05}O thin films prepared with different sputtering gases and presenting HTFM behaviour. The experimental data have been compared to ab-initio XANES computations performed at both the Zn and Mn K-edges. Our results indicate that contrary to previous claims, by assuming a reliable defect concentration randomly distributed the

presence of both oxygen and zinc vacancies is not detectable in the XANES spectra. Indeed, the theoretical computations presented here point out that Mn adapts its local environment by increasing the Mn-O interatomic distance with the nearest-neighbour oxygen atoms. Therefore, these results give theoretical support to our conclusions about the FM of ZnO systems.

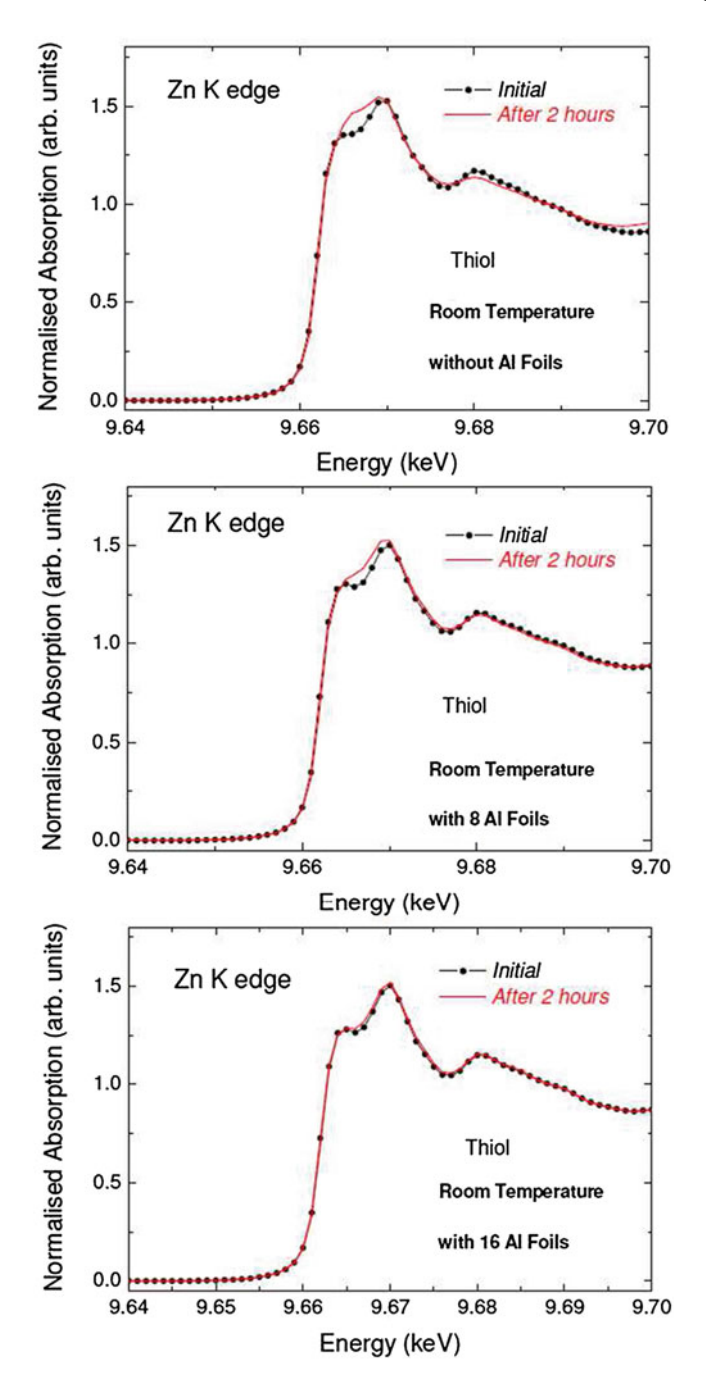
Appendix A: Degradation

We have verified that these long beam-exposure times do not degrade the samples. Only in the case of the THIOL sample (20-12C-1) we have found that exposition of the beam modifies the absorption profile of the samples recorded at room temperature (RT), as seen in Fig. A.1. In contrast, no degradation is found at lower temperatures on the same sample. It should be also noted that these measurements have been accumulated through a 3 year period on the same samples and specimens. No modification of both the XAS and XMCD spectra have been found on the same specimens measured at the initial run and up to three years later, either in different specimens prepared from the same sample. This indicates that the observed magnetic properties are intrinsic, stable in time and they do not depend on sample manipulation.

The new series of THIOL-capped NPs presented similar degradation effects upon beam exposition at room temperature (Fig. A.2).

Appendix B: Intrinsic Character of O K-edge XANES B and C Peaks

It is important to make clear that features of XANES spectra are intrinsic to the sample, especially regarding peak C at low temperature. Comparison with CO, CO₂, O₂ and water/ice O K-edge spectra [1–5] ruled out the possibility of C being a consequence of some kind of condensation in the sample chamber. On the other hand, the profile is reproduced at different positions of the layer, so is less likely due to surface contamination or layer degradation. As a final remark, peak C development is accompanied by changes in the general shape of the spectra, i.e the reduction of the white line. In similar way, the decrease of peak B follows the increase of the



 $\textbf{Fig. A.1} \quad \text{Comparison of the room temperature Zn K-edge XANES spectra of the 20-12C-3 sample recorded as a function of the beam exposition time with and without using Al filters to attenuate the beam intensity$

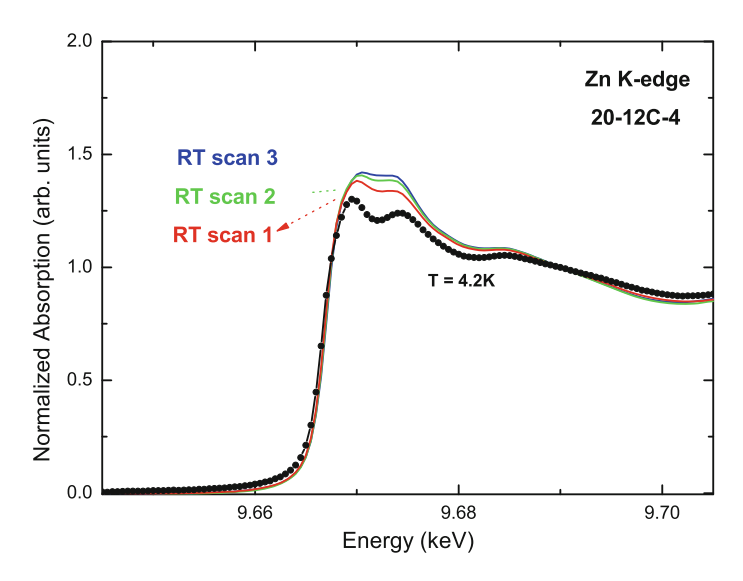


Fig. A.2 Comparison of the room temperature Zn K-edge XANES spectra of the 20-12C-4 sample recorded as a function of the beam exposition time with and without using Al filters to attenuate the beam intensity

intensity of pre-edge hump A. That strongly suggests the intrinsic character of the structures.

Thus, we considered the possibility of peak C being caused by preferential orientation effects, since O K-edge XANES spectra present a high polarization-dependence whatever octahedral or tetrahedral environment is displayed [6] and the experimental set-up entails the normal incidence of the electric field with respect of ZnO c axis. Based on polarized XANES measures of W-ZnO anisotropic nanorods [7, 8] (Fig. A.3a) the expected effects of the film orientation include the decrease of main peak D and enhancement of feature E. However, that is not observed in our case. Considering that the thickness of each sample layer is nominally 4 nm, so at the TEY probing depth, we should take into account interdiffussion of ZnS and ZnO layers and structural mismatches, hence the anisotropy and therefore polarization effects would be drastically reduced.

Similar B feature has been reported in the case of P-doped ZnO monolayers measured at RT in TEY mode [9] presented the same peak B before annealing (Fig. A.3b). On the other hand, no systematic modification of the O K-edge XAS profile of ZnO is found when doped with transition metals. While Mn (Fig. A.3c) does not entails neither peaks B or C, but the pre-edge peak A enhancement, the later being addressed to the hybridization with Mn 3d levels [10], peak B was found to increase in thin films as the percentage of Cu doping does [11] (Fig. A.3d). When ZnO thin films are doped with Co and Li [12, 13], the presence of peak B is more subtle. Indeed, Co-doping single layer films bring a low energy double feature shoulder close to the transition threshold, and a broadening of the spectral features. In addition, the

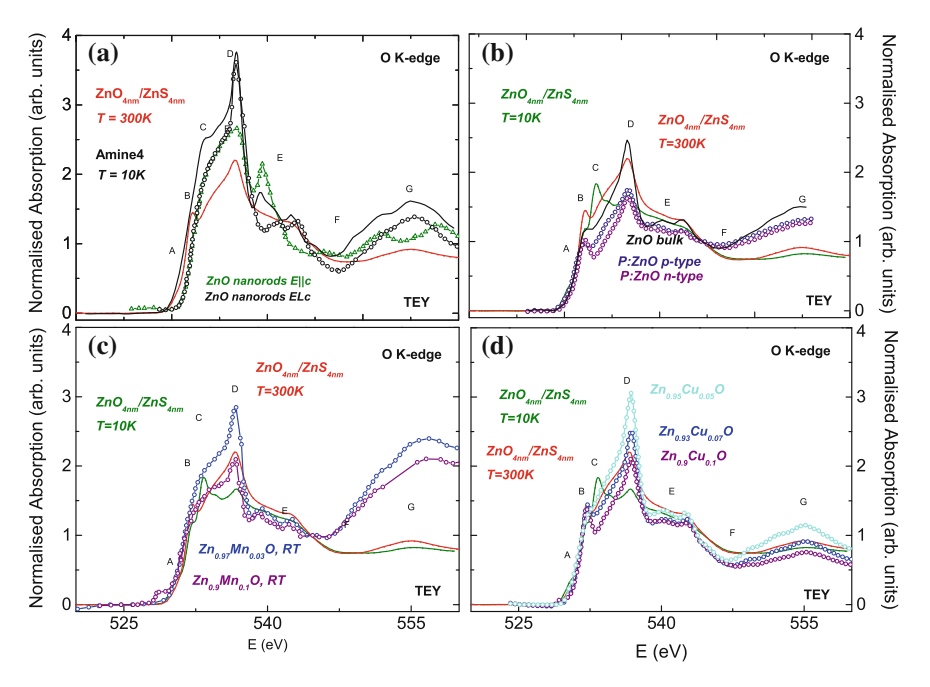


Fig. A.3 O K-edge XANES of **a** W-ZnO nanorods, being the electric field parallel or perpendicular to c axis (growth direction) [7, 8]; other nanostructured ZnO systems doped with different element, such as **b** P [9], **c** Mn [10] and **d** Cu [11]

onset of the spectra is shifted to lower energy and the white line is smeared out. A similar profile was found by doping ZnO thin film with a 7% of Cu [14], but in this case the effect of polarization should be involved too. Finally, for both Li and Co dopants the double structure is strongly enhanced and clearly separated as two peaks, of which the one at higher energy matches peak B. Similar inconclusive results are found in the case of $Zn_{1-x}Co_xO$ nanorods [15].

All these contradictory results point out to the extrinsic origin of the aforesaid findings. On the contrary, none of the of the previous work showed any trace of feature C. The possibility of peak C being due to the formation of some S-O bonds in the samples has been also explored. However the experimental spectra recorded in the case of S-O compounds [16–19] do not support this possibility. That is not surprising recalling that it is harder for sulfur and oxygen anions to bond together as long as the Zinc cations are present [20].

Appendix C: Ab-initio Calculations at the O K-edge

We built up a ZnO cluster in wurtzite structure, including the contributions from neighbouring atoms located within the first 8 Å around the photoabsorbing oxygen atom. The choice of the overlapping factor does not affect the relative position of computed spectral features but slightly their shape and intensity. Hence we imposed an overlapping factor of 1%, like for Zn K-edge calculations. Regarding the choice of the ECP we have found that the real Hedin-Lundqvist presents a better agreement with the experimental signal at higher energies beyond the first 35 eVs above the absorption edge. The real Dirac-Hara ECP yields the best reproduction of the relative energy positions and intensities at the white line and lower energy, the region of interest. This choice of ECP was kept for all the performed computations (Fig. A.4).

According to previous chapters assessment we studied next the influence on XANES spectra of the ZnO-ZnS interface developed in Thiol NPs and thin films. In that region it makes sense that interatomic distances are modified as the Zn atoms adapt from the ZnO core (NPs) or layer (thin films multilayers) to the ZnS configuration. Moreover scattering with sulphur atoms should be easily detectable, since the backscattering properties are quite different with respect to those from oxygen. Considering those factors, we may check the effects of both, the increment of Zn-O bond lengths and the presence of sulphur atoms, in the XANES signal.

We started to evaluate the Zn-O bonds lengthening. The original cluster was altered in such a way that the Zn-O interatomic distance around the absorber O atom resembles those of ZnS in the first coordination shell (Fig. A.5). The computations

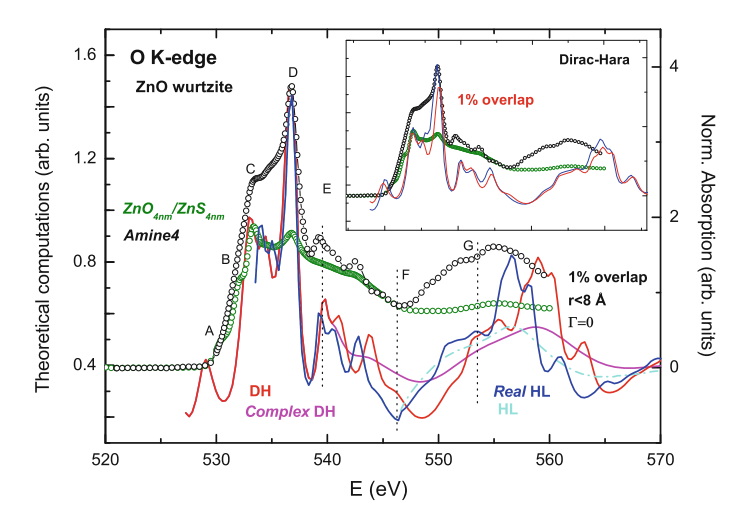


Fig. A.4 Experimental XANES and theoretical computations of a cluster of W-ZnO up to 8 Å. The calculations have been performed with different exchange and correlation potentials: Dirac-Hara and Hedin-Lundqvist (real and complex) with a 1% overlapping factor. Besides, the *inside panel* shows the same case with both 1 and 10% overlap

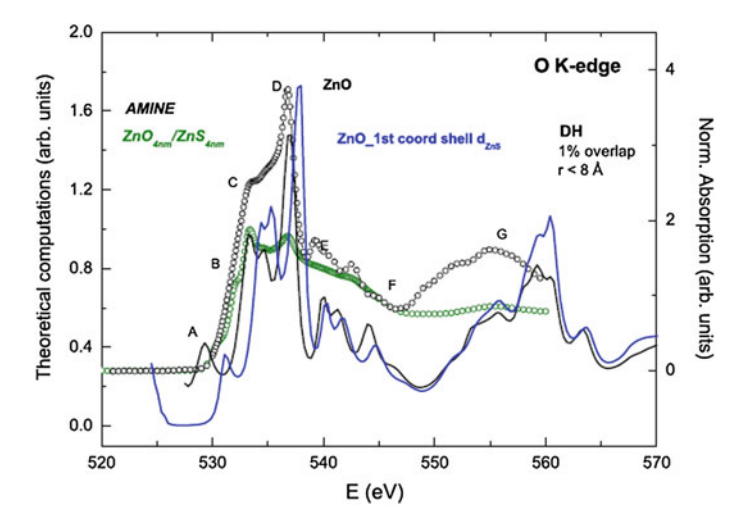


Fig. A.5 Comparison of AMINE and ZnO_{4nm}/ZnS_{4nm} spectra and theoretical XANES of a W-ZnO cluster with the first Zn-O bondlength extended

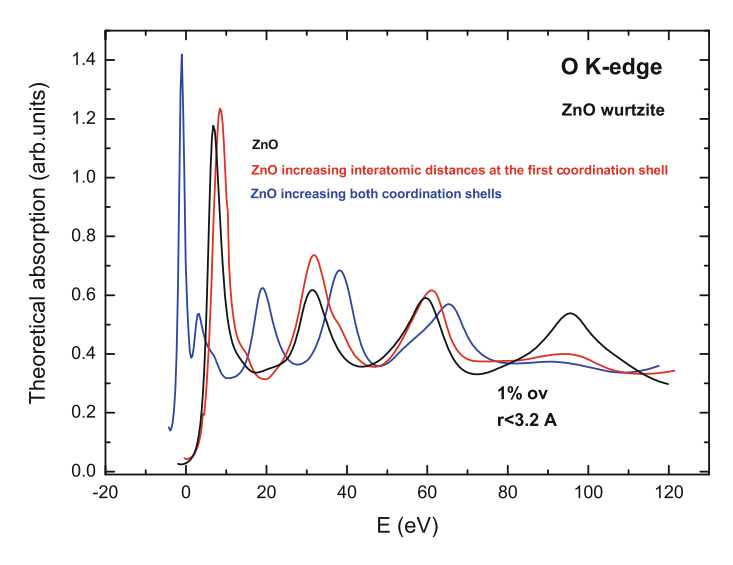


Fig. A.6 The position of the absorption edge is affected by the increment of interatomic distances in a cluster built up to 3.25 Å; when the full cluster is expanded (*blue line*) the *white line* moves to lower energy (See text for details)

displayed a shift of the white line to higher energy. This behaviour is certainly not expected. Shorter interatomic distances mean bigger binding energies, so the resonance at the spectra should be located at higher energies, in agreement to Natoli's rule [21]. However just by including a second shell the expected behaviour is obtained (Fig. A.6).

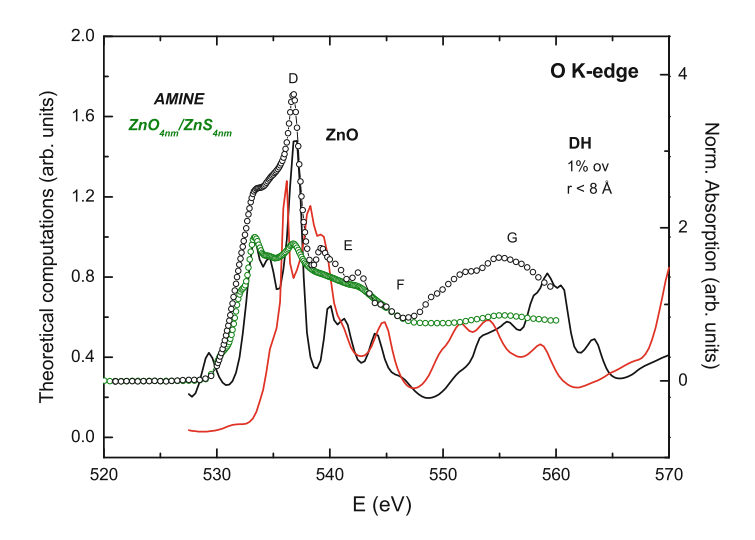


Fig. A.7 Comparison of AMINE and ZnO_{4nm}/ZnS_{4nm} spectra and theoretical XANES of a W-ZnO cluster in which oxygen atoms of the second coordination shell have been replaced by sulfur atoms

The second step was to introduce sulphur atoms in the original ZnO cluster, as plotted in Figs. A.7 and 6.2 (which was presented along the discussion). We placed substituted oxygen atoms from the second coordination shell by sulphur atoms, at both the original ZnO arrangement and taking O-Zn-S interatomic distances of ZnS. If sulphur atoms are introduced by keeping the O-Zn-S distances of W-ZnS the first high peak matches the peak C of ZnO_{4nm}/ZnS_{4nm} , as seen earlier.

References

- A. Nilsson, D. Nordlund, I. Waluyo, N. Huang, H. Ogasawara, S. Kaya, U. Bergmann, L.A. Naslund, H. Astram, P. Wernet, K.J. Andersson, T. Schiros, L.G.M. Pettersson, L.A. Naslund, H. Ostrom, L.G. Pettersson, J. Electron. Spectrosc. Relat. Phenom. 177, 99 (2010)
- 2. S. Myneni, Y. Luo, L. Näslund, M. Cavalleri, J. Phys.: Condens. Matter 14, L213 (2002)
- 3. C. Cappa, J. Smith, K. Wilson, J. Phys.: Condens. Matter 20, 205105 (2008)
- 4. C. Huang, K. Wikfeldt, T. Tokushima, PNAS 106, 15214 (2009)
- 5. T. Pylkkanen, A. Sakko, M. Hakala, J. Phys. Chem. B 115, 14544 (2011)
- 6. J. Chen, Surf. Sci. Rep. 30, 1 (1997)
- 7. J.W. Chiou, J.C. Jan, H.M. Tsai, C.W. Bao, W.F. Pong, M.H. Tsai, I.H. Hong, R. Klauser, J.F. Lee, J.J. Wu, S.C. Liu, Appl. Phys. Lett. **84**, 3462 (2004)
- 8. J. Guo, L. Vayssieres, C. Persson, J. Phys.: Condens. Matter 14, 6969 (2002)
- 9. V. Vaithianathan, S. Kim, B. Lee, Electron. Mater. Lett. 1, 121 (2005)
- P. Thakur, K.H. Chae, J.Y. Kim, M. Subramanian, R. Jayavel, K. Asokan, Appl. Phys. Lett. 91, 162503 (2007)
- 11. P. Thakur, V. Bisogni, J. Cezar, J. Appl. Phys. 107, 103915 (2010)
- 12. T. Tietze, M. Gacic, G. Schütz, G. Jakob, New J. Phys. 10, 055009 (2008)

13. S. Krishnamurthy, C. McGuinness, L.S. Dorneles, M. Venkatesan, J.M.D. Coey, J. Appl. Phys. **99**, 08M111 (2006)

- 14. D.J. Keavney, D.B. Buchholz, Q. Ma, R.P. Chang, Appl. Phys. Lett. 91, 012501 (2007)
- J.W. Chiou, H.M. Tsai, C.W. Pao, K.P. Kumar, S.C. Ray, F.Z. Chien, W.F. Pong, M.H. Tsai, C.H. Chen, H.J. Lin, J.J. Wu, M.H. Yang, S.C. Liu, H.H. Chiang, C.W. Chen, Appl. Phys. Lett. 89, 043121 (2006)
- 16. N. Pangher, L. Wilde, M. Polcik, J. Haase, Surf. Sci. **372**, 211 (1997)
- 17. M. Polcik, L. Wilde, J. Haase, B. Brena, G. Comelli, Surf. Sci. Lett. **381**, 568 (1997)
- 18. J.A. Rodríguez, T. Jirsak, A. Freitag, J. Hanson, Catal. Lett. 62, 113 (1999)
- 19. J.A. Rodríguez, T. Jirsak, S. Chaturvedi, M. Kuhn, Surf. Sci. **442**, 400 (1999)
- 20. P. Sadik, S. Pearton, D. Norton, J. Appl. Phys. **101**, 104514 (2007)
- 21. D. Koningsberger, R. Prins, *X-ray Absorption: Principles, Applications, Techniques of EXAFS, SEXAFS, and XANES* (Wiley, New York, 1988)